
CORNEAL CONTRIBUTION TO THE WAVEFRONT ABERRATION OF THE EYE

Thomas O. Salmon, O. D.

Submitted to the faculty of the University Graduate School
in partial fulfillment of the requirements
for the degree
Doctor of Philosophy
in the School of Optometry

November, 1999

Accepted by the Graduate Faculty, Indiana University, in partial fulfillment of the requirements for the degree of Doctor of Philosophy.

Larry N. Thibos, Ph.D., Chairman

Arthur Bradley, Ph.D.

Doctoral Committee

Douglas G. Horner, O.D., Ph.D.

Raymond A. Applegate, O.D., Ph.D.

October 15, 1999

P. Sarita Soni, O.D., M.S.

© 1999
Thomas O. Salmon
ALL RIGHTS RESERVED

This dissertation
is dedicated to the man
I love and respect most in all the world—my father:

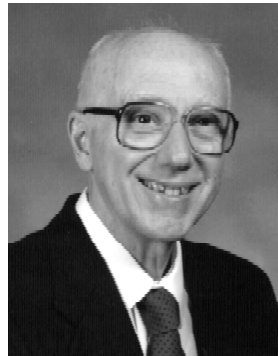
Thomas Oakley Salmon, Jr.

For his love, integrity, and wisdom, I am deeply thankful.

IN MEMORIUM

RAYMOND F. SEARS

(November 14, 1921 - June 2, 1999)



Ray Sears'
steadfast prayer,
love and Christian example
will always be remembered and treasured.

Acknowledgements

I gratefully acknowledge the contribution of the following people and organizations to my Ph.D. education.

Doctoral Committee

I have been particularly fortunate to have been associated with some of the world's leading vision scientists, and I sincerely appreciate their efforts on my behalf.

Larry N. Thibos, Ph.D., Chairman

Arthur Bradley, Ph.D.

Douglas G. Horner, O.D., Ph.D.

Raymond A. Applegate, O.D., Ph.D.

P. Sarita Soni, O.D., M.S.

Indiana University Faculty

I am thankful for the instruction and support other Indiana University faculty including Andrew J. Hanson, Ph.D., who taught all my graduate computer science courses; Drs. Daniel R. Gerstman and Clifford W. Brooks, my optics teachers who, along with Gordon G. Heath, O.D., Ph.D., encouraged me to pursue the Ph.D. degree.

Graduate students

The friendship and help of my fellow graduate students, especially that of Yi-Zhong Wang, are sincerely appreciated. Among my other colleagues were Nisha Jani, Maurice Rynders, Roger Anderson, Colleen Riley, Sassan Azarian, Fansheng Kong, Xin Hong, Dave Evans, Ron Tutt, John Buch, Jenny Hicks, Tracy Schroeder, Jie Zhou, Hui-Nan Zhang, Kevin Liedel, Salih Al-Oliky.

Librarians

Optometry librarians Doug Freeman and Anne Foster provided valuable research assistance.

Financial Support

Substantial financial support was provided by the following organizations:

Indiana University School of Optometry
National Eye Institute (through a grant to Larry N. Thibos, Ph.D.)
American Optometric Foundation Ezell Fellowship program
Northeastern State University College of Optometry
EyeSys Vision Group
American Academy of Optometry Student Travel Fellowship program
Indiana Chapter of the American Academy of Optometry

Technical Support

Kevin Haggerty provided critical computer programming support, and Doug Hodgson helped with data processing. Jeff Johnson and Judy Felty provided additional computer and technical support. Tim Thacker, Danny Jackson and Jason Wood assisted with construction of the laboratory apparatuses.

Indiana University Staff

Administrative support was provided by Jackie Olson and other staff members, including Ritsuko Noda, Gloria Cochran, Sue Gilmore, Anita Bastin, Craig Combs, Joanne DeLone, Cindy Lepore, Lee Wagoner.

Moral and Spiritual Support

The encouragement and prayers of many Christian friends, including those from the following churches are sincerely appreciated: Church of the Good Shepherd, Bloomington, Indiana; Matsumigaoka Christian Church, Tamagawagakuen, Japan; Higashinada Baptist Church, Kobe, Japan; First Evangelical Free Church, Tahlequah, Oklahoma. In addition I sincerely appreciate the encouragement of my fellow faculty members and optometry students at the Northeastern State University College of Optometry in Tahlequah, Oklahoma.

Finally, I am deeply thankful for the love and faithful support of my wife, Junko, who persevered with me through every step of the long Ph.D. course.

Preface

My appreciation for visual optics began when, as an eighth-grade student, my father took me to visit the local optometrist to be fit with contact lenses. When I stepped out of his office, I was astounded at what I could now see—every leaf in the trees and every brick in the buildings! My experience with contact lenses eventually led to an interest in optometry as a career. As a first-year optometry student, my favorite subject was optics, and since optometry school, my favorite part of clinical practice has been contact lenses. My interest in contact lenses developed into an interest in corneal optics at the same time that refractive surgery and measurement of corneal topography were becoming popular. Graduate courses in Fourier optics and optics of the human eye, as well as a memorable scientific meeting at the *Instituto de Optica* (CSIC) in Madrid, Spain, in 1995, stimulated a keen interest in new technologies and new research questions about optics of the human eye. Given my continuing deep interest in visual optics, the development of new clinical problems associated with refractive surgery, and the availability of critical new research tools, I found myself in a wonderful position to pursue a fascinating topic for my doctoral research—the corneal contribution to the wavefront aberration of the eye. The Ph.D. course has been long and challenging, but it has also been fun. Hopefully, this dissertation will convey, not just what I learned and the techniques I developed, but also the pleasure I had in doing this research.

“Ears that hear and eyes that see—the LORD has made them both.”

(Proverbs 20:12)

Thomas O. Salmon, O.D.

CORNEAL CONTRIBUTION TO THE WAVEFRONT ABERRATION OF THE EYE

Chairman: Larry N. Thibos, Ph.D.

Professor of Optometry, Indiana University School of Optometry

Introduction: The wavefront aberration function is one of the most informative descriptors of optical performance, and new techniques have recently been developed to measure this function in living human eyes. Corneal refractive surgery is creating a population of patients with abnormally large aberrations, and the key to improving optical results is a better understanding of the eye's aberrations. The purpose of this research was to determine the corneal contribution to the aberrations of three normal human eyes. Methods: An EyeSys computerized videokeratoscope was used to measure corneal topography, and the corneal wavefront aberration was computed. A Shack-Hartmann wavefront sensor was used to measure the ocular wavefront aberration. Corneal and ocular aberration data were fitted to Zernike polynomials, and corresponding coefficients were compared to determine the relationship between corneal, internal and total ocular aberrations. Results: Contrary to what other researchers had hypothesized, I did not find a general pattern of aberration balancing between the cornea and internal elements of the eye. Instead, within a range of normal values, the relationship between the optical elements varied with each eye. Conclusion: We cannot know the relationship between the corneal and ocular wave aberration functions without individually measuring these functions for each eye. Recent improvements in corneal topographers have made it clinically feasible to measure the corneal wavefront aberration function. Better correction of ocular aberrations will require new clinical instruments that can measure the wavefront aberration of the whole eye as well.

Contents

CHAPTER 1 - Introduction

1.1 APPROACHES TO VISUAL OPTICS	1
1.2 OPTICAL QUALITY VERSUS IMAGING PERFORMANCE	2
1.3 APPLICATIONS	3
FIGURE	4

CHAPTER 2 - Basic Principles of Wave Optics

2.1 OPTICAL PATH LENGTH	5
2.2 WAVEFRONT ABERRATION	7
2.3 FOURIER OPTICS	9
2.4 POLYNOMIAL EXPANSION OF ABERRATION FUNCTIONS	11
2.5 FIGURES	18

CHAPTER 3 - Corneal Topography Basics

3.1 IMPORTANCE OF CORNEAL OPTICS	21
3.2 CORNEAL SHAPE	23
3.3 HISTORY OF QUANTITATIVE CORNEAL MEASUREMENT	25
3.4 VIDEOKERATOSCOPE RECONSTRUCTION ALGORITHMS	28
3.5 CORNEAL TOPOGRAPHIC MAPS	31
3.6 BEYOND TOPOGRAPHY — CORNEAL OPTICS	39
FIGURES	40

CHAPTER 4 - Accuracy of the EyeSys Videokeratoscope

4.1 INTRODUCTION	47
4.2 METHODS	54
4.3 RESULTS	56
4.4 DISCUSSION	58
FIGURES	61

CHAPTER 5 - The Wavefront Aberration Function of Normal Human Corneas	
5.1 INTRODUCTION	64
5.2 METHODS	75
5.3 RESULTS	83
5.4 DISCUSSION	89
FIGURES	92
CHAPTER 6 - Accuracy of the Shack-Hartmann Wavefront Sensor	
6.1 INTRODUCTION	103
6.2 METHODS	106
6.3 RESULTS	110
6.4 DISCUSSION	114
FIGURES	116
CHAPTER 7 - Corneal Contribution to the Wavefront Aberration of the Eye	
7.1 INTRODUCTION	124
7.2 METHODS	130
7.3 RESULTS	140
7.4 DISCUSSION	147
FIGURES	153
REFERENCES	162
APPENDIX A - Excel Spreadsheet: Zernike coefficient to spectacle Rx conversion	178
Appendix B - Computing the Axial Radius of Curvature of an Ellipse	179
Appendix C - README File for the EyeSys Utility Program, CORSAG18.EXE	182
Appendix D - MATLAB Script: Compute the Corneal Wavefront Aberration	184
Appendix E - MATLAB Script: Zernike Polynomial Fitting of Wavefront Data	188
Appendix F - Complete List of Zernike Coefficients	192
Appendix G - Experimental Apparatus Photographs	195
Appendix H - Laser Safety with the Shack-Hartmann Wavefront Sensor	198
Curriculum vitae	

CHAPTER 1

Introduction

After decades with relatively few new discoveries, the field of visual optics has been energized by two recent developments: refractive surgery and adaptive optics. Refractive surgery created a clinical need to better understand the optics of the eye, and adaptive optics, borrowed from astronomy, provided new tools that would allow significantly improved measurement of the eye's optical aberrations. We are now prepared to investigate, beyond what was ever possible before, key issues in visual optics such as the role of the cornea in the aberrations of the eye. The specific question that I studied in this dissertation was, What is the corneal contribution to the monochromatic aberrations of the normal human eye? This basic issue has clinical applications to the correction of vision and medical imaging of the internal eye.

1.1

APPROACHES TO VISUAL OPTICS

A fundamental problem in visual optics is, How to best measure optical quality of the human eye? To an optometrist or ophthalmologist, who routinely measures the eye's refractive error, this may appear to be a simple question. Clinically, optical quality of the eye is described by the spherocylindrical spectacle prescription, which specifies two basic optical defects: defocus and astigmatism. The refractive error is specified in terms of the lens required to correct it. Optical aberrations beyond astigmatism and defocus also exist, but in current practice these are ignored for several reasons. First, in normal eyes, these residual aberrations degrade vision very little compared to defocus or astigmatism. Next, there is no clinical test available for measuring the higher order aberrations. Finally, even if the aberrations could be measured, conventional spectacle lenses cannot correct them. For the vast majority of patients, higher order optical aberrations are clinically insignificant. Until recently, and except for cases such as keratoconus, most doctors rarely saw patients with optical defects that could not be largely corrected with either spectacles or contact lenses.

Circumstances are quickly changing, and for many patients, higher order optical aberrations are becoming an important consideration. Three recent developments in eye care and vision science account for

this. First, the yet-to-be-perfected refractive surgeries are producing a population of patients with abnormally large optical aberrations (Maguire, 1994). Next, new methods have been developed to measure those aberrations (Salmon & Thibos, 1998). Finally, new devices are being developed that can correct the higher order aberrations of the eye. Deformable mirrors have recently been used in the laboratory to correct the eye's aberrations (Liang, Williams, & Miller, 1997), and liquid-crystal micro lens arrays, which may one day work like electronic spectacles, are under investigation (Thibos & Bradley, 1997; Vargas-Martin, Prieto, & Artal, 1998). Measurement of the eye's optical aberrations is therefore becoming both clinically relevant and technologically feasible. Correction for aberrations will certainly become an integral part of refractive surgery and contact lens fitting of the future.

1.2

OPTICAL QUALITY VERSUS IMAGING PERFORMANCE

One direct approach for evaluating an optical system, such as the eye, is to measure the properties of light passing through the system. Optical performance can also be evaluated indirectly by measuring image quality. For the human eye, a familiar test of image quality is the Snellen visual acuity test. If a patient has 20/15 vision, the doctor usually assumes that they have no significant refractive error (i.e., good optics). On the other hand, if the patient's visual acuity is 20/200 (i.e., poor image quality), the doctor can suspect a refractive error, though without actually measuring the refraction, he will not be able to correct it. Since the eye's aberrations are difficult to measure directly, visual optics research over the last half century has relied on tests of retinal image quality (indirect approach) to evaluate optical performance of the human eye. One technique, the double-pass method, has been used to estimate the eye's modulation transfer function (MTF). Newer tests, which directly measure aberrations in the light itself, can be used to compute, not only the MTF, but other measures of imaging performance such as the phase transfer function, and point spread function. The converse, however, is not true. Neither the optical defects nor the required optical correction can be determined from image quality alone. Shortly before I began this research, a Shack-Hartmann wavefront sensor was, for the first time, used to directly measure the aberrations of the human eye (Liang, 1991; Liang, Grimm, Goelz, & Bille, 1994), and I incorporated this new technology as a major component of my research.

Optical reflection, scatter, and absorption can all theoretically degrade image quality, but for most normal eyes these factors are relatively small and were not investigated in this study. Diffraction is another optical phenomenon that always affects image quality to some degree, and it was taken into account with the wavefront aberration functions when I evaluated imaging performance. In most natural conditions the human eye uses polychromatic light, and chromatic aberration is an important factor that limits retinal

image quality. Chromatic aberration varies little between individuals (van Meeteren, 1974). Because of its predictability, chromatic aberration can be calculated by integrating the spectral sensitivity weighted, wavelength dependent defocus across the visible spectrum (Bour, 1980; van Meeteren & Dunnewold, 1983; Thibos, 1987). Monochromatic aberrations, however, show large individual variations (Atchison, Collins, Wildsoet, Christensen, & Waterworth, 1995; Campbell, Bobier, & Roorda, 1995; Collins, Wildsoet, & Atchison, 1995), so they must be measured rather than calculated. This research was concerned with measuring the monochromatic aberrations of the corneal surface and whole eye for three normal eyes.

1.3

APPLICATIONS

A full knowledge of the eye's optical defects is the key to its complete optical correction. Better optical correction has applications in two broad areas of clinical eye care; namely, visual correction and diagnostic retinal imaging (Fig. 1). Obviously, excellent optical quality is necessary for excellent vision, since light travels inward, through the eye's optics, to form the retinal image. This is the starting point for the visual process. A better understanding of corneal optics and its role in the optics of the whole eye can help us evaluate and improve vision.

In the case of diagnostic retinal imaging, light is reflected out of the eye and passes outward through the eye's optics. The optical elements of the eye serve as the objective lens of an imaging system designed to view the internal eye. Correction of the eye's optical defects, including the higher order aberrations, has enabled scientists to visualize microscopic structures never before seen in the living eye (Liang, Williams & Miller, 1997), and this is creating new opportunities for basic research and early diagnosis of retinal diseases.

At this point, our understanding of the eye's optics is incomplete. This research is designed to address one of the key unresolved issues—the corneal contribution to the monochromatic aberrations of normal eyes. A knowledge of the aberration structure of normal eyes is a precursor to the correction of aberrations in both normal and anomalous eyes.

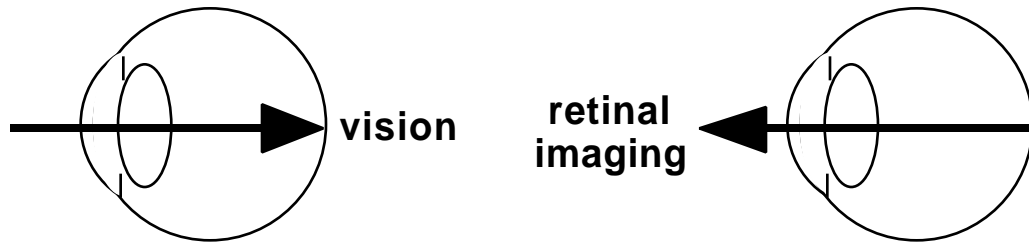


Figure 1

Light must pass through the same optical system, though in opposite directions, for both vision (left) and diagnostic retinal imaging (right). Better optical correction will benefit both.

Basic Principles of Wave Optics

Basic optometric education has emphasized geometric rather than wave optics, and this has been sufficient to prepare optometrists for the majority of optics problems they encounter in clinical practice. Geometric optics uses ray propagation to describe light, and clinical problems can usually be solved with its straightforward paraxial equations. The increasing importance of optical aberrations in vision research and in clinical practice requires that modern optometrists have a more thorough understanding of the wave properties of light. Chapter 2 reviews basic principles that were used in the experimental design, data analysis and interpretation of data in this research.

2.1

OPTICAL PATH LENGTH

Light propagates through space in the form of waves, somewhat like the ripples created when a stone is dropped in a pond. The pond ripples are formed as crests and troughs, expanding outward, and when seen from above, they look like expanding circles. Since all portions of the wavefront propagate through water with uniform velocity, all points on this circle are equidistant from the center, and all points will have been traveling for the same length of time. Similarly, for a pulse of light emitted from a point source in three-dimensional space, the wavefronts are like expanding spherical shells. At any instant, all points on a wavefront will be equidistant from the point source, and each point will have traveled for equal time. The wavefront expands very quickly since the waves propagate through space at the speed of light.

The velocity of light in a vacuum (v_0) is constant for all wavelengths but it is slower in other optical media, and the velocity will vary as a function of wavelength (λ). The refractive index (n) of a medium is defined for each wavelength as the ratio of the velocity of light in a vacuum to the velocity (v_m) of that wavelength in the medium (Eq. 2-1). A wavelength of 589 nm is commonly used as the reference wavelength when specifying the index of refraction for optical materials.

$$n = \frac{v_0}{v_m} \quad (2-1)$$

Frequency (f) is inversely proportional to wavelength (Eq. 2-2), and for a particular wavelength, its frequency remains constant in all optical media. In order for the frequency to remain constant, the wave-

$$f = \frac{v}{\lambda} \quad (2-2)$$

length in a new medium (λ_m) must change in proportion to its velocity (v_m) in that medium. For example, when crossing from air to a denser medium, velocity decreases and the wavelength also decreases. As a consequence, the wavelength of light in a new medium is equal to the wavelength in a vacuum (λ_0) divided by the index of refraction:

$$f = \frac{v_0}{\lambda_0} = \frac{v_m}{\lambda_m} \text{ therefore, } \frac{v_0}{v_m} = \frac{\lambda_m}{\lambda_0} = n, \text{ and } \lambda_m = \frac{\lambda_0}{n} \quad (2-3)$$

In some cases it is necessary to calculate the physical distance traveled by light in a new medium, and the relationship is developed in Eq. (2-4). The physical distance traveled by light in a vacuum in unit time (t) is d_0 , so the physical distance traveled in another medium (d_m) during the same time is the distance in a vacuum divided by the medium's index of refraction.

$$\frac{d_m}{t} = v_m = \frac{v_0}{n} = \frac{\left(\frac{d_0}{t}\right)}{n}, \text{ therefore, } d_m = \frac{d_0}{n} \quad (2-4)$$

In some cases the distance traveled by light in a medium is known (d_m), but we must calculate the distance it would have traveled in a vacuum (d_0) during the same time. This is known as the optical path

length (OPL), and it can be expressed in units such as micrometers. Equation (2-5), which is equivalent to Eq. (2-4), shows that the OPL is the product of distance d_m and the refractive index (n) of that medium.

$$OPL = d_m n \tag{2-5}$$

The distance traveled by light in any media may also be normalized by the wavelength in that medium (λ_m). As shown in Eq. (2-6), this is equal to the OPL divided by the wavelength in a vacuum. Since image formation and image quality depend on interference of wavefronts, it is useful to describe OPL errors, that is aberrations, in terms of wavelengths.

$$\frac{d_m}{\lambda_m} = \frac{d_m}{\left(\frac{\lambda}{n}\right)} = \frac{d_m n}{\lambda} = \frac{OPL}{\lambda} \tag{2-6}$$

2.2

WAVEFRONT ABERRATION

For light entering a theoretically perfect (defocus, aberration and diffraction free) eye, refracted light, after passing through the exit pupil, converges in the form of spherical wavefronts to a focal point on the retina. Recalling that an optical wavefront represents a surface of uniform distance and time traveled, all points on the wavefront are in phase. Therefore when the spherical wavefront collapses to the focal point, all the light arrives at this point in phase, and maximum radiant energy is delivered to that point (Williams & Becklund, 1989). If there were no diffraction (physically impossible), this would form a perfect point, but because of diffraction, even the most perfect optical system will form a focal point that is slightly blurred. For a round pupil, the diffraction pattern of a point source appears as a bright spot, the *Airy disk* (Fig. 2.1), surrounded by faint concentric rings. The angular width of the Airy disk in radians (θ) may be calculated for a circular aperture by Eq. (2-7), where the diameter (p) and wavelength (λ) are in meters.

$$\theta = \frac{2.44 \lambda}{p} \tag{2-7}$$

In the case of a square aperture, a factor of 2 rather than 2.44 is used. If the focal length is known, the

linear extent (s) of the Airy disk can be calculated from Eq. (2-8), where $f/\#$ is the ratio of focal length to aperture diameter.

$$= \frac{2.44}{p} = \frac{s}{f}, \text{ therefore, } s = \frac{2.44 f}{p} = 2.44 (f/\#) \quad (2-8)$$

These basic formulae apply when the intensity distribution across the light beam is uniform. If the intensity is Gaussian, as is true for most laser beams, the focal point will not be an Airy disk, but will be a Gaussian spot, and the formula for estimating spot size becomes (Saleh & Teich,):

$$s = 4 (f/\#) \quad (2-9)$$

This formula (Eq. 2-9) may be used to estimate the spot size in Shack-Hartmann wavefront sensor reference images.

Diffraction is a fundamental property of the wave nature of light whenever it passes through an aperture. Since all optical systems have a limiting aperture, it is impossible to build a diffraction-free optical device. It is possible, by careful design, to improve image quality in an optical system by reducing aberrations, but it is impossible to exceed the limits to image quality set by diffraction. Ultimate optical quality is therefore referred to as “diffraction limited”—that is, limited by diffraction only.

Light passing through an optical system, which is less than perfect, will produce a wavefront in the exit pupil that is aberrated from the ideal spherical surface, known as the *pupil sphere*. The apex of the pupil sphere coincides with the pupil center (Fig 2.2 point p), and its center of curvature is the paraxial focal point (f). Except in the case of very small pupils, where diffraction is large, aberrations are usually the major factor beyond defocus that degrades image quality. The wavefront aberration function, $W(x,y)$, is the scalar distance between the aberrated wavefront and the pupil sphere. Its precise definition varies slightly in different optics reference books. For the refracted ray (heavy line) shown in Fig. 2.2, the wavefront aberration at point a is defined as distance ab (Hopkins, 1950; Born & Wolf, 1980), or it may be defined at point a' as distance $a'b$ (Williams & Becklund, 1989; Smith, 1990). For the range of typical ocular wavefront aberrations, these distances are essentially equal (Welford, 1986). For points on the aberrated wavefront that have advanced ahead of the pupil sphere, the sign of $W(x,y)$ is positive. For portions of the wavefront that are retarded behind the pupil sphere, the sign is negative. The physical distance between the wavefront and pupil sphere is usually multiplied by the index of refraction (for OPL), divided by the wavelength in a vacuum (yields number of wavelengths), and multiplied by 2, to transform

the distance into a phase error. The wavefront aberration is the most important component of the *pupil function*, $P(x,y)$ shown in Eq. (2-10), which "incorporates complete information about the imaging properties of the optical system" (Williams & Becklund, 1989).

$$P(x,y) = A(x,y)e^{-i2\pi W(x,y)/\lambda} \quad (2-10)$$

In this equation, $A(x,y)$ is an amplitude function describing the relative efficiency of light passing through the pupil, and is usually given a uniform value of 1.0. In cases where the Stiles-Crawford effect is taken into account, it can be included here (van Meeteren, 1974). Once the aperture function is known, the principles of Fourier optics may be employed to compute the optical transfer function (OTF) and point spread function (PSF) which describe the imaging performance of the system. The surface plot in Fig. 2.3 represents a theoretical wavefront aberration function $W(x,y)$, for a cornea which has both astigmatism and spherical aberration. Wavefront aberration functions are usually sampled at many discrete locations within the pupil, and it may be summarized by a single numerical value such as the wavefront variance or root mean squared (RMS) wavefront error.

2.3

FOURIER OPTICS

Fourier optics is a powerful tool for analyzing and manipulating the optical transfer function (Thibos, 1993; Goodman, 1996). The optical transfer function (OTF) is one of the most useful descriptors of imaging performance for an optical system. It is a complex number whose magnitude is the modulation transfer function (MTF), and the phase is the phase transfer function (PTF). The MTF plots the relative contrast reduction between object and image as a function of spatial frequency, while the phase transfer function describes the lateral image shift as a function of spatial frequency. If the wavefront aberration function, $W(x,y)$ is known, the pupil function, $P(x,y)$, can be calculated (Eq. 2-10), and from this, the OTF may be computed by convolving the pupil function with its complex conjugate, $P^*(-x,-y)$, as shown in Eq. (2.11). The \otimes symbol represents convolution.

$$OTF(f_x, f_y) = P(x,y) \otimes P^*(-x,-y) \quad (2-11)$$

This is the same as taking the autocorrelation of the pupil function. By the convolution theorem, the parallel operation can be performed in the frequency domain by multiplication. Therefore, the Fourier transform (F) of the OTF is the product the Fourier transforms of the pupil function and its complex conjugate:

$$F[\text{OTF}(f_x, f_y)] = F[P(x, y)] \times F[P^*(-x, -y)] \quad (2-12)$$

The point spread function (PSF), another important measure of image quality, is the image of a point source formed by the optical system. In the case of a diffraction limited (no aberrations) system, the PSF is the Airy disk. Aberrations will cause additional spreading or blurring of the point. The Strehl ratio is sometimes used to describe image quality of a well corrected system, and it is defined as the maximum intensity of the PSF divided by the theoretical diffraction limited maxima of the same system (Born & Wolf, 1980; Freeman, 1990). The Fourier transform of the OTF is the PSF, therefore all important metrics of image quality (MTF, PTF, PSF, and Strehl ratio) can be calculated from the OTF. The OTF for a system can be computed if the wavefront aberration is known. Examples of the MTF and PSF corresponding to the wavefront of Fig. 2.3 are shown in Figs. 2.4 and 2.5, respectively.

If any scene imaged by an optical system is considered a collection of points, the image of each point in the scene will be the PSF, and the integration of all the points will build the image of the scene formed by those optics. Mathematically, this is the convolution of the PSF with the scene, and is summarized by Eq. (2-13). $U(x, y)$ is the light intensity distribution of the perfect image that would be predicted by paraxial optics—that is, without aberrations or diffraction. $U'(x, y)$ is the light intensity for the image formed by the optical system. For large images, it may be easier to compute $U'(x, y)$ by multiplication in the frequency domain rather than by convolution in the spatial domain. Since the OTF is the Fourier transform of the PSF, the product of the $U(x, y)$ frequency spectrum and the OTF is the frequency spectrum, or Fourier transform, of the aberrated image (Eq. 2-14).

$$U'(x, y) = U(x, y) \otimes \text{PSF}(x, y) \quad (2-13)$$

$$F[U'(x, y)] = F[U(x, y)] \times \text{OTF}(f_x, f_y) \quad (2-14)$$

The aberrated image is then found by taking the inverse Fourier transform (F^{-1}) of this result:

$$U'(x, y) = F^{-1}\{F[U'(x, y)]\} \quad (2-15)$$

If the eye's PSF or OTF are known, it is theoretically possible to construct the image of any scene formed on the retina by convolution (Camp, Maguire, Cameron, & Robb, 1990) or Fourier multiplication. Figure 2.6 uses these principles to simulate the view of a mountain scene for an eye with astigmatism and

spherical aberration.

The reverse process can be used to recover the unaberrated image (the scene) from the aberrated image by deconvolution of the aberrated image by the PSF (Fig. 2.6). This is performed in the frequency domain (Russ, 1995) by dividing the aberrated image spectrum by the OTF (Eq. 2-16), and transforming the result to the spatial domain (Eq. 2-17). Division with complex numbers is accomplished by dividing the magnitudes and subtracting the phases.

$$F[U(x,y)] = \frac{F[U'(x,y)]}{\text{OTF}(f_x, f_y)} \quad (2-16)$$

$$U(x,y) = F^{-1}\{F[U(x,y)]\} \quad (2-17)$$

A practical application of this process is the recovery of unaberrated images of the retina taken through the aberrated optics of the eye by a retinal camera. Using deconvolution or the corresponding operations in the frequency domain, it is theoretically possible to recover high resolution images of the retina if the eye's OTF is known.

2.4

POLYNOMIAL EXPANSION OF ABERRATION FUNCTIONS

It is sometimes useful to trace light through an optical system by considering the path of a point on the wavefront. Within one optical medium, this point proceeds in a straight line (a ray) perpendicular to the wavefront but will change directions upon entering a new medium. This bending of light is refraction. Using Snell's law (Eq. 2-18) we can calculate the change of direction of the rays, and determine the location of the image point formed by different parts of the optical wavefront. Ray tracing can be used to study optical aberrations.

$$n_i \sin \theta_i = n_r \sin \theta_r \quad (2-18)$$

2.4.1 Taylor series expansion of the sine function

From the perspective of ray tracing, aberrations are present whenever a ray misses the ideal focal point (Fig. 2.2 point f) and may be expressed as a longitudinal distance along the optic axis or a transverse displacement of the ray above or below the focal point. Since the path of the light ray is proportional to the sine function, it is possible to analyze aberrations based on a Taylor series expansion (Freeman, 1990)

of the sine function:

$$\sin \theta = \theta - \frac{\theta^3}{3!} + \frac{\theta^5}{5!} - \frac{\theta^7}{7!} + \frac{\theta^9}{9!} - \dots \quad (2-19)$$

If the angle of incidence is very small, as when rays from a distant axial object strike the surface near the optic axis, $\sin \theta$ is closely approximated by the first term, θ , and all higher terms of the series may be ignored. Ray tracing with this paraxial approximation gives the location of an image point for an aberration free system, and is the basis for *Gaussian*, or *first order* optics. For larger angles of incidence, the second and higher terms of the series become increasingly important for describing the actual path of light. In this case, the rays depart increasingly from the paraxial prediction, and this departure from the path of the paraxial rays is an expression of the optical aberrations. The aberrations contained in the second term of the series are known as the *third order*, or primary aberrations; the next term contains the *fifth order*, or secondary aberrations, and so on. Most optics texts consider expansion as far as the third order sufficient to explain the most important optical aberrations. Ludwig von Seidel (1821-1896) studied the third order aberrations, and broke them down into five components, now known as the five monochromatic Seidel aberrations (spherical aberration, coma, astigmatism, Petzval curvature of field and distortion). Modern computers make it possible to accurately trace rays without these approximations, but analysis of aberrations into components, such as the Seidel aberrations, is still useful in studying the optics of a system.

2.4.2 Rotationally symmetric systems

Returning to the wavefront aberration, the wavefront surface may also be analyzed into components by expanding the function as a power series. For the relatively simple case of a rotationally symmetric system, one expansion of the wavefront aberration is shown in Eq. (2-20) (Williams & Becklund, 1989; Smith, 1990). This takes into account the distance of the object point from the optic axis (r) and expresses the pupil sphere coordinates (x,y) in polar terms, where ρ is the distance from the optic axis, and angle θ is measured from the vertical meridian. The coefficient C before each polynomial is subscripted with three numbers that indicate, from left to right, the power of the r , ρ , and $\cos \theta$ terms, respectively. The first three terms describe first order optics and include, in order, a constant, prism, and defocus. The next five terms (Eq. 2-20 second line) correspond to the third order Seidel aberrations, spherical aberration, coma, astigmatism, Petzval curvature and distortion. Addition of fifth order or higher terms will improve the polynomial approximation to the wavefront aberration, though the higher terms

normally account for a much smaller portion of the aberration. From this equation, we note that, for a point object located on the optic axis, the value for r is zero, and all Seidel aberrations except spherical aberration drop out.

$$W(r, \cos \theta) = {}_0C_{00} + {}_1C_{11}r \cos \theta + {}_0C_{20}r^2 + {}_0C_{40}r^4 + {}_1C_{31}r^3 \cos \theta + {}_2C_{20}r^2 \cos^2 \theta + {}_2C_{22}r^2 \cos^2 \theta + {}_3C_{11}r^3 \cos \theta + \dots \quad (2-20)$$

2.4.3 Asymmetric systems with axial objects

In contrast to most man made optical systems, the human eye is normally not rotationally symmetric, therefore asymmetric aberrations can arise even with an axial point source. Equation (2-21) is an aberration polynomial which includes this consideration and is sometimes used to analyze the wavefront aberration of the human eye (Howland & Howland, 1977).

$$W(x,y) = A + Bx + Cy + Dx^2 + Exy + Fy^2 + Gx^3 + Hx^2y + Ixy^2 + Jy^3 + Kx^4 + Lx^3y + Mx^2y^2 + Nxy^3 + Oy^4 \dots \quad (2-21)$$

The terms associated with coefficients B and C represent horizontal and vertical prism; D, E and F are transforms of the spectacle sphere, cylinder and axis while, the K, M and O terms are components of third order spherical aberration.

2.4.4 Zernike polynomials

The Zernike polynomials have been used in optical engineering (Born & Wolf, 1980; Malacara & DeVore, 1992; Mahahan, 1994) for over 60 years, and recently these have been applied to aberrations of the human eye (Webb, 1992; Liang, Grimm, Goelz, & Bille, 1994; Liang & Williams, 1995) and corneal topography (Schwiegerling, Greivenkamp, & Miller, 1995; Schwiegerling, Greivenkamp, Miller, Snyder, & Palmer, 1996; Schwiegerling & Grievenkamp, 1996). This polynomial series offers the advantage of terms which are orthogonal for continuous curves, which is beneficial for surface fitting and analysis. Orthogonality cannot be assumed, however for discrete data or for nonuniform sampling (Wang & Silva, 1980). In some cases it may be necessary to perform a Gram-Schmidt orthogonalization to accurately apply Zernike polynomials (Schwiegerling, *et al.*, 1995). Either polar and Cartesian Zernike polynomials may be used, and depending on the reference, angles may be referenced to vertical or horizontal meridian. The

TABLE 2.1 A subset of the normalized Cartesian Zernike polynomials used in this dissertation.

Order	Mode	Polynomial	Description
0	1	1	piston
1	2	2y	vertical prism
1	3	2x	horizontal prism
2	4	6(2xy)	astigmatism axis 45/135
2	5	3(2x ² + 2y ² - 1)	defocus
2	6	6(x ² - y ²)	astigmatism axis 180/90
3	7	8(3x ² y - y ³)	triangular astigmatism
3	8	8(3x ² y + 3y ³ - 2y)	primary coma
3	9	8(3x ³ + 3xy ² - 2x)	primary coma
3	10	8(x ³ - 3xy ²)	triangular astigmatism
4	11	10(4x ³ y - 4xy ³)	
4	12	10(8x ³ y + 8xy ³ - 6xy)	
4	13	5(6x ⁴ + 12x ² y ² + 6y ⁴ - 6x ² - 6y ² + 1)	primary spherical
4	14	10(4x ⁴ - 3x ² + 3y ² - 4y ⁴)	
4	15	10(x ⁴ - 6x ² y ² + y ⁴)	
5	16	12(5x ⁴ y - 10x ² y ³ + y ⁵)	
5	17	12(15x ⁴ y - 12x ² y - 5y ⁵ + 4y ³ + 10x ² y ³)	
5	18	12(10x ⁴ y + 20x ² y ³ + 10y ⁵ - 12x ² y - 12y ³ + 3y)	secondary coma
5	19	12(10x ⁵ + 20x ³ y ² + 10xy ⁴ - 12x ³ - 12xy ² + 3x)	secondary coma
5	20	12(5x ⁵ - 10x ³ y ² - 4x ³ - 15xy ⁴ + 12xy ²)	
5	21	12(x ⁵ - 10x ³ y ² + 5xy ⁴)	

mode numbering scheme and order may also vary. Table 2.1 shows the Cartesian form of the first 21 Zernike modes, which I used. Note that the Zernike terms labeled primary coma or spherical aberration do not correspond directly with the Seidel aberrations of the same name. Zernike polynomials were used to analyze the corneal and ocular wavefront aberrations in this dissertation.

2.4.5 Converting Zernike second order polynomials to the equivalent ophthalmic spectacle prescription

The second Zernike order is made up of three modes, which are labeled 45/135 astigmatism (mode 4), defocus (mode 5) and 90/180 astigmatism (mode 6). They describe the optical defects that are corrected by conventional spectacles, namely myopia or hyperopia (defocus) and astigmatism. It is possible to convert this portion of the wavefront aberration to the equivalent ophthalmic spectacle prescription by the steps outlined below.

- 1) Compute the wavefront error (W) at the pupil edge, in meters, using Eq. (2-22) for mode 5 (defocus), Eq. (2-23) for mode 4 and Eq. (2-24) for mode 6 use.

$$W_5 = -a_5(2/3)(6.33 \times 10^{-7}) \quad (2-22)$$

$$W_4 = -a_4(6/6)(6.33 \times 10^{-7}) \quad (2-23)$$

$$W_6 = -a_6(6/6)(6.33 \times 10^{-7}) \quad (2-23)$$

Variable a , subscripted with the mode number, is the Zernike coefficient for the respective modes. A myopic wavefront error has a positive sign, but by clinical convention, myopic prescriptions are given a minus sign. Therefore all three equations include a minus sign. In my analysis, the Zernike coefficients described the wavefront errors in wavelengths, where one wavelength is 633 nm. The constant at the end of each equation converts the wavefront error in wavelengths to meters.

- 2) Strictly speaking the Zernike profiles are parabolic and a large number of parabolas must be summed to better approximate a circle. This would require that the higher order astigmatic modes contained in orders 4, 6, 8, and 10 also be included (Schwiegerling, *et al.*, 1995). In the wavefront analysis of normal eyes, the wavefront profile for astigmatic modes 4 and 6, as well as defocus mode 5, may be considered nominally circular (Webb, 1992), and the equivalent ophthalmic prescription may be computed from these modes. Treating these modes as circles W_4 , W_5 and W_6 represent the sags. The chord associated with each of these sags is the pupil diameter. Based on these assumptions and the geometry shown in Fig. 2.7, the dioptric curvature associated with each sag (W_4 , W_5 and W_6) may be computed by Eq. (2-24, 25 and 26) for modes 5, 4 and 6 respectively. Variable y is the pupil radius in the same unit used for W (meters).

$$M = 2W_5 / (y^2 + W_5^2) \quad (2-24)$$

$$J_{45} = 2W_4 / (y^2 + W_4^2) \quad (2-25)$$

$$J_0 = 2W_6 / (y^2 + W_6^2) \quad (2-26)$$

Variable M represents the mean spherical power, while J_{45} and J_0 are Jackson crossed cylinders with axes at 45/135 and 180/90 respectively.

3) Having been converted to diopters, the M, J_{45} and J_0 terms constitute the coefficients in a Cartesian Fourier decomposition of a spherocylindrical ophthalmic lens (Thibos, Wheeler, & Horner, 1997). The power derived from Zernike mode 4 (J_{45}) corresponds with sine term of the Fourier series and the mode 6 coefficient is used to compute the cosine term (J_0). The M, J_{45} and J_0 terms may be converted to the minus cylinder spectacle notation by the following formulas:

$$\text{Cylinder} = -2 (J_0^2 + J_{45}^2) \quad (2-27)$$

$$\text{Sphere} = M + \text{Cylinder} / 2 \quad (2-28)$$

$$\text{Axis} = \text{atan}(J_{45} / J_0) / 2 \quad (2-29)$$

In order to ensure that the computed axis agrees with clinical convention and is expressed as a positive angle, in degrees between 0 and 180, it may be necessary to add 90 or 180 degrees to the Axis value computed from Eq. (2-29) (Salmon & Horner, 1996). Table 2.2 organizes the conditional tests required to correctly change the value of Axis in Eq. (2-29) to the correct minus cylinder value. This can be summarized by the following computer pseudocode: “If $J_0 < 0$, add 90, else if $J_{45} < 0$, add 180, else no change.”

4) To express the refractive error in plus cylinder form, use Eq. (2-30) to compute the cylinder power. The Sphere and Axis values may be computed using Eqs. (2-28) and (2-29) as before, but the Axis value must be corrected according to the conditional tests shown in Table 2.3. This can be summarized by the following computer pseudocode: “If $J_0 > 0$, add 90, else if $J_{45} > 0$, add 180, else no change.”

$$\text{Cylinder} = 2 (J_0^2 + J_{45}^2) \quad (2-30)$$

TABLE 2.2 The value of Axis in Eq. (2-29) must be corrected according to the conditions summarized here, in order to obtain the correct minus cylinder axis.

Minus cylinder	If J_0 is ...		
	-	+	
If J_{45} is ...	-	axis = Axis + 90	axis = Axis + 180
	+	axis = Axis + 90	axis = Axis

TABLE 2.3 The value of Axis in Eq. (2-29) must be corrected according to the conditions summarized here, in order to obtain the correct plus cylinder axis.

Plus cylinder	If J_0 is ...		
	+	-	
If J_{45} is ...	+	axis = Axis + 90	axis = Axis + 180
	-	axis = Axis + 90	axis = Axis

An Excel spreadsheet that implements the Zernike-to-spectacle prescription conversion is included as Appendix A. This conversion will be used in Chapters 5 and 7 to compare clinically measured refractive errors with the corresponding Zernike coefficients.

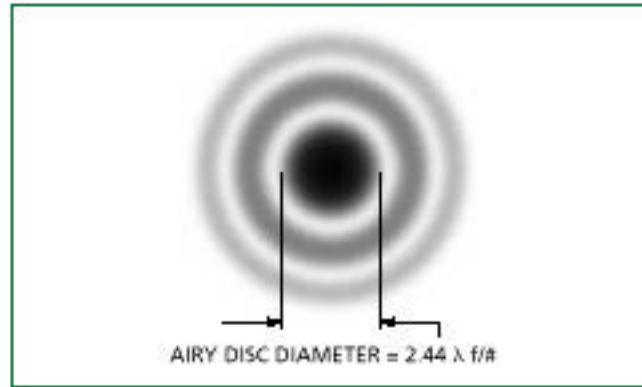


Figure 2.1

The Airy disc is the central intensity distribution in the focal plane of a diffraction limited optical system.

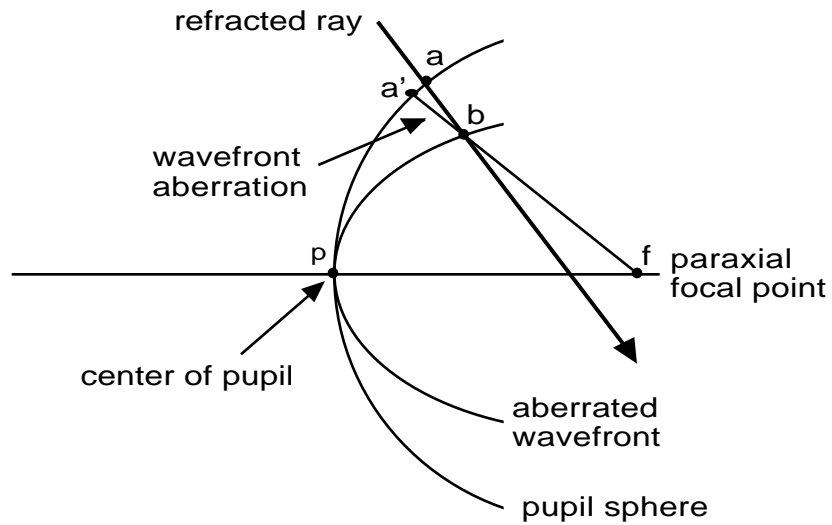


Figure 2.2

The wavefront aberration is the distance between the aberrated wavefront and the pupil sphere; that is, either distance ab or $a'b$, depending on the precise definition.

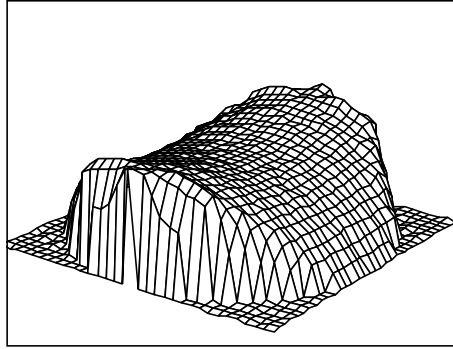


Figure 2.3

The wavefront aberration function may be represented by a surface centered in the exit pupil. Here astigmatism and spherical aberration form an asymmetric saddle shaped contour.

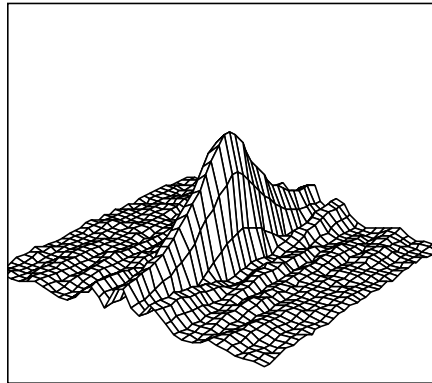


Figure 2.4

Surface plot of an MTF for a theoretical cornea with astigmatism and spherical aberration. This corresponds with the wavefront shown in Fig. 2.3.

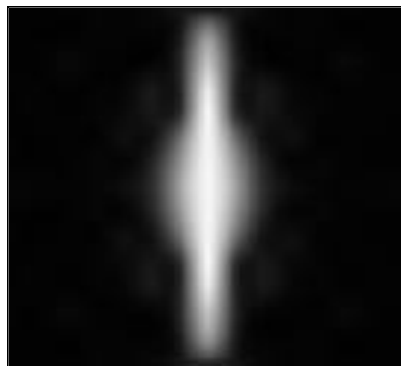


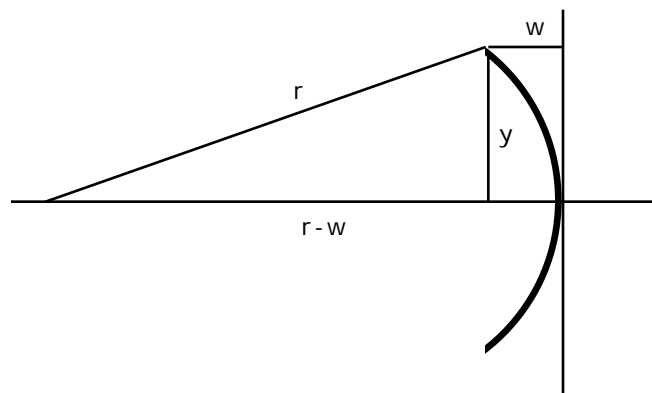
Figure 2.5

Point spread function for a theoretical toric cornea at the "circle" of least confusion. This corresponds with the wavefront of Fig 2.3 and MTF of Fig. 2.4.



Figure 2.6

Convolving the scene on the left with the PSF of Fig. 2.5 yields the blurred image on the right and simulates the effect of corneal astigmatism and spherical aberration. Deconvolution would recover the scene (left) from the aberrated image (right).



$$\begin{aligned}
 r^2 &= (r-w)^2 + y^2 \\
 r^2 &= r^2 - 2rw + w^2 + y^2 \\
 2rw &= w^2 + y^2 \\
 r &= \frac{(w^2 + y^2)}{2w}
 \end{aligned}$$

Figure 2.7

Geometry used to find the radius of curvature (r) of a circle based on measurements of its sag (w) at a distance y from the apex. If the r is measured in meters, the inverse of r is the curvature in diopters (D). This is a familiar problem in ophthalmic optics.

CHAPTER 3

Corneal Topography Basics

One of the newest advanced-technology instruments that optometrists and ophthalmologists use to evaluate cornea and contact lens patients, is the computerized videokeratoscope. These devices are primarily being used to examine the cornea for subtle shape anomalies, such as keratoconus. Corneal surgeons are particularly concerned with keratoconus since its presence would contraindicate refractive surgery. The videokeratoscope also helps doctors manage corneal distortion in contact lens patients, and by using these instruments, it is possible to design contact lenses to precisely match each eye's corneal contour. This technology is relatively new, and I found that even among doctors who use corneal topography maps, there is considerable confusion about how to interpret the corneal maps actually show. To improve my understanding of this subject, I studied the underlying principles of corneal topography, and using theoretical cornea data, created examples of the various corneal maps that may be produced by modern videokeratoscopes. This exercise provided valuable insight into what these maps really show about the cornea and was organized into an article that was published in *Optometry and Vision Science* (Salmon & Horner, 1995). It was expanded and subsequently published as a chapter (Horner, Salmon, & Soni, 1998) in the 1998 edition of *Borish's Clinical Refraction*, a standard optometry textbook. Much of the information from these two publications is summarized in the following pages of this chapter and this provides background information for the research described in Chapters 4 and 5.

3.1

IMPORTANCE OF CORNEAL OPTICS

We should be able to learn much about the eye's aberrations from corneal topography since the anterior corneal surface is the primary refractive element in the eye. Fortunately, this very important optical surface is also easily accessible to noninvasive measurement. The corneal surface alone accounts for

about 70% of the eye's refractive power, and some reduced eye models, which use only a single refracting surface (a modified cornea), are able to simulate optical performance for the whole eye quite well (Thibos, 1987; Thibos, 1992; Thibos, Ye, Zhang, & Bradley, 1997). Scientists studying optical aberrations of the eye have long recognized that the asphericity of the cornea is a major factor that determines the amount of spherical aberration in the eye (Westheimer, 1963; Millodot & Sivak, 1979; Atchison, 1984).

Since the optical properties of a transparent surface are primarily determined by its shape, a detailed knowledge of corneal optics requires high quality surface topography data. For over 100 years keratometry has given clinicians a rough estimate of corneal shape based on data from four paracentral points. Thanks to recent advances in computer technology, we can now sample and process data for 5-10,000 points, and map the topography of the cornea to micrometer accuracy (Horner & Salmon, 1998). From the topographic data, it is possible to calculate sophisticated measures of optical performance (Camp, Maguire, Cameron, & Robb, 1990; Maguire, Zabel, Parker, & L, 1991), including the corneal wavefront aberration function (Hemenger, Tomlinson, & Oliver, 1994; Oliver, Hemenger, Corbett, & al., 1997; Oshika, Klyce, Applegate, Howland, & El Danasoury, 1999). This advanced application of corneal topography may one day be included in the routine clinical evaluation of the eye's optical quality, but today corneal topography maps are mainly being used to detect anomalies of surface shape.

The measurement of corneal optics has clinical application to areas such as refractive surgery and high resolution retinal photography. In laser refractive surgery, the excimer laser vaporizes corneal tissue to reshape it into a new lens, thereby correcting the patient's refractive error. This is usually performed with no regard for induced optical aberrations (Camp, *et al.*, 1990; Stein, Cheskes, & Stein, 1995; Schwiegerling & Snyder, 1998), and often complicated aberrations result (Oliver, *et al.*, 1997; Oshika, *et al.*, 1999). Patients may experience reduced vision, especially with low contrast targets or in low illumination (Maguire, 1994; Verdon, Bullimore, & Maloney, 1996; Gauthier, *et al.*, 1998; Bullimore, Olson, & Maloney, 1999). By studying corneal topography, we can understand exactly how changes in surface shape affect optical quality.

The correct management of many retinal diseases depends on high quality fundus images of microscopic features (Kinyoun, *et al.*, 1989; Aiello, 1994), but these are limited by aberrations of the eye. Using adaptive optics, a technique borrowed from astronomy, scientists at the University of Rochester were able to neutralize ocular aberrations and photograph individual photoreceptors *in vivo* (Liang, Williams, & Miller, 1997). A better knowledge of the eye's aberrations may also help us understand the etiology of visual anomalies such as myopia or amblyopia (Atchison, Collins, Wildsoet, Christensen, & Waterworth, 1995; Collins, Wildsoet, & Atchison, 1995). New technologies are providing us with the tools to study visual optics in ways that were never before possible. Given the importance of the cornea and the availability of videokeratoscopy, a logical place to begin new research on the eye's optical system is the

cornea.

3.2

CORNEAL SHAPE

3.2.1 Mean shape of the human cornea

Viewed from the front, the cornea is slightly oval, with vertical and horizontal dimensions of approximately 11 and 12 mm, respectively (Last, 1968). Normally, pupil diameter ranges from 3-6 mm, and this limits the optical zone of the cornea to the central 6 mm under most conditions (Holladay & Waring, 1992). In profile, most corneas are nearly circular near the center, with an average apical radius of curvature of about 7.8 mm. The normal range is 7-8.5 mm. The horizontal radius is usually 0.05-0.25 mm flatter than the vertical (with the rule astigmatism) (Gullstrand, 1924). This equates to 0.25-1.25 diopters (D) of corneal astigmatism; average corneal astigmatism is about 0.70 D. In general, the mean apical radius decreases with higher myopia (Carney & Henderson, 1993; Carney, Mainstone, & Henderson, 1997).

3.2.2 Two dimensional models of the general corneal shape

Beyond the paraxial region, the corneal normally flattens, and a useful first order approximation of the typical corneal profile is an ellipse (Mandell & St Helen, 1971; Howland, Buettner, & Applegate, 1994; Mandell, Klein, & Corzine, 1998). Figure 3.1 shows the general features of an ellipse that you might see in a textbook on analytical geometry. The origin is placed at the center of the ellipse, and the major axis lies on the x axis, while the minor axis is on the y axis. An ellipse is defined (Washington, 1986) as “the locus of a point P(x,y), which moves so that the sum of its distances from two fixed points is constant.” These two fixed points, called foci, are located at coordinates (-c,0) and (c,0) in Fig. 3.1. The eccentricity (e) parameter describes the degree of elongation of an ellipse and may be defined by the ratio of the distances, c and a:

$$e = c / a \quad (3-1)$$

The eccentricity of an ellipse has a value, $0 < e < 1.0$, where a value of $e = 0$ represents a sphere, and a value of $e = 1.0$ is associated with another conic section, the parabola (Benjamin & Rosenblum, 1992).

Baker’s formula (1943), Eq. (3-2), is another general mathematical expression for conic sections, including ellipses, and has been popular among vision scientists for modeling the general corneal profile (Bennett & Rabbetts, 1989a; Burek & Douthwaite, 1993; Lam & Douthwaite, 1994; Salmon & Horner,

1995) in two dimensions (Fig. 3.2). This formula places the origin at the corneal apex and can describe a wide range of normal corneal shapes by varying just two parameters, the apical radius (r) and shape factor (p). The value of p , is related to the conic eccentricity (e) by Eq. (3-3).

$$y = \sqrt{2rx - px^2} \quad (3-2)$$

$$p = 1 - e^2 \quad (3-3)$$

A shape factor of $0 < p < 1$ describes a prolate, or flattening ellipse. The portion of an ellipse at either end of the major axis is prolate in shape, since the local curvatures gradually flatten with departure from the vertex. A value of $p = 1.0$ indicates a sphere, and $p > 1.0$ indicates an oblate or steepening ellipse. The portion of an ellipse at either end of a minor axis is oblate in shape, since the local curvatures gradually steepen for points departing from the minor vertices.

The mean corneal shape factors (p) reported in several corneal topography studies were between 0.74 and 0.89, and the range of reported values was 0.19-1.47 (Eghbali, Yeung, & Maloney, 1995). These are summarized in Table 3.1. Though most normal corneas are similar to prolate ellipsoids, 5-20% may be oblate (Eghbali, *et al.*, 1995; Carney, *et al.*, 1997). Refractive surgery usually produces an oblate surface, which is flat centrally and steep peripherally. Shape factors may vary with meridian, and Eghbali found an average standard deviation of 0.17, though no specific trend was identified (Kiely, Smith, & Carney, 1982).

Referencing work by Bonnet, Lotmar developed a polynomial expression for an aspheric model cornea (Lotmar, 1971):

$$x = \frac{y^2}{2r} \left[1 + \frac{5}{28} \left(\frac{y}{r} \right)^2 - \frac{1}{12} \left(\frac{y}{r} \right)^4 \right] \quad (3-4)$$

Variable r represents the apical radius of curvature, y is the radial distance from the center, and x is the surface elevation. An ellipse with a 7.8-mm apical radius (r) and shape factor (p) of 0.6 matches Lotmar's formula within $1.0 \mu\text{m}$ across a 6.0 mm diameter zone, so Lotmar's model cornea is close to an ellipse.

A rotationally symmetric ellipsoid provides a realistic model cornea that can predict many of its optical properties. As will be discussed in more detail later (Section 3.5.1), toricity can be added to better simulate a real cornea (Burek & Douthwaite, 1993; Salmon & Horner, 1995). Applegate hypothesized that

the corneal shape tends to become more spherical (p value approaches 1.0) in high myopia (Applegate, *et al.*, 1994), and this relationship was verified in another study of 113 eyes (Carney & Henderson, 1993). Chapter 5 contains more detail on the computation of corneal optics from topography.

TABLE 3.1 Corneal shape factors (p) reported in various studies (Eghbali, *et al.*, 1995; Carney, *et al.*, 1997).

Study	# eyes	Shape factor (p)	Comment
Townsley (1970)	350	.75	range .19-.84
Mandell (1971)	8	.76	range .27-.96
Bibby (1976)	2,100	.85 ±.18	
Bibby (1976)	32,000	.79 ±.15	horizontal meridian
Kiely (1982)	176	.74 ±.18	range .24-1.47
Kiely (1984)	196	.79 ±.19	range .24-1.47
Guillon (1986)	220	.83 ±.13 / .81 ±.16	flat / steep meridian; range .21-1.20
Sheridan (1989)	56	.88	
Carney (1997)	113	.69 ±.23	range .03-1.29

3.3

HISTORY OF QUANTITATIVE CORNEAL MEASUREMENT

3.3.1 Keratometry

The most widely used instruments for measuring corneal curvature are the keratometers, sometimes called ophthalmometers. In 1796, Ramsden built an apparatus to measure corneal curvature to determine if the cornea changes during accommodation (Mandell, 1960). His instrument employed a telescope to magnify the image of mires reflected off the corneal surface. As with modern keratometers, a doubling device was used to allow stable measurement in spite of microscopic eye movements. Ramsden's work was largely forgotten, but a generation later other scientists began to build similar devices for measuring the curvature of the central cornea. Kohlrausch, in 1839, built an instrument that included a telescope and size adjustable luminous mires. In 1854, Helmholtz added a doubling device, as Ramsden had done earlier, to

eliminate the problem of an unstable image caused by eye movements; he is usually credited with the invention of the keratometer. The Helmholtz ophthalmometer measured the curvature of the cornea and other optical surfaces of the eye as well. In 1881, Javal and Schiotz improved Helmholtz' laboratory apparatus and built an ophthalmometer designed for clinical use. With only minor changes, the same design is still in use today as the Haag-Streit ophthalmometer.

The Javal-Schiotz instrument and the many that have followed it are designed expressly to determine the curvature, and particularly the astigmatism, of the cornea only. It would thus appear appropriate to call them keratometers (cornea measurers), leaving the terms ophthalmometer and ophthalmometry for the wider field of investigation of the refracting surfaces of the eye generally. (Emsley, 1946).

Bausch & Lomb added several useful features to their keratometer, which was introduced in 1932. It included a Scheiner's disk to improve focusing, circular mires to allow better qualitative assessment of the corneal surface, and the capacity to measure two orthogonal corneal meridians simultaneously. The Bausch & Lomb keratometer, now manufactured by Reichert, has remained essentially unchanged since 1932. Along with copies built by other companies, this is the most popular clinical instrument for measuring corneal curvature.

For nearly a century, clinicians relied almost exclusively on keratometry for quantitative corneal surface data. As an adjunct to refraction and for contact lens fitting, the keratometer was adequate for most normal corneas. Keratometry also proved valuable for other applications, such as the calculation of intraocular lens power, or in the management of surgically induced astigmatism. Modern computerized corneal topographers are closely tied to the keratometer tradition, and they usually provide simulated keratometer data along with their color maps.

3.3.2 Keratoscopy

Using keratoscopy, it is possible to examine a much greater area of the cornea than is possible with keratometry. Clinical keratoscopy has been used since 1870, when Placido studied the corneal surface by observing the shape of concentric rings reflected off the cornea (Fig. 3.3). Most modern videokeratoscopes are based on the same principle, and use a pattern of reflected rings, called a Placido's disk. Depending on the size of the Placido's disk, it is possible to qualitatively evaluate most of the corneal surface. Various keratoscope designs were developed for clinical and surgical use, and until recently, they provided only a gross qualitative assessment of the cornea.

In the 1880's, Javal recognized the importance of recording the keratoscope image photographically (Reynolds, 1992), and in 1896, Gullstrand developed the first photokeratoscope. This opened the way for

detailed mathematical analysis of corneal shape, and Gullstrand developed algorithms to derive quantitative data from careful measurements of the keratograph rings (Gullstrand, 1966). Unfortunately, until recently, the process was too tedious to be clinically useful. In the 1970's, several photokeratoscopes were designed with attached Polaroid cameras. One version, the Corneoscope (Fig. 3.3), and its companion device for image analysis, the Comparator, allowed fast, in-office evaluation of the Polaroid keratograph (Lundergan, 1992). These instruments were used primarily for advanced contact lens fitting and did not become widely accepted among clinicians, who continued to rely on the simpler, more familiar keratometer.

In the 1980's, keratorefractive surgery provided the impetus to develop better corneal topographers, but a major obstacle continued to be the volume of data and tedious data analysis (Klyce & Wilson, 1989). While keratometry evaluates the cornea based on four paracentral points, modern computerized videokeratoscopes evaluate thousands of points covering most of the cornea. Advances in video and personal computer technology made it possible to instantaneously acquire and analyze high quality images. These improvements made quantitative keratometry practical for routine clinical use (Koch & Haft, 1993). Since 1987, color topographic maps have been the standard method for displaying computerized videokeratographic data (Maguire, Singer, & Klyce, 1987). The Corneal Modeling System (CMS) produced by Computed Anatomy (Gormley, Gersten, Koplin, & Lubkin, 1988), became the first widely used computerized videokeratoscope. With instrument improvements, reduced costs and a greater demand for precise corneal information, newer generations of computerized videokeratoscopes came into widespread use in the early 1990's.

3.3.3 Other technologies

In an effort to improve accuracy and avoid the assumptions necessary to compute three-dimensional surface estimates from two-dimensional Placido images, one videokeratoscope, the EyeSys System 2000 (EyeSys Vision Group, formerly EyeSys Technologies), shown in Fig. 3.4, added side cameras which view the cornea in profile. Some companies developed non-Placido methods for measuring the corneal surface. The PAR Corneal Topography System (PAR Vision Systems Corporation) uses a rasterstereographic principle (Arffa, Warnicki, & Rehkopf, 1989) to locate a square grid of surface points by stereo-triangulation (Belin, Cambier, Nabors, & Ratliff, 1995). Employing different technology, the ORBSCAN (ORBTEK, Inc.) rapidly scans a sequence of optical slits across the cornea, and analyzes these images to reconstruct the anterior and posterior corneal surfaces. The CLAS 1000 (Eye Technology, Inc.) is based on laser holographic imaging and provides very high resolution corneal surface maps without reliance on projected patterns. The University of Masstricht, in the Netherlands, recently developed a "Fourier Profilometry" method, which is the basis for the Euclid ET-800 Corneal Topography System (Euclid Systems Corporation), the newest entry in the corneal topography market. These alternate

technologies possess theoretical advantages (Applegate & Howland, 1995), but videokeratoscopy is still the most popular method for mapping the corneal surface.

3.4

VIDEOKERATOSCOPE RECONSTRUCTION ALGORITHMS

3.4.1 Limitations based on instrument design

While trying to construct an accurate topographic map of the cornea, all videokeratoscopes face inherent problems that can introduce error, and these must be minimized by the instrument design and data processing (Applegate, 1992). Instrument design considerations include the working distance and size of the illuminated Placido's disk. Interestingly, the two major manufacturers have taken opposite approaches to instrument design with regard to these factors. The Tomey (formerly Computed Anatomy) Topographic Modeling System (TMS-2) uses a small target with a short working distance. This maximizes corneal coverage and allows for a smaller instrument, but the short working distance is very sensitive to focus and alignment errors (Applegate & Howland, 1995). Tomey's main competitor, EyeSys, chose a different approach. The EyeSys 2000 Corneal Analysis System uses a larger target and longer working distance. These reduce the effects of focusing and alignment errors (Mandell & Horner, 1993) but require a larger Placido's disk, which may be partially obscured by the patient's nose or brow. Reconstruction algorithms require that the entire Placido's disk image be in focus at the videokeratoscope working distance, but it is impossible for all the keratoscope rings to be focused in the same plane for all corneas. The shape of the keratoscope face is designed to minimize this source of error. Also, the concentric ring target has inherent limitations. It cannot measure the cornea inside the central ring, and though designed to collect data along radial meridians (Fig. 3.5), these targets provide no information about corneal shape in the circumferential direction (Applegate, 1994; Rand, Howland, & Applegate, 1997). In spite of these limitations, algorithms have been developed which minimize error and allow noninvasive measurement of the cornea, which is sufficiently accurate support a wide range of clinical and research applications.

3.4.2 Overview of corneal reconstruction algorithms

The process of building a topographic map of the cornea from keratoscopic data goes through the following general steps:

- 1) Capture a video image of the keratoscope rings.
- 2) Measure the angular size at discrete points on each ring.
- 3) Mathematically reconstruct the corneal surface point by point.

- 4) Compute an appropriate index to describe each surface point.
- 5) Create a pseudocolor map to show these indices across the cornea.

Clark (1973) published a comprehensive historical review of photokeratoscopy and their mathematical analyses that covered the work of Gullstrand through the developments of the early 1970's. Since then, several important articles describing keratoscope algorithms have appeared (Doss, Hutson, Rowsey, & Brown, 1981; Klyce, 1984; Wang, Rice, & Klyce, 1989; van Saarloos & Constable, 1991; Klein, 1992; Halstead, Barsky, Klein, & Mandell, 1995; Klein, 1997b). The actual algorithms used by the commercial instruments are closely guarded secrets, and they may not be the same as those that appear in the open literature. Nevertheless, it is beneficial to study published algorithms, since they clarify the basic methods used to reconstruct the corneal surface from videokeratographic data.

Corneal reconstruction begins with analysis of the rings contained in the videokeratograph. A polar coordinate system is imposed on the image, and each point on a ring is specified by its meridian and distance from the center (Fig. 3.6). The objective of the algorithm is to estimate the location, in three-dimensional space, of the corneal surface points that gave rise to the image. By analyzing the cornea meridian by meridian, these instruments simplify analysis by treating the surface as a set of many two-dimensional radial profiles. It is important to note that this approach treats each meridian as one slice out of a rotational symmetric surface. In this geometry, the incident and reflected rays remain in the same plane. Most corneas, however, are not rotationally symmetric, so this simplifying approximation of corneal shape can introduce errors, depending on the actual shape of the cornea. For example, in a toric cornea, the incident and reflected rays are coplanar for the principal meridians only, but in oblique meridians the reflected rays are always skewed out of the incident plane. For the range of toricities seen in normal corneas, however, the skew ray error is negligible (Hilmantel, Blunt, Applegate, & Howland, 1997; Klein, 1997a). Therefore, except for severely distorted corneas, two-dimensional reconstruction algorithms are accurate enough for most clinical applications.

3.4.3 The van Saarloos algorithm

Newer videokeratoscopes have turned to “arc-step” reconstruction methods, and van Saarloos wrote a summary of one such algorithm (van Saarloos & Constable, 1991). Considered in two-dimensions, the keratoscope rings represent object points located at different distances from the optic axis, and after reflection off the corneal surface, chief rays can be traced through the camera nodal point to its corresponding image point in the camera image plane (Fig. 3.7). The known position of each object point, the camera working distance (wd) and angular size of each image point (α) are required to compute the corneal reflection points. Unfortunately, as shown in Fig. 3.7, without additional assumptions, this does

not lead to a unique solution (Wang, *et al.*, 1989). This algorithm requires the following constraints to determine a unique location for each reflection point.

- Successive corneal points are joined by small circular arcs.
- Adjoining arcs have a single slope value at their junctions.

The van Saarloos algorithm uses several iterative calculations to refine the estimate of each reflection point. Figure 3.8 shows the geometry, and the algorithm is summarized by the following steps, each of which includes numerous iterations.

- 1) Estimate the corneal apical radius (r).
- 2) Calculate coordinates for the first corneal reflection point and its slope.
- 3) Using data for the previous point, calculate the coordinates and slopes for subsequent reflection points.
- 4) Repeat the process for the next meridian.

Readers may refer to the article (van Saarloos & Constable, 1991) for the details of this algorithm. Two misprinted equations in that article have been corrected in the footnote below^a.

3.4.4 The Klein algorithm

A shortcoming of arc-step algorithms is that corneal points are connected with circular arcs that have abrupt changes in curvature at each point. Klein designed an algorithm which connects the corneal reflection points with a smooth continuous curve that better models the corneal surface (Klein, 1992). As with the previously described algorithm, calculations are based on the angular height of each reflection point, and two constraints, listed below, are necessary to limit the answer to a unique point.

- The surface is modeled by a cubic polynomial curve.
- The sampled surface point is located at the intersection of the reflected ray and the calculated polynomial curve.

This efficient iterative algorithm can be implemented with a few lines of computer code, and a BASIC program is included in Klein's paper. Referring to the geometry of Fig. 3.9, this algorithm is summarized as follows:

- 1) Estimate the first reflection point position (a) on the reflected ray, directly above the

^a In the left column of page 961, the bottom equation should read, $\theta = 1/2[(2\phi - \alpha) - \alpha]$. On page 962, the equation on the last paragraph, first line should read, $1/2(wd + d_0 - y_{i-1})$.

corneal apex.

- 2) Compare the incident ray-normal angle with the reflected ray-normal angle at this point. If the first angle is larger than the second, increment along the reflected ray for a better estimate of the reflection point (b).
- 3) Calculate the polynomial curve joining the apex and point (b).
- 4) Repeat steps 2) and 3) until the incident and reflected angles become equal within a predetermined tolerance.
- 5) Using data for this reflection point, calculate subsequent points similarly.
- 6) Repeat for the other meridians.

These algorithms illustrate the process by which three-dimensional coordinates for corneal surface points are computed using two-dimensional algorithms. This is repeated for all semi-meridians in small radial increments. Depending on the videokeratoscope, 5,000-10,000 points may be computed to reconstruct the corneal surface. More recently, Halstead published a unique three-dimensional algorithm (Halstead, *et al.*, 1995), which reconstructs the cornea by analyzing data for the entire surface without geometric constraints. A rough computer simulation of the cornea surface is constructed, and successive iterations improve the correspondence between the real and simulated cornea by analyzing a theoretical keratograph for the simulated surface. Even in 1999, the major videokeratoscopes still use two-dimensional reconstruction algorithms, but future instruments may turn to three-dimensional routines, such as Halstead's, to more accurately compute cornea surface shape.

3.5

CORNEAL TOPOGRAPHIC MAPS

Computerized videokeratoscopy provides a tremendous volume of information about the corneal surface. By representing the data in the form of a color map, the experienced clinician can quickly evaluate corneal shape or other features closely associated with shape. A variety of corneal surface descriptors may be used, so different kinds of color maps can be created for any cornea. The type of map that is used in most clinical situations is the axial curvature map. Sometimes it is better to show the instantaneous curvature, surface elevation or refractive power distribution across the cornea. The following sections explain the principles of each of these kinds of maps.

3.5.1 The ellipsotric model cornea

A reasonable, relatively simple mathematical model of a general cornea is an ellipsotric surface

(Burek & Douthwaite, 1993). The corneal profile in each meridian is an ellipse described by Baker's formula Eq. (3-2). Equation (3-5) is equivalent except that variable y has been replaced with the Greek letter ρ (rho), and the former variable, x , has been replaced by z . The ellipsoidal profile (Eq. 3-5) may be then applied to any radial meridian, in a cylindrical coordinate system, such that variable ρ represents radial

$$\rho = \sqrt{2r_{\theta}z - pz^2} \quad (3-5)$$

distance from the optic axis, z specifies distances in the direction of the optic axis, and r_{θ} is the apical radius of curvature in the meridian of interest. It is possible to specify a different shape factor, p , for each meridian, but for simplicity I kept the p value constant for all meridians. The variables are illustrated in Fig. 3-10. In creating a mathematical model of the cornea, all variables except z are usually defined ahead of time, and it is necessary to solve for z . Equation (3-6) solves for z in terms of the other variables.

$$z = \frac{r_{\theta} - \sqrt{r_{\theta}^2 - p\rho^2}}{p} \quad (3-6)$$

All that remains to define a model cornea in three-dimensions is a describing function for variable r_{θ} . This is shown by Eq. (3-7), which interpolates meridional curvature ($1/r_{\theta}$) based on user defined values for the maximum (r_h) and minimum (r_v) radii. When modeling a with the rule cornea, r_h is the radius of curvature in the horizontal (180 degree) meridian, and r_v is the radius of curvature in the vertical (90 degree) meridian. Equation (3-7) is based on the familiar optometric principle that the apical curvature in an oblique meridian of a toric surface varies as a sine squared function of the oblique angle (Churms, 1981).

$$\frac{1}{r_{\theta}} = \left[\frac{1}{r_h} \cos^2 \theta + \frac{1}{r_v} \sin^2 \theta \right] \quad (3-7)$$

Based on Eqs. (3-6) and (3-7), a simple computer program may be written to generate cylindrical coordinates (ρ , θ , z), for a surface that includes two important features of a generalized cornea—an ellipsoidal flattening profile, and corneal toricity, as defined by input variables, r_h and r_v . This model

(Salmon & Horner, 1995) is appealing from an optometric point of view since the two variables, r_h and r_v , are the same parameters that are routinely recorded in clinical keratometry. The example corneal maps in Figs. 3.11, 3.12 and 3.13 are based on this ellipsotopic model, with $r_h = 8.00$ mm, $r_v = 7.50$ mm and a constant shape factor (p) of 0.85. This represents a cornea with 2.81 D of astigmatism. The relatively large astigmatism was selected to better illustrate the difference between the various kinds of corneal maps used on today's videokeratoscopes.

3.5.2 Surface elevation maps

Since surface shape is the primary determinant of corneal optics (Applegate, 1994; Applegate & Howland, 1995), a logical way to map the cornea is to show the surface elevation of each point, relative to a reference surface. With topographic land maps, elevations are measured from a reference "plane" at sea level. However, for the cornea, elevations measured from a plane are nearly useless, because even minute changes in elevation (on the order of micrometers) can be optically significant, but these are lost in the larger total height of the cornea (Klyce & Wilson, 1989; van Saarloos & Constable, 1991; Holladay & Waring, 1992). A better method for presenting the true topography (surface elevation) is to measure from a reference sphere, ellipsoid or other surface that approximates the general corneal shape (Salmon & Horner, 1995). Figure 3.11 shows four surface elevation maps for the 2.81 D with the rule astigmatic model cornea, mentioned above. Elevations were measured relative to a plane as well as to a flat, median and steep reference spheres. Note that surface toricity is readily apparent when reference spheres are used but it cannot be distinguished when elevation is measured relative to a plane.

3.5.3 Dioptric curvature maps

Most corneal topography systems do not plot surface elevations, but describe the surface in terms of dioptric values. These dioptric maps are popular because they use the terminology of keratometry, with which clinician are familiar (Roberts, 1994a). Just as different elevation maps of the same cornea can be drawn, dioptric data for the same surface can also be expressed in different ways (Klein, 1992; Mandell, 1992). In optometry, diopters are sometimes used to quantify surface curvature; in other cases diopters express surface refractive power. Near the corneal apex, surface curvature and power are so closely related that they are sometimes treated synonymously. When the data are appropriately scaled, this works for keratometry, since measurement are limited to the paraxial region. However, outside the paraxial zone, it is important to make a distinction between dioptric curvature and dioptric power. Three kinds of dioptric curvature maps will be described in the following paragraphs. These include the axial and instantaneous maps, which are available on most commercial instruments used today and a new type of map called the

Gaussian curvature map.

As was mentioned in Section 3.4.1, all current videokeratoscopes map the three-dimensional corneal surface by applying the two-dimensional geometry of Fig. 3.10 to each corneal meridian. In effect, this assumes that the surface normal for each surface point intersects the videokeratoscope axis. This is not strictly true for most meridians of a non-rotationally symmetric surface, such as a toric cornea or one with keratoconus. The error in axial curvature caused by this simplifying assumption is clinically negligible for normal corneas with regular astigmatism, but for abnormally shaped corneas, as seen in keratoconus or following refractive surgery, the error can be large (Klein, 1997c). Since the purpose of this chapter was to explain and compare the basic types of corneal maps produced by current machines, I resort to the same two-dimensional geometry assumed by all modern videokeratoscopes. This simplifying assumption is also used with the refractive power maps described in Section 3.5.4.

a. Axial curvature maps

As illustrated in Fig. 3.10, it is possible to define a local radius of curvature for a corneal surface point (B) as the distance from that point to the optic axis along the normal (BC_a). This is the same radius that is measured in keratometry (Bennett & Rabbetts, 1989c; Mandell, 1994), and this definition assumes that the center of curvature (C_a) is located on the optic axis. The radius (BC_a) thus derived is called the *axial* radius of curvature (r_a). It is sometimes also called the sagittal radius, though this is technically correct only for a rotationally symmetric surface (Applegate, 1994). The center of curvature for all surface points lies on the optic axis for spherical surfaces only, and since most corneas are nearly spherical near the apex, this assumption is acceptable for keratometry. However, this assumption introduces major errors in the periphery of an asphere. In the example of an ellipse, the center of curvature for more peripheral points gradually departs from the optic axis (Roberts, 1994b). In the ellipsotopic model, we can compute the axial radius (r_a) of curvature from Eq. (3-8) (Bennett, 1988; Douthwaite, 1995; Salmon & Horner, 1995). Equation (3-8) is based on Baker's equation (Eq. 3-2 and 3-5), and the derivation is presented in Appendix B.

$$r_a = \sqrt{r_\theta^2 + (1 - p) \rho^2} \quad (3-8)$$

The radius (r_a) in meters is usually converted to dioptric curvature (K_a) using the keratometer formula (Eq. 3-9). In this way, curvature values across the cornea are computed, and these may be presented in an axial curvature map such as that shown in Fig. 3.12a. Axial curvature maps are the default map used in most

clinical instruments.

$$K = \frac{(1.3375 - 1.0)}{r} \quad (3-9)$$

b. Instantaneous curvature maps

If the goal is to describe the local curvature within the meridional plane (plane of the page in Fig. 3.10), the axial, or keratometer based radius will be correct for a sphere but incorrect for an asphere such as an ellipse. For this reason, many computerized videokeratoscopes provide another estimate of local curvature that is based on the standard definition for curvature from plane geometry. In the jargon of modern videokeratoscopy, this is called the *instantaneous, tangential*, or sometimes *meridional* radius of curvature, and is represented by segment BC_i . The formula to compute the instantaneous radius for a two-dimensional function is shown in Eq. (3-10). It uses the first (dp/dz) and second (d^2p/dz^2) derivatives of the equation for the curve (Eq. 3-6) to calculate this local radius (r_i):

$$r_i = \frac{\left[1 + \left(\frac{dp}{dz}\right)^2\right]^{\frac{3}{2}}}{\pm \left(\frac{d^2p}{dz^2}\right)} \quad (3-10)$$

In the case of an ellipsoid, if the apical radius (r_θ , or AC_0) and axial radius (r_a) are known, the instantaneous radius (r_i) is easily calculated from the following relationship (Bennett & Rabbetts, 1989b):

$$r_i = \frac{r_a^3}{r_\theta^2} \quad (3-11)$$

For a prolate ellipse, which is similar to most corneas, the instantaneous radius is increasingly longer than the axial radius for more peripheral points. As with the axial radius, the instantaneous radius is usually converted to dioptic curvature using the keratometer formula (Eq. 3-9). Figure 3.12 compares an instantaneous curvature map (Fig. 3.12b) with an axial curvature map (Fig. 3.12a) for same model cornea.

The axial and instantaneous curvature maps describe features of the cornea that are familiar to most clinicians. The apical values are the same on both maps, and these represent either dioptric curvature or power. They both show a decrease in diopters from center to periphery, indicating a flattening contour. In the ellipsoidal example of a with the rule cornea (horizontal principal meridian is flatter), a vertically oriented dumbbell pattern is seen. A major difference between the axial and instantaneous maps of the same cornea is that instantaneous maps show a greater decrease in dioptric values from center to periphery. Computerized videokeratoscopes originally calculated only axial curvature maps, but now most instruments also offer instantaneous (tangential or meridional) curvature maps as well.

c. Gaussian curvature maps

For a rotationally symmetric cornea, the instantaneous and axial maps represent the minimum and maximum curvatures, respectively, at each point across the cornea. An asymmetric surface will also have maximum and minimum curvatures for any point, and these will always be orthogonal to each other. A group working at the University of California at Berkeley suggested another type of dioptric curvature map, the Gaussian power map (Barsky, Klein, & Garcia, 1997), which displays the geometric mean of these two curvatures across the cornea. This map also includes a vector overlay which shows the orientation of the minimum curvature and the difference between the maximum and minimum curvatures. The Gaussian display offers advantages over the more traditional axial curvature maps; the pattern is shape-invariant, irrespective of the instrument optic axis location, and it better reveals the cone shape in decentered keratoconus.

3.5.4 Refractive power maps

Axial and instantaneous maps are based on a local radius of curvature for each corneal point. In paraxial optics, incident light rays are nearly normal to the corneal surface, and in that case, the approximate refractive power of the cornea is inversely proportional to the local radius. The keratometer formula, which converts both axial and instantaneous radii to diopters (Eq. 3-9), uses this assumption to estimate corneal surface “power”. It is incorrect, however, to assume that either axial or instantaneous dioptric maps describe refractive properties of the cornea outside the paraxial region. In that case, it is better to use ray tracing based on Snell’s law to compute the refractive power of the cornea (Camp, *et al.*, 1990; Maguire, *et al.*, 1991).

Roberts summarized the reason why the paraxial formula closely approximates refractive power near the apex only, but not in the periphery (Roberts, 1994a). Assuming the meridional geometry of Fig. 3.10, the refractive power (K) at any point on the corneal surface, through which a ray is traced, is (Klein, 1992):

$$K = n'/(z+f), \quad (3-12)$$

In Eq. (3-12), n' is the refractive index of the cornea (often taken to be 1.3375), and f is the axial distance from the point of incidence (P) to the focal point (F') for an off-axis parallel ray. For collimated incident rays, the angle of incidence (θ_i) is defined by Eq. (3-13),

$$\theta_i = \sin^{-1} \left(\frac{\rho}{r_a} \right) \quad (3-13)$$

where r_a is the axial radius of curvature (Salmon & Horner, 1995). Using Eq. (3-13) and Snell's law (Eq. 3-14), we can solve for the angle of refraction θ_r using Eq. (3-15).

$$n(\sin\theta_i) = n'(\sin\theta_r) \quad (3-14)$$

$$\theta_r = \sin^{-1} \left(\frac{\rho}{n'r_a} \right) \quad (3-15)$$

In this case, the index of refraction for the medium of the incident ray (n) is equal to 1.0 and n' is 1.3375. Klein has shown (Klein, 1992) that, for meridional ray tracing, the refractive power of a corneal point can also be defined as:

$$K = \frac{n'}{z+f} = \frac{n'}{z + \frac{\rho}{\tan(\theta_i - \theta_r)}} \quad (3-16)$$

For very small angles, both the sine and tangent of an angle may be approximated by the angle itself (Smith, 1990), and in that case, z is approximately equal to zero, and Eq. (3-16) reduces to the paraxial equation for surface power (Eq. 3-17 and Eq. 3-9).

$$K = \frac{(1.3375 - 1.0)}{r_a} \quad (3-17)$$

From this, it is clear that the paraxial formula for refractive power (Eq. 3-17) is an approximation of Eq. (3-16), which applies only near the corneal apex, where both the incident angle and sag (z) are close to zero. Further from the apex, however, the angle of incidence is too great to be approximated by the angle itself; sag increases and Eq. (3-16) must be used instead of the approximation in Eq. (3-17).

A corneal surface refractive power map based on meridional ray tracing is shown in Fig. 3.13a. Compared to the dioptric curvature maps of the same cornea in Fig. 3.12, the dioptric power map is very different. The dumbbell pattern is now oriented horizontally and, though the apical values are the same, the ray tracing maps shows a large *increase* in dioptric values from center to periphery.

The large increase in power peripherally may be counterintuitive to clinicians who are accustomed to seeing a decrease, but recalling Snell's law and noting that peripheral rays strike the cornea at increasing angles of incidence, it should be no surprise that power increases peripherally. This represents the spherical aberration of the cornea, a peripheral phenomena which will not appear if paraxial equations are used (Salmon & Horner, 1995).

In the mid 1990's some instruments began to incorporate refractive power maps as a display option. An example is the Holladay Diagnostic Summary, provided by the EyeSys 2000 Corneal Analysis System (Holladay, 1995).

Although this is an improvement over the keratometer formula for calculating surface refractive power, meridional ray tracing (Fig. 3.13a) still oversimplifies corneal optics. Small pencils of light refracted through the peripheral cornea do not actually form a single focal point, but an astigmatic interval. This oblique astigmatism is compounded by the toricity and asphericity of the surface. Theoretically, it would be better to represent the power of this cornea with a pair of maps that show the astigmatic sagittal and tangential powers associated with each point (Fig. 3.13). Sagittal and tangential powers were computed by skew ray tracing and the Coddington equations and example maps showing the respective powers are shown in Figs 3.13b and 3.13c (Salmon & Horner, 1995).

3.5.5 Comparison of corneal surface descriptors

First generation corneal topography systems offered only axial curvature maps, but newer instruments have added instantaneous (tangential or meridional) curvature maps. Some current instruments also provide surface elevation and ray tracing refractive power displays. These basic descriptors of the

cornea can also be presented in a variety of display formats. Each descriptor shows a different picture of the same cornea, and depending on the specific application, one descriptor may be more useful than another. When an appropriate reference surface is chosen, surface elevation maps reveal details of the corneal surface that may be particularly useful in the pre and post operative management of refractive surgery patients. Surface elevation data was particularly important in this dissertation because it is the information that was used to compute the corneal wavefront aberration. Some instruments that do not display surface elevation maps per se but convey the same information in the form of simulated fluorescein patterns.

Dioptric curvature maps are the most familiar, and they effectively present changes in local contour. They are therefore useful in monitoring surface shape changes, such as those seen in keratoconus or in contact lens induced distortion. The instantaneous curvature map is more sensitive to subtle changes than the axial curvature map, but is also more subject to data noise (Mandell & Horner, 1993; Mandell, Barsky, & Klein, 1994). The axial curvature map may be particularly useful in measuring axially centered surfaces. For example, lathe-cut aspheric contact lenses can be verified using videokeratoscopy (Pole & Sather, 1995). As mentioned above, dioptric curvature maps are sometimes erroneously thought of as refractive power maps. It is important to remind users that, though labeled in diopters, neither axial nor instantaneous maps show local refractive power. Instead, they show a variant of local curvature.

Ray tracing refractive power maps show certain optical effects that are not apparent from any of the other maps, and may therefore be better for visualizing certain optical properties of the surface.

3.6

BEYOND TOPOGRAPHY—CORNEAL OPTICS

When studying corneal optics, it is important to remember that each point in an image is formed by all the light passing through the pupil. Descriptors of corneal optical performance should therefore consider the corneal optical zone as a whole. If the goal is to depict optical performance, other descriptors such as the point spread, optical transfer and wavefront aberration functions may be more appropriate than any of the topographic maps described above. Each of these can be computed from the topography (Hemenger, *et al.*, 1994; Hemenger, Garner, & Ooi, 1995; Oliver, *et al.*, 1997; Oshika, *et al.*, 1999), but these functions are generally not available on current clinical instruments. In Chapter 5, I will use the wavefront aberration function to describe corneal optics. In Chapter 7, I will compare this to the wavefront aberration function for the entire eye and analyze the corneal contribution to the aberrations of the eye.

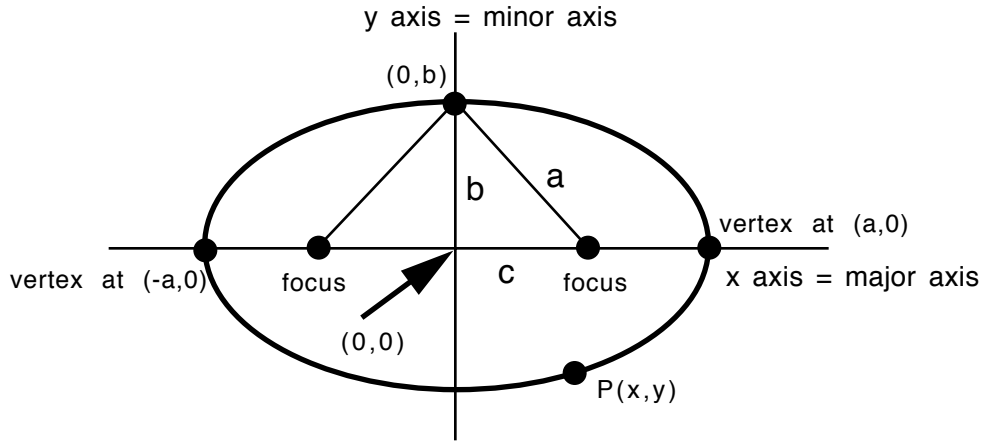


Figure 3.1

Basic geometry of an ellipse. The sum of the distance from each focus to any point on the ellipse is a constant value equal to $2a$. The parameter describing elongation, eccentricity (e), is defined as: $e = c/a$; $e = 0$ for a circle; $e = 1$ for a parabola.

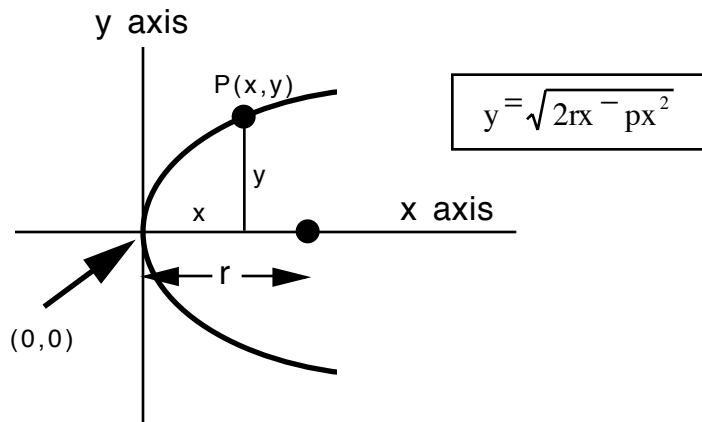


Figure 3.2

Coordinate system and variables used by Baker's formula (inset) to trace an ellipse. Variable r represents the apical radius of curvature.

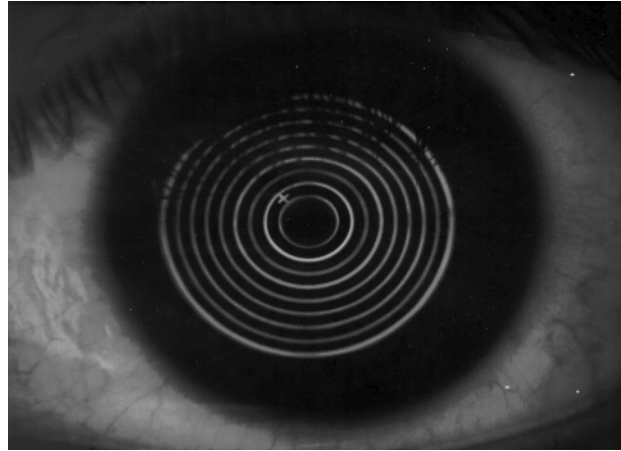


Figure 3.3

A Placido's disk or keratoscope consists of a series of concentric illuminated rings that are reflected off the cornea to evaluate its surface shape. The oval shape of the reflected rings is caused by nearly 6 diopters of corneal astigmatism. This image was taken from a Corneoscope polaroid photograph.



Figure 3.4

The EyeSys 2000 Corneal Analysis System, one of the most popular computerized videokeratoscopes. (Photograph courtesy of EyeSys Vision Group.)

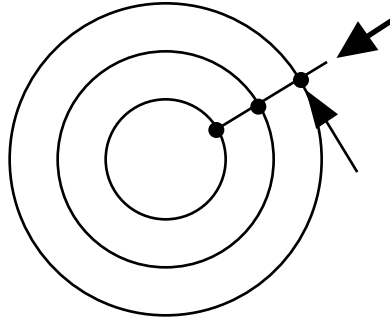


Figure 3.5
Videokeratoscopes measure the cornea at discrete points within multiple radial planes (short arrow) only, but ideally they should also measure in the orthogonal sagittal plane (long arrow) as well.

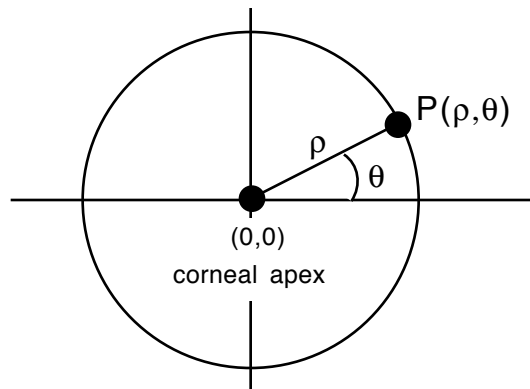


Figure 3.6
A polar coordinate system used with most videokeratoscopes.

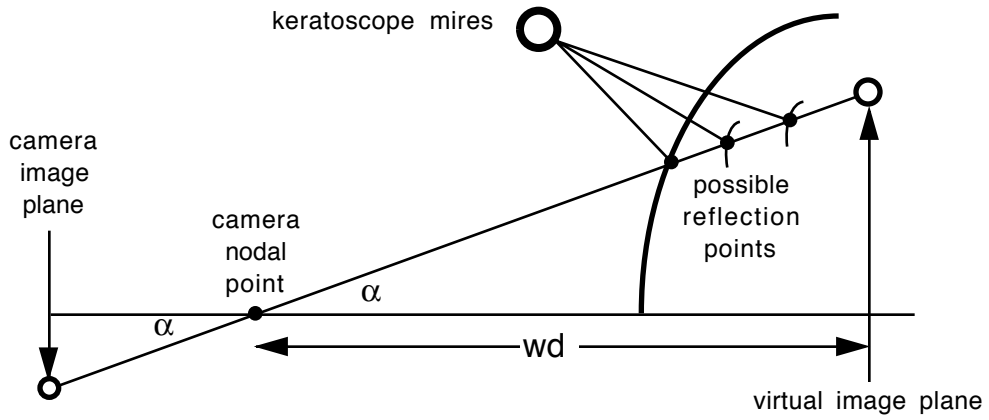


Figure 3.7
 General geometry of videokeratoscopy. The algorithm computes a surface point which may give rise to the reflected image, but without certain assumptions about the surface shape, there is insufficient information to calculate a unique corneal reflection point.

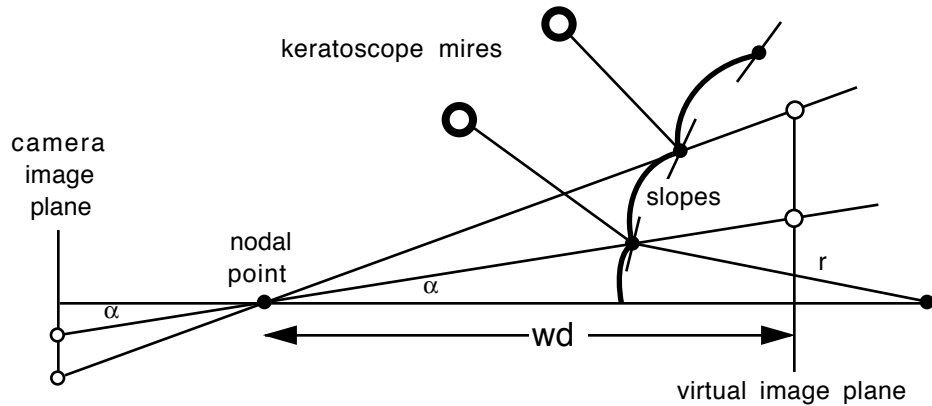


Figure 3.8
 Geometry of the van Saarloos algorithm. Iterative processes estimate corneal reflection points that are joined by circular arcs, which have common slopes at their junctions.

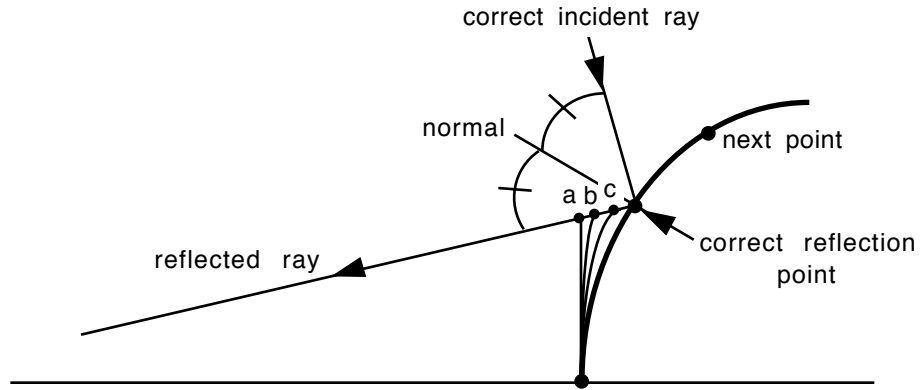


Figure 3.9

The Klein algorithm. Successive estimates (a,b,c, ...) of the corneal reflection point are made until the incident and reflected angles become equal. Points are then joined with a smooth cubic spline curve.

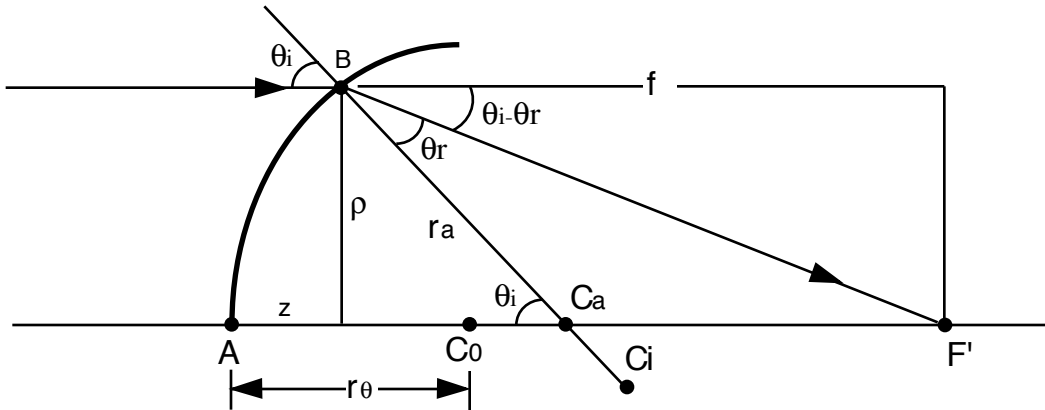


Figure 3.10

Two dimensional corneal curve described by Eqs. (3-5) and (3-6). The apical radius of curvature (r_θ) is segment AC_0 ; axial radius (r_a) is segment BC_a ; instantaneous radius (r_i) is segment BC_i . Arrows show the path of rays traced through point B.

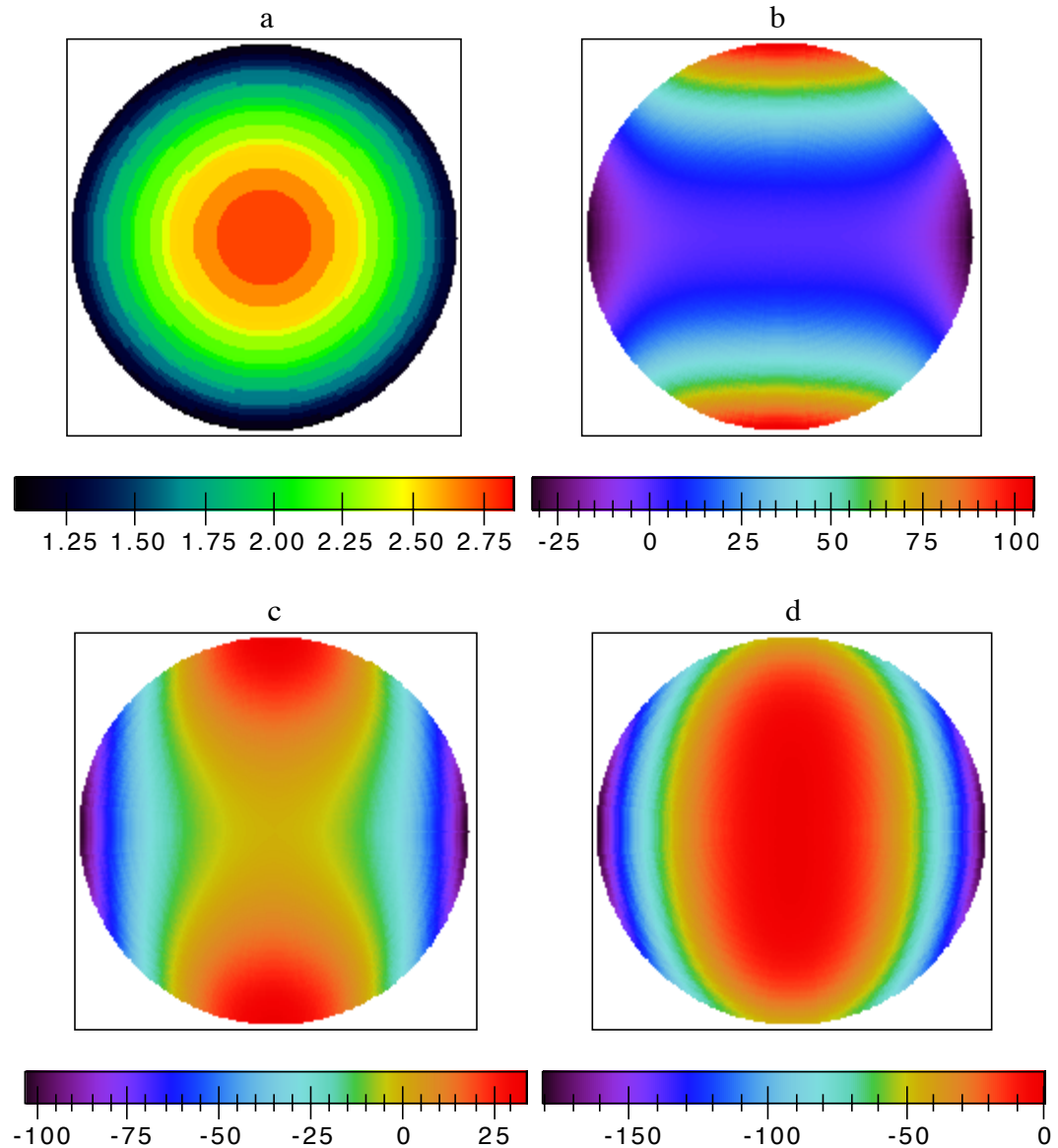


Figure 3.11

Four surface elevation maps of an ellipsoidal model cornea, with a horizontal apical radius of 8.00 mm, vertical apical radius of 7.50 mm, and shape factor of $p = 0.85$. In (a) elevations are measured from a reference *plane* and the 2.81 D of surface toricity cannot be visualized. The toricity is readily apparent when elevations are measured relative to spherical surfaces, as in (b,c,d). The reference surface in (b) has curvature equal to the flatter, horizontal corneal meridian; the reference surface in (c) has curvature midway between the steep and flat meridians; the reference surface in (d) parallels the steeper, vertical meridian. (Copied with permission: TO Salmon, DG Horner. Comparison of Elevation, Curvature and Power Descriptors for Corneal Topographic Mapping. **Optometry and Vision Science**, 72 (11) 800-808. © American Academy of Optometry 1995)

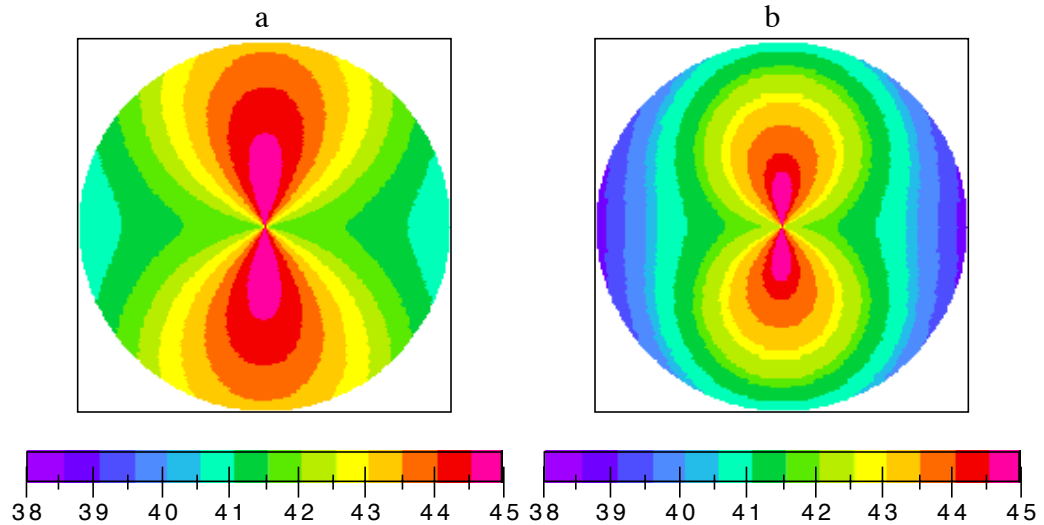


Figure 3.12
 Axial (a) and instantaneous (b) curvature maps of the same model cornea shown in Fig. 3.10. (Copied with permission: TO Salmon, DG Horner. Comparison of Elevation, Curvature and Power Descriptors for Corneal Topographic Mapping. **Optometry and Vision Science**, 72 (11) 800-808. © American Academy of Optometry 1995)

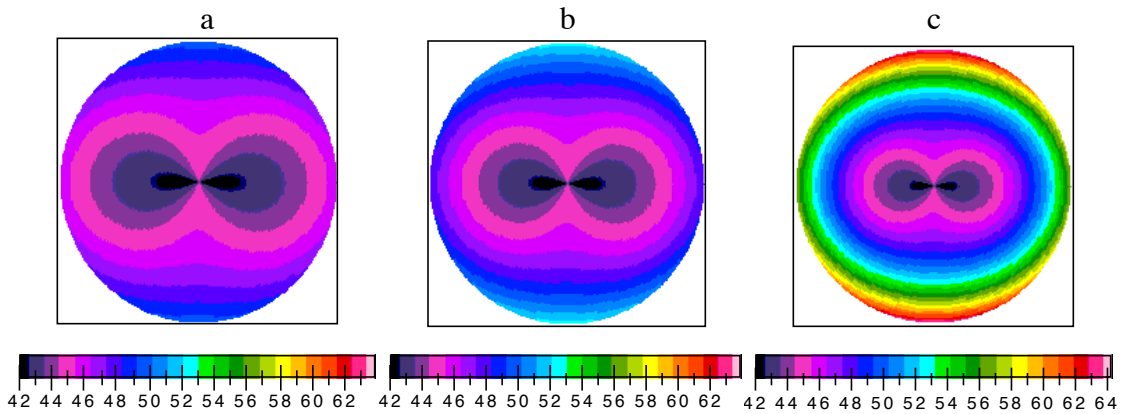


Figure 3.13
 Refractive power maps based on ray tracing. Map a, above, is based on simple meridional ray tracing; maps b and c are based on skew ray tracing and the Coddington equations. They show the sagittal (b) and tangential (c) powers associated with each corneal point. In contrast to the maps in Fig. 3.12, dioptric power increases from center to periphery. (Copied with permission: TO Salmon, DG Horner. Comparison of Elevation, Curvature and Power Descriptors for Corneal Topographic Mapping. **Optometry and Vision Science**, 72 (11) 800-808. © American Academy of Optometry 1995)

CHAPTER 4

Accuracy of the EyeSys Videokeratoscope

4.1

INTRODUCTION

In current clinical practice, computerized videokeratoscopes are primarily being used to diagnose subclinical corneal conditions that distort the corneal surface. Examples include keratoconus, Terrien's, and Pellucid's marginal degenerations (Horner, Salmon, & Soni, 1998). The highly detailed color maps produced by these instruments allow doctors to detect subtle surface anomalies, which cannot be seen even by careful slit-lamp biomicroscopy. In theory, videokeratographic data should also allow computation of the cornea's optical properties, including its wavefront aberration function. Prior to this study, it was unclear whether this new technology could provide sufficiently accurate measurements of corneal topography to allow meaningful computation of the corneal wavefront aberration function. For most clinical applications, a surface elevation error of a few micrometers is acceptable, as long as the measurements are repeatable. Optical studies of the cornea and its role in the optics of the eye demand much greater accuracy. Therefore, before proceeding with my investigation of corneal aberrations, I had to test the accuracy of the EyeSys computerized videokeratoscope and determine if it could provide surface elevation measurement with less than one micrometer of error. Early results were published (Horner & Salmon, 1998) in the contact lens journal, *International Contact Lens Clinics*, and a closely related project, which I performed for the United States Army Aeromedical Research Laboratory (USAARL), in Fort Rucker, Alabama, was published as a USAARL report (Salmon, Rash, & Mora, 1998).

4.1.1 The Keratometer tradition

Before computerized videokeratography, the only instrument available to most clinicians for measuring corneal surface shape was the keratometer. The keratometer estimates the central corneal radius of curvature in two principal meridians based on measurements at four paracentral points, and these radii are usually transformed to refractive power based on a paraxial power formula (Eq. 4-1). If the apical radius (r) is expressed in meters, the corneal refractive power (K) is in diopters. Variable n is the refractive index of

the cornea, which is usually taken to be 1.3375.

$$K = (n-1) / r \quad (4-1)$$

By the mid 1990's, computerized videokeratography had come into widespread clinical use, and it represented a quantum leap beyond keratometry, in terms of the amount of data provided. These instruments estimate the local radius of curvature at 5,000-10,000 points, thereby covering most of the cornea. The radii are typically transformed to axial curvatures using Eq. (4-1), according to the process described in Section 3.5.3. The 5-10,000 dioptric curvature values are normally presented in a color "topographic" map, and dioptric color maps became the standard way to display videokeratographic data. Typically, these maps show the axial curvature across the cornea, but the axial curvature can lead to misinterpretations about corneal power. This is because, as was discussed in detail in Section 3.5.4, the axial curvature uses the paraxial keratometer equation (Eq. 4-1) for the entire cornea, even though this equation was originally designed to estimate corneal power near the apex only (Mandell, 1992; Roberts, 1994a; Salmon & Horner, 1995). Since these maps do not correctly represent refractive power across most of the cornea, it is better to simply interpret them as maps which show the local curvature, expressed in diopters, across the cornea (Klein, 1997a).

4.1.2 Improved aspheric reconstruction algorithms

Well into the 1990's, the two most popular corneal topographers, the EyeSys 2000 Corneal Analysis System and the TMS-1, continued to rely on spherically based algorithms to measure the cornea, which is generally aspheric (Roberts, 1994b; Cohen, Tripoli, Holmgren, & Coggins, 1995). In theory, algorithms that do not assume a spherical surface should do a better job of measuring the cornea (Doss, Hutson, Rowsey, & Brown, 1981; Wang, Rice, & Klyce, 1989; van Saarloos & Constable, 1991). In an effort to improve accuracy, the Keratron (Alliance Medical) turned to an aspheric algorithm, which eliminates many of the assumptions required by the older machines. One article reported that, indeed, the Keratron's "arc-step" algorithm significantly improved accuracy (Tripoli, Cohen, Holmgren, & Coggins, 1995). EyeSys Technologies redesigned their instrument in 1994 by adding side cameras to accurately locate the corneal apex and an automatic focus mechanism to minimize operator error. In October of 1996, they released software version 3.2, which incorporated a new aspheric reconstruction algorithm designed to improve accuracy and eliminate problems associated with the previous spherically based programs. Earlier versions of the EyeSys videokeratoscope were not accurate enough to support my research, but shortly before I began to collect corneal topography data, the new version with the improved algorithm became available. Subsequently EyeSys has released software version 4, but it uses the same aspheric algorithm

that came with version 3.2. The purpose of the study described in this chapter was to test whether the new EyeSys aspheric algorithm was accurate enough to allow meaningful computation of corneal aberrations.

4.1.3 Videokeratoscope accuracy with spherical surfaces

Keratometers are calibrated using spherical test surfaces (steel ball-bearings, etc.), and early studies of computerized videokeratoscope accuracy similarly tested these instruments with calibrated spherical surfaces. Results were usually reported in diopters (D). First generation instruments had accuracies of ± 0.25 D, which was similar to the accuracy expected with standard keratometry (Hannush, *et al.*, 1989; Heath, Gerstman, Wheeler, Soni, & Horner, 1991). Current instruments claim to measure the corneal surface to an accuracy of ± 0.1 D (Bores, 1997).

Most manufacturers still specify videokeratoscope accuracy in diopters, but for the purposes of computing corneal optics, it is preferable to specify accuracy in terms of a height error in micrometers (Applegate, Nunez, Buettner, & Howland, 1995; Schwiegerling, Greivenkamp, & Miller, 1995). Based on the geometry of a representative corneal profile (ellipse; apical radius 7.8; shape factor 0.8; 3.0 mm from center), I calculated theoretical dioptric error (axial curvatures) and micrometer height errors, and found that these are related by a simple linear equation (Eq. 4-2). Variable x represents dioptric power error and y represents the elevation error in micrometers (μm). A simple rule of thumb is, 0.1 D axial curvature error equals approximately 1.5 μm error at 3 mm from the center.

$$y = 14.6x \quad (4-2)$$

4.1.4 Accuracy with aspheric surfaces

Until recently, videokeratoscope algorithms assumed that local regions of the cornea could be represented by a series of spheres centered on the instrument's optic axis, and as a result, these instruments had a spherical bias (Roberts, 1994a; Roberts, 1994b). Accuracy tests that used spherical surfaces overestimated the expected accuracy with real corneas. Since the normal cornea is better modeled by an asphere rather than a sphere, later studies have tested videokeratoscope accuracy using ellipsoidal or other aspheric surfaces. Those results are usually expressed in micrometers of elevation, rather than diopters of power.

Table 4.1 summarizes selected results from several studies and gives a general indication of accuracy for several videokeratoscopes. Measurement error is defined as the difference between the measured and known elevation for a test surface, and the root mean squared (RMS) error summarizes the height errors across the entire measured zone, usually 8-9 mm in diameter, with a single number. This statistic was available or could be computed for the first four of five studies listed in Table 4.1. These studies used

rotationally symmetric test surfaces, so it was also possible to compute a mean error for each keratoscope ring. Error generally increases with ring, or radial distance from the center. For the purposes of my study, I was interested in optical quality of the cornea and eye with a 5-6 mm pupil. This is the typical ablation zone diameter used in photorefractive keratectomy (PRK) and laser in-situ keratomileusis (LASIK). The procedures, in effect, produce a bifocal cornea, with the distance optical correction in the central 5-6 mm zone and a more myopic correction in the surrounding peripheral cornea. With videokeratoscopy, errors generally increase monotonically from center to periphery, so another logical way to express accuracy is the maximum error at the edge of the optic zone. I therefore included errors at the edge of a 6.0 mm diameter zone in Table 4-1.

TABLE 4.1 Videokeratoscope accuracy in measuring surface elevation of aspheres, as reported in several studies. Accuracy is expressed as an RMS error for an 8-9-mm diameter zone or as the maximum error within a 6-mm zone. Units are in micrometers (μm).

Study	Instrument and (software version)	Test surface	RMS error (8-9 mm zone)	Maximum error (6 mm zone)
Applegate ^a	TMS-1 (1.41)	ellipsoids	11.6 - 18.5	5 - 16
Applegate ^b	TMS-1 (1.41)	ellipsoids	2.3 - 5.0	2 - 5
Douthwaite ^c	EyeSys (2.00)	ellipsoids	7 - 11	6 - 8
Cohen	TMS-1 (1.41)	aspheres	8 - 28	4 - 8
Tripoli ^d	Keratron	aspheres	<1	0.1 - 0.25

^a With default TMS algorithm

^b With a rewritten reconstruction algorithm

^c RMS error not reported but estimated from results

^d RMS error not reported but estimated from figures

Applegate and Nunez (Applegate, *et al.*, 1995) tested the Tomey TMS-1 using rotationally symmetric spheres, ellipsoids and bicurves. They used two different algorithms to estimate surface elevation of the test surfaces. Besides the standard TMS algorithm, they wrote their own version to compute surface elevation from the raw keratoscope data. Table 4.1, rows 1 and 2 summarize results from this study for the ellipsoidal test surfaces only. Row 1 shows the accuracy with the default TMS program; row 2 shows that better accuracy was obtained when elevations were computed using the Applegate and Nunez algorithm. This instrument has since been replaced with the TMS-2, but they demonstrated that, with well designed algorithms, even older instruments had the potential to measure surface elevation of ellipsoids with a maximum error of 5 μm for both the RMS and 6-mm zone edge error.

Douthwaite (Douthwaite, 1995) tested an older version of the EyeSys system using 24 ellipsoids

of varying apical radii (r) and shape factors (p) to represent a range of normal corneal surfaces. After each measurement, the EyeSys instrument stores data files containing the axial radii (.XX file) and radial distance (.RA file) for each point measured on the corneal surface. Equation (4-3) shows that for an ellipse, a linear relationship exists such that, if the axial radius squared (ra^2) is plotted on the ordinate as a function of radial distance squared (y^2) on the abscissa, the y-intercept is equal to the apical radius squared (r_0^2), and the slope is equal to $(1-p)$. Variable p in Baker's equation represents the aspheric shape factor, which is related to conic eccentricity (e) by the formula, $p = 1 - e^2$. The derivation of Eq. (4-3), from Baker's equation

$$ra^2 = r_0^2 + (1-p)y^2 \quad (4-3)$$

(Eq. 3-2), is presented in Appendix B. By computing the y-intercept and slope for the linear equation described by Eq. (4-3), Douthwaite determined an apical radius and shape factor for each surface. These were plotted against known values to evaluate the instrument's accuracy. He developed the following empirical formula that showed the relationship between the true apical radius (r_0) and the radius (r_E) derived from the EyeSys measurement.

$$r_E = 1.01 r_0 + 0.036 \quad (4-4)$$

Similarly the relationship between the true shape factor (p) and EyeSys-derived shape factor (p_E) was:

$$p_E = 0.839p + 0.185 \quad (4-5)$$

Using Eqs. (4-4) and (4-5), I computed the apical radius (r_E) and shape factors (p_E) that the EyeSys would measure for various ellipses with known parameters r_0 and p , according to Douthwaite. Using the r_E and p_E with Eq. (3-6), I was able to compute the sags that the EyeSys should measure and compare these data with the true sags of the known ellipses. In this way I reconstructed theoretical error data for the EyeSys at discrete points and computed RMS (10.0 mm zone) and maximum (6.0 mm zone) errors, for Douthwaite's study. These are listed in Table 4.1. The overall RMS error was 7-11 μm , and maximum error for a 6.0 mm zone was 6-8 μm , depending on the apical radius and p value.

Cohen (Cohen, *et al.*, 1995) tested the TMS-1 using the default TMS program for surface elevation on four test surfaces. Two of the surfaces were constructed with a combined elliptical/parabolic

profile, while the other two surfaces were non-conic aspherics. His RMS errors (8-28 μm) were similar to those measured by Applegate using the default TMS-1 program, and 6.0 mm zone edge error (4-8 μm) was similar to the Douthwaite results.

Using the same four surfaces as Cohen, Tripoli (Tripoli, *et al.*, 1995) tested the accuracy of a newer instrument, the Keratron (Alliance Medical), which claims to use a highly accurate arc-step surface reconstruction algorithm. RMS errors were not reported, but from the figures showing error at different radial distances, it is clear that overall error within a 9 mm corneal zone error was less than 1.0 μm . This was entered in Table 4.1 under the RMS column. For a 6.0 mm zone, maximum error 0.10-0.25 μm .

These studies showed that older videokeratoscopes using old software were be able to measure the surface elevation of ellipsoids to within 10-30 μm , but with better software, accuracy with the same instruments improved to 2-5 μm or better. Since these results do not take into account sources of error inherent in the calibration procedure itself (imperfect calibration surfaces, misalignment, etc.) they are likely to have overestimated the error. The corneal wave aberration (W) can be estimated directly from surface elevation data by,

$$W = s(n-1), \quad (4-6)$$

where s is the elevation difference between the cornea and theoretical aberration-free reference surface, and n is the index of refraction of the cornea, usually about 1.34 (see Section 5.1.3c). A 2-5 μm surface elevation error, therefore, would results in approximately a one third that amount of wavefront error (Howland, Buettner, & Applegate, 1994; Applegate, *et al.*, 1995), or about 0.7-1.7 μm . For 633 nm light this is 1.0-2.67 wavelengths (λ). Since maximum wavefront aberrations for the human eye are in the 2-10 λ range (Charman, 1991), it is desirable to measure corneal topography more accurately than this. A reasonable goal is to reduce error to less than 1.0 μm , which corresponds to a 0.3 μm wavefront error or $\lambda/2$. Tripoli's paper indicates that, with rotationally symmetric aspheric test surfaces, the Keratron is capable of better than this degree of accuracy. My question was, Can the newest version of the EyeSys 2000 Corneal Analysis System achieve similar accuracy?

4.1.5 The problem of asymmetric surfaces

Because the videokeratoscope mires are rotationally symmetric, with no cues for meridional position, reconstruction algorithms assume that every point on the data image is reflected from a point on the mires that is in the same meridian (Applegate & Howland, 1995). This assumption simplifies computations since it breaks up the three-dimensional corneal surface into a set of two-dimensional meridional curves. In effect, this assumes that the corneal profile within each meridian is one slice out of a

rotationally symmetric surface and precludes any skew ray reflections (Klein, 1997a). Current videokeratoscopes make this assumption, so for rotationally symmetric surfaces, accuracy may be better than with asymmetric surfaces such as most real corneas. A common cause of corneal asymmetry is corneal toricity (astigmatism). One study (Greivenkamp, *et al.*, 1996) tested three older videokeratoscopes for accuracy in measuring toric surfaces designed to model 0-7 D of corneal astigmatism. Table 4.2 summarizes these results. For 1 diopter of astigmatism the EyeSys (version 2.1) was accurate to 0.7 μm (RMS), while the TMS-1 (version 1.41) and Alcon EH-270 (version 3.0) were accurate to 3.7 and 1.9 μm respectively. For higher degrees of toricity, accuracy with the TMS and EH-270 improved slightly, while the EyeSys was worse. For all three instruments, error for the most extremely toric (7 D) surface was less than 10 μm . This is the same magnitude of error reported for the TMS and EyeSys when they were tested with rotationally symmetric surfaces (Table 4.1).

TABLE 4.2 RMS error (μm) for toric test surface with three older videokeratoscopes (8-mm diameter zone). From (Greivenkamp, *et al.*, 1996)

Toricity (D)	TMS-1 (v 1.41)	EyeSys (v 2.01)	Alcon EH-270
0	0.7	0.6	0.8
1	3.7	0.7	1.9
2	2.5	5.3	1.2
3	1.7	7.5	1.5
7	4.2	9.7	2.4

Klein (Klein, 1997a) investigated the magnitude of videokeratoscope errors in measuring asymmetric surfaces of a variety of shapes. He found that for toric ellipsoids the error was very small and could be estimated using the formula,

$$\text{skew ray error} \approx C^2 / 2S, \quad (4-7)$$

where C is one half the corneal toricity (that is, C equals one half of the keratometer astigmatism) in diopters, and S is equal to the mean axial curvature at the apex. Among my subjects (Chapter 5), the largest corneal toricity was less than 1 diopter ($C=0.5$), and the mean axial curvature was approximately $S=43$ diopters. Based on Eq. (4-7), the skew ray error caused by the corneal toricity in this case should be about 0.003 D, which, according to Eq. (4-2) equates to about a 0.04- μm maximum height error for a 6.0-

mm corneal zone. This is negligible compared to the 0.25- μm error I found with most of the symmetrical test surfaces in this study. In terms of optical path length, 0.04 μm of corneal height error leads to approximately $\lambda/25$ of wavefront error. For abnormally shaped corneas (keratoconus, photorefractive keratectomy, etc.), the skew ray error can be much larger than this. To deal with this problem, Klein developed an arc-step algorithm that eliminates the skew ray error (Klein, 1997b).

Hilmantel (Hilmantel, Blunt, Garret, Howland, & Applegate, 1999) tested accuracy on asymmetric test surfaces by measuring three ellipsoids that had been tilted up to 15 degrees. This would induce surface asymmetries much greater than I expected to find in any of my subjects. For my subjects, the angular tilt between the keratoscope axis and line of sight was on the order of 1 degree. He used the TMS-1 with an improved reconstruction algorithm, and for no tilt, the mean RMS error was approximately 2 μm ; for 15 degrees of tilt it was approximately 5 μm .

These studies indicate that for small degrees of asymmetry, on a normal cornea, videokeratoscope accuracy is not much different from that found with well centered, symmetric test objects.

4.2

METHODS

4.2.1 Test surfaces

I measured six rotationally symmetric, aspheric test surfaces to assess instrument accuracy. The black PMMA (polymethymethacrylate) surfaces were manufactured by Sterling International Technologies, which guarantees the surface elevations to $\pm 1.0 \mu\text{m}$ of the specified value within a 10.0 mm diameter zone. Samples of the surfaces were verified by the manufacturer using Rank Taylor Hobson Talysurf, a device that makes stylus measurements to a resolution of better than 0.1 μm . The manufacturer claims that these surfaces are therefore accurate to 0.1 μm , though they guarantee 1.0 μm accuracy.

The radial profile of each surface was an ellipse, which can be described by Baker's formula, (see Section 3.2.2, 3.5.1 and Appendix B):

$$y = \sqrt{2rx - px^2} \quad (4-8)$$

Variable r represents the apical radius of curvature and p is the shape factor, which has been described previously. Five of the six surfaces were prolate ellipsoids designed to represent the range of shapes expected for most normal corneas. One surface was an oblate ellipse designed to represent a post-refractive surgery cornea. A small number of normal corneas are also oblate in shape (Keiley, Smith, & Carney, 1982; Eghbali, Yeung, & Maloney, 1995). Table 4.3 summarizes parameters for the test surfaces.

TABLE 4.3 Parameters for the test surfaces used in this study.

Surface #	Apical radius (mm)	Shape factor (p)	Eccentricity (e)	Description
1	7.8	1.0	0.00	sphere
2	7.8	0.7	0.55	average prolate cornea
3	7.8	0.5	0.71	more prolate cornea
4	7.8	1.3	NA	oblate cornea
5	7.3	0.7	0.55	steep prolate cornea
6	8.3	0.7	0.55	flat prolate cornea

4.2.2 Procedures

Before making measurements, I calibrated the EyeSys videokeratoscope according to the operator's manual. Each test surface was mounted in a holding device and coaxially aligned with the videokeratoscope. An initial keratograph was taken, and the color map was examined for centration and alignment. Fine adjustments were made, and these steps were repeated until optimal alignment was achieved based upon a criteria of zero surface toricity, correct apical radius and map symmetry. I took three images of each surface.

Most videokeratoscopes, including the EyeSys, do not display surface elevation data, but they show different forms of dioptric data. For example, the familiar axial curvature maps, which are the ones commonly used by clinicians, represent local curvature in diopters. The corneal wavefront aberration function must be computed from surface elevation height data, so it was necessary to convert the default dioptric data to height measurements in micrometers. EyeSys Technologies provides, upon request, a utility program which uses the standard ".RA" (radial distance) and ".XX" (axial radius) files to compute surface elevations. The EyeSys keratoscope consists of 18 rings, and topography is sampled at 1-degree radial intervals. Following a short header, each data file contains a 360 5 19 (rows 5 columns) data matrix. The first column specifies the meridian in degrees from 0 to 359, and the remaining 18 columns hold the surface data for each ring. With this information, the utility program computes the surface elevation in tenths of micrometers, and saves it as an ".SG" (sag) file. I processed and manipulated the data files using several computer programs: Transform 3.3, Excel 5.0, MATLAB 4.2c and Kaleidagraph 3.0.

4.2.3 Data analysis

From the known apical radius and shape factor for each test surface, it was possible to compute the true surface elevation at any point on the surfaces. For each test surface, a root mean squared error (RMSE) was computed by the following formula:

$$\text{RMSE} = \sqrt{\frac{1}{n} \sum (s_m - s_k)^2} \quad (4-9)$$

Variable s_m is the measured elevation, s_k is the known elevation, and n is the number of sample points for the entire surface.

Taking advantage of the rotationally symmetry for each surface, a mean surface elevation for each ring was also computed to show how error changed as a function of radial distance from the center. The analysis included the first 17 rings only because of incomplete data for the outermost ring. Results were expressed both as an sag error (SE) and fractional sag error (FSE) for each ring according to the following definitions.

$$\text{SE} = (\text{measured}) - (\text{known}) \quad (4-10)$$

$$\text{FSE} = \text{SE} / \text{measured} \quad (4-11)$$

Each surface was measured three times and analyzed. The data set with the least error for each surface was selected as the best measurement, and reported results were based on those data sets. I was particularly interested in accuracy within a 6.0-mm corneal zone (3.0 mm from the center), since this was the maximum pupil size I was planning to use when comparing corneal aberrations to ocular aberrations measured with the Shack-Hartmann wavefront sensor (Chapter 7).

4.3

RESULTS

The RMS error and diameter measured for each surface are listed in Table 4.4. The best results were for the oblate ellipsoid ($r = 7.8$, $p = 1.3$), with an RMS error of $1.8 \mu\text{m}$. The range of error for the five prolate surfaces was $3\text{-}7 \mu\text{m}$. Four of the surfaces had the same apical radius of 7.8 mm but differed in p values ($p = 0.5, 0.7, 1.0, 1.3$). Among them accuracy was better for surfaces with higher p values. Three

surfaces had the same p value (0.7) but differed in their apical radii ($r = 7.3, 7.8, 8.3$). RMS error for the three surfaces varied only slightly around $5 \mu\text{m}$. Depending on the surface, the EyeSys sampled an 8.8- to 9.6-mm corneal zone.

TABLE 4.4 RMS error for measurement of each test surface.

Parameter (r/p)	RMS error (μm)	Measured zone diameter (mm)
7.8 / 1.0	3.4	8.8
7.8 / 0.7	5.6	9.2
7.8 / 0.5	6.7	9.4
7.8 / 1.3	1.8	8.4
7.3 / .7	5.0	8.6
8.3 / .7	5.4	9.6

TABLE 4.5 Mean sag error (μm) at ring #12 before and after compensation for systematic error.

parameter (r/p)	Before compensation	After compensation ^a	Distance from center (mm)
7.8 / 1	- 3.3	- 0.13	3.1
7.8 / .7	- 4.7	- 0.17	3.2
7.8 / .5	- 5.1	0.36	3.2
7.8 / 1.3	- 1.8	0.11	3.0
7.3 / .7	- 4.1	0.02	3.0
8.3 / .7	- 4.5	0.24	3.4

^a See Section 4.4.1, Compensation for systematic instrument error.

Table 4.5 shows the mean sag error for ring 12 of each surface, which corresponded with a location approximately 3.0 mm from the center, or about a 6.0-mm corneal zone. The distance varied with each test surface because of the different apical radii and p value of each. This expression of measurement error is listed in the “Before compensation” column of Table 4.5. After analyzing the pattern of mean sag error as a function of the distance from the center for each surface, a procedure was developed to compensate for systematic instrument error; after doing so, the mean sag errors at ring 12 were significantly reduced. These are listed in the “After compensation” column. The compensation procedure is explained in detail in

Section 4.4.1.

Figures 4.1 and 4.2 present the mean sag error for each ring, and they show how measurement error varies with distance from the optic axis. Figure 4.1 shows results for surfaces that had the same apical radii (7.8 mm) but differed in their shape factors ($p = 0.5, 0.7, 1.0, 1.3$). Figure 4.2 compares the error for three surfaces, that shared the same shape factor ($p = 0.7$) but differed in apical radii ($r = 7.3, 7.8, 8.3$). For all surfaces the EyeSys underestimated surface elevations, and the error increased monotonically from center to periphery. Within 3.0 mm of the center, maximum error was approximately $4.0 \mu\text{m}$, and in the far periphery, error exceeded $12.0 \mu\text{m}$ in four of the six surfaces. Figure 4.1 shows that accuracy was much better for surfaces with higher p values, and in Fig. 4.2 error was slightly smaller for longer apical radii.

Within 1.5 mm of the center, sag errors were negligible (Figs. 4.1, 4.2). Beyond 1.5 mm (rings 6 through 17), fractional sag error (defined in Eq. 4-11) increased in a nearly linear fashion for all surfaces. Figure 4.3 plots the fractional sag error between rings 6 and 17, for four surfaces that had the same apical radius. Linear regression equations and correlation coefficients appear under the graph.

4.4

DISCUSSION

4.4.1 Compensation for systematic instrument error

RMS error and sag error using EyeSys version 3.2 were in the same range reported for the TMS-1 version 1.41, when used with an improved reconstruction algorithm developed by Applegate and Nunez (Table 4.1, row 2); namely, $5.0 \mu\text{m}$ or better. Figures 4.1 and 4.2 show that error increases monotonically as a function of radial distance from the center of the ellipsoid. The shape factor (p) also appears to have an effect on the amount of error (Fig. 4.1)—more so than apical radius (Fig. 4.2). Figure 4.3 provides a closer look at the relationship between fractional sag error (FSE, defined in Eq. 4-11) and radial distance. Between 1.5 and 5.0 mm from the center, FSE's change as nearly linear function of radial distance, though the best fit line differs for each different shape factor. Based on these observations, I developed a linear formula to predict EyeSys FSE based on the known shape factor and radial distance (Eq. 4-14). With a good prediction of the error it is then possible to compensate for the systematic measurement error and improve accuracy with the EyeSys. The following paragraph explains how I developed the linear formula (Eq. 4-14) to predict the FSE for each surface, based on its p value.

In Fig. 4.3, the regression line slopes decrease for surfaces with lower p value. The y intercepts are also smaller for the surfaces with lower p values. Analyzing the slopes and y intercepts for the four lines shown in Fig. 4.3, I found that the slope is directly related to the surface p value as shown in Fig. 4.4. It also shows that there is a linear relationship between the p value and y intercept of the regression lines shown in Fig. 4.3. The linear regressions in Fig. 4.4 are described by Eqs. (4-12) and (4-13), and

from these it is possible to predict a value for the slope and y intercepts respectively.

$$\text{slope} = 0.003165 \times p - 0.003445 \quad (4-12)$$

$$\text{intercept} = -0.003664 \times p - 0.0003363 \quad (4-13)$$

With these equations and a knowledge of the surface's shape factor (p), I worked backwards and estimated the linear equation (Eq. 4-14) describing the FSE as a function of radial distance (d). That is, based on a knowledge of the surface's p value alone, I predicted the regression lines shown in Fig. 4.3

$$\text{FSE} = \text{slope} \times d + \text{intercept} \quad (4-14)$$

With a predicted value for the FSE, I computed a corrected a corrected sag (CS) for each measured sag value according to Eq. (4-15).

$$\text{CS} = \text{measured} \times (1 - \text{FSE}) \quad (4-15)$$

Using this process, which required a knowledge of the p value, the measured sag, and the radial distance from the center, I corrected the measured surface elevations (sags), and compensated for much of the systematic instrument error. Figure 4.5 shows the sag error after compensation. Error still increased peripherally, but maximum error within a 10.0-mm zone (5.0-mm radial distance) for most of the surfaces was less than $1.0 \mu\text{m}$. Maximum error within 3.0 mm of the center was less than $0.25 \mu\text{m}$ for five of the six surfaces. For the surface with a shape factor of 0.5, the error was approximately $0.4 \mu\text{m}$. This is the same level of accuracy reported for the Keratron (Tripoli, *et al.*, 1995), and demonstrates that, with the correction for systematic bias, the EyeSys videokeratoscope (version 3.2) can measure the surface elevation of a rotationally symmetric model cornea to sub-micrometer accuracy.

4.4.2 Conclusion

These studies estimate videokeratoscope accuracy for best case conditions. In measurements of human eyes, factors such as alignment, focus, eye movements, or tear film changes, may introduce additional error. The newest corneal topographers include hardware improvements such as side cameras and automatic focus to improve accuracy. Software improvements in image processing and better reconstruction algorithm can also enhance accuracy. The EyeSys 2000 Corneal Analysis System,

operating with software version 3.2, is capable of measuring the surface elevation of model corneas to within $5.0 \mu\text{m}$ over a 6.0 mm optical zone. The algorithm still contains some systematic error, and if compensated, error can be reduced to less than $0.25 \mu\text{m}$ (maximum error at 3.0 mm from the center) for most surfaces. This would result in an optical path error of approximately $0.09 \mu\text{m}$ or about $\lambda/7$ ($\lambda = 633 \text{ nm}$).

Systematic error in the EyeSys measurements could be caused by errors in acquisition of the raw data images, or by errors in the algorithms, which analyze that data. The linear increase in fractional sag error with distance from the center (Fig. 4.3) suggests an error which accumulates from center to periphery. If the EyeSys reconstruction algorithm, like the von Saarloos and Klein algorithms, relies on slope estimates for the inner rings in order to compute values for the subsequent peripheral rings, a small initial error could accumulate in successive rings. Raw image data for the inner rings are more susceptible to error than the outer rings, since they use smaller images, smaller angles of reflection, and fewer sampling pixels. By studying the pattern of error across machines, it is possible to learn more about the source of the error. A similar pattern of errors across machines would suggest problems with the algorithm (software); a more variable pattern would suggest hardware-related errors. In either case, error that is systematic can be compensated, thereby improving accuracy significantly, as I demonstrated in this study.

The degree of accuracy required in videokeratometry depends on the specific application. For clinical diagnosis of abnormal corneas, or to monitor changes following refractive surgery, a 1-2- μm error is small. But for the purposes of understanding corneal optics, or to design the PRK ablation profile needed to minimize aberrations, it is desirable that errors be less than a $1.0 \mu\text{m}$. When measuring normal corneas under optimal conditions, the newest instruments, using the best available software, with compensation for instrument error, are able to provide this level of accuracy.

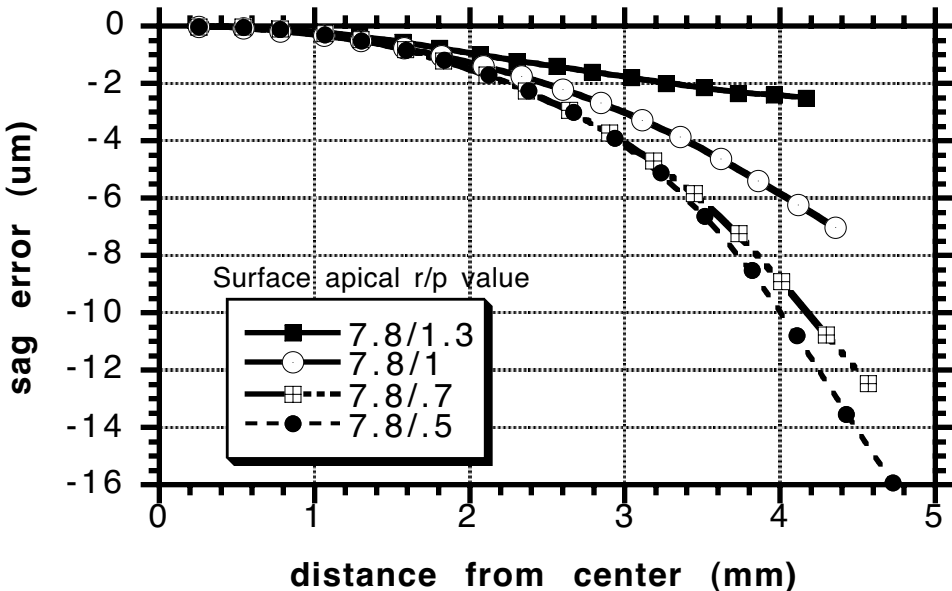


Figure 4.1
Radially averaged sag error as a function of distance from the center. For four surface with same apical radii but differing p values.

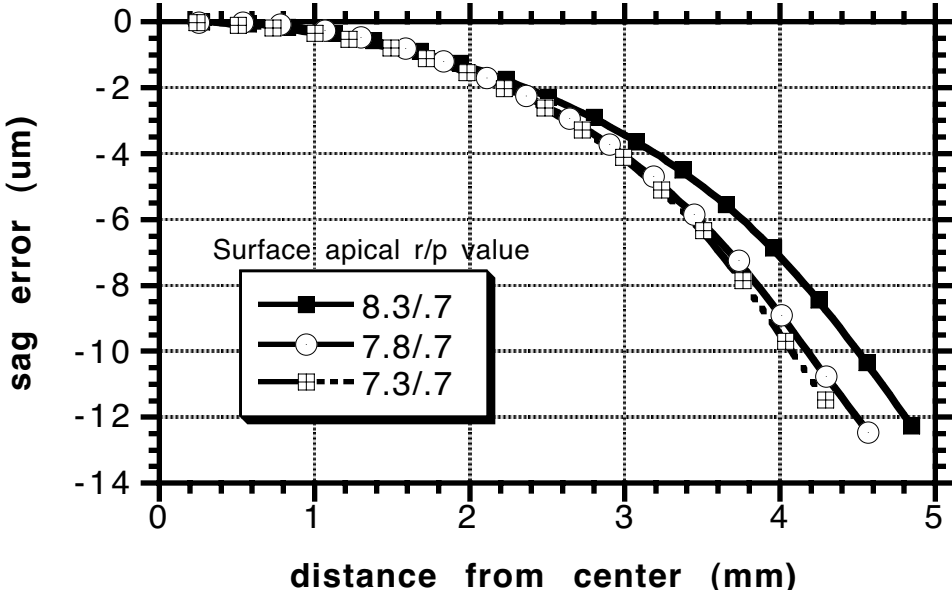
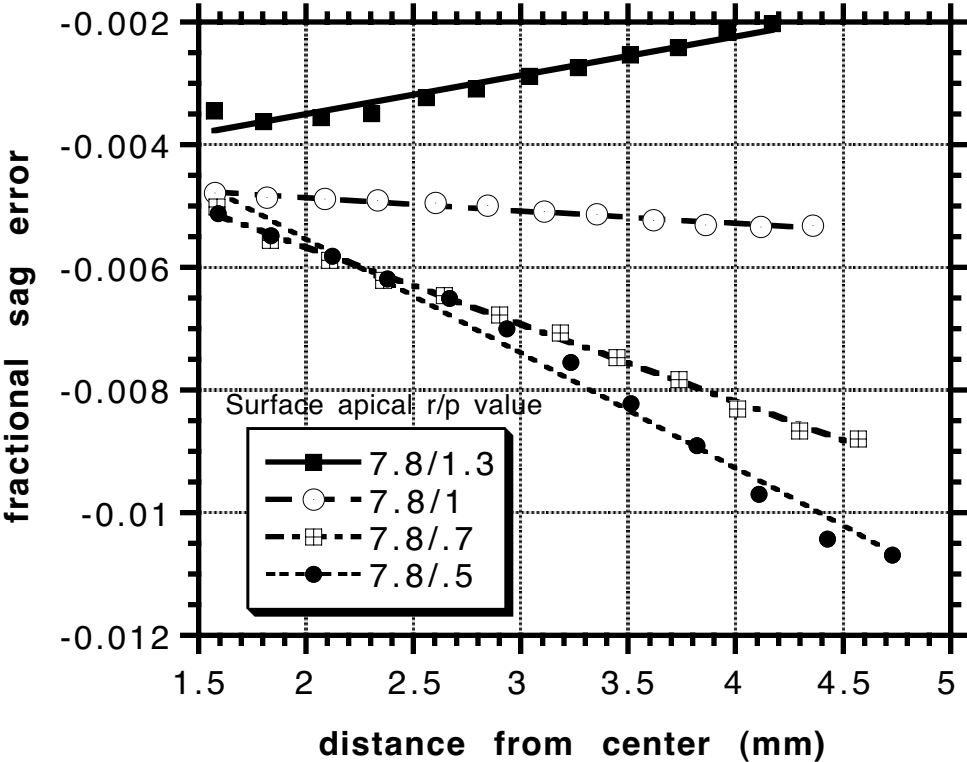


Figure 4.2
Radially averaged sag error for three surfaces with the same p value.



—■—	$y = -0.00476 + 0.000633x$	R= 0.97
-○-	$y = -0.00443 - 0.000211x$	R= 0.98
-□-	$y = -0.00315 - 0.001257x$	R= 1.00
-●-	$y = -0.00181 - 0.001868x$	R= 0.99

Figure 4.3
 Fractional sag error (defined in Eq. 4-11) between rings 6 and 17 for four surfaces, which had the same apical radii but different shape factors. These show a nearly linear relationship between radial distance and fractional error. The linear equations change for each different p value.

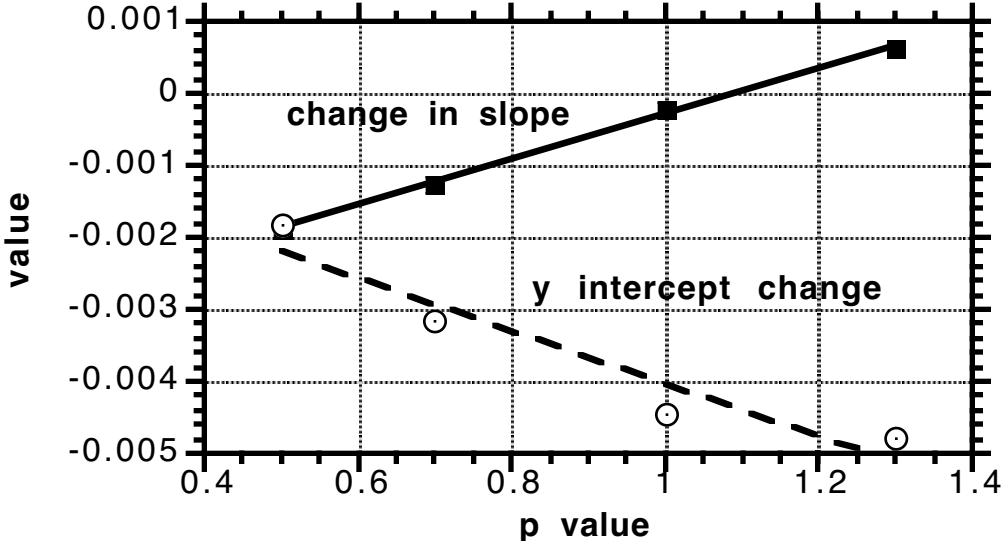


Figure 4.4 Change in linear regression slope and y intercept as a function of p value for the surfaces plotted in Fig. 4.3.

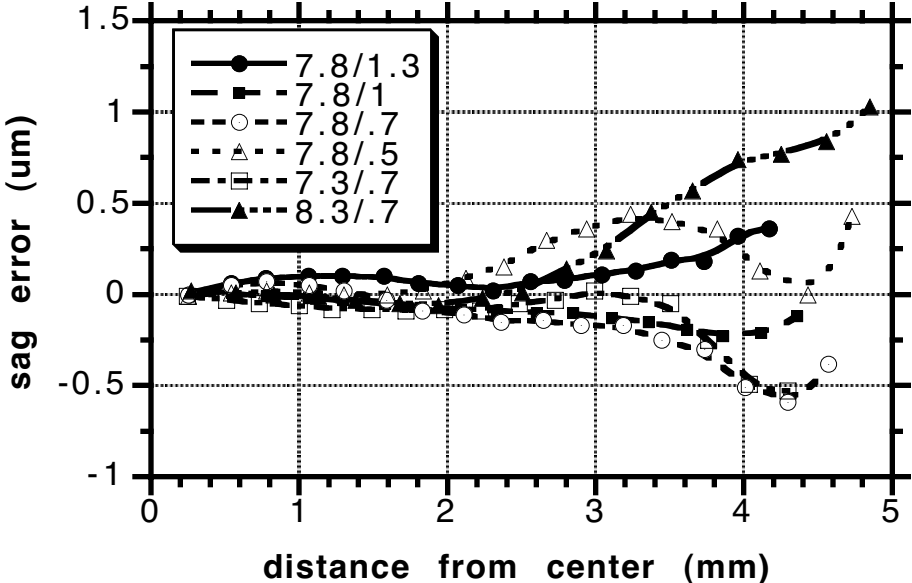


Figure 4.5 Radially averaged sag error after compensation for instrument bias for all six surfaces.

The Wavefront Aberration Function of Normal Human Corneas

5.1

INTRODUCTION

5.1.1 Current knowledge of the normal corneal aberrations

In order to completely understand the eye's optical system and correct its errors by reshaping the cornea, the aberrations of the whole eye, as well as those contributed only by the cornea, should be known. The front of the cornea is the single most important optical surface in the eye, and any modification of its shape, as in refractive surgery, can have a significant effect on the optics of the entire system. Our knowledge of the aberrations of normal corneas is still limited because, until recently, there was no practical means to measure the surface shape of the cornea with sufficient accuracy or detail. The new technology of computerized videokeratography has recently made highly accurate measurement possible, and from this, its corneal aberrations can be studied in detail.

In spite of the large number of articles and books on corneal topography, relatively little research has been done to study aberrations of the normal cornea. In one study of nine normal eyes, Howland *et al.*, found that, on average, these corneas had a slight negative spherical aberration, though this was not true for all subjects (Howland, Buettner, & Applegate, 1994). Hemenger estimated the wavefront aberration for one cornea, and found 2 wavelengths (λ) of positive spherical aberration at the edge of a 5.5- mm pupillary zone (Hemenger, Tomlinson, & Oliver, 1994). Other studies (Carney & Henderson, 1993; Applegate, *et al.*, 1994b; Carney, Mainstone, & Henderson, 1997) have suggested that highly myopic eyes tend to have higher p values^a (more spherical), and this would result in greater positive spherical aberration. Beyond astigmatism, asymmetric aberrations such as coma are also expected, and the cornea may be the major

^a The "p value" describes the shape of a conic section and is related to eccentricity (e) by the formula, $p = 1 - e^2$. A sphere has a p value of 1.0, and p values between 1.0 and 0 describe flattening ellipses. See Chapter 3 for more information on typical p values for human corneas.

source of asymmetric aberrations for the eye as a whole (Howland, *et al.*, 1994). Hemenger (1994) found “substantial” corneal coma based on topography data for one cornea, though the amount of coma was not quantified.

Several studies (Camp, Maguire, Cameron, & Robb, 1990; Maguire, Zabel, Parker, & L, 1991; Maguire, Camp, & Robb, 1993) used computer ray tracing to evaluate the optical quality of real corneas. They did not compute wavefront aberrations functions, but rather point spread functions based on data from a first-generation computerized videokeratoscope, the CMS (Corneal Modeling System). Camp convolved the point spread functions with both high and low contrast Snellen letters to create simulated images for several normal and abnormal corneas. These demonstrated the degree to which image quality would be degraded as a result of keratoconus and epikeratophakia. Using similar methods, Maguire evaluated optical quality for five PRK eyes three months after surgery. The simulated images of high to low contrast Snellen letters showed reduced image quality for lower contrast letters.

In recent years, more research has been done to study the effect of refractive surgery on corneal optical aberrations and visual performance. In the correction of myopia, these procedures flatten the central 5-6 mm of the cornea but leave an abrupt transition to a steeper peripheral region. This is radically different from the natural cornea profile (Applegate, Howland, Sharp, Cottingham, & Yee, 1998), which gradually flattens from center to periphery, and we can expect to see unusual aberrations in eyes which have been modified by refractive surgeries. After both radial keratotomy (RK) and photorefractive keratotomy (PRK), large amounts of positive spherical aberration (Seiler, Reckmann, & Maloney, 1993; Applegate, *et al.*, 1994a; Applegate, Hilmantel, & Howland, 1996; Martinez, *et al.*, 1996; Applegate, *et al.*, 1998) were found, and higher refractive corrections were associated with more severe spherical aberration. These optical results were associated with decreased visual performance, measured by a loss in contrast sensitivity and/or low contrast visual acuity (Applegate, *et al.*, 1995a; Verdon, Bullimore, & Maloney, 1996; Applegate, *et al.*, 1998; Gauthier, *et al.*, 1998; Bullimore, Olson, & Maloney, 1999). Using Zernike analysis of corneal height data following RK, Schwiegerling isolated higher order surface shape aberrations from which he modeled the expected effect on visual performance (Schwiegerling J & JE, 1997). He predicted a reduction in contrast sensitivity which would be most noticeable at mid spatial frequencies. Another study of 50 eyes corrected for -6.00 (D) diopters of myopia with PRK showed significant increases in Zernike spherical aberration and coma and a significant decrease in the MTF, especially between 2 and 15 cycles per degree (Oliver, Hemenger, Corbett, & al., 1997). A study of 22 patients corrected with PRK in one eye and LASIK in the other eye showed significant increases in the wavefront variance, especially with large pupils (Oshika, Klyce, Applegate, Howland, & El Danasoury, 1999). In a normal eye, pupil dilation from 3 to 7 mm causes a 5-6 fold increase in the wavefront variance, but Oshika, *et al.*, found a 25-32 fold increase in post-PRK eyes and a 28-46 fold increase following LASIK.

My ultimate goal was to study the cornea's role in the monochromatic aberrations of the normal eye. This chapter presents my findings for the wavefront aberration of the cornea in isolation from the rest of the eye. Recent improvements in videokeratoscope algorithms have made it possible to measure the corneal surface accurately enough to compute the wavefront aberration function (Chapter 4). The results of this research will add to our still limited knowledge of normal corneal aberrations, and the methods developed here will simplify future analysis of corneal optics.

5.1.2 Wavefront aberration expected for a mean cornea

Since the mean shape of the human cornea is well known (Chapter 3), and the wavefront aberration is directly related to surface geometry, we can predict the average corneal wave aberration function. A first order approximation of the normal human cornea can be modeled by an ellipsotoric surface with an apical radius of 7.80 mm horizontally, 7.65 mm vertically, and a shape factor of $p = 0.8$. Figure 5.1a shows a simulated corneal topography map (axial curvature map) of such a model cornea. The vertically oriented dumbbell pattern is typical of with the rule astigmatism, in this case 0.85 (D). Figure 5.1b shows a surface plot of the corresponding wavefront aberration function for a 5.6-mm-diameter pupil. It has a saddle-like shape due to astigmatism, and the minimum and maximum wavefront values are -0.6 and 6.5 wavelengths respectively. The wavefront aberration for a real cornea would probably show greater asymmetry than this (Howland, *et al.*, 1994). Across the range of normal apical radii and shape factors, and for this pupil size, the spherical aberration could conceivably range from a maximum edge height of -0.25 to 8 ; 1.25 diopters of astigmatism would add about ± 3 wavelengths to this.

5.1.3 Computing the wave aberration function from corneal topography

Three methods may be used to compute the corneal wavefront aberration from a known elevation contour. Using the an elliptical model cornea, the accuracy of the three methods, which I refer to as, ray tracing, the Fermat and the surface aberration methods, were compared.

a. Ray tracing

The basic way to compute the wavefront aberration at discrete points across and optical surface is by ray tracing. In this particular application of ray tracing, the corneal front surface and pupil are considered in isolation from the rest of the eye (Fig. 5.2). Ray tracing based on Snell's law allows us to mathematically construct the optical wavefront that propagates through the pupil after refraction at the cornea. In the case of a theoretical aberration free cornea, the wavefront will be spherical with its radius centered on focal point F. This "pupil sphere" is the reference surface from which wavefront aberrations are measured. If aberrations are present due to the shape of the corneal surface, the actual wavefront will depart

from the pupil sphere, and the optical path distance between these surfaces is the wavefront aberration. The distance is measured along the refracted ray (Hopkins, 1950; Born & Wolf, 1980), which is segment AB in Fig. 5.2. This can be closely approximated by segment CB, which is on a radius of the reference sphere (Welford, 1986). This definition for the wavefront aberration is used by some references (Williams & Becklund, 1989; Smith, 1990). For the range of normal corneal shapes, the difference between distances AB and CB is less than $\lambda/1000$ wavelengths, and defining the aberration as BC simplifies calculations. Multiplying CB by the refractive index converts this physical distance to optical path distance, which can be expressed in micrometers or wavelengths.

Assuming an elliptical corneal profile, with apical radius r and shape factor p , the wavefront aberration may be computed by ray tracing using the following steps (see Fig. 5.2).

- 1) The height of an incident parallel ray, which intersects the cornea at point Q, is defined as y_q .
- 2) From Baker's formula for a conic section (see Eqs. 3-2, 3-5 and 3-6), the x coordinate (x_q) of point Q is computed using Eq. (5-1).

$$x_q = \frac{r - \sqrt{r^2 - py_q^2}}{p} \quad (5-1)$$

- 3) The angles of incidence and refraction at point Q are measured from the surface normal, which is related to the first derivative of Eq. (5-1). In the case of a parallel incident ray, the angle of incidence (θ_i) is equal to the angle which the normal makes with the optic axis. This angle is computed using Eq. (5-2).

$$\theta_i = \text{atan} \left(\frac{y_q}{r - px_q} \right) \quad (5-2)$$

- 4) Using an assumed value for the index of refraction (n), the angle of refraction (θ_r) is computed using Eq. (5-3), which is Snell's law.

$$r = \sin^{-1} \left(\frac{\sin i}{n} \right) \quad (5-3)$$

5) The location of point B on the refracted wavefront can be determined because the angle of the refracted ray is known and the optical distance traveled by the ray from point T to B must be equal to the optical distance that an axial ray travels between the corneal apex (O) and the pupil center (P). Angle θ , which the refracted ray makes with the vertical is,

$$\theta = \frac{r}{2} - i + r, \quad (5-4)$$

and the distance QB is computed from Eq. (5-5). OP represents the physical distance from the corneal apex to the pupil.

$$QB = \frac{n(OP) - x_q}{n} \quad (5-5)$$

The coordinates for point B are then computed from Eqs. (5-6) and (5-7).

$$x_b = (QB)\sin \theta + x_q \quad (5-6)$$

$$y_b = y_q - (QB)\cos \theta \quad (5-7)$$

6) Since the wavefront aberration is defined along the normal to the reference sphere, the wavefront aberration (W) for this ray is:

$$W = (BC)n = (PF - BF)n. \quad (5-8)$$

Ray tracing requires a knowledge of the surface normal. This is easily computed for a model cornea based on a known analytical formula, but for real eyes, the surface normal must be estimated by

approximating the corneal surface with a polynomial and differentiating, or by calculating the cross product of vectors connecting the point of interest and other nearby points. Ray tracing through real corneas, based on videokeratoscope data, can become complex, and it depends on certain assumptions about the surface. These are relative disadvantages for the ray tracing method compared to two simpler methods, which will be described next.

b. Fermat's principle

Fermat's principle of least time, which is the basis for Snell's law and refraction, defines the path taken by a ray of light as that which will take the least time. When light crosses into a medium that has a different refractive index, the least time to travel between two points will not necessarily be a straight line between the points. It will, however, be the shortest optical path, which is defined as the physical distance multiplied by the refractive index. In a hypothetical, aberration-free optical system, any two rays, which depart from a point source in object space and travel through an optical system, will arrive at the image point at the same time, in phase, as shown in Fig. 5.3. That is, the optical path length for a marginal and axial ray must be equal, and the difference between their optical paths will be zero.

$$\text{optical path} = TQ + n(QF) = n(OF) \quad (5-9)$$

If the two optical paths are not equal, the two light rays will not arrive at the image point in phase, and this will indicate that an aberration or phase shift was introduced somewhere along the path. In the case of a single refracting surface such as the anterior cornea, the phase shift must be due to the surface shape. Therefore another definition for the wavefront aberration (W) is the difference in path lengths between a reference ray (in this case the axial ray) and other rays which pass through the surface (Thibos, 1992; Thibos, Ye, Zhang, & Bradley, 1997).

$$W = TQ + n(QF) - n(OF) \quad (5-10)$$

This was the method used by Hemenger (1994) to compute the corneal wavefront aberration from corneal topographic data for one eye. Hemenger also calculated the optical path between the anterior and posterior corneal surfaces to estimate a wavefront aberration for the entire cornea.

This method, which I will refer to as the Fermat method, is simpler than ray tracing because it is not necessary to know the corneal surface normals. The basic data required to compute the wavefront aberration by this method are the coordinates for an object point, its paraxial image point, a corneal reference point (O in Fig. 5.3), and the other surface coordinates. Figure 5.3 illustrates the Fermat method

with a schematic cornea which is symmetric about its optic axis. Here, the corneal reference point (O) is the intersection of the optic axis and corneal surface, but is not necessary that the reference point lie on the optic axis. In the case of real corneas, a better reference point would be the intersection of the line of sight with the cornea. This point is known as the corneal sighting center and is discussed further in Section 5.1.4. The freedom to select any reference point makes the Fermat method versatile, and this was the method that I used to compute the corneal wavefront aberration for my subjects. The relative accuracy of the Fermat method, compared with ray tracing, is discussed in Section 5.1.3d.

c. Surface aberration method

The optical path differences which cause aberrations arise because of the shape of the corneal surface. Therefore, it should be possible to directly calculate the corneal wavefront aberration from the surface data. In the case of a rotationally symmetric cornea, the surface shape that will be free of aberrations is an ellipsoid with an eccentricity (e) equal to the inverse of the refractive index (1/n) (Klein & Mandell, 1995). This is known as a Cartesian oval. Any departure from this surface will result in aberrations. I refer to the relative elevation of the cornea compared to the best fit Cartesian oval as the “surface aberration”, and if this is known, the corneal wavefront aberration can be computed using a very simple formula (Thibos, 1996), which may be derived based on the geometry shown in Fig. 5.4.

For an aberration-free cornea, represented by arc OS, a ray from a distant axial point is refracted at point S and propagates to the focal point, F. In a real cornea (arc OQ) with a surface shape other than the Cartesian oval (arc OS), the optical distance traveled between the object and image points will be aberrant compared to the distance traveled in the aberration-free case. The difference between the aberration-free path through the Cartesian oval and the path taken through the real cornea is the estimated corneal wavefront aberration (W). This is developed in the following equations, which refer to Fig. 5.4. The aberration-free optical path length is represented by

$$TS + (SF)n, \tag{5-11}$$

and the optical path through the real cornea is

$$TQ + (QF)n. \tag{5-12}$$

The difference between this is defined as the wavefront aberration (W) for that ray height.

$$W = [TS + (SF)n] - [TQ + (QF)n]. \tag{5-13}$$

CHAPTER 5: Wavefront Aberration Function of Normal Corneas

Substituting (TS + SQ) for TQ and simplifying, the equation becomes,

$$W = (SF)^n - SQ - (QF)^n. \quad (5-14)$$

Substituting (SA + AF) for SF and simplifying, we get,

$$W = (SA)^n + (AF)^n - SQ - (QF)^n. \quad (5-15)$$

Because the distances, QF and AF are very large compared to QA (Fig. 5.4), distance AF can be approximated by QF without significant loss of accuracy. The equation then converts to,

$$W \approx (SA)^n + (QF)^n - SQ - (QF)^n, \quad (5-16)$$

which further simplifies to,

$$W \approx (SA)^n - SQ \quad (5-17)$$

Segment SA is equal to $SQ(\cos \theta)$, therefore by substitution the equation becomes,

$$W \approx SQ(\cos \theta)^n - SQ, \quad (5-18)$$

and then,

$$W \approx SQ[(\cos \theta)^n - 1]. \quad (5-19)$$

I call segment SQ the “surface aberration”, and angle θ is the angular height of the incident point from the paraxial focal point, F. For the range of normal pupil sizes and corneal curvatures, the value for $\cos \theta$ is between 0.99 and 1.00, so another approximation yields,

$$W \approx SQ(n-1). \quad (5-20)$$

If $n = 1.376$, the corneal wavefront aberration function is simply the surface aberration multiplied by 0.376. Since this method tends to slightly overestimate the wavefront aberration, a slightly smaller value, $n =$

1.363, gives an estimate which agrees more closely with the ray tracing result for the same cornea. Howland and Applegate also noted the same simple relationship between corneal topography and its wavefront aberration function, though they used the keratometer index of 1.3375 (Howland, *et al.*, 1994; Applegate, Nunez, Buettner, & Howland, 1995b). Approximations at several stages are necessary to develop this formula, but it is a simple solution for finding the wavefront aberration directly from corneal topography. The surface aberration method does not require a knowledge of the corneal surface normals and is therefore simpler than ray tracing. For a symmetrical cornea centered on the videokeratoscope axis, the wave aberration computation is straight forward, but computations become more complex if the aberrations must be referenced to point that is not on the optic axis. This is a problem with most real corneas since the line of sight is the preferred reference axis for studying corneal optics, but it usually does not coincide with the videokeratoscope axis. Before the surface aberration method can be used to compute the corneal wave aberration, the corneal data must first be transformed so that the line of sight becomes the central reference axis.

Once the corneal elevation data is centered on the desired reference axis, the wave aberration may be computed by the following steps.

- 1) Starting with the mean apical radius and assumed index of refraction, compute the Cartesian oval, which will be the reference surface.
- 2) Compute the elevation difference between the cornea and the reference surface.
- 3) If Eq. (5-19) will be used, compute the angle θ , and solve for the wavefront aberration. Equation (5-20) can also be used to compute the wave aberration directly from the elevations.

d. Three methods compared

Formal computation of the wavefront aberration function requires ray tracing to construct the refracted wavefront in the pupil. This is difficult to implement with real corneal data because corneal topography instruments do not provide information on the surface normals at the sampled points. The Fermat and surface aberration methods are advantageous since they can compute the corneal aberrations directly from elevation data without the normals. I tested the accuracy of the Fermat and surface aberration methods relative to ray tracing, using mathematical model corneas that had elliptical parameters similar to my subject's corneas. Ray tracing is considered the "gold standard" in this computation of the wavefront aberration since it is based on a direct application of Snell's law to the cornea, without approximations or assumptions. You would expect to have the greatest error for corneas with steep apical radii and high p values, therefore I selected reasonable worse case parameters for each of my subjects, and applied these to the wavefront computations. Since the model corneas were symmetric and centered, only spherical

aberration was present, and the maximum aberration occurs at the pupil edge. Results of the comparison are summarized in Table 5.1. Both the Fermat and surface aberration methods gave identical answers, which departed from the ray tracing answer by less than $\lambda/10$ or about 1.3% of its value. The negligible difference between the ray tracing result and that of the other two methods is probably due to subtle differences in the basic definitions of the wavefront aberration used by the different methods. For the purposes of my research, the agreement is close enough that I can consider the wave aberrations computed by all three methods as equivalent. The Fermat method was selected used in this study since it allows direct computation of the corneal aberrations even when the line of sight is not centered on the corneal topography data.

TABLE 5.1 Comparison of the three methods for computing the spherical aberration (W) for an elliptical model cornea. Corneal apical radii and shape factors were chosen to estimate the theoretical maximum spherical aberration for each subject. Pupillary diameters were 5.6 mm. Distances from the corneal apex to the pupil plane were 3.04 mm for AB and DH and 3.84 for LT. Maximum wavefront aberrations in wavelengths ($\lambda = 633$ nm) were computed by ray tracing, the Fermat, and surface aberrations methods. Error, expressed in wavelengths and percent indicate how much the wavefront computed by the Fermat and surface aberration methods differed from ray tracing.

Subject	Apical radii (mm)	Shape factor (p)	W by Ray tracing (λ)	W by Fermat (λ)	W by Surface aberration (λ)	Fermat/Surf Error (λ)	Fermat/Surf Error (%)
AB	7.7	1.0	5.69	5.74	5.74	.05	0.8
DH	8.2	1.0	4.67	4.70	4.70	.03	0.7
LT	7.7	1.1	6.79	6.88	6.88	.09	1.3

5.1.4 Central reference axis for corneal optics

Before we can correctly compute the cornea wave aberration from videokeratoscopic data using instruments such as the EyeSys Corneal Analysis System or the Tomey TMS-2, another fundamental consideration must be addressed. About which corneal reference point and reference axis should the corneal elevations be measured? Vision science has defined several major reference axes of the eye, such as the visual axis (foveal achromatic axis), pupillary axis and line of sight, but for this study of the eye's aberrations, the reference axis should be the line of sight (Mandell, 1992; Mandell, Chiang, & Klein, 1995; Applegate, *et al.*, 2000—In press). The line of sight, also referred to as the fixation axis, is the line which connects the center of the entrance pupil with the fixation point. It is the chief ray of the pencil of light coming from the point of fixation, which is limited by the pupil, and after passing through the eye's

optics, terminates on the fovea. This study is concerned with the optics of foveal vision, and since the wavefront aberration function is centered on the pupil, the logical reference axis is the line of sight. The visual axis, which runs between the fixation point and fovea, through the nodal point, is useful for other purposes, such as calculating image magnification, but it is not the reference axis needed for this study.

During normal videokeratoscope alignment, the patient fixates a small light located at the center of the Placido disk pattern, and as required by the surface reconstruction algorithm, the instrument optic axis (FC in Fig. 5.5) must be normal to the cornea. The optic axis of the instrument is therefore directed toward the corneal center of curvature (C), but this does not necessarily pass through the center of the entrance pupil (E). In fact, in most cases, as shown in Fig. 5.5, the entrance pupil center is slightly displaced from the videokeratoscope axis, and the line of sight (FE) is displaced from the videokeratoscope axis. The point where the line of sight intersects the corneal surface (S) is called the corneal sighting center, and Mandell recommends that, for the purposes of studying corneal optics, the videokeratographic data should be centered on the corneal sighting center (Mandell, 1992; Mandell & Horner, 1993; Mandell, Barsky, & Klein, 1994; Mandell, 1995; Mandell, *et al.*, 1995).

If the Fermat method is used to compute the wave aberration, the corneal data can be centered mathematically on the line of sight by defining the reference ray as the ray which travels from a distant object point, on the line of sight, through the corneal sighting center (which is usually decentered in the keratograph) and eventually terminates on the image point. Other rays can be drawn between the object and image points through other corneal points sampled by the videokeratoscope. The optical path differences between the reference ray and all other rays intersecting the cornea defines the wavefront aberration, associated with those intersection points. Coordinates for the corneal sighting center are therefore needed to compute the corneal wavefront aberration. The specific steps I used to determine the corneal sighting center location are described in Section 5.2.6.

5.1.5 Ellipsoid fitting of real corneal topography

Videokeratoscopes do not measure the cornea within the inner ring, and this leaves a 0.5-mm-diameter zone at the center of the cornea which is unsampled. It is possible to estimate the central apical radius based on data obtained from the innermost ring. It is also possible to estimate the apical radius (r) and shape factor (p) for a best fit ellipse of each corneal meridian. Computerized videokeratoscopes, such as the EyeSys Corneal Analysis System, sample thousands of points in a polar grid, meridian by meridian. After acquiring and processing the image, the EyeSys stores data files that contain the radial distance to each sample point (*.RA file) and the axial radius (*.XX file) at each point. Referring to the geometry described in Fig. 3.2 or Appendix B, the radial distance (y) and axial radius (r_a) at any point on an ellipse are related

by Eq. (5-21) (Bennett & Rabbetts, 1989).

$$r_a^2 = (1-p)y^2 + r^2 \quad (5-21)$$

This formula shows that, for an ellipse, a linear relationship exists between y^2 and r_a^2 in which $(1-p)$ is the slope and r^2 is the y intercept. Plotting a linear regression, within each meridian, for r_a^2 (from the *.XX file) as a function of y^2 (from the *.RA file) allows computation of the apical radius (r) and p value for the best fit ellipse for each meridian (Bennett & Rabbetts, 1989; Douthwaite, 1995; Douthwaite, Pardhan, & Burek, 1996) by the following formulae:

$$r = \sqrt{(\text{y intercept})} \quad (5-22)$$

$$p = (1 - \text{slope}) \quad (5-23)$$

These principles were used to determine the p value for the best fit ellipse in each meridian. Once the p value was known, it was possible to compute and compensate for much of the instrument error and thereby improve the accuracy of the surface topography data (see Chapter 4). Section 5.2.5 specifically describes how I implemented this data correction procedure.

5.2

METHODS

After describing the human subjects used for this study, this section will summarize the specific steps I used to compute the corneal wavefront aberration function from measurements of corneal topography using the EyeSys videokeratoscope. The important steps in this process are listed below.

- 1) Calibrate the EyeSys videokeratoscope
- 2) Acquire corneal topography data images
- 3) Compute mean corneal surface elevations
- 4) Correct EyeSys data for instrument bias
- 5) Compute the corneal sighting center location
- 6) Compute the corneal wavefront aberration
- 7) Transform data from polar to Cartesian coordinates

- 8) Fit data to Zernike polynomials

5.2.1 Subjects

The corneal wavefront aberration function for three normal corneas was based on data collected from the EyeSys 2000 Corneal Analysis System, one of the major corneal topography systems used in clinical practice today. The Institutional Review Board approved the research protocol, and informed consent was obtained from the subjects prior to taking measurements. The right eye of three subjects were measured. Clinical data describing these eyes are listed in Table 5.2.

TABLE 5.2 Clinical data describing the right eye of the three subjects.

Subject	Refraction	BVA	Keratometry
AB	+0.88 - 0.50 x 030	20/15	42.51@003 / 43.32 (7.94@003 / 7.79)
DH	+0.13 - 0.38 x 088	20/15	39.85@175 / 40.47 (8.47@175 / 8.34)
LT	-0.63 - 0.88 x 090	20/15	42.83@100 / 43.38 (7.88@100 / 7.78)

5.2.2 Instrument calibration

A preliminary study to verify the accuracy of the EyeSys videokeratoscope is described in Chapter 4. The results of that study indicate that, after compensation for systematic instrument bias, surface elevation measurement error, for the area of the cornea which I would be measuring, could be reduced to less than $\pm 0.25 \mu\text{m}$ (Fig. 4.6). This would lead to an error of approximately ± 7 in the wavefront aberration function. Following the directions in the EyeSys operator's manual, the instrument software was recalibrated prior to taking measurements.

5.2.4 Corneal topography data acquisition

Mandell suggests that patients be given an appropriate peripheral fixation point so that topographic measurements will be centered on the corneal sighting center. For this reason, subject AB was instructed to fixate a point located 1 degree to the left (nasal) and 0.2 degrees below the EyeSys fixation light (Table 5.3 right column). Because of the difficulty in precisely shifting fixation by very small angles, this did not exactly center the corneal sighting center and a slight residual angle remained, which was mathematically compensated for later. Subjects DH and LT were instructed to fixate the central fixation

light, and EyeSys images were taken using standard alignment. Approximately 20 good quality images were acquired for each eye, and data was stored for later processing.

Although the EyeSys instrument uses 18 rings and is designed to measure up to about a 9-mm corneal diameter, it is common for a patient's nose or brow to obstruct portions of the peripheral rings. I attempted to maximize corneal coverage by having subjects turn their faces and open their eyes widely, but still some data was missing from the outer rings. Only complete rings were used in my analysis. Table 5.3 summarizes the number of rings, extent of corneal coverage and number of good images for each subject.

TABLE 5.3 Summary of EyeSys images collected for each subject.

Subject	Number of good rings	Corneal diameter measured (mm)	Number of good images
AB	12	6.2	15
DH	11	6.0	15
LT	13	6.6	19

5.2.4 Surface elevation computation from raw EyeSys data

The standard EyeSys software does not compute corneal elevations since this is not usually used in clinical practice. Upon request the manufacturer provides a utility program entitled, CORSAG18.EXE, which uses input from previously stored data files to compute the elevations. The README file, which accompanies this program, is included in Appendix C. Among the six data files that are normally saved for each image, the two which are needed to compute the surface elevations are the *.XX and *.RA files. The *.XX file contains the axial radius of curvature associated with each sampled point in hundredths of a mm; i.e., 7.89 mm is recorded as 789. The *.RA files records the radial distance of each point from the corneal center, also in hundredths of a mm; i.e., 0.25 mm is recorded as 25.0. Radial distances were approximately 0.25 mm from the videokeratoscope axis to ring #1, and were about 4.5 mm for ring #18. Each of the raw EyeSys data files are organized with a one-line header followed by 360 rows, with 19 numbers in each row. The first number gives the angular meridian (0-359) in degrees. This is followed by 18 numbers, which are the data associated with each EyeSys ring from center to periphery.

The CORSAG18.EXE program, uses the *.XX and *.RA files to compute the surface elevations, which are stored in an ascii text file with a *.SG extension. Elevations in the *.SG files are specified with reference to a plane perpendicular to the instrument axis and tangent to the cornea apex. Data are recorded in

units of tenths of a micrometer; i.e., 1 μm is recorded as 10.0). The raw EyeSys data set for each subject included these three data files for each good image. For example, subject AB had 15 good EyeSys images, and 15 *.XX, *.RA and *.SG files. For each subject I computed a mean *.RA and *.SG file with values scaled to micrometers. A mean *.XX file, scaled to mm, was also computed for each subject. The mean *.XX and *.RA files were used to compute the elliptical shape factor (p value), which was needed to correct the mean *.SG elevation data for systematic instrument error (see Section 5.2.5). Finally, the mean *.RA and *.SG files were used to compute the wavefront aberration (Section 5.2.7).

5.2.5 Correction for systematic instrument error

In the study described in Chapter 4, I discovered that the EyeSys surface elevation data contains an error that varies as a function of the ellipsoid shape factor and increases from the center to periphery of the cornea. The procedure developed in Section 4.4.1 to compensate for systematic instrument error was applied to the elevation data for each subject before computing the wavefront aberration.

It is important to keep in mind that the EyeSys, and all clinical videokeratoscopes, measure corneal topography meridian by meridian, presumably because of the difficulty of implementing a true three-dimensional reconstruction algorithm. In effect the three-dimensional corneal surface is treated as a set of 360 two-dimensional slices. In compensating for EyeSys error, I retained the two-dimensional approach and corrected the data meridian by meridian, using the process which I will describe next.

The steps required to correct the EyeSys surface elevation data (mean *.SG file for each subject) were:

- 1) Compute the square of each of the axial radius values, which were contained in the mean *.XX data file. Each subject's mean *.XX file was organized into 360 rows (one for each radial meridian) and within each meridian there were 11-13 axial radius values, depending on the subject. This step yielded a data array with 360 rows, and in each row there were 11-13 squared radius values.
- 2) Compute the square of the radial distances contained in the mean *.RA data file. This step also produced a data array with 360 rows, each of which had 11-13 squared distance values.
- 3) For each meridian, there was now a data vector of squared axial radii (r_a^2) values and another data vector of squared radial distance values (y^2), which, as described in Section 5.1.5, are related by Eq. (5-21), which is repeated here.

$$r_a^2 = r_0^2 + (1 - p)y^2 \quad (5-21)$$

CHAPTER 5: Wavefront Aberration Function of Normal Corneas

Variable r_0 represents the apical radius of curvature, and p is the elliptical shape factor. Solving for the slope of the linear regression between r_a^2 (ordinate) and y^2 (abscissa), as described in Section 5.1.5, I found the elliptical shape factor (p) for each meridian according to Eq. (5-23), which is also repeated here.

$$p = (1 - \text{slope}) \quad (5-23)$$

4) Knowledge of the p value allowed me to compute components for a linear equation that would be used to estimate the fractional sag error (FSE) of the EyeSys instrument. The linear equation was composed of a slope and an intercept, both of which were computed based on the p value, by the following formulas. Equations (5-24) and (5-25) are the same as Eqs. (4-12) and (4-13) respectively.

$$\text{slope} = 0.003165 \times p - 0.003445 \quad (5-24)$$

$$\text{intercept} = -0.003664 \times p - 0.0003363 \quad (5-25)$$

5) Using the linear equation build from the slope and intercept components computed in the previous step, I computed the fractional sag error (FSE), which is defined as the sag error divided by the measured sag (Eq. 4-11), using Eq. (5-26). Equation (5-26) is the same as Eq. (4-14). Variable d represents the radial distance of each EyeSys sampled point from the optic axis and was contained in the mean *.RA files.

$$\text{FSE} = \text{slope}(d) + (\text{intercept}) \quad (5-26)$$

6) With a value for the FSE, I computed a corrected a corrected sag (CS) for each measured sag value contained in the *.SG file according to Eq. (5-27), which is the same as Eq. (4-15).

$$\text{CS} = \text{measured} \times (1 - \text{FSE}) \quad (5-27)$$

I imported the basic data arrays (*.XX, *.RA and *.SG) into an Excel spreadsheet and applied each

of the steps listed above to each meridian of data. The end product was a data array with the corrected surface elevations, in micrometers, for each subject.

5.2.6 Compute the corneal sighting center location

I used the Fermat method to compute the corneal wavefront aberration function. In order to center the function on the line of sight, it was necessary to trace a ray from a distant object, located on the line of sight, through the corneal sighting center, to the corresponding image point. An important intermediate step, therefore, was to determine the location of the corneal sighting center.

In order to compute the three-dimensional coordinates for the corneal sighting center, I needed to know the corneal apical radius, horizontal and vertical angle λ ^b, distance to the entrance pupil and distance from the cornea to the EyeSys fixation light. Mean corneal apical radii were provided by the EyeSys simulated keratometer function. To measure angle λ , an apparatus similar to that described by Mandell (1995) and illustrated schematically in Fig. 5.6, was constructed. A micrometer attached to a slit-lamp biomicroscope was used to measure the distance from the corneal surface to the entrance pupil. Side alignment cameras on the EyeSys ensure that the corneal apex is always in the same location during measurements, and the distance from this point to the fixation light is 119 mm. Table 5.3 summarizes the basic parameters used to compute the location of the corneal sighting center for each subject.

TABLE 5.3 Parameters used to compute the location of the corneal sighting center for the right eye of each subject. Angle λ is expressed in degrees. A positive horizontal angle means the pupillary axis is temporal to the line of sight. Positive vertical angle means the pupillary axis is below the line of sight. The fixation angle (in degrees) shows where each subject fixated with respect to the EyeSys optic axis.

Subject	Horizontal λ	Vertical λ	Entrance pupil (mm)	Cornea mean apical radius	Fixation angle
AB	+1.09	+0.59	2.50	7.87	1.0 nasal & 0.2 down
DH	+0.47	-0.60	2.50	8.41	On axis
LT	-2.34	-2.26	3.27	7.83	On axis

Using this data, the x and y coordinates for the corneal sighting center were computed based on the geometry of Fig. 5.5, where angle λ is represented by variable θ , the entrance pupil distance is segment SE, the corneal apical radius is segment VC, and the distance from the cornea to the videokerato-

^b Angle λ is defined as the angle between the line of sight and the pupillary axis. The line of sight joins the fixation point and the entrance pupil center. The pupillary axis is the line which passes perpendicular to the cornea and through the center of the entrance pupil.

scope fixation light is represented by segment FV. The following steps were be used.

- 1) Compute the length of arc PF.

$$(\text{arc PF}) = (\text{FS} + \text{SE}) \quad (5-28)$$

- 2) Find the length of arc SA.

$$(\text{arc SA}) = \frac{\text{SE}}{(\text{FS} + \text{SE})} (\text{arc PF}) \quad (5-29)$$

- 3) Find the length of arc AV

$$(\text{arc AV}) = \frac{\text{VC}}{(\text{FV} + \text{VC})} (\text{arc PF}) \quad (5-30)$$

- 4) Compute angle VCS.

$$\text{VCS} = \frac{(\text{AV} - \text{SA})}{\text{VC}} \quad (5-31)$$

- 5) Finally, the displacement (x) of the corneal sighting center (S) form the videokeratoscope axis (FC) is,

$$x = (\text{VC})\tan(\text{VCS}). \quad (5-32)$$

This procedure was used to compute both the x and y coordinates of the corneal sighting center relative to the apex of the cornea (V). The z coordinate was then computed based on Baker's ellipse equation (Eq. 5-1) and a knowledge of the corneal apical radius and p value. Coordinates for the corneal sighting center relative to the center of the keratographs are listed in Table 5.4.

TABLE 5.4 Estimated position of the corneal sighting center, in mm, relative to the center of the EyeSys corneal topography map. The x and y dimensions refer to standard Cartesian coordinates on the map. Negative z refers to distances behind the corneal apex.

Subject	x	y	z
AB	0.082	0.003	0.000
DH	-0.046	0.057	0.000
LT	0.173	0.171	-0.004

5.2.7 Compute the corneal wavefront aberration function

The Fermat method, described in Section 5.1.3b, was chosen to compute the wavefront aberration. In addition to the corneal surface data, the three-dimensional coordinates for an object point, the corneal sighting center, and the paraxial image point were required to compute the optical path length for the chief ray and other rays. The chief ray was defined as the ray between the object and image point, which passed through the corneal sighting center. The object point was a hypothetical fixation point located 10,000 meters in front of the cornea, on the line of sight, and for my purpose, it was essentially located at optical infinity. The object point and corneal sighting center coordinates defined an incident chief ray, and using an estimated normal to the corneal surface at the corneal sighting center, I used skew ray tracing (Freeman, 1990), through two paraxial surface points, to determine the paraxial image point. Once these points were known, I was able to compute the optical path length for the chief ray. The path length between the object and image points through the other known corneal surface point were also computed, and the optical path difference between the chief ray and each ray through the other corneal points was the corneal wavefront aberration at each surface point. A MATLAB program, which I used to compute the wavefront aberration function, given the object point, corneal sighting center and image point coordinates, is included as Appendix D.

5.2.8 Polar to Cartesian transformation

Up to this point all corneal data had been organized on a polar grid, but in preparation for later comparison with Shack-Hartmann wavefront data (Chapter 7), it was necessary to interpolate the corneal wavefront data to a Cartesian grid. Unless the corneal surface is perfectly symmetrical about the instrument optic axis, the reflected EyeSys rings will not be perfectly circular, and the instrument will measure points located on an irregular polar grid with radial spacing that varies with each meridian. A cubic spline interpolation was fitted to the data within each meridian to interpolate data to a regular polar grid (see

Appendix D). Data points were radially spaced at every 0.1 mm for 360 meridians on this regular polar grid. Next, using Transform 3.3 (Fortner), the polar data was interpolated to a square Cartesian grid with 0.2-mm spacing, which was centered on the line of sight.

5.2.9 Fitting to Zernike polynomials

In order to match the pupil sizes measured with the Shack-Hartmann device (Chapter 7), the corneal data was limited to a 5.6-mm-diameter pupillary zone for subjects AB and LT, while a 5.2-mm zone was used for DH. A MATLAB program was used to fit the wavefront data to a series of Zernike polynomials, which included terms up to the tenth order. A copy of MATLAB program used for Zernike analysis is included in Appendix E. The wavefront data was expressed in wavelengths ($\lambda = 633$ nm).

5.3

RESULTS

5.3.1 Quality of the data

Example corneal topography maps for each subject are shown in Figs. 5.7-5.9. Chapter 4 established that the EyeSys topography system is accurate enough to estimate the corneal wavefront aberration to within $\pm 1/7$ across most of the central cornea. The repeatability (precision) of surface elevation measurements is shown by Figure 5.10, which plots the radially averaged standard errors, as a function of radial distance for the three subjects. Standard errors increased from center to periphery and reached a value of about 0.6 μm at 2800 μm from the center (5.6-mm-diameter pupil). If the confidence interval for the mean surface elevation is defined as ± 2 standard errors, at the edge of the pupil where variability was largest, the confidence interval was ± 1.2 μm . This means that the confidence interval for the corneal wavefront aberration computed from mean EyeSys sags was $\pm 2/3$ or better across the measured pupil. Wavefront errors equivalent to the standard errors are shown along the right side of Fig. 5.10a. Fig. 5.11 shows the radially averaged signal-to-noise ratio (SNR), which is defined as the mean surface elevation, divided by the standard deviation. The SNR increases from center to periphery, indicating that the instrument's relative precision improves peripherally. This is fortunate since variability is larger near the pupil edge. The increasing SNR from center to periphery may be due to the fact that the instrument makes use of larger images and steeper reflection angles when analyzing peripheral corneal data.

Ultimately the corneal wavefront aberrations would have to be compared to the ocular eye aberrations measured by the Shack-Hartmann system. Since the Shack-Hartmann data was sampled on a regular Cartesian grid, and since it is easier to fit regular Cartesian data to Zernike polynomials, the EyeSys data, which was sampled on an irregular polar grid was interpolated to regular cartesian coordinates. The

interpolated data was then fitted to Zernike polynomials, and the end product of this process, 66 Zernike coefficients, could be used to analyze or synthesize the wavefront aberration. To test how well the Zernike coefficients fit the interpolated data, I compared the wavefront which was reconstructed using the Zernike coefficients with the interpolated data to which the Zernike polynomials had been fitted. The RMS differences between the two wavefronts, listed in Table 5.6, are $\lambda/20$ or less for all subjects. In addition, the ratio of wavefront variances (reconstructed / fitted data) are also listed. These statistics show that the Zernike polynomial fit using 66 modes (10 orders) very closely matched the input data and any error introduced by Zernike fitting was well below measurement error for the original data.

TABLE 5.6 Comparison of wavefronts reconstructed using 66 Zernike polynomials, which had been fitted to interpolated wavefront data, to the input data. The RMS difference between the reconstructed wavefront and fitted data, in wavelength ($\lambda = 633$ nm), is listed for each subject. The reconstructed wavefront variance divided by the fitted wavefront variance is also shown.

Statistic	AB	DH	LT
RMS difference: reconstructed vs actual wavefront (λ)	0.05	0.02	0.03
Ratio of wavefront variances	1.01	.99	.99

How faithful was the Zernike fit to the original raw EyeSys data? To assess this, I used the Zernike coefficients to reconstruct the wavefront on the same points originally sampled by the EyeSys (polar grid with irregular radial spacing). Using data for one subject (LT), the reconstructed wavefront was compared to the wavefront aberration computed directly from the original EyeSys data. The RMS difference between the two wavefronts was $\lambda/33$ for a 5.6-mm pupillary zone. Figure 5.12 shows contour plots of the two wavefronts superimposed. Near the center of the cornea, very small wavefront height variations were smoothed out by the data processing, but they were $\lambda/20$ or less. For the rest of the cornea, the two wavefront are essentially identical.

A Gram-Schmidt orthogonalization can also be used to transform irregularly sampled polar data prior to Zernike polynomial fitting, and this is the process used by Schwiegerling (1995) to decompose corneal elevation data to Zernike polynomials. He tested the accuracy of the Gram-Schmidt orthogonalization plus Zernike fitting routine with simulated corneal data and found an RMS error of less than $0.02 \mu\text{m}$, which equates to about $\lambda/100$ in the wavefront aberration. This is nearly the same magnitude of fitting error that I found following data interpolation, and this demonstrates that any error contributed by either interpolation or Gram-Schmidt orthogonalization is insignificant compared to the measurement accuracy of the original data.

5.3.2 Total corneal wavefront aberrations

Subsequent results are based on the wavefront aberrations determined by reconstruction using the Zernike coefficients. A complete list of the 66 Zernike coefficients for each subject may be found in Appendix F.

The wavefront aberration for each subject was reconstructed after removal of piston, tilt, and defocus. The major components of this “total” wavefront aberration were astigmatism and residual aberrations up to the tenth order. Figure 5.13, shows contour and surface plots of the wavefront aberration functions for the three subjects. Table 5.7 lists parameters which summarize the wavefronts.

TABLE 5.7 Summary statistic describing the total corneal wavefront aberration functions. Piston, tilt and defocus were removed and the “total” wavefront consisted of astigmatism plus aberrations up to the tenth order. The wavefront aberrations were measured in wavelengths ($\lambda = 633$ nm).

Subject	Pupil diameter (mm)	Wavefront magnitude (λ)	Total Wavefront variance	Astigmatism variance	Astigmatism % of total variance
AB	5.6	-2.66 to 3.67	1.54	1.41	91.8
DH	5.2	-1.84 to 2.52	0.40	0.31	77.5
LT	5.6	-1.67 to 2.35	0.45	0.31	68.9

From the appearance of the maps and the wavefront statistics in Table 5.7, it is clear that astigmatism is the largest component (69-98%) of the total corneal wavefront aberration for all three subjects. In comparison, the higher order aberrations in these normal eyes are small. To get a better feel for the amount of astigmatism contained in these wavefronts, the Zernike coefficients for primary astigmatism (modes 4 and 6) were converted to ophthalmic prescription notation in the following steps.

The polar form of the Zernike polynomials that represent astigmatism are shown by Eq. (5-33) for mode 4 (astigmatism with axis at 45° or 135°) and by Eq. (5-34) for mode 6 (astigmatism with axis at 90° or 180°). For both modes, the maximum and minimum wavefront heights (s ; in μm), which are at the pupil edge, may be computed using Eq. (5-35), where a is the Zernike coefficient.

$$W = a Z_4 \sin 2\theta, \quad (5-33)$$

$$W = \frac{1}{2} a^2 \cos 2\theta, \tag{5-34}$$

$$s = a \sqrt{\frac{1}{6}} (.633), \tag{5-35}$$

This may be converted to diopters (D) using the sag formula:

$$D = \frac{2s}{\sqrt{y^2 - s^2}} (1 \times 10^6) \tag{5-36}$$

Converting both Zernike coefficients for astigmatism to diopters and combining the crossed cylinders, the corneal astigmatism for each subject was computed. (See Section 2.4.5.) The corneal astigmatism represented by the Zernike coefficients are summarized in Table 5.8. For comparison, the EyeSys simulated keratometer values are also shown. The power and axis values obtained by the two methods are in close agreement.

Strictly speaking, a more perfect transformation of the Zernike astigmatism coefficients to the clinical notation requires that the higher astigmatic terms contained in orders 4, 6, 8, and 10 also be included (Schwiegerling, *et al.*, 1995). This is because ophthalmic astigmatism is circular in profile along the major meridians, while the Zernike profiles are parabolic, and a large number of parabolas must be summed to better approximate a circle. For my purposes, the higher order coefficients were small enough that they can be ignored, and for the relatively shallow curvature of these wavefronts, the astigmatic profiles across these pupils can be considered nominally circular (Webb, 1992).

TABLE 5.8 Corneal astigmatism in minus cylinder form, derived from the Zernike coefficients and those computed by the EyeSys simulated keratometry function.

Subject	Zernike coefficients	EyeSys simulated keratometry
AB	-0.94 x 013	-0.82 x 003
DH	-0.54 x 175	-0.62 x 175
LT	-0.47 x 108	-0.55 x 100

5.3.3 Higher order corneal wavefront aberrations

Higher order aberrations are defined here as the aberrations contained in orders 3-10, which are beyond the clinically correctable optical defects. These results differ from those described in the previous section in that astigmatism has been removed. Plots of the higher order aberrations are shown in Fig. 5.14, and certain aspects are summarized in Table 5.9. Various combinations of Zernike spherical aberration, coma and other aberrations were present in the three subjects, and in each case the resulting wavefront surfaces have unusual asymmetric shapes. Because spherical aberration and coma are relatively familiar aberrations, their relative contributions to the higher order wavefront aberrations are listed. Aberrations other than spherical aberration or coma make significant contributions to the wavefront aberration for all subjects. Note that the Zernike terms that are labelled “spherical aberration” or “coma” are not the same as the corresponding classic Seidel aberrations. For example, Seidel primary spherical aberration increases monotonic from the pupil center to its edge, but the Zernike primary spherical aberration is high in the center, decreases in the mid-periphery and then sharply increases at the edge of the pupil. The Zernike spherical aberration term contains a constant which shifts the wavefront away from a mean value of zero, while the other modes have mean wavefront values equal to zero.

TABLE 5.9 Summary statistics for the higher order corneal wavefront aberrations. The contribution of certain aberrations to the higher order wavefront variance are listed to show the relative contribution of each.

Subject	Wavefront magnitude ()	Wavefront variance	1° + 2° spherical aberration contribution (%)	1° + 2° coma contribution (%)	Contribution of other aberrations (%)
AB	-0.74 to 1.88	0.13	45.9	3.3	50.8
DH	-0.62 to 1.20	0.09	13.1	63.9	23.0
LT	-0.91 to 1.92	0.14	62.4	1.8	62.3

5.3.4 Higher order corneal wavefront by order and mode

Figure 5.15 compares the relative contribution of each Zernike order to the higher order aberrations in terms of percentage of the total wavefront variance. Third order aberrations include modes 7-10 (triangular astigmatism and primary coma); fourth order aberrations include modes 11-15 (spherical aberration and others). Table 5.10 shows the cumulative percentage of total wavefront variance as additional orders are added. Over 90% of the aberrations are accounted for in the third and fourth orders and the addition of fifth order (up to mode 21) aberrations accounts for 95% of the aberrations. Ten orders are able to account for 100% of the total wavefront variance in the reconstructed wavefronts, which account for

99% of the variance in the fitted data.

The bar graphs in Figs. 5.16, 5.17, and 5.18 show the relative contribution, in percent, of each of modes 7-21 (orders 3,4,5) to the higher order wavefront variance. The relative contribution of individual modes between 22-66 are insignificant, so they are not shown. In AB modes 7 and 10 combine to form triangular astigmatism, which contributes to 38% of the wavefront variance. The values for this aberration range over ± 0.6 wavelengths. Primary spherical aberration, represented by mode 13, contributes 45% and has minimum and maximum values of -0.3 and +0.5 wavelengths respectively. All other aberrations combined make up about 18% of the total variance. The contour plots in Fig. 5.19 illustrate how the major aberration components sum to form the total higher order wavefront aberrations.

TABLE 5.10 Cumulative contribution of each order to the higher order wavefront variance. Numbers indicate percent of the higher order wavefront variance. The wavefront reconstructed closely matched the original wavefront data (see Table 5.6). The ratio of the variances of the reconstructed wavefront to the input data are also shown.

Order	Modes	AB	DH	LT
3	7 - 10	40.8	74.0	11.0
4	11 - 15	93.73	95.8	93.1
5	16 - 21	95.1	98.9	95.9
6	22 - 28	97.6	99.3	97.9
7	29 - 36	98.9	99.6	98.5
8	37 - 45	99.4	99.8	99.2
9	46 - 55	99.8	99.9	99.6
10	56 - 66	100.0	100.0	100.0
Reconstructed : input wavefront variance ratio		1.01	.99	.99

Figure 5.17 reveals that the dominant aberration for DH is primary coma, which is the sum of modes 8 and 9. Primary coma accounts for 64% of the wavefront variance and minimum and maximum values are ± 0.7 wavelengths. The next largest contribution is made by mode 13, primary spherical, which accounts for 13% of the wavefront variance. The extreme values for primary spherical in DH are -0.1 and +0.2 wavelengths. The other aberrations combined contribute to about 24% of the total aberrations. Figure 5.19 shows how these components, plus the other aberrations sum up to form the total wavefront aberration.

TABLE 5.11 Summary of major components of the higher order wavefront aberrations for three subjects.

Subject	Dominant modes	Description	% of wavefront variance	Min/max values ()
AB	7 + 10	triangular astigmatism	37.6	± 0.63 -0.27 to 0.54
	13	1° spherical aberration	44.5 (remainder 17.9)	
DH	8 + 9	1° coma	63.8	± 0.67 -0.11 to 0.22
	13	1° spherical aberration	12.6 (remainder 23.6)	
LT	13	1° spherical aberration	62.3	-0.32 to 0.65 ± 0.51
	11 + 14	quadrilateral astig	18.4 (remainder 19.3)	

The breakdown for subject LT is show in Fig. 5.18. Primary spherical aberration far exceeds all other components, accounting for 62% of the wavefront variance. The minimum and maximum values of this aberration in isolation are -0.3 and 0.6 wavelengths. Mode 14, which I refer to as quadrilateral astigmatism, contributes 18% to the total variance and has a range of ± 0.5 wavelengths. All other aberrations combined make up about 19% of the total aberrations. Figure 5.19 shows contour plots of these components and their sum. Table 5.11 summarizes the dominant aberration components for each subject.

5.4 DISCUSSION

The methods used in this project enabled me to obtain an accurate picture of the corneal wavefront aberration, centered on the line of sight, for three normal subjects. Although the ultimate goal is to compare corneal aberrations with those of the whole eye, a study of the corneal aberrations in isolation from the rest of the eye gives valuable insight into the characteristics of this important optical component.

For the three subjects, the magnitude of the total wavefront aberrations (including astigmatism) were in the range expected from model eye calculations. When corneal astigmatism (~ -0.50 to -1.00 D) was included in the analysis, the peak to value magnitude of the wave aberrations was about 4-6 μ . In comparison, the higher order aberrations were smaller (1-2 μ), but depending on the subject, they still made up 10-30% of the total wavefront aberration. A common feature in all subjects was that over 90% of the higher order aberrations could be accounted for by the third and fourth orders. All of these subjects had positive spherical aberration, but the relative importance of spherical aberration varied in each eye. In LT

spherical aberration alone contributed to over 60% of the higher order wavefront variance and coma was small, while in DH spherical aberration was relatively small, and coma alone accounted for over 60% of the variance. In all subjects, other Zernike modes besides those associated with spherical aberration and coma played an important role in the total higher order aberrations.

A question when planning this research was, how many Zernike modes should be used to analyze the corneal wavefront aberration? Liang (1992) originally used 15 modes in his analysis of ocular eye aberrations, and Williams later extended his Zernike analysis of ocular eye wavefront data to 66 modes. As shown in Fig. 5.15, the bulk of the aberrations are contained in orders 3 and 4, which includes up to mode 15. The contribution of higher orders diminishes rapidly, but it took 10 orders, or 66 modes to account for 100% of the wavefront variance. This is to be expected for normal healthy corneas with relative smooth contours, but in post-refractive surgery corneas, or in eyes with keratoconus or other diseases, we can expect to see larger aberrations in orders 5-10.

Another question was, Did compensation for the line of sight tilt make a difference in the measured higher order aberrations? To evaluate this, I recomputed the corneal wave aberration for subject LT, who had the largest angle lambda (approximately 3 degrees), using the surface aberration method. This computational procedure is much simpler than the Fermat method, and in effect, it assumes that angle lambda is zero. Table 5.12 lists the Zernike coefficients for selected modes of LT's corneal wavefront aberration, and it compares the results for the Fermat method (with line of sight compensation) and the surface aberration method (no compensation). Differences (right column) for the tilt coefficients (shaded rows) are large, but for the other modes, the value of the Zernike coefficient changed by 0.01 or less. Only the modes with the largest differences are shown. Note that this was for a 5.6-mm-diameter pupil, and the differences would probably be larger for a larger pupil. This analysis shows that, had I ignored line of sight tilt, it would have made little difference in my measurement of the higher order corneal aberrations. The maximum value for angle lambda among my subjects was 3.3 degrees (subject LT). Some articles report average values for angle lambda as large as 9 degrees (Mandell, *et al.*, 1995). Further study is needed to determine if compensation for line of sight tilt can be ignored in normal eyes with large angle lambdas. If so, it would greatly simplify computation of the corneal wavefront aberration from videokeratographic data.

In summary, the higher order wavefront aberrations of normal corneas appear to have peak-to-valley magnitudes of about 2 μm , or about 1.2 μm , and most of the aberrations are contained in the third and fourth Zernike orders. This study does not indicate that either spherical aberration or coma is the major cornea aberration. Both aberrations were present in all subjects, but their relative weights varied with each individual. Aberrations other than spherical aberration and coma were also significant. The techniques developed in this project will simplify future research on the aberrations of normal and abnormal human corneas.

TABLE 5.12 Comparison of subject LT's Zernike coefficients for selected modes when the corneal wavefront aberration was computed using the Fermat method (with line of sight compensation) and by the surface aberration method (without compensation). As expected, coefficients for tilt (shaded rows) are significantly different. For all other modes the difference was 0.01 or less in the value of the Zernike coefficient. The other higher order modes had differences less than 0.01 and are not listed.

Zernike Mode no.	Description	Zernike coefficients		Difference (No comp - With comp)
		With LOS comp	No LOS comp	
1	Horizontal tilt	-0.16	0.06	0.22
2	Vertical tilt	-0.62	-0.40	0.23
4	45/135 astigmatism	0.35	0.34	-0.01
6	90/180 astigmatism	0.49	0.48	-0.01
7	Primary coma	-0.06	-0.07	-0.01
8	Primary coma	-0.14	-0.15	-0.01
13	Primary spherical	0.33	0.33	0.01
25	Secondary spherical	-0.01	0.01	0.01

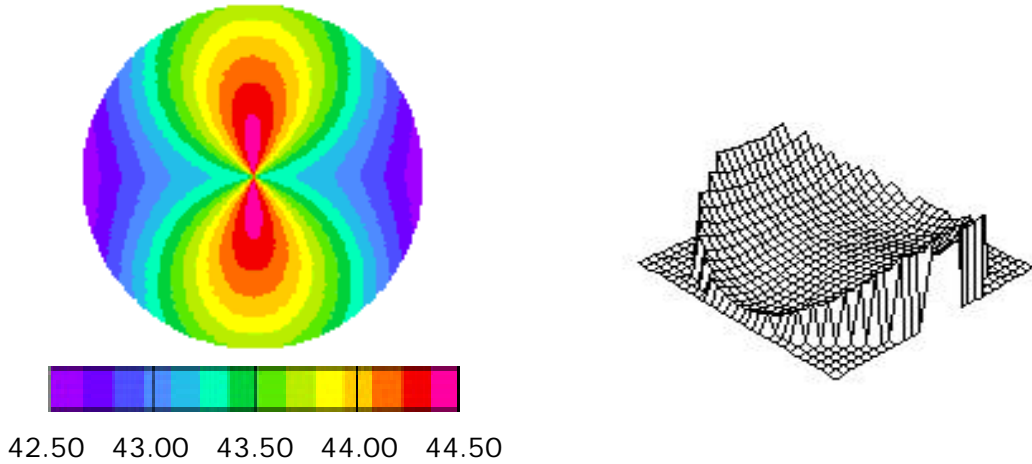


Figure 5.1

Example corneal topography map (left) showing axial curvatures for a model cornea with horizontal and vertical apical radii of 7.80 and 7.65 mm, respectively and with a shape factor of $p = 0.8$. Corneal zone diameter is 5.6 mm. Surface plot (right) of the corresponding wavefront aberration function. Minimum and maximum wavefront values are -0.6 and $6.5 \mu\text{m}$, respectively.

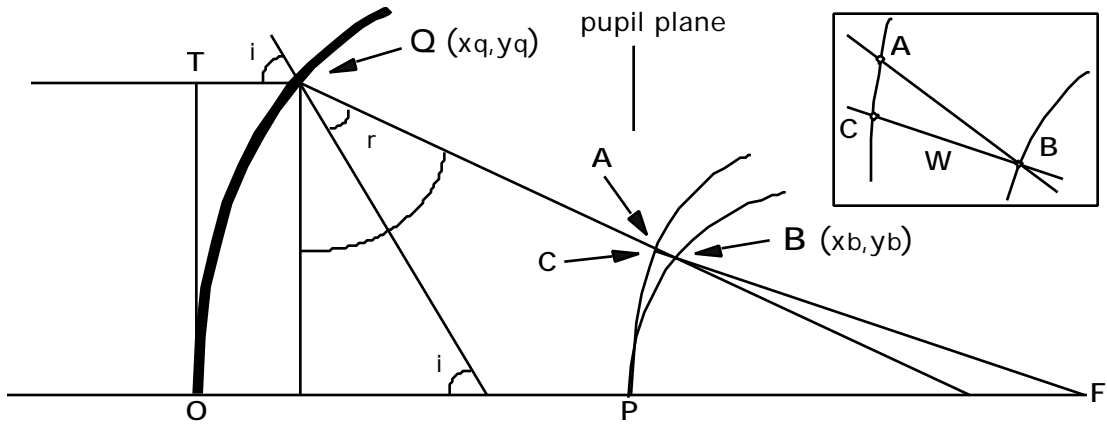


Figure 5.2

Section 5.1.3a explains the steps to determine the wavefront aberration (W) by ray tracing, based on the geometry shown here. The inset clarifies the relationship between points A, B, and C. Some references define W as segment AB, others as CB. For normal corneal dimensions, the difference between the two distances is <0.001 wavelengths. I used the CB definition for W .

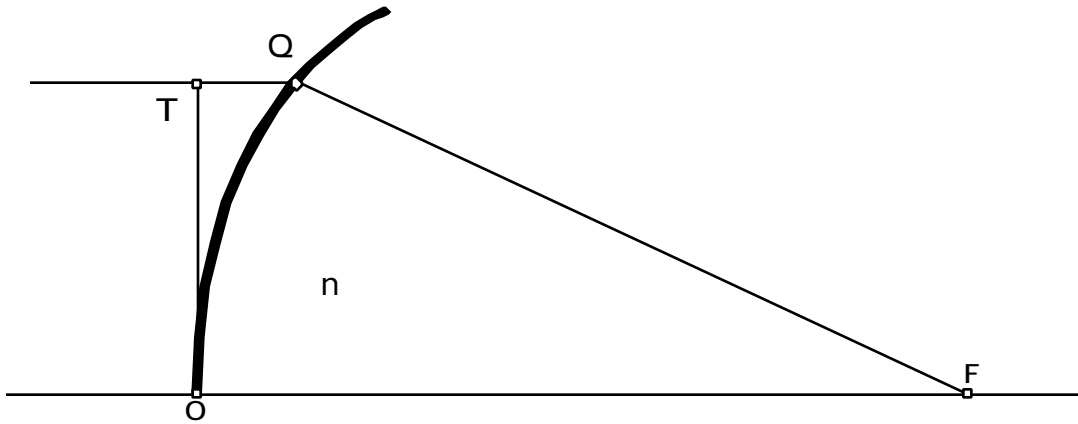


Figure 5.3

This schematic shows that the geometry and requirements for computing the wavefront aberration by the Fermat method (Section 5.1.3b) are much simpler than for ray tracing (Fig. 5.2). The Fermat method makes some approximations, but if the positions of points O, Q, F and the corneal index of refraction (n) are known, an acceptably accurate estimate of the wavefront aberration can be made for normal corneas.

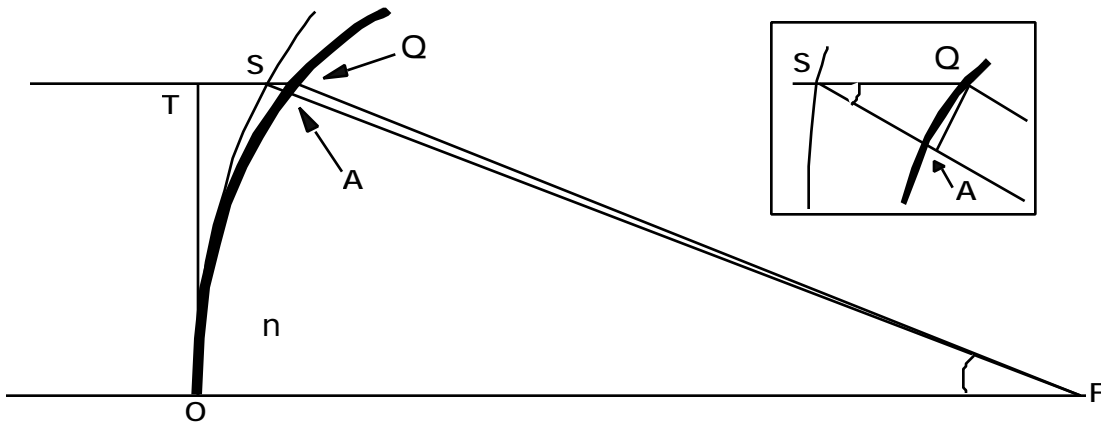


Figure 5.4

The surface aberration method (Section 5.1.3c) is based on Fermat's principle and an approximation that equates distances AF and QF . For most normal corneas, this does not contribute significant error and allows direct computation of the wavefront aberration from distance SQ , which is the "surface aberration" between the Cartesian oval (arc OS) and the cornea (arc OQ). The inset clarifies the relationship between points S , Q , and A .

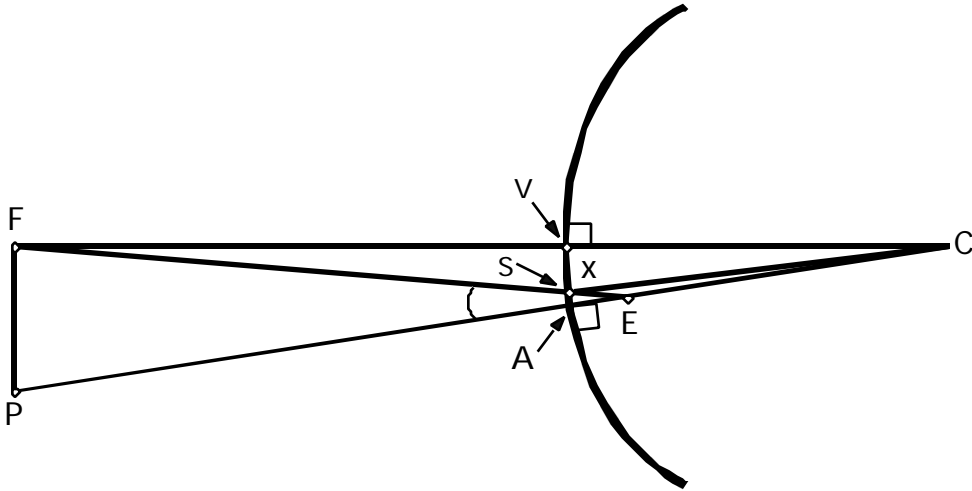


Figure 5.5

During standard videokeratoscope alignment, the patient fixates a light at the center of the keratoscope (F) while the instrument axis (FC) is aligned normal to the cornea. The line of sight (FE) connects the fixation point with the entrance pupil center (E). The pupillary axis (PE) is normal to the cornea and passes through the entrance pupil center. C represents the corneal center of curvature. Corneal topography measurements should be centered on the line of sight, but if angle lambda (λ) is not zero, the line of sight will be displaced. The point where the line of sight intersects the corneal surface is called the corneal sighting center (S), and if its coordinates are known, the corneal wavefront aberration, centered on the line of sight, can be computed (Section 5.1.4). Variable x is the distance from the keratoscope axis to the corneal sighting center (S).

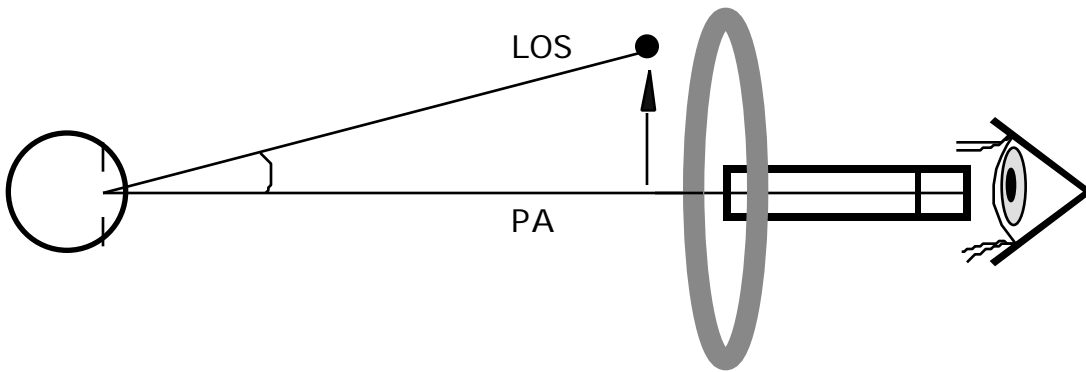


Figure 5.6

The device to measure angle lambda (λ) consisted of an illuminated annulus centered on a short focus telescope. With the subject's head stabilized, the fixation target's position was adjusted until the image of the annulus, reflected off the subject's cornea, appeared to be centered within their pupil. This aligned the subject's pupillary axis (PA) with the telescope axis, while the line of sight (LOS) was directed toward the fixation target. The horizontal and vertical angle lambdas were then easily computed.

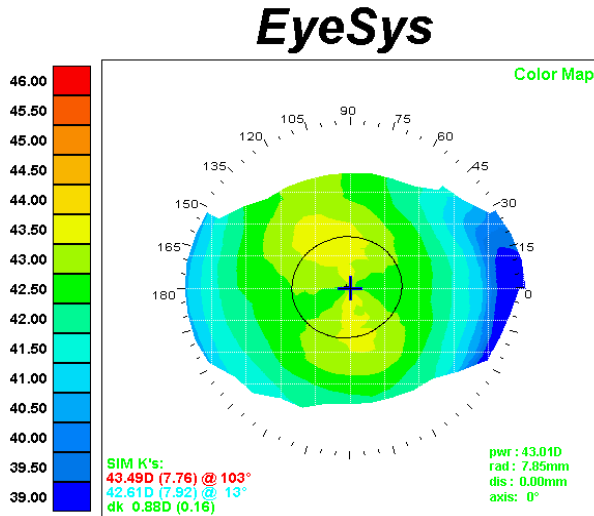


Figure 5.7 EyeSys axial curvature map for AB.

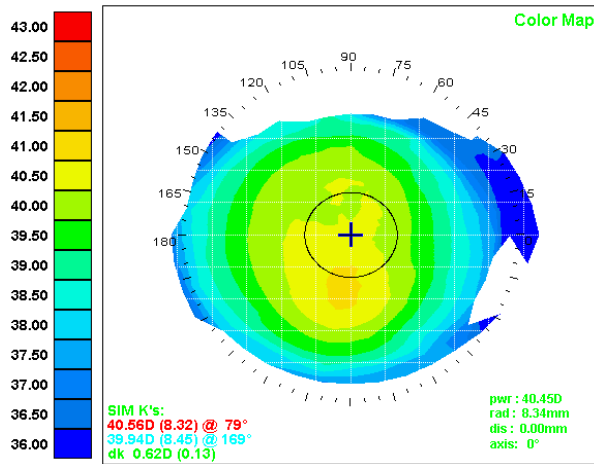


Figure 5.8 EyeSys axial curvature map for DH.

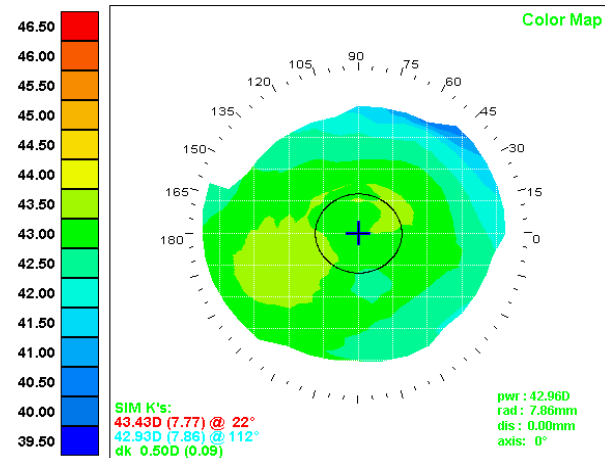


Figure 5.9 EyeSys axial curvature map for LT.

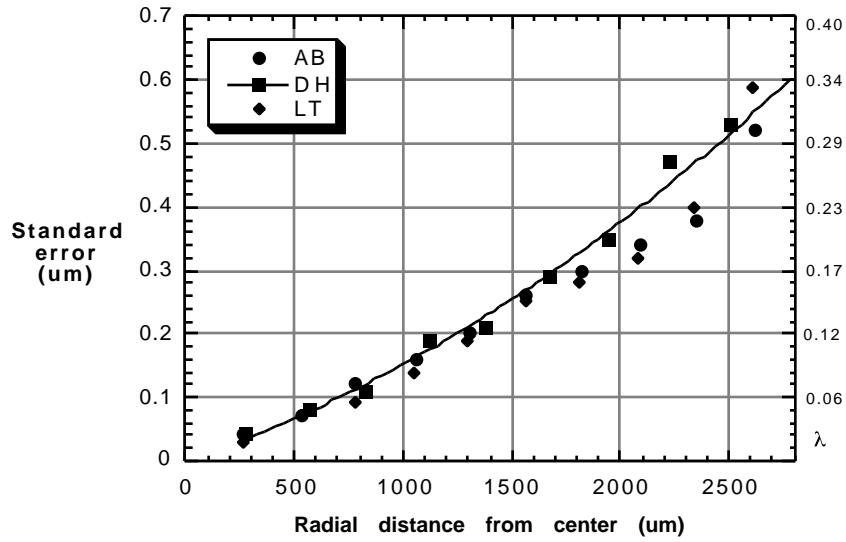


Figure 5.10

Repeatability of EyeSys surface elevation data is indicated by the radially averaged standard errors, plotted as a function of radial distance from the center. Elevation data obtained from 15-19 images were averaged to give a mean surface elevation and standard errors at approximately 4,000 points. Each ring contained 360 points, all at approximately the same radial distance from the center of the cornea. For each subject, the average of 360 standard errors within each ring are plotted.

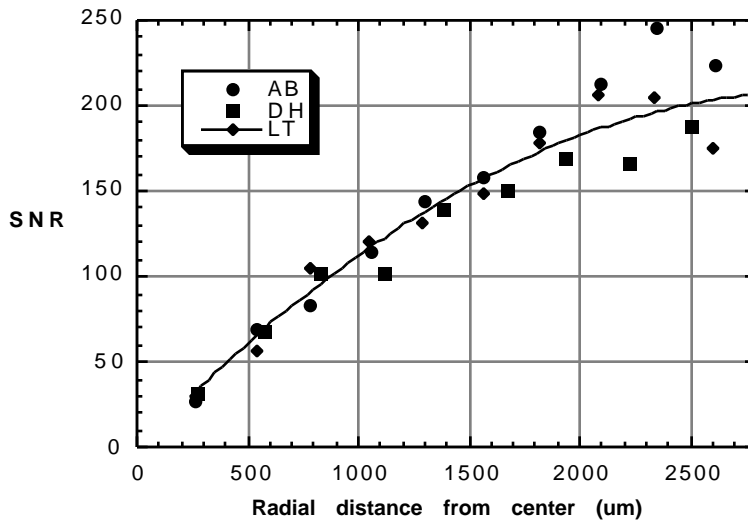


Figure 5.11

Signal-to-noise ratio (SNR) plotted as a function of radial distance from the center.

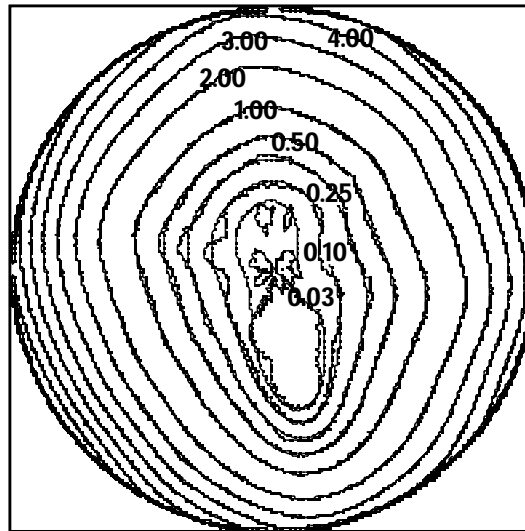


Figure 5.12

Wavefront aberrations can be computed directly from the surface elevation data, but the raw data are arranged on a slightly irregular polar grid. This was interpolated and transformed to a regular Cartesian grid for Zernike analysis. Here the contour plots for the original wavefront (EyeSys irregular polar grid), and wavefront reconstructed after Zernike analysis (evaluated at the same locations), are superimposed. Subtle wavefront irregularities, in the original data, near the center, were smoothed out by the interpolation and surface fitting process, but the difference between these and the reconstructed wavefront were less than 0.05 wavelengths. For most of the wavefront, the two contours superimpose perfectly. This indicates that the wavefront described by the Zernike coefficients closely matches the original data.

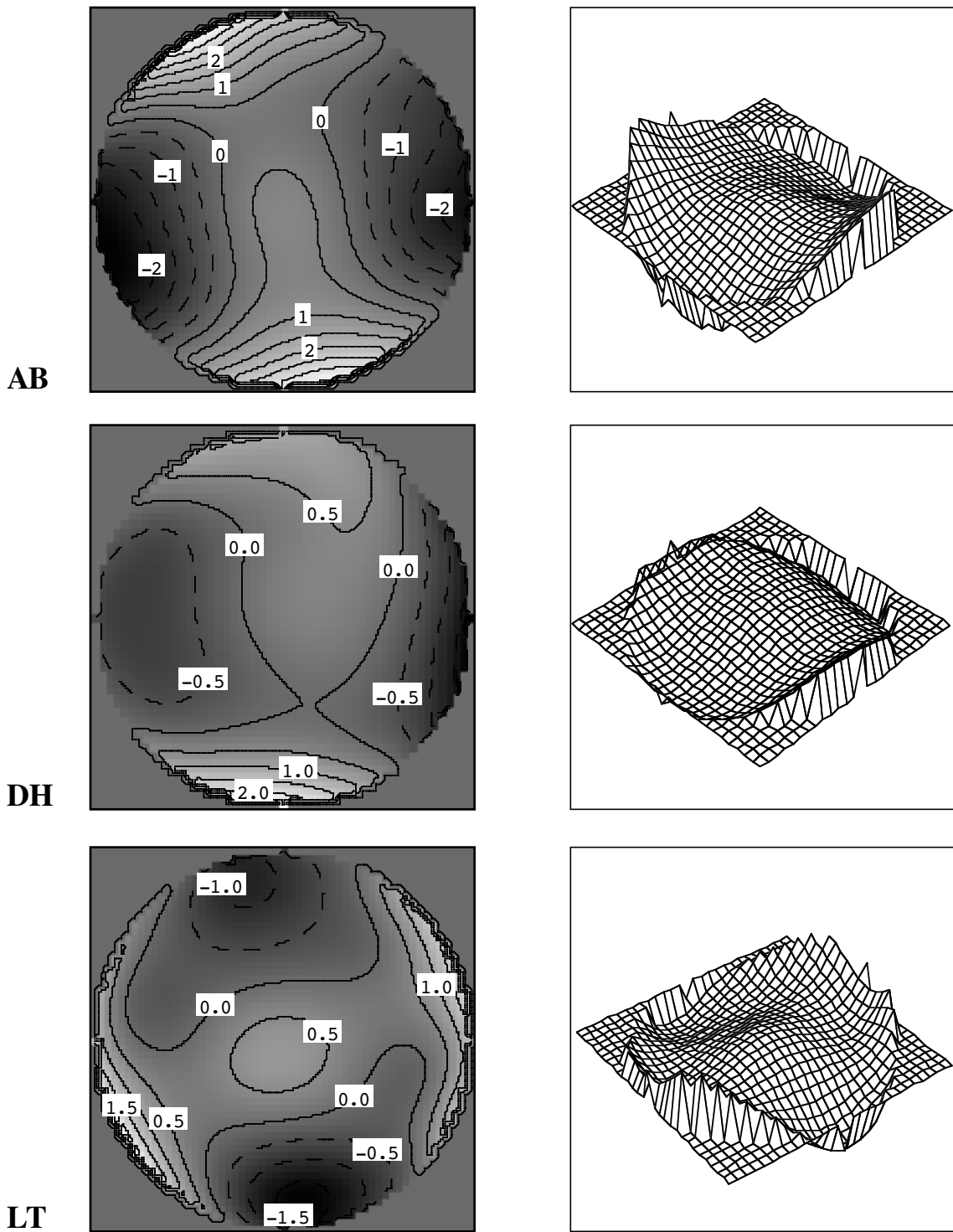


Figure 5.13

Corneal wave aberration plots that include astigmatism and higher order aberrations. Contour lines show 0.5λ intervals; dashed lines show negative values. Pupil diameters: AB, LT 5.6 mm; DH 5.2 mm.

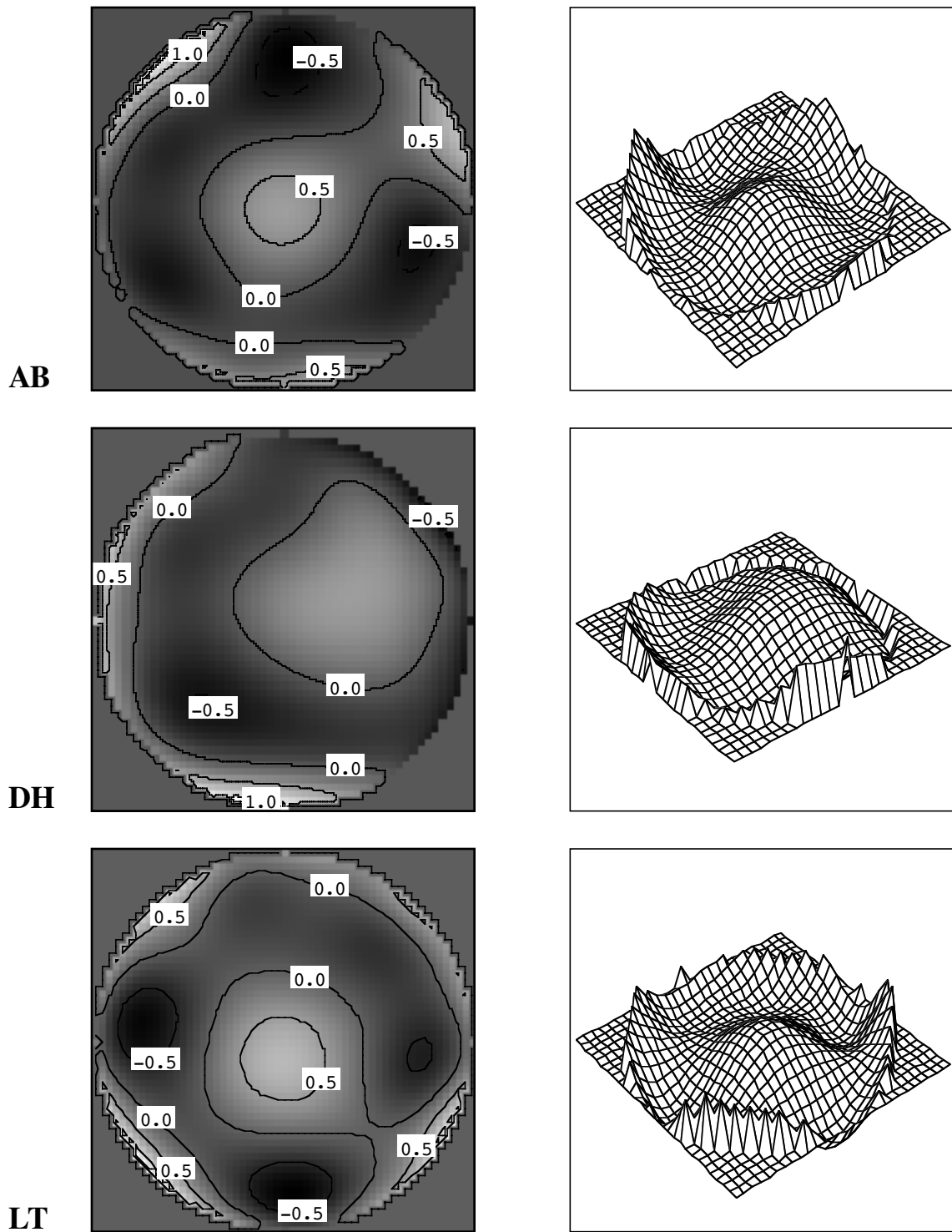


Figure 5.14
 Plots showing the corneal wavefront aberrations after removal of astigmatism, defocus, tilt and piston. Lines show 0.5λ contour intervals. Dashed contour lines indicate negative values. Pupillary diameters are 5.6 mm for AB and LT, 5.2 mm for DH.

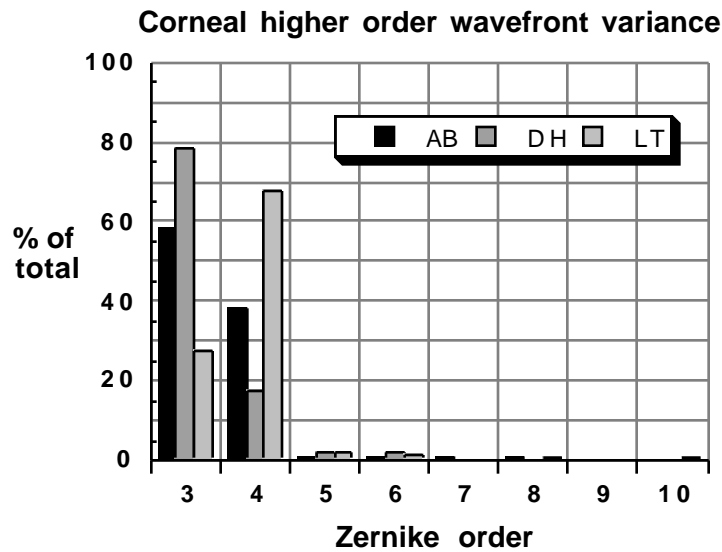


Figure 5.15

Relative contribution of each Zernike order in the corneal aberrations expressed as a percentage of the higher order wavefront variance.

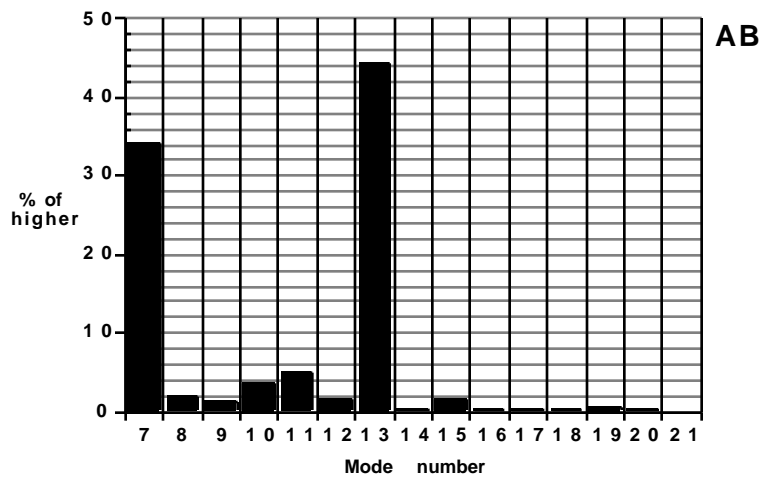


Figure 5.16

The relative contribution of the aberrations in Zernike modes 7-21 (3rd, 4th and 5th orders) for subject AB. Modes 7 and 10 combine to form triangular astigmatism. Mode 13 is primary spherical aberration. Primary coma is formed by the combination of modes 8 and 9. Modes 22-66 are not shown since they contribute very little to the higher order wavefront variance.

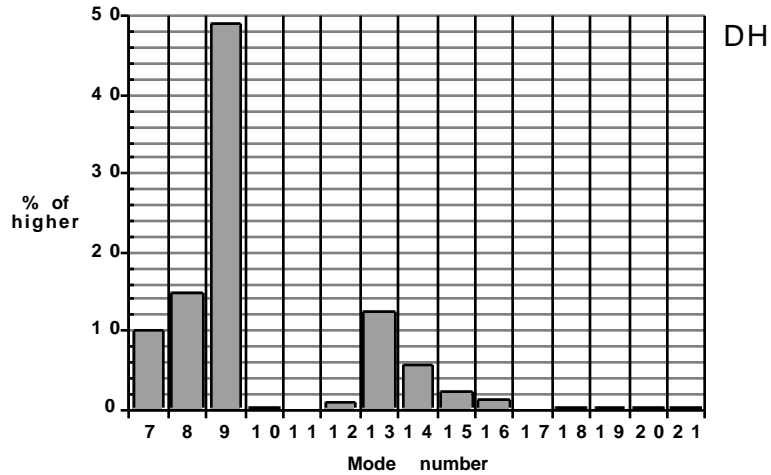


Figure 5.17

The relative contribution of the aberrations in Zernike modes 7-21 (3rd, 4th and 5th orders) for subject DH. Modes 8 and 9 combine to form primary coma. Primary spherical aberration is represented by mode 13. Modes 22-66 are not shown since they contribute very little to the higher order wavefront variance.

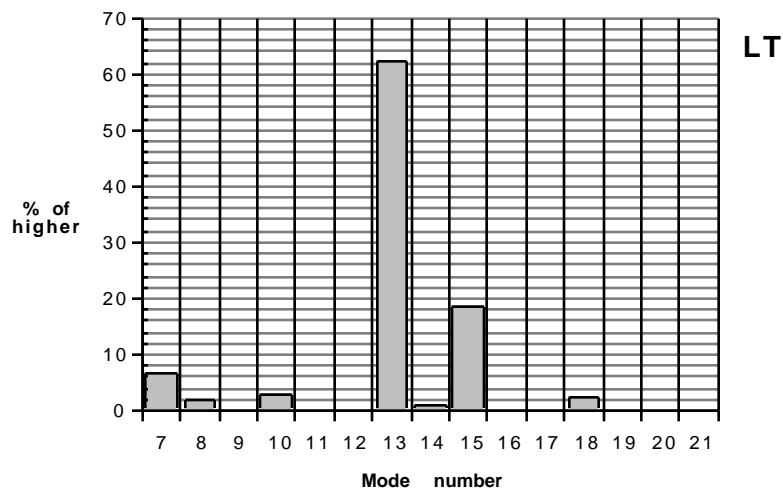


Figure 5.18

The relative contribution of the aberrations represented by Zernike modes 7-21 (3rd, 4th and 5th orders) for subject LT. Mode 13 is primary spherical aberration. Modes 22-66 are not shown since they contribute very little to the higher order wavefront variance.

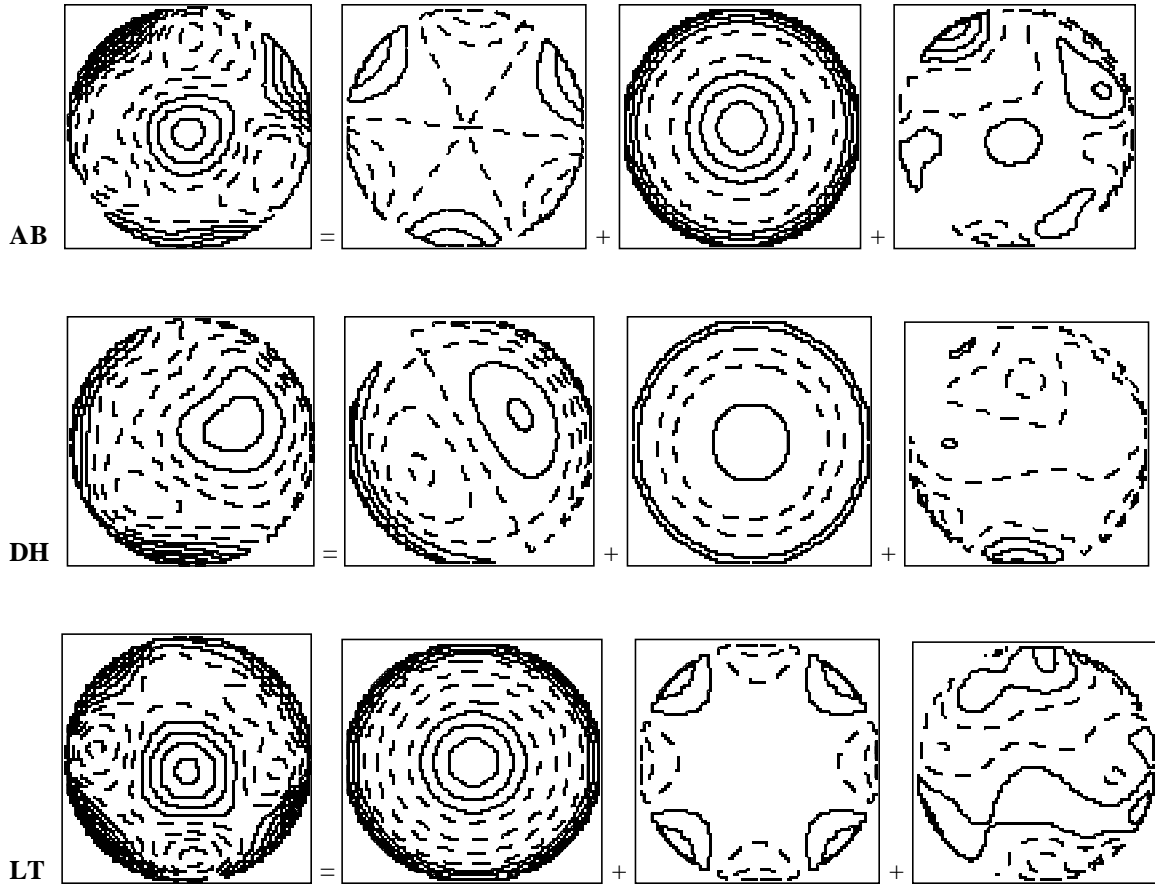


Figure 5.19

Higher order aberration components. From left to right, the plots show: for AB; total, triangular astigmatism, 1° spherical, remainder; for DH; total, 1° coma, 1° spherical, remainder; for LT; 1° spherical, quadrilateral astigmatism, remainder. The contour intervals are 0.2 ; dashed lines shows negative contours.

Accuracy of the Shack-Hartmann Wavefront Sensor^a

6.1

INTRODUCTION

The wavefront aberration function is a fundamental description of the eye's optical characteristics from which traditional measures of image quality, such as the point spread function or the optical transfer function, may be calculated (Williams & Becklund, 1989; Goodman, 1996). However, the inverse problem of determining the wave aberration, given the point spread or optical transfer function, does not yield a unique solution, and for this reason the wave aberration function is a richer description of the optical properties of the eye. Furthermore, for applications such as supernormal vision and high-resolution imaging of the fundus (Liang, Williams, & Miller, 1997), which require aberration correction, methods for direct measurement of the wavefront aberration of the human eye are required. Currently available methods fall into two broad categories, subjective and objective, but they are all based on a common principle: The direction of rays passing through select points in the pupil are monitored, and aberrations are quantified by the deviation of these select rays from the trace of rays in an aberration-free system.

Subjective methods for measuring ray aberrations all require that the subject judge the apparent visual direction of discrete points in the retinal image that result from rays passing through specific points in the pupil plane. In the aberroscope method, for example, a grid is placed over the pupil and the eye is deliberately defocused in order to produce a blur circle that replicates the shape of the pupil, including the grid of opaque lines (Tscherning, 1894; Howland & Howland, 1977). Since each intersection of grid lines corresponds to a specific pupil location, distortions seen in the retinal shadows of the grid may be used to infer the directions of identified rays as they leave the eye's pupil and eventually intersect the retina. In

^a With only minor changes, this chapter was published under the title, "Comparison of the eye's wave-front aberration measured psychophysically and with the Shack-Hartmann wave-front sensor" (Salmon, Thibos & Bradley 1998).

effect, the subjective aberroscope is an entoptic ray-tracing device that allows the simultaneous monitoring of multiple rays as they pass through known pupil locations. The subject's task in this case is to estimate the apparent visual direction of each point on the grid by perceptually interpreting the retinal stimulus as if it were the conventional image of a real object formed by the eye's optical system. An alternative approach developed originally by Smirnov (Smirnov, 1961; Webb, Penney, & Thompson, 1992; Woods, Bradley, & Atchison, 1996) uses a modified Scheiner principle to implement a nulling technique which avoids the requirement for magnitude estimation of visual direction. In this method a single pinhole aperture is used to isolate a narrow bundle of rays from an axial point source as they pass through a known location in the eye's pupil. In an aberrated eye, the retinal intersection of this ray bundle will not coincide with the paraxial retinal image of a reference point source. The subject will therefore perceive the test and reference point sources as having different visual directions. To nullify this difference in visual direction, the subject displaces the test light until it appears to coincide with the reference light. In this way the ray aberration is transferred from image space to object space, where it may be measured quantitatively (Thibos, Bradley, Still, Zhang, & Howarth, 1990). Unfortunately, the method of subjective magnitude estimation (used in the aberroscope) is inherently unreliable, and the nulling method (used in the Smirnov technique) is very time consuming^b (Charman, 1991). Consequently, both methods place an excessive demand on the subject, which makes both techniques unsuitable for routine use with patients in a clinical setting.

In response to the manifest problems of subjective techniques, two objective methods for measuring the wavefront aberration function of the eye have been developed. The first is an objective aberroscope that uses a fundus camera to record an image of the distorted grid on the retina (Walsh, Charman, & Howland, 1984; Atchison, Collins, Wildsoet, Christensen, & Waterworth, 1995; Walsh & Cox, 1995). One of the limitations of the objective aberroscope is that the eye's optical system serves as the objective lens for the fundus camera. Consequently, the eye's imaging quality limits the minimum usable spacing between grid lines in the pupil plane to about 1 mm, thus limiting the resolution with which the eye's aberrations may be specified (Charman, 1991). For the same reason, a highly aberrated eye may not yield an image of sufficient quality to allow reliable measurements of the aberration function. Both of these problems with the aberroscope method are avoided by the second objective method, the Shack-Hartmann (S-H) wavefront sensor, which characterizes the eye's aberrations in object space. Developed originally for astronomical applications and adapted recently for the eye by Liang *et al.*, (1991), this wavefront sensor uses an array of lenses and a video detector to measure rays of reflected light emerging

^b Recently a redesigned, partially automated version of the Webb spatially resolved refractometer was used to subjectively measure the wavefront aberration at 39 pupillary locations, on a two dimension grid, in about 4 minutes (He, *et al.*, 1998)

from the eye. In the S-H method a narrow beam of light is directed into the eye to produce a high-quality point source of light on the fundus. Light reflected from the fundus is then subdivided into a large number of ray bundles as it leaves the eye. This is achieved by placing an array of tiny lenses in a plane conjugate with the eye's pupil plane. A video detector (CCD) located at the focal plane of the lenslet array thus records an array of point images, one for each lens in the array. For an eye free of defocus and aberrations, all of the exiting ray bundles would be parallel, and therefore the CCD would record an array of point images with the same geometry as the lenslet array. Deviations from this geometry may therefore be attributed to aberrations in the exiting beam. Given that high-density lenslet arrays are available commercially, the S-H method for measuring the wave aberration function in human eyes is emerging as the method of choice, since it is fast, objective, and has high spatial resolution in the pupil plane.

Measurement of the eye's wavefront aberration function is becoming an important goal of clinical optometry and ophthalmology (Thibos, 1997) and is a critical first step towards the optical correction of ocular aberrations using adaptive or active optics (Liang, *et al.*, 1997; Wu, 1997). Given the great potential of wavefront sensing for advancing fundamental and applied research in visual optics, it becomes essential that the validity of this new technique be thoroughly assessed with human eyes. Recently Liang and Williams tested repeatability of the S-H technique by repeated measurements of the wavefront aberration function along the eye's vertical meridian (Liang & Williams, 1997). They reported average standard deviations of $\sim\lambda/14$ ($n=20$, 3.4 mm pupil) and $\sim\lambda/12$ ($n=3$, 7.3 mm pupil) for two observers. They also tested accuracy by two methods. First, they measured the wavefront of a laser beam which had been defocused by known amounts across an 8 diopter (D) range. Error was less than 0.17 D. Next, they compared modulation transfer functions (MTF's) for human eyes derived from S-H measurements with MTF's derived from double pass and interferometer measurements recorded previously on the same three observers (Williams, Brainard, McMahon, & Navarro, 1994). Comparisons were limited to a single vertical cross section of the MTF's. They found reasonable, though not perfect agreement and discussed theoretical considerations which could account for the discrepancies. Although all of these tests provided valuable evidence of the S-H sensor's validity, none directly assessed the ability of the wavefront sensor to accurately measure the wavefront aberration of the human eye. Indeed, there is reason to be skeptical, given the complexity of the fundus as a multiple-layered reflector with scattering, specular, and wave-guide attributes (van Blokland & van Norren, 1986; Gorrand & Delori, 1995), and the fact that object-space and image-space characterizations of the eye's aberrations rely on different ray paths and therefore might reasonably be expected to differ.

My purpose was to evaluate accuracy of the S-H method by directly comparing the wave aberration function measured objectively with that measured by an alternative method. I chose the Smirnov technique for this purpose because, although it is time consuming, the nulling psychophysical method produces

reliable results with negligible measurement variance (e.g. a typical vernier threshold of 15 arc seconds in these experiments corresponds to an mean wavefront aberration measurement error of less than $\lambda/20$). The experiment consisted of three parts. First, prior to measuring human eyes, accuracy of the S-H system was tested by measuring wavefronts which had known spherical curvatures. Next, multiple S-H images for two observers were collected, and mean wavefronts and standard errors were computed to assess repeatability with human eyes. Finally, wave aberration functions for the same subjects were measured psychophysically, and the results compared to the S-H aberration functions to evaluate accuracy with human eyes.

6.2

METHODS

6.2.1 Comparison of the two methods

In principle, the Smirnov and S-H methods are optically equivalent except for the direction of ray propagation: the S-H technique measures the deviation of rays exiting the eye, and the Smirnov technique measures the deviation of rays entering the eye. In both cases the geometry of ray deviations is the same, as illustrated schematically in Fig. 6.1, and the ray aberrations as specified in object space are the same. To see why this is true, consider first the subjective Smirnov method (Fig. 6.1, bottom) in which a distant axial point source serves as a fixed reference point. In an aberration-free eye, the dashed rays from the reference source travel parallel to the axis in object space and converge on the fovea in image space. To achieve the same end in an aberrated system, rays must enter the entrance pupil of the eye obliquely. For example, if a particular point in the entrance pupil is isolated by a pinhole aperture, rays from a test target must enter at an angle $\theta = \Delta s/d$ to the reference ray to intersect the retina at the fovea. Now consider the S-H method (Fig. 6.1, top) in which rays of light emanate from the fovea and exit the eye through the same point in the entrance pupil. (For the purposes of explaining the Shack-Hartmann principle, Fig. 6.1 shows the lenslet array inside the eye, but it is actually located outside the eye in a plane conjugate with the entrance pupil.) The emerging bundle of rays is focused by a lenslet in the array onto the CCD sensor, and for an aberration-free eye the image would fall upon point y_0 . In the case of an aberrated eye, however, the image is displaced from the reference location by an amount Δy and the ray deviation angle $\theta = \Delta y/f$. Thus, although there are differences of implementation, both methods measure the same angle θ , which represents the ray aberration at the given pupil location. Given that rays are orthogonal to wavefronts, θ also represents the slope of the wavefront W in object space, from which W may be derived by integration. Since the reference wavefront in object space is planar, W also represents the axial distance between the aberrated wavefront and the reference wavefront and therefore, by definition, is equal to the wavefront aberration function.

6.2.2 The Shack-Hartmann wavefront sensor

The layout of my Shack-Hartmann (S-H) wavefront sensor is shown in Fig. 6.2 and photographs of the apparatus are in Appendix G. The apparatus may be divided into two main parts: an illumination branch, which projected a point of light onto the retina; and a sensor branch, which measured the eye's wavefront aberration. The illumination branch included the components between the laser and eye. The beam from a helium-neon laser (632.8 nm, 10 mW) passed through neutral density filters, an electronically controlled shutter and a spatial filter that consisted of a microscope objective (focal length, 8 mm) and a 25- μm pinhole. Lenses L1-L3 (achromatic doublets; focal length, 100 mm) along with an ophthalmic lens (Rx) and the eye's optics, formed an image of the pinhole on the subject's retina. Aperture A1 limited the beam diameter to 2 mm to ensure that the point source imaged on the retina would be a diffraction-limited spot (i.e. Airy's disk). Lens L2 allowed the subject to fine tune the focus of the incoming beam subjectively. Beyond lens L3, a pellicle beam splitter (8% reflectance, 92% transmittance) reflected the beam into the eye. A laser power meter verified that power entering the eye was less than 6 μW , which for a 2.0-second exposure is 1% of the American National Standards Institute maximum permissible exposure (Sliney & Wolbarsht, 1981; ANSI, 1993). A summary of laser safety calculations is included as Appendix H.

The sensor branch included optics between the eye and the slow-scan CCD camera (Model MCD600, SpectraSource Instruments). The CCD sensor (Kodak KAF 1400) was composed of 6.8- μm square pixels arranged in a 1340 \times 1037 array. Lenses L4 and L5 were achromatic doublets (focal lengths, 100 mm). Lens L4 was one focal length from the eye's entrance pupil. Lenses L4 and L5 were separated by two focal lengths, and the lenslet array was one focal length from L5. The CCD was placed in the focal plane of the lenslets. The lenslet array (MLM 0400-24-S-1, Adaptive Optics Associates) contained 0.4-mm square lenslets with focal lengths of 24 mm. With this arrangement the CCD was conjugate to the retina, while a unit-magnification image of the pupil was formed in the plane of the lenslets. A 1-mm confocal aperture (A2) blocked the corneal Purkinje image but transmitted light from the retina. Lens Rx was used to correct the subject's spherical refractive error for both the ingoing and outgoing beams.

At the beginning of an experimental session a reference image was captured by introducing a plane wave into lens L4 of the sensor branch. The image of the lenslet focal spots was analyzed using a Macintosh computer to locate the x and y positions of each dot centroid. This provided the reference positions from which dot displacements would be measured.

The subject's head was stabilized with a bite bar, and the right eye was positioned so that the primary line of sight (also known as the fixation axis) coincided with the sensor's optic axis. The line of sight is defined in object space as the line connecting the fixated object point with the entrance pupil center.

The line of sight is the preferred reference axis for specifying the eye's wave aberration function (Mandell, 1992; Mandell, 1994; Applegate *et al.*, 2000—in press) because the aberration function is traditionally specified with respect to the center of the pupil, and the line of sight, by definition, connects the fixation point to the center of the eye's entrance pupil and connects the center of the exit pupil to the fovea. Line-of-sight alignment was accomplished as follows. Laser radiance was attenuated to a safe level for continuous viewing, and the shutter was opened while the subject fixated the pinhole. The subject attended to the position of aperture A2, which was translated axially back and forth between lenses L4 and L5. The eye's horizontal (x) and vertical (y) positions were adjusted until, for all locations of aperture A2, its blurred image always appeared to be centered on the red pinhole. Since the experiment would be conducted in total darkness except for the brief image exposure, it was necessary to provide the subject with another fixation target, which was optically aligned with the line of sight. It consisted of a dimly illuminated cross that was reflected into the illumination branch by a pellicle placed between lenses L2 and L3. Since I did not paralyze accommodation, the fixation target was slightly defocused in the myopic direction to minimize any stimulus to accommodation.

The eye's entrance pupil was placed at the focal plane of lens L4 by the following procedure. Aperture A2 was temporarily replaced with a mirror so that the experimenter could view the eye through a telescope (focused at optical infinity), lens L4, and the ophthalmic trial lens Rx. The eye was translated along the optic axis until the iris margin was seen clearly focused by the experimenter.

The electronic shutter and camera shutter were synchronized for 1-2-second exposures, and five images for each subject were taken. Following each exposure the subject would dismount from the bite bar and rest 2-4 minutes while the experimenter evaluated and preprocessed the images. Example raw images are shown in Figs. 6.4a, and 6.4d.

A computer program (MATLAB, Mathworks, Inc.) was written to locate the dot centroids with minimal user input, and wavefront aberration functions were computed by the following steps:

- 1) Horizontal (x) and vertical (y) displacements for each dot from the reference positions were computed;
- 2) Displacements, divided by lenslet focal length (24 mm), converted the data into deviation angles in the x and y directions, which were interpreted as wavefront slopes or partial derivatives of the wavefront with respect to x and y.
- 3) The wavefront aberration function was determined by numerical integration of the partial derivatives across the pupil to produce a two-dimensional array of wavefront aberration values in micrometers. With normalization by one wavelength (0.6328 μm) these values were converted to wavelengths.

6.2.3 Psychophysical apparatus and procedures

Figure 6.3 shows a schematic of the psychophysical apparatus, which is similar to that used by Woods *et al.* (1996). The subject directly viewed a fixed white annular target that had an inner diameter of 3.5 minutes of arc (arc min). The annulus was seen through the entire pupil, and the subject was instructed to fixate the center of the target. Through a second optical channel the subject also saw a red light-emitting diode (LED; dominant wavelength, 640 nm) that had a diameter of approximately 3 arc min. Light from the LED was polarized and blocked from entering most of the pupil by a crossed polarizer positioned before the eye. A 0.6-mm pinhole in this polarizing filter allowed light from the LED to enter the pupil in only one discrete location. To locate the center of the eye's entrance pupil the pinhole aperture was displaced right and left until the pinhole was vignetted by the iris. This process was repeated for a vertical traverse, and the midpoint of the two traverses was taken as the pupil center. The line connecting this pupil center to the annulus center thus defined the fixed line of sight for the experiment. To conduct the experiment, the experimenter then positioned the pinhole aperture at a predetermined sequence of positions along the horizontal meridian of the eye's pupil. At each position the LED appeared to the subject to be displaced from the annulus center by an amount that was indicative of the degree of aberration at that pupil location. The subject repositioned the LED until it appeared to be centered in the annulus, and the LED's new x and y coordinates were recorded. This process was repeated for approximately 15 locations of the pinhole across the horizontal midline of a 5.6-mm pupil. Since this procedure required approximately 3 hours, I limited psychophysical measurements to the horizontal meridian of the pupil.

Measured deviation angles θ in the horizontal direction were interpreted as local wavefront slopes that could be fitted by the method of least squares to a fifth order polynomial of the form

$$\theta = dW/du = B_0 + B_1u + B_2u^2 + B_3u^3 + B_4u^4 + B_5u^5 \quad (6.1)$$

where dW/du represents the wavefront slope in radians; u is the horizontal pupil location measured in micrometers; and the B coefficients are associated with the classic aberrations: prism (B_0), defocus (B_1), primary coma (B_2), primary spherical aberration (B_3), secondary coma (B_4) and secondary spherical aberration (B_5). With omission of the prism and defocus terms and with normalization by one wavelength, the resulting polynomial was integrated to give a one-dimensional wavefront aberration function $W(u)$ in wavelengths of the form,

$$W(u) = B_2u^3/3 + B_3u^4/4 + B_4u^5/5 + B_5u^6/6. \quad (6.2)$$

To permit direct comparison of the aberrations measured by the two methods, the two-dimensional S-H wavefront slope data were interpolated along the horizontal meridian to produce one-dimensional data that were also fitted with Eq. (6-1) and integrated to the form of Eq. (6-2).

6.2.4 Experimental protocol

Experiments were performed on the right eye of two subjects without cycloplegia. Under dark-room illumination the diameter of the natural pupil was about 5.6 mm. This permitted sampling of approximately 150 pupil locations with the S-H method, which is more than sufficient to represent the significant ocular aberrations (up to the tenth order) reported by Liang and Williams (Liang & Williams, 1997). Each of the five S-H images were processed to yield a wavefront aberration function. The five aberration functions were interpolated using bicubic interpolation to 0.2-mm spacings, and the mean and standard errors ($n = 5$) were computed. Data for the Smirnov experiment were collected in a single 3-hour session for subject DH and in two 3-hour sessions on the same day for LT. Information about the subjects is summarized in Table 6.1.

TABLE 6.1 Summary data for two subjects whose right eyes were measured with the Shack-Hartmann wavefront sensor and Smirnov psychophysical method.

Subject	Age	Refractive error	Corrected visual acuity
LT	49	-0.25 -1.00 x 090	20 / 15
DH	29	-4.25 sphere	20 / 15

6.3

RESULTS

6.3.1 Shack-Hartmann sensor calibration

Prior to measuring human eyes, we tested accuracy of the S-H sensor with calibrated spherical wavefronts formed by introducing collimated light into lens L4 of the sensor branch, then focusing it to known distances by either moving lens L5 or by placing a lens over L5. The two test wavefronts had focal points located 3535 and 470 mm distal to the lenslets. A 5.6-mm-diameter beam was analyzed. The measured wavefronts were fitted to Zernike polynomials, and the wavefront elevation contributed by the 4th mode, representing defocus, was isolated. The 4th Zernike mode contains a constant term, which was factored out to make the wavefront height in the pupil center equal to zero. The resulting wavefronts, which represented measured defocus, were compared with the expected wavefront based on the known focal

distances. Errors, defined as measured minus expected wavefront heights, were calculated at approximately 150 points within the pupil. Table 6.2 summarizes parameters of the two calibrated wavefronts and the accuracy results. RMS wavefront measurement errors were $\sim\lambda/33$ and $\sim\lambda/50$. Corresponding dioptric equivalents were -0.008 and 0.006 D. This level of accuracy was at least as good as the accuracy with which we could measure either the lens power or focal distances used to create the test wavefronts. It was well below the maximum instrument error (0.17 D) reported by Liang and Williams (1997) and indicated that my apparatus itself was highly accurate.

TABLE 6.2 Parameters describing spherical test wavefronts used for calibration of the Shack-Hartmann wavefront sensor and measurement errors. Beam diameters were 5.6 mm.

Test wavefront radii (mm)	Wavefront edge height (λ)	Number of points sampled	Measured wavefront radii (mm)	RMS wavefront error (λ)	Error in diopters
3535	2.0	147	3636	.03	-0.008
470	13.8	148	469	.02	0.006

6.3.2 Human eye wavefronts measured by the Shack-Hartmann apparatus

Figure 6.4 shows raw images, mean wavefront aberration, and standard error contour plots for subject LT (left-hand column) and DH (right-hand column). Figs. 6.4a, and 6.4d are examples of typical raw images. Centrally the dots were bright and round, but peripherally some dots were dim and distorted. This variance in dot contrast and shape was more pronounced in LT. To speed up the centroid finding algorithm, images were filtered to brighten the dimmer dots before proceeding. The resulting dots were more uniformly bright, but scattered artifacts appeared near the pupil edges. The mean wavefronts were interpolated to draw smooth wavefront aberration contour plots (Figs. 6.4b, and 6.4e). In Fig. 6.4b, aberrations are larger, and contour lines indicate $1\text{-}\lambda$ intervals. Here subject LT's astigmatism is apparent by the vertically elongated contour lines that are most clearly evident in the temporal (figure left) half pupil. The nasal half pupil contained additional irregular aberrations that were subsequently investigated more thoroughly as will be described in Section 6.3.4. The wavefront aberration values are smaller in Fig. 6.4e, which shows $0.3\text{-}\lambda$ intervals. The more nearly circular contours are consistent with the lack of astigmatic refractive error for subject DH, although some asymmetry in the contours is evident. The lower plots, which show standard errors, use contour intervals of 0.25λ and 0.10λ (Figs. 6.4e, and 6.4f). Mean

standard errors for these plots were $\sim\lambda/2$ and $\sim\lambda/5$ for LT and DH, respectively. Comparing the standard errors and raw images, we see that between-measurement variance in the aberration function was greatest in the peripheral parts of the pupil where the wavefront slopes were greatest and dots were dimmest.

6.3.3 Comparison of wavefront aberration profiles measured psychophysically and with the Shack-Hartmann wavefront sensor

Figure 6.5 directly compares one-dimensional wavefront profiles measured by the two methods. Prism and spherical components were mathematically removed to reduce variance due to fluctuations in accommodation or small eye movements, and, indeed, I found a better match between the two curves after these were removed. S-H mean wave aberrations ($n=5$) are shown by the filled circles, and the squares indicate the mean Smirnov wavefront profiles for LT ($n=2$) and DH ($n=5$). For both subjects, the wavefront profiles measured by the two methods agreed closely in terms of shape, and centrally the curves were nearly superimposed. Except for the nasal (Fig. 6.5, right) half of LT's pupil and two points near the nasal edge of DH's pupil, the difference between the curves was less than $\sim\lambda/4$. RMS differences were $\sim\lambda/2$ for LT and $\sim\lambda/6$ for DH. Error bars indicate one standard error for the S-H measurements, and, except for the extreme nasal part of LT's pupil, most standard errors were smaller than $\lambda/4$. The mean standard errors were $\sim\lambda/7$ and $\sim\lambda/22$ for LT and DH respectively. The magnitude and shape of these wave aberrations are consistent with those reported elsewhere (Charman, 1991; Liang, *et al.*, 1994; Liang & Williams, 1997). The wavefront profiles in Fig. 6.5 show a central zone that is free of significant aberrations surrounded by increasing aberrations that reach a maximum of $2-4 \lambda$ at the pupil edge. If we adopt Rayleigh's quarter-wavelength rule for a well-corrected optical system (Born & Wolf, 1980), the critical pupil diameter within which diffraction rather than aberrations limit optical quality is approximately 3.0 mm for my subjects. In comparison, the median critical diameter for 55 subjects in Howland's subjective aberroscope study (Howland & Howland, 1977) was 2.8 mm, and for 11 subjects measured using an objective aberroscope the mean was 3.3 mm (Walsh, *et al.*, 1984).

The relative contribution of each primary and secondary aberration to the one-dimensional S-H wavefront aberrations are summarized in Table 6.3. Mean values for the coefficients B_2, B_3, B_4, B_5 (corresponding to primary coma, primary spherical, secondary coma and secondary spherical aberration, respectively) may be used to compute the wavefront slopes in radians by Eq. (6-1) and to compute the wavefront aberrations in micrometers using Eq. (6-2). For these coefficients, the pupil dimensions represented by variable u in Eq. (6-1) and (6-2), must be expressed in micrometers. For each component aberration, wavefront variance and longitudinal ray aberration in diopters for a marginal ray (5.6 mm pupil) are also listed in Table 6.3, and they show the relative contribution of each of aberration. Primary spherical

was the dominant aberration, more so in subject DH than in subject LT, and the dioptric expressions of longitudinal spherical aberration (bold type) agree with the range of values reported in other studies (Thibos, Ye, Zhang, & Bradley, 1997).

TABLE 6.3 Mean coefficients used in Eqs. (6-1) and (6-2) and other parameters describing 5th order polynomial fits to Shack-Hartmann wavefront slope data. Coefficients are associated with primary coma (B_2), primary spherical aberration (B_3), secondary coma (B_4), and secondary spherical aberration (B_5). Longitudinal aberration is computed for a 5.6 mm pupil marginal ray. Bold type highlights primary spherical aberration.

Coefficient	Mean (n=5)	Wavefront variance (λ^2)	Longitudinal aberration (diopters)
Subject LT			
B_2	5.895×10^{-11}	.08	.17
B_3	7.932×10^{-14}	.36	0.62
B_4	-1.359×10^{-17}	.07	-0.30
B_5	2.801×10^{-21}	.01	0.17
Subject DH			
B_2	-1.395×10^{-11}	0.00	-0.04
B_3	1.289×10^{-13}	0.94	1.01
B_4	2.180×10^{-18}	0.00	0.05
B_5	-6.402×10^{-21}	0.06	-0.39

The components aberrations are plotted in Fig. 6.6. For subject LT, primary spherical aberration alone (filled circles) closely approximates the total wavefront aberration (solid curve). Considered separately, both primary and secondary coma are sizeable aberrations relative to primary spherical, but in combination they contribute little to the overall aberration function since they have nearly equal magnitudes but opposite sign. Had data been limited to only first order aberrations, the resulting wavefront would have erroneously appeared to be more asymmetrical. In contrast to measurements by other methods, aberroscope measurements (Howland & Howland, 1977; Walsh, *et al.*, 1984) have generally found large comatic aberrations in the wave aberration functions, which could be exaggerated in some cases by the fact that second-order coma and higher aberrations are generally not measured by the aberroscope. The example of subject LT's wavefront profile demonstrates that methods to measure the wavefront aberration should be

capable of measuring aberrations beyond the first order, and this requires an instrument with a sufficiently fine sampling rate. This is a relative advantage of the S-H sensor, which can sample the pupil in intervals as small as 0.2 mm, and it can analyze aberrations up to at least the tenth order (Liang & Williams, 1997). A small amount of positive secondary spherical aberration was present in LT's eye. For DH, primary spherical is the dominant aberration, and the comas are negligible, though it is possible that coma could have been larger had some meridian other than the horizontal midline been measured. Beyond 2 mm from the pupil center, secondary spherical aberration for both subjects becomes significant, and, in the case of DH, its negative sign negates some of the primary spherical aberration.

6.3.4 Subtle local aberration detected by both methods

During the psychophysical experiment, subject LT observed that when the pinhole was translated horizontally in the nasal half of his pupil a fixed LED appeared subjectively to trace out a looplike trajectory indicative of a highly irregular aberration. Subsequently I searched for objective evidence of this refractive anomaly in the psychophysical data by tracking changes in the x and y wavefront slopes as the pinhole moved across the pupil. The abscissa of Fig. 6.7 represents wavefront slopes in the x direction, and the ordinate represents wavefront slopes in the y direction. Symbols indicate the slopes in these two orthogonal directions at each point along a horizontal traverse of the pupil, and numbers adjacent to selected symbols indicate sampled pupil locations. Thus the dashed line connecting the diamond shaped symbols represents a trajectory of slopes parameterized by pupil position as measured by the Smirnov technique. To obtain independent, objective evidence of this anomaly I reexamined the slope data from the S-H experiment, and the result is shown by the solid line in Fig. 6.7, which represents the corresponding trajectory as measured by the objective S-H method. Both results confirm the looping trajectory which the subject reported in the nasal side of his pupil. Additionally, the pupil locations at which miniscule and abrupt slope changes occur correspond relatively well between the two methods. A change in slopes of this kind in the x and y dimensions suggests an unusual aberration beginning near the pupil center and extending nasally along the midline. Reviewing the two-dimensional wavefront plot for subject LT (Fig. 6.4b), we see a confluence of irregular depressions in the wavefront aberration in the corresponding region, which is delineated in Fig. 6.4b by the rectangular overlay .

6.4

DISCUSSION

In theory the S-H wavefront sensor should provide highly accurate measurements of the aberrations of any optical system, including the human eye. We have verified this expectation for spherical calibration

wavefronts by showing that a S-H apparatus assembled from stock optical components is capable of measuring wavefront shape with RMS measurements errors of $\sim\lambda/30$ or less. Good repeatability for the wavefront profiles in an eye with relatively smoothly changing aberrations (Fig. 6.4e) was indicated by a mean standard deviation ($n = 5$) of $\sim\lambda/10$. This is similar to the $\sim\lambda/12$ mean standard deviation reported by Liang and Williams (Liang & Williams, 1997) for subject JL, who also had smoothly changing aberration contours. They used cycloplegic drops to paralyze accommodation, and three images, taken within 60 seconds, were averaged. In my experiments no cycloplegia was used, and the subject dismounted the bite bar for several minutes between S-H measurements. It was encouraging, therefore, to encounter similar low levels of variability despite the relaxed conditions of my experiments.

Lacking an absolute method for assessing accuracy of the S-H apparatus when used with human eyes, I estimated relative accuracy by directly comparing wave aberration profiles measured by the S-H method with those measured psychophysically by the Smirnov technique. The very close correspondence which I found (Fig. 6.5) is strong evidence that they are measuring the same thing: the wavefront aberration functions of the tested eyes. The RMS difference between the two methods was $\sim\lambda/5$ (Fig. 6.5, bottom) in the eye with smoother wave aberration contours (Fig. 6.4e) and lower between-measurement variance (Fig. 6.4f). Where the wavefront aberration was larger, measurement variance was also larger, especially near the margins of the pupil. Some of this increased variance may have been due to poorer image quality in parts of the S-H images. Also, the extended time required to collect the psychophysical wavefront data made the subjective results more susceptible to temporal fluctuations (e.g., tear film changes or accommodation).

The largest difference between wavefront aberration functions measured by the two methods was found in the nasal (Fig. 6.4b, right) half of LT's pupil. For this subject, the temporal half of the wavefront aberration function appears to be dominated by regular astigmatism (Fig. 6.4b), and in this region the wavefront measured by the two techniques were almost perfectly superimposed, with an RMS difference of $\sim\lambda/9$ (Fig. 6.5, top). In the nasal half, however, the difference between wavefront aberrations was much larger with an RMS difference of $\sim 2\lambda/3$. The most likely explanation for this large difference was the presence of localized, irregular aberrations in the nasal half of the pupil. Because the aberration function changes dramatically just above and just below the horizontal midline of this subject's pupil, slight vertical discrepancies between the locations of the horizontal traverses in the two experiments could have introduced large differences in results. For this reason the detailed vertical and horizontal wavefront slope changes shown in Fig. 6.7 are more revealing. The looplike traces in Fig. 6.7 correspond with shallow depressions in the wavefront aberration function (Fig. 6.4b) that were less than $\lambda/2$ deep. The subtle optical anomalies were not measurable by clinical refraction or slit lamp biomicroscopy of the ocular media, yet it was conspicuous in the wavefront slopes measured by both methods. Interestingly, a similar aberration was

noted in the same pupil location for this subject several years earlier when he sat for a chromatic aberration experiment (Simonet & Campbell, 1990), which suggests that this subtle refractive anomaly is a permanent feature in this subject's eye.

In conclusion, these results indicate that the Shack-Hartmann wavefront sensor can provide accurate and repeatable measurements of the wavefront aberration function of human eyes and that these measurements are in good agreement with independent measurements determined by the traditional Smirnov psychophysical technique. The two methods appear to be equally sensitive for detecting subtle irregular aberrations of the eye. Considering its numerous advantages of speed, objectivity, and high spatial resolution, I believe the Shack-Hartmann wavefront sensor is an attractive, valid instrument for basic and applied studies of the optical quality of the human eye.

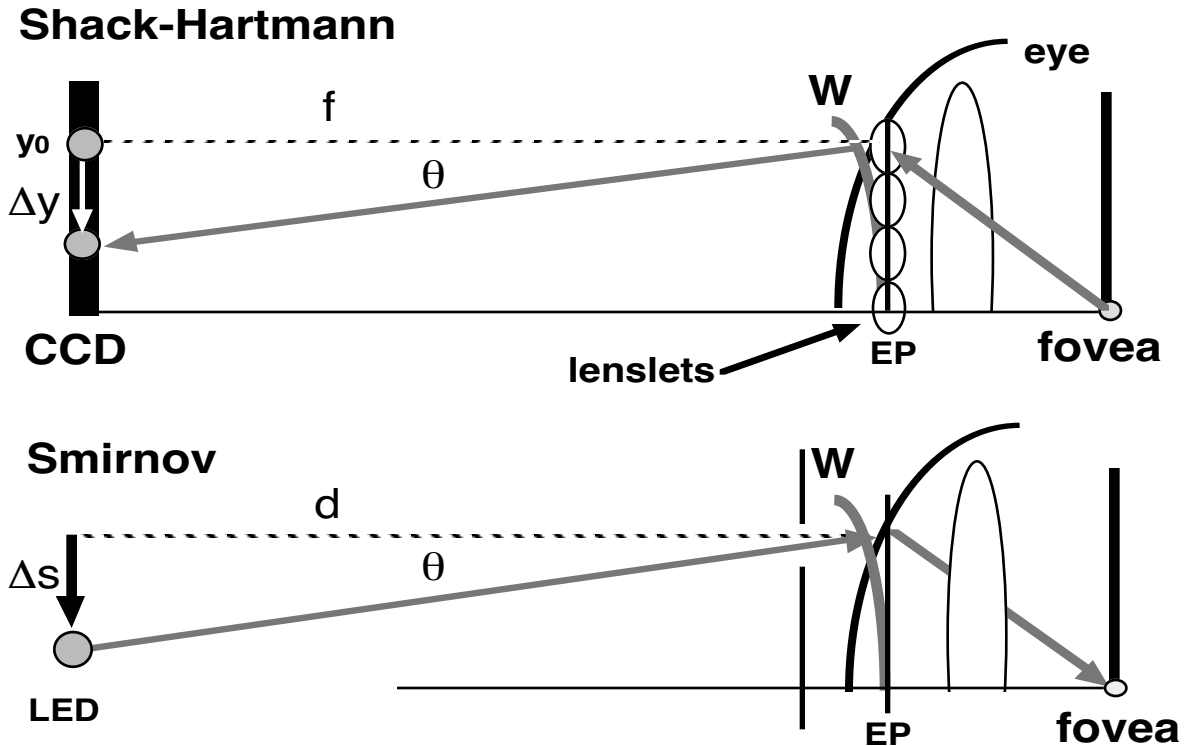


Figure. 6.1

Principle of wavefront sensing in the Shack-Hartmann (top) and Smirnov psychophysical (bottom) apparatus. (Δy = displacement of point image from reference position, f = focal length of lenslet. Δs = displacement of point object from the reference axis, and d = object distance) In the Shack-Hartmann (S-H) apparatus, a point source is placed on the fovea, and light is reflected out of the eye. The optical system relays an image of the eye's entrance pupil to the plane of an array of microlenslets that in effect, samples the emerging beam in the entrance pupil (EP). For the purposes of illustrating the principle the lenslet array is shown inside the eye in the plane of the entrance pupil, though the optical sampling of the entrance pupil actually occurs outside the eye. In a theoretical aberration-free eye, a bundle of rays is isolated by a lenslet and rays converge to point y_0 on the CCD. For an aberrated eye the image is displaced from reference point y_0 by an amount Δy and the ray deviation angle $\theta = \Delta y/f$. In the Smirnov method rays from a distant axial point object are isolated by a pinhole near the eye, and in the aberration-free case, these rays converge on the fovea. In the aberrated eye, the subject must displace the object by an amount Δs in order to center its image on the fovea. Here the ray deviation angle $\theta = \Delta s/d$. Both methods measure the same angle θ , which is the ray aberration at the isolated pupil location. Since rays are orthogonal to wavefronts, θ also represents the slope of the wavefront W in object space, from which W may be derived by integration.

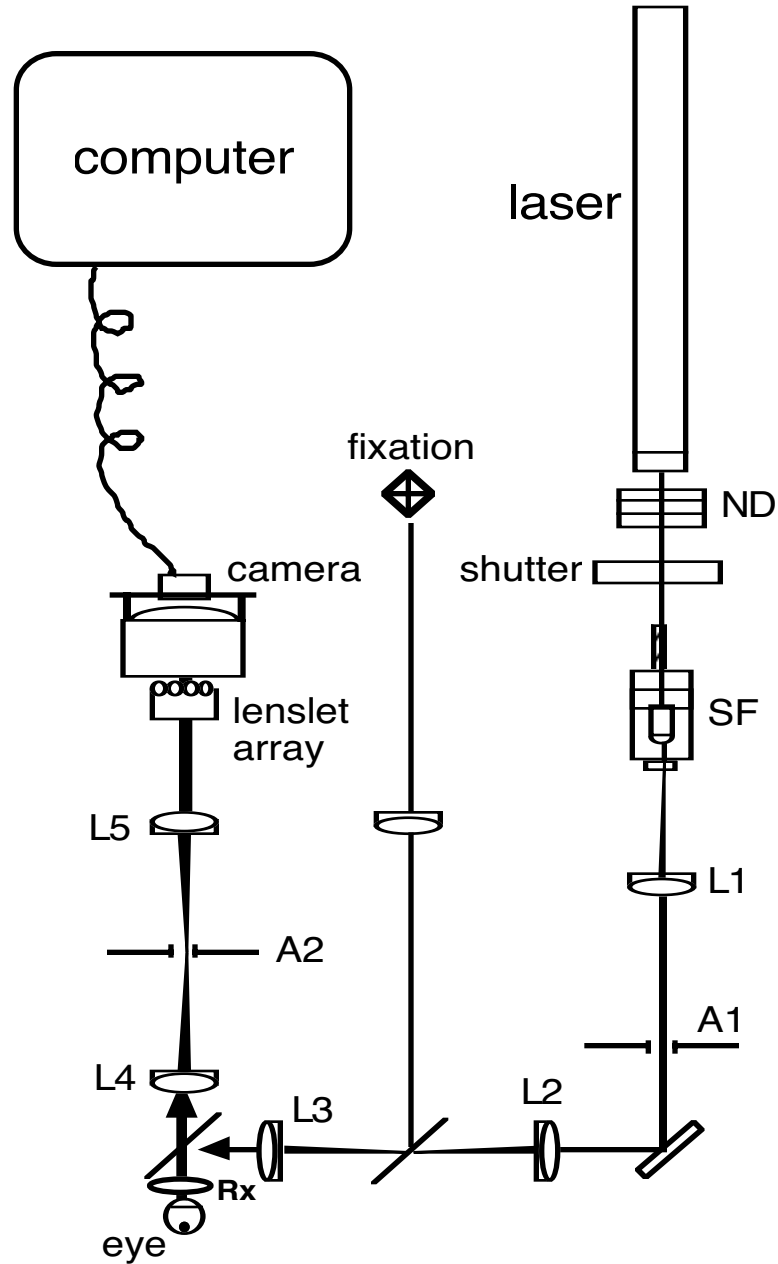


Figure 6.2

Shack-Hartmann wavefront sensor layout. A laser beam passes through neutral density filters (ND), an electronic shutter, spatial filter (SF), lenses L1-L3, lens Rx and the eye's optics to form a point of light on the fovea. The subject observes a fixation target during measurement. Light reflected off the retina passes out of the eye, through lenses Rx, L4 and L5 so that an image of the pupil is formed in the plane of the microlenslet array, and each lenslet forms an image of the retinal spot on the CCD. A confocal aperture, A2, prevents corneal reflections from reaching the camera while transmitting light from the retina. Digital images are stored on a computer, and are analyzed to reconstruct the eye's wavefront aberration function.

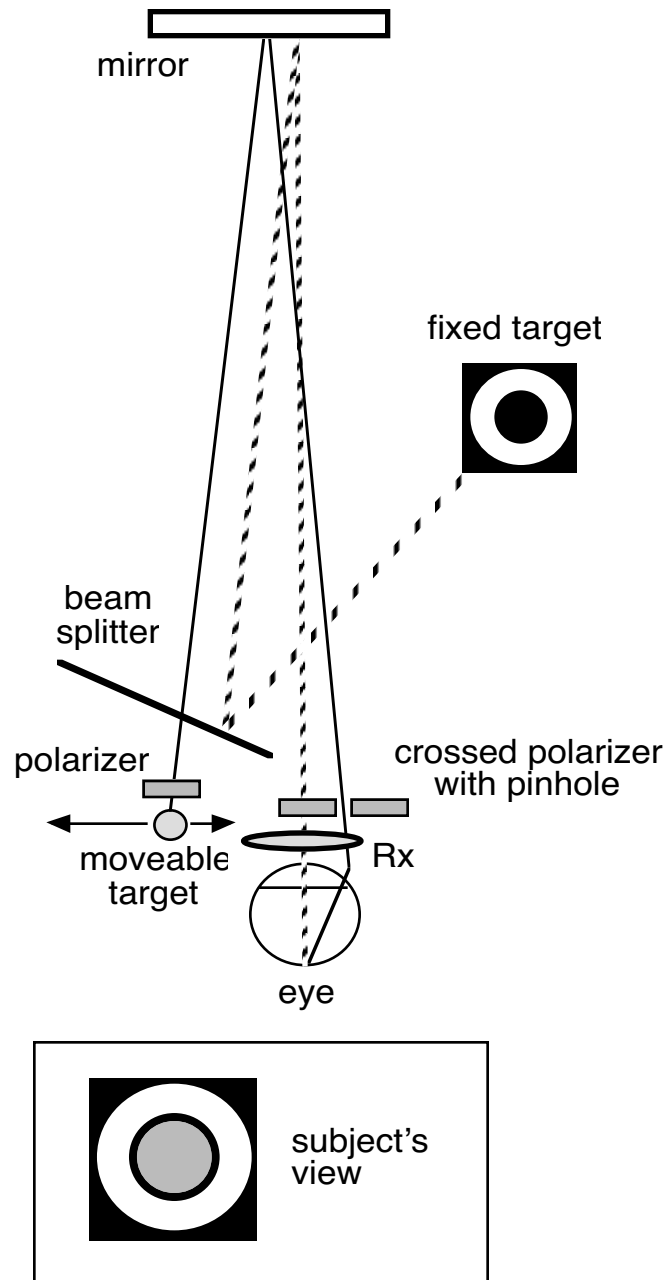


Figure 6.3

Psychophysical apparatus based Smirnov's principle. The subject observes a fixed annular target through his entire pupil while polarized light from an LED enters the pupil only through a small pinhole aperture drilled in a cross polarized filter that is positioned in front of the eye. The pinhole is used to isolate predetermined locations within the pupil, and for each position the subject adjusts the LED until it appears centered in the annulus, making it conjugate with the fovea. The positions of the LED and pinhole allow computation of the wavefront slope for the pupil location isolated by the pinhole, as described in Fig. 6.1.

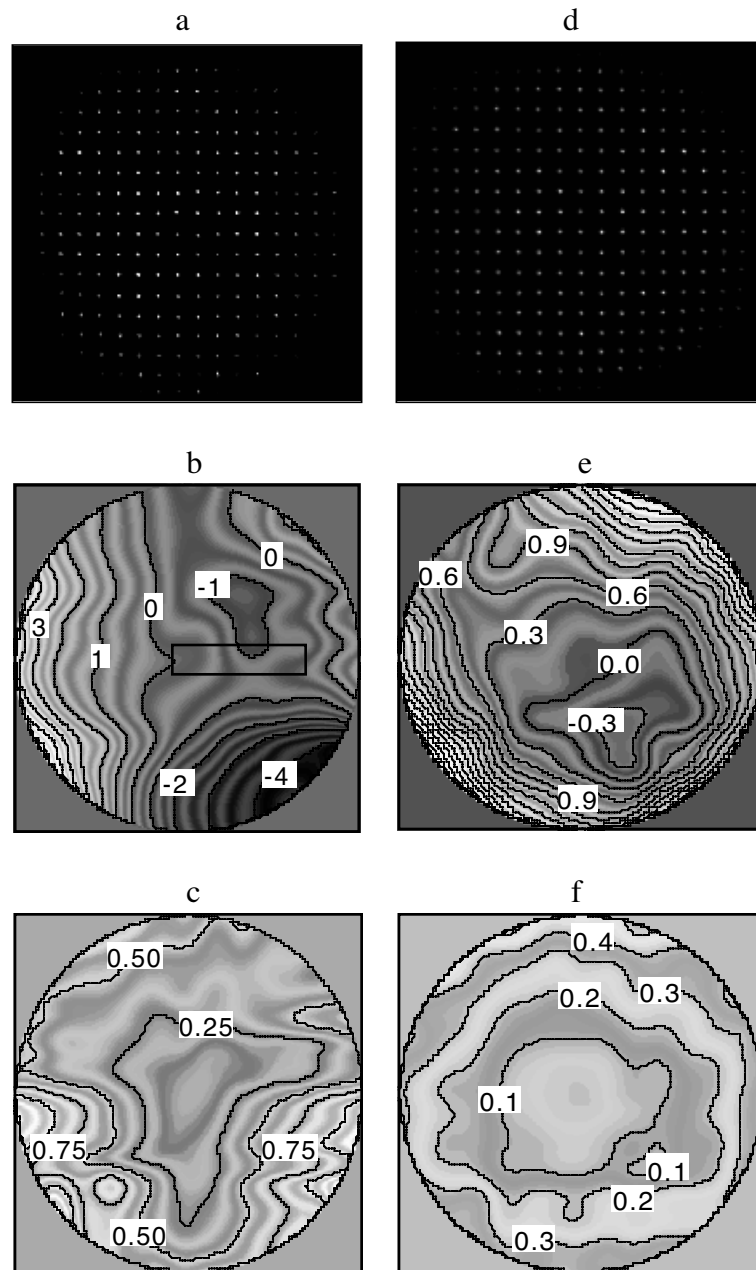


Figure 6.4

Two-dimensional wavefront aberration data from the Shack-Hartmann wavefront sensor. Data for subject LT is shown in the left column (a,b,c). The right column (d,e,f) shows data for DH. Example of raw data images are shown in the first row (a,d). The middle row shows mean ($n = 5$) wavefront aberration maps for LT (b) with 1λ contour intervals and for DH (e) with 0.3λ intervals. The rectangle in b delineates the region that contains a subtle wavefront anomaly described in detail in the text and graphed in Fig. 6.7. Corresponding standard error maps are shown for LT (c) with 0.25λ contour intervals and for DH (f) with 0.1λ intervals. Pupil diameters were 5.6 mm.

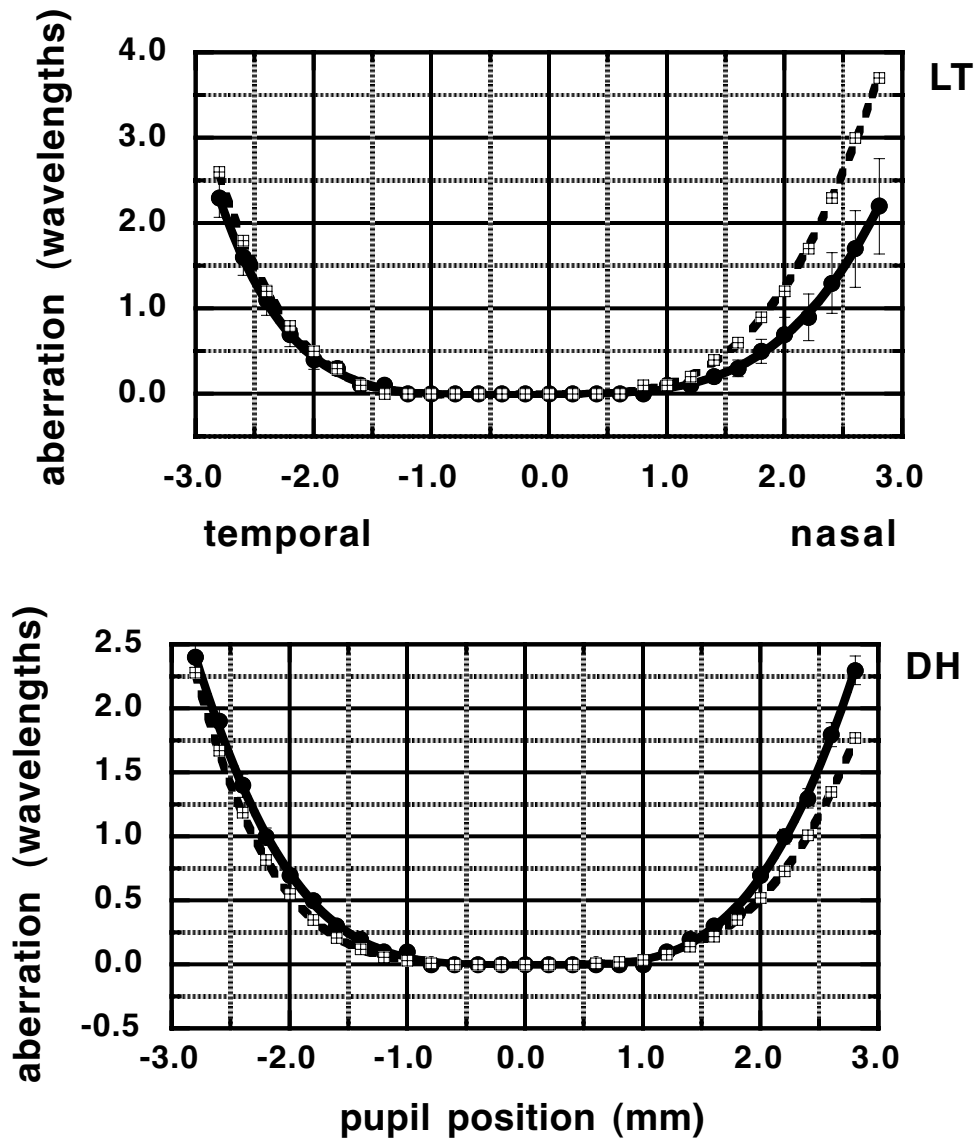


Figure 6.5

Direct comparison of wavefront aberration profiles measured by the Shack-Hartmann sensor (solid curve, circles) and Smirnov apparatus (dashed curve, squares) for subjects LT (top) and DH (bottom). Prism and defocus were removed, leaving only higher order aberrations for the comparison. The wavefront aberration in wavelengths ($\lambda = 632.8 \text{ nm}$) across the 5.6 mm diameter pupils show close agreement between the two methods in terms of shape and magnitude. The greatest difference between the two techniques is noted in the nasal portion of LT's pupil.

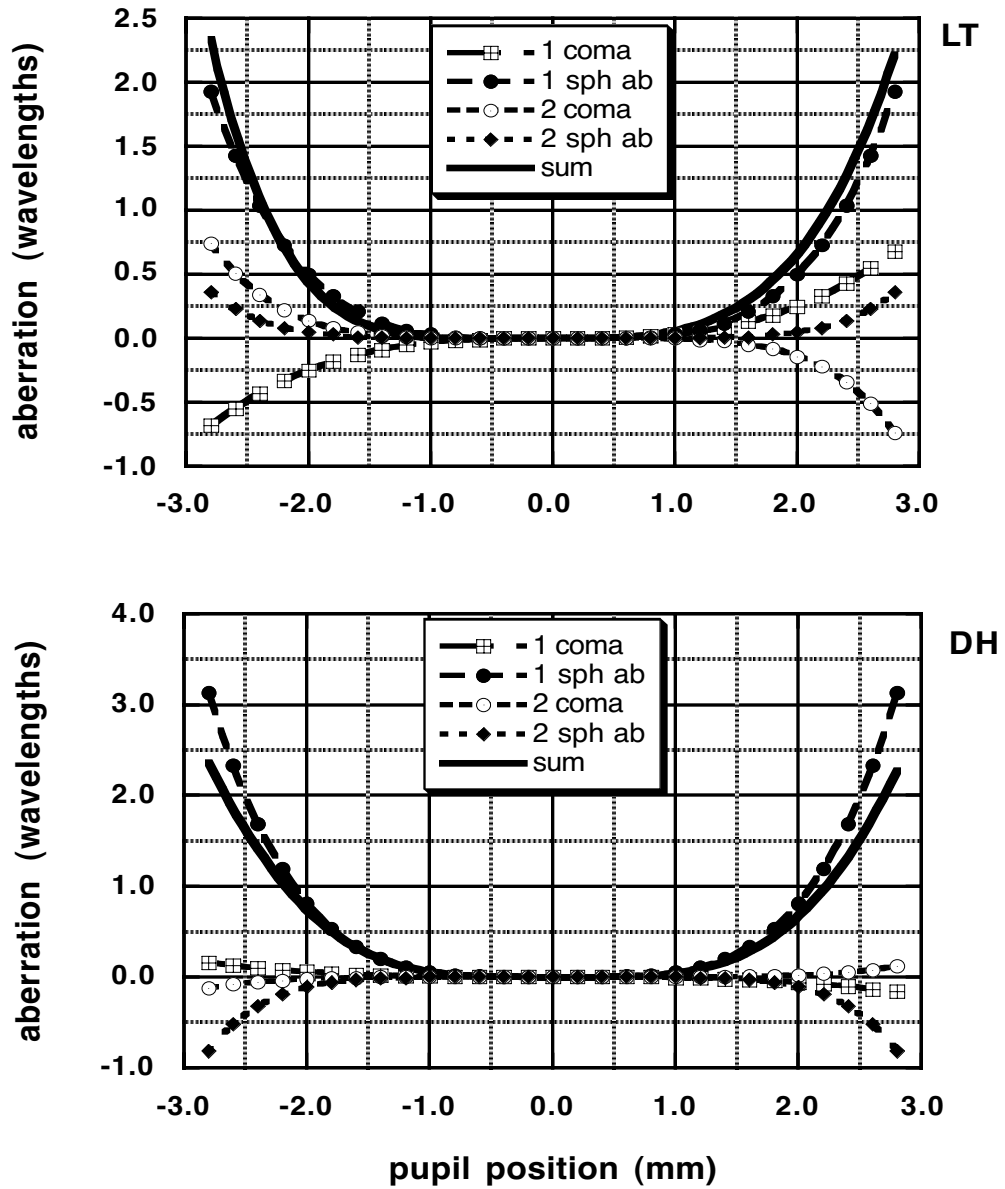


Figure 6.6

The relative contribution of primary coma (squares), primary spherical aberration (filled circles), secondary coma (open circles) and secondary spherical aberration (filled diamonds) to the total wavefront aberration profile (solid line) for subject LT (top) and DH (bottom). For LT, primary spherical aberration alone closely approximates the total aberration function. Combined primary and secondary coma make a minimal contribution to the total aberrations since they have similar magnitude but opposite signs and cancel each other out. A small amount of positive secondary spherical aberration is also present. For DH, primary spherical aberration also dominates, while primary and secondary coma are negligible. A small amount of negative secondary spherical aberration partially negates the large positive primary spherical aberration in the peripheral pupil.

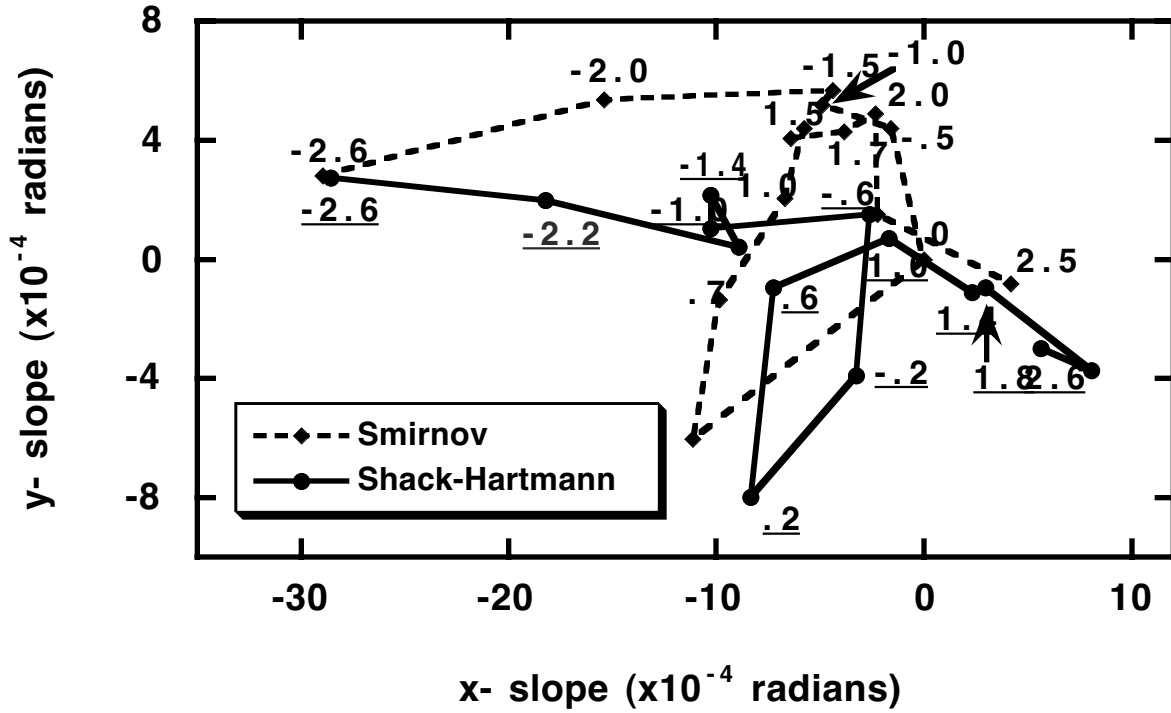


Figure 6.7

During psychophysical measurements of LT's wavefront aberration function, he observed that, as the pinhole moved horizontally across the nasal half of his pupil, a fixed LED appeared to move in a loop-like trajectory. This unusual aberration was verified in both the psychophysical (dashed line) and Shack-Hartmann (solid line) measurements and is visualized by plotting the x and y wavefront slopes measured at successive points across the pupil. Numbers near selected symbols indicate the horizontal distance in mm of each sample point from the pupil center. Negative values indicate the temporal half-pupil; positive, the nasal. Labels for the Shack-Hartmann data are underlined. Though slightly shifted from each other, both curves show the same loop-like reversal in the same part of the pupil where the pattern was noted subjectively. Additionally, miniscule and abrupt changes in wavefront slopes occur at corresponding pupil locations in both traces.

Corneal Contribution to the Wavefront Aberration of the Eye

7.1

INTRODUCTION

New problems in clinical eye care, along with the availability of new research techniques, are creating exciting new challenges and opportunities for the modern vision scientist (Thibos, 1997). Within the field of visual optics, corneal optics research is becoming particularly significant. The corneal surface is the most important element in the eye's optical system, accounting for approximately 70% of its total refractive power, and it is the major source of astigmatism in most eyes. Keratometry, long used to measure corneal curvature, has been at the heart of clinical contact lens practice; recently, corneal refractive surgery has stimulated the development of new instruments that provide even greater detail about the surface topography of the cornea. These instruments are primarily being used to screen for certain corneal surface diseases, but the newest generation of corneal topographers have become accurate enough that they can also be used to study the optical aberration structure of the cornea (Horner & Salmon, 1998; Salmon, Rash, & Mora, 1998).

Optometrists and ophthalmologists routinely correct errors of defocus and astigmatism, but generally ignore the more complex and subtle higher order aberrations. This is because, for normal eyes, these optical aberrations are relatively small compared to the correctable refractive errors. In addition, they are difficult to measure and correct. Refractive surgery, however, is inadvertently creating a population of patients (Maguire, 1994; Halliday, 1995) with large unnatural aberrations (Seiler, Reckmann, & Maloney, 1993; Applegate, Hilmantel, & Howland, 1996; Schwiegerling, Greivenkamp, Miller, Snyder, & Palmer, 1996; Hemenger, Tomlinson, & Caroline, 1997; Oliver, Hemenger, Corbett, & al., 1997; Applegate, Howland, Sharp, Cottingham, & Yee, 1998; Gauthier, *et al.*, 1998; Bullimore, Olson, & Maloney, 1999; Oshika, Klyce, Applegate, Howland, & El Danasoury, 1999), which significantly degrade optical quality

and vision. For more and more patients therefore, aberrations are becoming a problem with clinical consequences which cannot be ignored. With a better understanding of the eye's optics, we can expect refractive surgery to improve to the point that, not only are unwanted aberrations minimized, but one day we may be able to routinely provide patients with "supernormal" vision (Liang, Williams, & Miller, 1997; Wu, 1997).

Although a hundred years have passed since Javal developed his rule to generalize the cornea's role in ocular astigmatism (Mote & Fry, 1939), we still know little about the contribution of the cornea to the higher order aberrations of the eye. Progress in this field would require better methods to more accurately measure the surface topography of the cornea. In the early 1990's two new technologies, which would open the door to new progress in corneal optics research, became available; namely, improved computerized videokeratoscopes and the Shack-Hartmann wavefront sensor (Liang, Grimm, Goelz, & Bille, 1994; Liang & Williams, 1997; Salmon & Thibos, 1998). Employing both of these new tools, my goal was to study the contribution of the anterior corneal surface to the optical aberrations of the normal human eye.

7.1.1 The aberrations of normal corneas

One way to study the role of the cornea in the aberrations of the eye is to measure the aberrations of the cornea alone, and then separately measure the aberrations of the whole eye. Another method is to effectively eliminate the cornea, by immersing the eye in water, and measure the aberrations of the eye minus the cornea, and compare this to the aberrations of the eye as a whole. Our current knowledge of normal corneal aberrations was summarized in Chapter 5 (Section 5.1) and is based largely on a knowledge of normal corneal surface shape. Corneal shapes can vary widely with individuals, but based on the average cornea (Carney & Henderson, 1993; Applegate, *et al.*, 1994; Carney, Mainstone, & Henderson, 1997), the average corneal wavefront aberration should be similar to that plotted in Fig. 5.1b, which shows astigmatism and spherical aberration (piston, tilt and defocus were removed). Based on shape analysis, the normal cornea could have spherical aberrations with a maximum value of between $-\lambda/4$ to 8λ at the margin of a 5.6-mm pupil. An average astigmatism of 1.25 diopters (D) would contribute a maximum wavefront aberration of $\pm 3\lambda$. Averaging corneal data across a population tends to remove asymmetric aberrations such as coma, but these are likely to be present in individual corneas (Hemenger, Tomlinson, & Oliver, 1994; Howland, Buettner, & Applegate, 1994). Beyond these very basic concepts, little is known about the aberration structure of normal corneas.

7.1.2 The aberrations of normal eyes

In a review of research to that time, Charman (1991) summarized general features of the human ocular wavefront aberration function. Within the central 2-3 mm of the pupil, the function is usually close

to zero, but it increases to 1-10 λ near the edge of 6-7-mm-diameter pupils. There is great intersubject variability, and coma or other asymmetries are often present. When studying mean aberrations for a number of subjects, the asymmetries tend to average out, and symmetric aberrations, such as spherical aberration appear to dominate.

Liang and Williams recently reported Shack-Hartmann wavefront aberration measurements for 12 eyes with a pupil size of 3.4 mm and for 14 eyes with a pupil size of 7.3 mm (Liang & Williams, 1997). Wavefront errors within the small pupil size were small—generally less than $3/4 \lambda$. For a 6-mm pupil, the maximum wavefront error (excluding astigmatism and defocus) was in the range of 2-6 λ . The shape of the wavefront aberration varied from person to person; some eyes showed large symmetric spherical-like aberrations, but about one third of the eyes showed almost no spherical aberration. Some wavefronts showed multiple, localized, peak-like irregularities, which were $\lambda/2$ to 2λ high. Figure 7.1 shows the distribution of wavefront variances, by Zernike order, based on data from this and a companion article (Liang, *et al.*, 1997), for three pupil sizes. Values represent the mean wavefront variances in each order for 12 eyes (3.4-mm pupil), 4 eyes (6-mm pupil) and 14 eyes (7.3-mm pupil). For the larger pupil sizes, the bulk of higher order aberrations were contained in Zernike orders 3 and 4, while aberrations in orders 5-10 contributed relatively little. Liang described the overall magnitude of the wavefront variance as an RMS wavefront error, which is the square root of the wavefront variance. For my purposes, wavefront variance was a more convenient descriptor, since it is equal to the sum of the squared normalized Zernike coefficients. I therefore squared Liang's RMS wavefront errors to yield wavefront variances, which are presented in Fig. 7.1. By this conversion, Liang found mean higher order (orders 3-10) wavefront variances of 0.02, 0.26 and $0.56 \lambda^2$ for the respective pupil sizes of 3.4, 6.0 and 7.3 mm. To put the magnitude of these higher order aberrations in perspective, the mean astigmatism (a second-order aberration) for the subjects with 7.3-mm pupils was 0.6 D, and this corresponded to a wavefront variance of about $1.48 \lambda^2$.

7.1.3 Comparison of corneal and ocular aberrations

Two basic strategies have been employed to isolate the aberrations of the cornea for comparison to the aberrations of the whole eye. One is to neutralize the cornea by immersing it in water and, in effect, measure the aberrations of the eye without the cornea. This was originally tried by Thomas Young (1801), and the same technique has been used in recent research as well (Millodot & Sivak, 1979; Artal & Guirao, 1998). Another approach is to derive the aberrations of the cornea from careful measurements of its surface shape. This is the method used by myself and several other researchers (El Hage & Berny, 1973; Tomlinson, Hemenger, & Garriott, 1993; Artal & Guirao, 1998).

In the two hundred years since Thomas Young's classic experiment, relatively little work has been done to study the role of the cornea in the aberration structure of the whole eye. Most of these studies

specifically compared spherical aberration of the cornea and crystalline lens, often in just one meridian. El Hage and Berney (El Hage & Berny, 1973) measured the corneal topography of one subject using photokeratoscopy, and computed the corneal wavefront aberration in the horizontal meridian only. This was compared to the ocular wavefront aberration measured in the same meridian using the Foucault knife-edge test. In this eye, corneal aberrations were larger than the ocular aberrations, so they concluded that the crystalline lens compensates for the spherical aberration of the cornea.

Using Young's approach, Millodot and Sivak (Millodot & Sivak, 1979) had subjects wear swimming goggles filled with saline solution and measured aberrations (for the eye minus the cornea) in the horizontal meridian for 17 eyes. Using a Scheiner's disk with one pinhole on the foveal achromatic axis and another exposing a more peripheral pupillary location, they measured the refractive error at several positions across the pupil. Those results were compared to measurements of aberrations for the whole eye, made for the same subjects without the saline. A few eyes had negative lenticular spherical aberration, which balanced positive spherical aberration of the cornea, but in most of their eyes, ocular aberrations were actually larger than corneal aberrations. This indicates that the lens does not generally compensate—rather it often adds to—corneal aberrations.

Tomlinson *et al.*, (1993) employed an indirect method to estimate the spherical aberration of the lens from the corneal modulation transfer function (MTF) and the contrast sensitivity (CSF) function. Radially averaged corneal MTF's were computed based on photokeratoscopy, and the difference in computed MTF's for large and small pupils was used to estimate the spherical aberration of the cornea. Similarly, the difference in the CSF for large and small pupils was used to estimate the eye's total spherical aberration. The difference between the ocular and corneal spherical aberration was interpreted as the lenticular spherical aberration. Out of 20 eyes tested, most had negative lenticular spherical aberration that almost completely (7 eyes) or partially (4 eyes) compensated for the cornea's positive spherical aberration. One eye had an equal amount of corneal and ocular spherical aberrations, which suggests a lens with no significant spherical aberration. In two eyes the ocular aberrations were slightly larger, indicating a small amount of positive lenticular spherical aberration.

Recently Artal and Guirao (1998) employed the double-pass method to estimate the ocular wavefront aberration function, which they then compared to the corneal aberrations derived from videokeratoscopy. Their procedure for measuring the corneal wavefront aberration was similar to my own, but for the ocular wave aberration, they used a much more complex, indirect approach. They first reconstructed the eye's single pass point spread function (PSF), and from this, computed the wave aberration. The following steps summarizes their procedure for estimating the ocular wavefront aberration function.

- 1) A traditional symmetric-double-pass method (Williams, Brainard, McMahon, & Navarro, 1994; Artal, Marcos, Navarro, & Williams, 1995b) was used to estimate the modulation transfer function (MTF) of the eye, based on Eq. (7-1). It states that the aerial image of a point of light reflected out of the eye $[I(x,y)]$ is the autocorrelation of the eye's single-pass PSF $[P(x,y)]$. In the equation, \otimes denotes convolution.

$$I(x,y) = P(x,y) \otimes P(-x,-y) \quad (7-1)$$

The MTF of the eye is then computed as the magnitude (mag) of the square root of the Fourier transform of $I(x,y)$.

$$\text{MTF} = \text{mag} \sqrt{F[I(x,y)]} \quad (7-2)$$

In addition to the MTF, the phase transfer function (PTF) is also needed to compute the eye's single-pass PSF. However, because of the autocorrelation operation involved in the symmetric-double-pass procedure, phase information is lost and the PTF cannot be recovered.

- 2) Artal then used the asymmetric-double-pass technique (Artal, Ignacio, & Lopez-Gil, 1995a; Navarro & Losada, 1995) to obtain a low resolution image of the PSF and a partial PTF. A small (1.5-mm-diameter) entry beam was used to form a spot on the retina, which was considered diffraction limited. The reflected light passed through a 4-mm-diameter exit pupil, and the aerial image, $[I_d(x,y)]$, was formed by the convolution of the diffraction-limited PSF, $[P_d(x,y)]$, and the eye's single-pass PSF, $[P(x,y)]$.

$$I_d(x,y) = P_d(x,y) \otimes P(x,y) \quad (7-3)$$

Since $I_d(x,y)$ was measured, and $P_d(x,y)$ was known, based on the assumption that it was a diffraction limited spot (i.e., an Airy disk), $P(x,y)$, could be computed by deconvolving $I_d(x,y)$ by $P_d(x,y)$. This is equivalent to division in the Fourier domain and, as shown in Eq. (7-4), the quotient is the Fourier transform of the PSF. This is also equal to the optical transfer function (OTF), from which the PTF can be computed (Eq 7-5).

$$\frac{F[I_d(x,y)]}{F[P_d(x,y)]} = F[P(x,y)] = \text{OTF} \quad (7-4)$$

$$\text{PTF} = \tan^{-1} \left(\frac{\text{Im}\{F[I_d(x,y)]\}}{\text{Re}\{F[I_d(x,y)]\}} \right) \quad (7-5)$$

Though the PSF and PTF can be computed in this way, the spatial frequency content of both is limited to the cutoff frequency of the incoming beam in the asymmetric-double-pass apparatus.

- 3) The symmetric double pass provided a high resolution version of the MTF, while the asymmetric double pass provided a low resolution PSF and PTF. With this information, Artal used a complex iterative phase retrieval process (Iglesias, Lopez-Gil, & Artal, 1998) to compute the remainder of the PTF (up to the MTF's cutoff frequency) and reconstructed the complete PSF.
- 4) He then implemented additional phase retrieval techniques to estimate the wavefront aberration from the PSF (Iglesias, Berrio, & Artal, 1988). This is also a complex process, which does not necessarily yield a unique solution. On average, it required 20 hours of iterative computing to estimate 15 Zernike coefficients describing the ocular wavefront aberration for one subject.

The end product of this process was a set of Zernike coefficients for the ocular wavefront aberration, which were compared to corresponding Zernike coefficients for the corneal wave aberration. The differences between corresponding ocular and corneal Zernike coefficients were interpreted as Zernike coefficients for the crystalline lens. Artal's analysis for five subjects (pupil size 4.0 mm) showed that the overall ocular aberrations, including small amounts of astigmatism, were smaller than those of the cornea. He computed Seidel spherical aberration and coma, and for all five eyes the lenticular aberrations were of opposite sign to the corneal aberrations, thereby compensating for corneal aberrations and improving optical quality for the eye as a whole. Only the very small, asymmetric fourth order aberrations were found to be larger in the whole eye than they were in the cornea alone.

In an ideal eye, higher order aberrations of the cornea and lens would be perfectly balanced; that is, they would be of equal magnitude but opposite sign. In view of the fact that optical defects (i.e., defocus and astigmatism) are common, and the optical surfaces of most eyes are neither rotationally symmetric or coaxially aligned, we should not necessarily expect a general trend toward aberration balancing in all real

eyes. Prior research is sparse and inconclusive with regard to any particular theory about corneal/lens aberrations balancing. Early work was limited to analysis in one meridian only (El Hage & Berny, 1973; Millodot & Sivak, 1979), or to indirect estimates of the relationship between corneal and lenticular aberrations (Tomlinson, *et al.*, 1993). Artal's research breaks new ground by using videokeratoscopy and the double-pass method to directly compare two-dimensional corneal and ocular wavefront aberrations functions. The results of this recent study appear to support the hypothesis that the corneal and internal aberrations tend to balance each other out.

A unique aspect of my research was the use of both videokeratoscopy and the Shack-Hartmann (S-H) wavefront sensor. The S-H technique is the newest method for measuring the eye's optical quality and has numerous advantages over older techniques, including the double-pass method. While the double-pass technique can indirectly provide wavefront aberration data, as previously described, the process is requires certain assumptions, is protracted and demands considerable computer processing time. Because of the complexity of the phase retrieval algorithms, analysis must be limited to moderate pupil sizes, Zernike analysis up to only about the fourth order and eyes that do not have very large aberrations (Iglesias, *et al.*, 1988). In comparison, the S-H device directly measures the shape of the wavefront aberrations itself; data processing is simpler and faster. I measured the aberrations of normal eyes, but some laboratories are beginning to use the S-H method to measure highly aberrated eye, such as those seen after refractive surgery. The S-H technique has theoretical advantages over the double-pass method since it directly analyzes wavefront slopes, rather than the quality of a retinal spot, reflected out of the eye. Compared to the aberroscope, and subjective ray isolation techniques (He, Marcos, Webb, & Burns, 1998), the S-H method can sample a greater number of data points (Salmon & Thibos, 1998), thereby making it possible to study aberrations to a higher order. In summary, the Shack-Hartmann apparatus is the most direct way to measure the eye's wavefront aberration, and it provides more complete data than other techniques. By using this, in combination with videokeratoscopy, my project has been designed to employ the best available technologies to investigate the corneal contribution to the overall aberration structure of the eye.

7.2

METHODS

7.2.1 Approach

In order to determine the contribution of the corneal surface to the wavefront aberration of the whole eye, it was necessary to measure the corneal and ocular aberrations separately. The wavefront aberration of the cornea was computed based on corneal topography measurements made with a clinic videokeratoscope—the EyeSys 2000 Corneal Analysis System. Details of the corneal aberrations were

discussed in Chapter 5, and those results will be compared to ocular aberrations in this chapter. The wave aberration function for the whole eye was measured using a S-H wavefront sensor. The apparatus and methods are the same as those described in the S-H calibration study (Chapter 6), but this chapter includes data collected on additional subjects.

The EyeSys and S-H devices use different principles to measure optical properties of the eye. Both techniques specify the respective wavefront aberration functions in the entrance pupil of the eye, but they both do not necessarily use the same central reference axis. For studies of visual optics, the preferred reference axis is the primary line of sight (or fixation axis), which is defined in object space as the line joining the fixation point and the entrance pupil center (Mandell, 1992; Mandell, Chiang, & Klein, 1995; Applegate, *et al.*, 2000—In press). While our Shack-Hartmann sensor was designed to make measurements directly on the line of sight, videokeratoscopes, such the EyeSys, usually do not center their measurements on the line of sight. Instead, they measure along an axis that is slightly skewed with respect to the line of sight, by an amount that varies with each eye. Therefore, when computing the corneal wavefront aberration function, I compensated for the skew angle between the videokeratoscope axis and the line of sight (Mandell & Horner, 1993; Mandell, 1995). This provided a corneal wave aberration that could be compared to the S-H measurements, since they were then on a common reference axis. The data processing steps to accomplish this will be summarized below (Section 7.2.3).

The sampling array used by the EyeSys videokeratoscope and S-H sensor are different. Corneal topography was measured on a polar grid with 360 radial meridians and approximately 12 samples per meridian. This provided about 4,000 data points within the pupil. The S-H measurements were sampled on a 16 × 16 square grid (0.4-mm intervals), which provided between 160 and 220 data points, depending on centration and pupil size. Data from the EyeSys and S-H sampling arrays had to be processed to a comparable, common format. This was accomplished by interpolating the corneal data to a Cartesian grid, and fitting the data to Zernike polynomials. The S-H data were also fitted to Zernike polynomials, and corneal and ocular Zernike coefficients were directly compared to determine the relationship between the corneal and non-corneal component of the eye's aberrations.

7.2.2 Subjects

After obtaining informed consent, corneal topography and Shack-Hartmann measurements were made on the right eye of three subjects. Each eye had a low refractive error, and best corrected visual acuity for each was 20/15. Slit lamp biomicroscopy and corneal topography measurements verified that all eyes were healthy and normal. Table 7.1 summarizes other parameters describing the eyes that were measured.

TABLE 7.1 Summary statistics describing eyes measured in this study.

Subj	Age	Refraction	BVA	Pupil dia (mm)	Keratometry
AB	41	+0.88 -0.50 x 030	20/15	5.6	42.51@003/43.43
DH	40	+0.18 -0.38 x 088	20/15	5.2	39.85@175/40.47
LT	49	-0.63 -0.88 x 090	20/15	5.6	42.83@100/43.38

7.2.3 Aberrations of the cornea

The corneal wavefront aberration function was computed from corneal topography data acquired using the EyeSys 2000 Corneal Analysis System, with software version 3.2. The important steps in this process are listed below and described in the paragraphs which follow. This was also discussed in detail in the Methods section of Chapter 5.

- 1) Calibrate the EyeSys videokeratoscope
- 2) Acquire corneal topography data images
- 3) Compute mean corneal surface elevations
- 4) Correct EyeSys data for instrument bias
- 5) Compute the corneal sighting center location
- 6) Compute the corneal wavefront aberration
- 7) Transform data from polar to Cartesian coordinates
- 8) Fit data to Zernike polynomials

a. Instrument calibration

Although the EyeSys has a proven track record for clinical diagnosis of corneal diseases, it was unclear whether the instrument was sufficiently accurate to allow computation of subtle optical aberrations on the order of those expected for a normal cornea. This prompted an accuracy study of the EyeSys videokeratoscope, which was presented in Chapter 4 (Horner & Salmon, 1998; Salmon, *et al.*, 1998). I concluded that, with the appropriate correction for systematic instrument error, the EyeSys (version 3.2), is capable of measuring the surface elevation of a normal cornea with less than $0.25 \mu\text{m}$ of error, for a 6.0-mm pupillary zone. For the wavelength used in this study, (633 nm) this equates to $\sim\lambda/7$, which is similar to the magnitude of error expected with the S-H sensor (Chapter 6). As required by the operator's manual, the instrument's software was calibrated prior to taking measurements.

b. Corneal topography data acquisition

Other than a slightly modified fixation procedure for one subject (see Section 5.2.4), I instructed the subjects to fixate the central fixation light, and EyeSys images were taken using standard alignment. Approximately 20 good quality images were acquired for each eye, and data was stored for later processing. Although the EyeSys uses 18 keratoscope rings and is designed to measure up to about a 9-mm corneal diameter, it is common for a patient's nose or brow to obstruct portions of the peripheral rings. I attempted to maximize corneal coverage by having subjects turn their faces and open their eyes widely, but still some data was missing from the outer rings. At least a 6.0-mm-diameter portion of the central corneal was measured in each subject.

c. Surface elevation computation from raw EyeSys data

The standard EyeSys software does not compute corneal elevations since this is not normally used in clinical practice. Upon request, the manufacturer provides a utility program entitled, CORSAG18.EXE, which uses input from regularly stored data files to compute the elevations. The README.TXT file that accompanies this program is included as Appendix C. Among the six data files that are normally saved for each image, the two which are used to compute the surface elevations are the *.XX and *.RA files. The *.XX file contains the axial radius of curvature associated with each sampled point in hundredths of a mm (i.e., 7.89 mm is recorded as 789). The *.RA files records the radial distance of each point from the corneal center, also in hundredths of a mm (i.e., 0.25 mm is recorded as 25.0). Radial distances correspond to ring #1 are approximately 0.25 mm and about 4.5 mm for ring #18. Each of the raw EyeSys data files are organized with a one-line header followed by 360 rows, with 19 numbers in each row. The first number gives the angular meridian (0-359) in degrees. This is followed by 18 numbers, which are the data associated with successive EyeSys rings, from center to periphery.

After computing the surface elevations, the CORSAG18.EXE program stores the data in an ascii text file with a *.SG extension. Elevations are specified with reference to a plane perpendicular to the instrument axis and tangent to the cornea apex. Data are recorded in units of tenths of a micrometer (i.e., 1 μm is recorded as 10.0). The EyeSys data set for each subject included *.XX, *.RA and *.SG data files for each good image taken. Fifteen data images were used for subjects AB and DH, and nineteen were used for subject LT. For each subject I computed a mean *.RA and *.SG file with values scaled to micrometers. A mean *.XX file, scaled to mm, was also computed. The mean *.XX and *.RA files were used to compute the elliptical shape factor (p value), which was needed to correct the mean *.SG elevation data for systematic instrument error (paragraph d). Finally, the mean *.RA and *.SG files were used to compute the wavefront aberration (paragraph f).

d. Correction for systematic instrument error

In the study described in Chapter 4, I discovered that the EyeSys surface elevation data contains an

error that varies as a function of the ellipsoid shape factor and increases from the center to the periphery of the cornea. The procedure developed in Section 4.4.1 to compensate for systematic instrument error was applied to the elevation data for each subject before computing the wavefront aberration.

The EyeSys, as well as all clinical videokeratoscopes, measure and analyze corneal topography meridian by meridian, presumably because of the difficulty of implementing a true three-dimensional reconstruction algorithm. In effect the three-dimensional corneal surface is treated as a set of 360 two-dimensional slices. In compensating for EyeSys error, I retained the two-dimensional approach and corrected the data meridian by meridian. The steps used to correct the EyeSys surface elevation data (mean *.SG file for each subject) were:

- 1) Compute the square of each of the axial radii, contained in the mean *.XX data file. Each subject's mean *.XX file was organized into 360 rows (one for each radial meridian) and within each meridian there were 11-13 axial radius values, depending on the subjects.
- 2) Compute the square of the radial distances contained in the mean *.RA data file. This step also produced a data array with 360 rows, each of which had 11-13 squared distance values.
- 3) For each meridian, there was now a data vector of squared axial radii (r_a^2), from the *.XX file, and another data vector of squared radial distance values (y^2), from the *.RA file. As described in Section 5.1.5 (also see Appendix B), these parameters are related by the following equation.

$$r_a^2 = r_0^2 + (1 - p)y^2 \quad (7-6)$$

Variable r_0 represents the apical radius of curvature, and p is the elliptical shape factor. Solving for the slope of the linear regression between r_a^2 (ordinate) and y^2 (abscissa), as described in Section 5.1.5, I found the elliptical shape factor (p) for each meridian according Eq. (7-7).

$$p = (1 - \text{slope}) \quad (7-7)$$

- 4) Knowledge of the p value allowed me to compute the components of a linear equation that would be used to estimate the fractional sag error (FSE) in the raw EyeSys

Chapter 7: Corneal Contribution to the Wavefront Aberration of the Eye

data. The linear equation was composed of a slope and y intercept, both of which were computed based on the p value, by the following formulas.

$$\text{slope} = 0.003165 \times p - 0.003445 \quad (7-8)$$

$$\text{intercept} = -0.003664 \times p - 0.0003363 \quad (7-9)$$

5) Using the linear equation built from the slope and intercept found in Eq. (7-8) and (7-9), I used Eq. (7-10) to compute the fractional sag error (FSE), which is defined as the sag error divided by the measured sag (Eq. 4-11). Variable d represents the radial distance of each EyeSys sampled point from the optic axis and was contained in the mean *.RA files.

$$\text{FSE} = \text{slope} \times (d) + (\text{intercept}) \quad (7-10)$$

6) With a value for the FSE, I computed a corrected a corrected sag (CS) for each measured sag value contained in the *.SG file according to Eq. (7-11).

$$\text{CS} = \text{measured} \times (1-\text{FSE}) \quad (7-11)$$

I imported the basic data arrays (*.XX, *.RA and *.SG) into an Excel spreadsheet and applied each of the steps listed above to each meridian of data. The end product was a data array with the corrected surface elevations, in micrometers.

e. Compute the corneal sighting center location

As described in Section 7.2.1, it was necessary to estimate the deviation of the videokeratoscope measurement axis from each subject's line of sight. Specifically, I determined the point where the line of sight intersects the corneal surface. The intersection point is known as the corneal sighting center (Mandell, 1992; Mandell & Horner, 1993; Mandell, 1995; Mandell, *et al.*, 1995). This may be computed based on the geometry illustrated in Fig. 7.2, and described in detail in Sections 5.1.4 and 5.2.6. The basic information needed to compute the location of the corneal sighting center are the videokeratoscope fixation point, corneal apical radius, entrance pupil location and angle lambda. The fixation point is set by the instrument design; corneal apical radius was measured by the videokeratoscope. A micrometer attached to a slit-lamp biomicroscope was used to measure the distance from the corneal surface to the entrance pupil.

Angle lambda is formed by the intersection of the line of sight and the pupillary axis, which is defined as the line perpendicular to the cornea that passes through the entrance pupil center. The pupillary axis shares a common point with the line of sight at the center of the entrance pupil, and it also shares a common point with the videokeratoscope axis at the center of curvature of the cornea. With a knowledge of angle lambda and the other data mentioned above, it is possible to compute the corneal sighting center location relative to the videokeratoscope axis. I measured angle lambda in both the vertical and horizontal directions, using an apparatus described by Mandell (Mandell, 1995) and illustrated schematically in Fig. 5.6. From this, the x, y, and z coordinates of the corneal sighting center were computed according to the following procedure.

- 1) Compute the length of arc PF.

$$(\text{arc PF}) = \lambda(\text{FS} + \text{SE}) \quad (7-12)$$

- 2) Find the length of arc SA.

$$(\text{arc SA}) = \frac{\text{SE}}{(\text{FS} + \text{SE})} (\text{arc PF}) \quad (7-13)$$

- 3) Find the length of arc AV

$$(\text{arc AV}) = \frac{\text{VC}}{(\text{FV} + \text{VC})} (\text{arc PF}) \quad (7-14)$$

- 4) Compute angle VCS.

$$\text{VCS} = \frac{(\text{AV} - \text{SA})}{\text{VC}} \quad (7-15)$$

5) Finally, the displacement (x) of the corneal sighting center (S) from the videokeratoscope axis (FC) is computed by Eq. (7-16). This procedure was used to compute both the x and y coordinates of the corneal sighting center relative to the corneal apex (V). The z coordinate was computed based on the sagittal depth of the cornea, using the known corneal apical radius and elliptical shape

factor (p value).

$$x = VC[\tan(VCS)] \quad (7-16)$$

f. Compute the corneal wavefront aberration function

In addition to the corneal surface data, the three-dimensional coordinates for an object point, the corneal sighting center, and an image point were required to compute the optical path length for the chief ray and other rays. The object point was a hypothetical fixation point located 10,000 meters in front of the cornea, on the line of sight, and for my purpose, the object distance was equivalent to infinity. The object point and corneal sighting center coordinates defined an incident chief ray, and using an estimated normal to the corneal surface at the corneal sighting center, I used skew ray tracing (Freeman, 1990) to compute the paraxial image point. Once these points were known, I was able to calculate the optical path length for the chief ray. The path length between the object and image points through the other corneal surface point were also computed, and the difference between the optical distance for the chief ray and all other rays was taken as the corneal wavefront aberration. As was done with the S-H wavefronts, corneal wave aberrations were normalized by a wavelength of 633 nm. A MATLAB program, which I used to compute the wavefront aberration function, given the object point, corneal sighting center and image point, is included as Appendix D.

g. Polar to Cartesian transformation

The original EyeSys sample points are arranged on a polar grid, with 360 equally spaced radial meridians. The distance between sample points within each meridian is approximately 0.25 mm, but the exact spacing can vary from meridian to meridian. Raw EyeSys wavefront data, therefore, was originally arranged in an irregular polar grid. The last part of the MATLAB program, mentioned above, (Appendix D) interpolated the data to a regular polar grid, and a scientific visualization program (Transform 3.3, Fortner Research LLC), was used to convert the data to a regular Cartesian array.

h. Fitting to Zernike polynomials

In order to match the pupil sizes measured with the S-H device (Chapter 7), the corneal data was limited to a 5.6-mm-diameter pupillary zone for subjects AB and LT, and a 5.2-mm zone for DH. A MATLAB program (Appendix E) was used to fit the wavefront data to a series of Zernike polynomials that included terms up to the tenth order. The resulting Zernike coefficients described the corneal wavefront aberration function mode by mode. In this form, individual components of the wavefront aberration could be compared to the corresponding aberration for the whole eye.

7.2.4 Shack-Hartmann measurements and data processing

The S-H apparatus is described in detail in Chapter 6 and in a recently published article (Salmon &

Thibos, 1998). A schematic diagram of the S-H wavefront sensor is shown in Fig. 6.2, and photographs are included in Appendix G. The major components of the apparatus included the following:

- Helium-neon laser light source (632.8 nm, 10 mW)
- Spatial filter (8-mm focal length, 25- μ m pinhole)
- Microlenslet array (400 μ m square lenslets, 24 mm focal length; product no. MLM 0400-24-S-1, Adaptive Optics Associates)
- Scientific grade, cooled, slow-scan camera (Kodak KAF 1400 sensor, 6.8 μ m square pixels in 1340 5 1037 array; product no. MCD600, SpectraSource Instruments)

The S-H device is designed to form an image of the illuminated spatial filter (25 μ m) pinhole on the retina, and this becomes the source of light that is reflected out of the eye, thereby allowing measurement of its aberrations. The quality of the spot on the retina was optimized by limiting the entry beam diameter to 2 mm by aperture A1, correcting the subject's spherical refractive error using lens Rx, and by fine tuning the focus with lens L2. A pellicle beam splitter (8% reflectance, 92% transmittance) near the eye reflected the beam into the eye.

The S-H principle has been described in detail in several recent articles (Liang, *et al.*, 1994; Liang & Williams, 1997; Liang, *et al.*, 1997; Salmon & Thibos, 1998). As represented in Fig. 6.1 (top), the optical system transfers the wavefront of light exiting the eye's entrance pupil to the plane of a microlenslet array. Each lenslet focuses a portion of the wavefront onto the camera sensor, forming an image of the retinal spot there. From the location of the image spot, the angular tilt of the ray joining the lenslet center and spot image (angle θ in Fig. 6.1), maybe be computed. This angle is equal to the local wavefront slope in the lenslet. The wavefront incident on the lenslet array was an unmagnified image of the wavefront exiting the eye's entrance pupil. Thus the S-H sensor directly measures the wavefront slopes at discrete locations in the pupil. The two-dimensional array of slope values were numerically integrated to give wavefront heights at those locations.

Raw S-H data collected by the camera consisted of an image with an array of spots (Fig. 6.4a and 6.4d). These were analyzed by computer to locate the centroid of each spot, and from this, the wavefront slopes and wavefront heights were computed at approximately 200 discrete locations in the pupil. As was done with the corneal wavefront data, ocular wavefront height data were fitted to Zernike polynomials up to the tenth order, and the Zernike coefficients summarized the shape of the ocular wavefront aberration mode by mode.

Prior to making measurements, a laser power meter verified that the power entering the eye was

less than $6 \mu\text{W}$, which is two log units below the American National Standards Institute (Sloney & Wolbarsht, 1981; ANSI, 1993; Matthews & Garcia, 1995) maximum permissible exposure (See Appendix H). The subject mounted a bite bar, and his right eye position and orientation were adjusted so that the primary line of sight coincided with the optic axis of the S-H sensor. The camera and laser shutters were synchronized for 1-2-second exposure times and five images were taken of each eye. No cycloplegic or dilating drops were used, and measured pupil diameters were 5.6 mm for two subjects and 5.2 mm for one subject (see Table 7.1).

7.2.5 Comparison of Zernike modes

The end products of data processing were two sets of Zernike coefficients—one describing the wavefront aberration function of the cornea and another describing the wavefront aberration for the whole eye. The human eye consists of multiple refracting surfaces, but for this project I chose to analyze the optical system as a linear sum of just two major components: 1) the front surface of the cornea and 2) the remaining internal optics. Most studies have assumed that the internal (non-corneal) optics are entirely provided by the crystalline lens, but the posterior corneal surface and vitreous body probably also play a minor role. I have therefore avoided calling the non-corneal optics “lenticular”; rather I refer to that component as the “internal optics.” Both the corneal wavefront aberration and ocular wavefront aberration were specified in the plane of the eye’s entrance pupil, therefore the third set of Zernike coefficients, describing the internal aberrations, were computed by subtracting the corneal coefficients from the corresponding ocular coefficients for each mode.

A generally accepted numbering scheme for the Zernike polynomials has not been established, but for this study I followed the ordering recommended in by Thibos and the Optical Society of America committee that is currently planning standards for the specification and measurement of ocular aberrations (Malacara, 1992; Thibos, 1999). The first 21 modes, their Cartesian formulas and descriptions were summarized in Table 2.1. In this scheme, the zero-order aberration is piston, which is labeled as mode 1. The first order aberrations are the two prism terms, labeled modes 2 and 3. The second order aberrations include astigmatism (modes 4 and 6) and defocus (mode 5). Zernike orders 3-10 encompass modes 7-66, which I refer to as the higher order aberrations. Although some of these terms have familiar labels, such as coma (modes 8 and 9) and spherical aberrations (mode 13), the Zernike terms are not the same as the classic Seidel aberrations of the same name. In addition, many of the higher order aberrations have no corresponding term in the classic Seidel set.

I was primarily interested in studying the relationship between corneal and internal higher order aberrations (orders 7-10). The lower order terms for piston, prism and defocus were removed prior to analysis. Astigmatism, contained in Zernike modes 4 and 6, is included in some of the analyses which

follow. It is a familiar clinical entity, and the Zernike coefficients can be converted to the equivalent ophthalmic prescription by the procedure outlined in Chapter 2, Section 2.4.5.

7.3

RESULTS

7.3.1 Corneal aberrations

a. Quality of the data

The quality of the corneal wavefront data can be judged by the instrument's accuracy, repeatability and closeness of the Zernike polynomial fit to the original data. From the EyeSys accuracy study summarized in Chapter 4, I concluded that this instrument allowed me to measure the corneal wavefront aberration function with an error of less than $\lambda/7$ across most of the pupil. Repeatability, expressed as the radially averaged standard error was shown in Fig. 5.10 and discussed in Section 5.3.1. Measurement variability increased from the pupil center to the periphery with a standard error of $< 0.05 \mu\text{m}$ near the center and approximately $0.6 \mu\text{m}$ at 2.8 mm from the pupil center. If the confidence interval for the mean surface elevation is defined as ± 2 standard errors, at the edge of the pupil where variability was largest, the confidence interval was $\pm 1.2 \mu\text{m}$. This means that the confidence interval for the corneal wavefront aberration computed from mean EyeSys sags was $\pm 2/3 \lambda$ or better across the measured pupil. Mean interpolated corneal wavefront data were fitted to Zernike polynomials for later comparison with the corresponding coefficients derived from S-H measurements. Closeness of the Zernike fitting of corneal data was presented in Table 5.6, which showed that the RMS difference (Eq. 7-17) between the input wavefront data (W_d) and the wavefront described by the Zernike coefficients (W_z). The RMS difference was $\lambda/20$ or less for all subjects. The quality of the Zernike polynomial fit was also indicated by the close agreement in wavefront variances for the input wavefront data and the wavefront reconstructed by Zernike polynomials.

$$\text{RMS} = \sqrt{\frac{1}{n} \sum^n (W_d - W_z)^2} \quad (7-17)$$

b. Magnitude of the corneal wavefronts

Table 7.2 lists parameters which describe the magnitude of the corneal aberrations for the three subjects. Total aberrations and the major subcomponents, astigmatism and higher order aberrations, are quantified by their wavefront variances (upper number) and peak-to-valley wavefront errors (parentheses). Total aberration magnitudes were within the range expected for normal corneas, with wavefront variances less than $2 \lambda^2$, and peak-to-valley aberrations less than 7λ . Figure 5.13 showed gray scale and surface

plots of the total corneal wavefront aberrations. In all subjects, astigmatism accounted for most of the total wavefront variances, and higher order aberrations were relatively small. Corneal astigmatism for each subject, expressed in clinical minus cylinder notation, was listed in Table 5.8 and will be discussed in more detail in section 7.3.3.

TABLE 7.2 Magnitude of the corneal wavefront aberration for three normal eyes, expressed as wavefront variance (λ^2 ; upper number) and peak-to-valley wavefront error (λ ; parentheses).

Subj	Pupil	Wavefront aberration component		Total
		Astigmatism	Higher order	
AB	5.6	1.41 (5.78)	0.21 (2.62)	1.62 (6.87)
DH	5.2	0.35 (2.86)	0.09 (1.84)	0.44 (4.67)
LT	5.6	0.36 (2.90)	0.19 (2.83)	0.55 (4.82)

Corneal higher order wavefront variances were approximately $0.2 \lambda^2$ or less and peak-to-valley errors were less than 3λ . Gray scale and surface plots for the higher order aberrations were shown in Fig. 5.14. These relatively small aberrations are analyzed further in Fig. 7.3 (same as Fig. 5.15), which shows the breakdown of higher order aberrations per Zernike order. In all three subjects, over 95% of the higher order aberrations were contained in Zernike orders 3 and 4, though the mix between these orders varied with each subject. In these normal subjects, there was an abrupt drop-off in aberrations beyond the fourth order. Figure 5.19 showed contour plots of major subcomponents of the higher order aberrations. The overall shape of the higher order wavefront aberration and its subcomponents was different for each subject. Tables 5.9-11 provided additional analyses of the higher order corneal wavefront aberrations.

7.3.2 Ocular aberrations

a. Quality of the data

As with the corneal data, quality of the ocular (S-H) wavefront data can be judged by the instrument's accuracy, repeatability and closeness of the Zernike polynomial fit to the input wavefront data. Accuracy of the S-H technique was described in Chapter 6, and depending on the shape of the wavefront, the RMS measurement error for these pupil sizes was between $\lambda/6$ and $\lambda/2$. Repeatability is illustrated by the contour plots in Fig. 7.4, which shows the standard errors for repeated measurements of each subject's total wavefront (left column) and for higher order aberrations only (right column). For AB and DH, standard

errors were $< \lambda/10$ for most of the pupil. For LT, when astigmatism was included, the maximum standard error near the pupil edge was approximately $\lambda/2$. For higher order aberrations alone it was $< \lambda/5$ across most of the pupil. Mean standard errors, averaged across the pupil, are summarized in Table 7.3. Quality of the Zernike polynomial fitting procedure was described by computing the RMS difference (Eq. 7-17) between the input wavefront data and the wavefront described by the Zernike coefficients for each image. The mean RMS fitting error for each subject is summarized in Table 7.4. The difference was less than or equal to $\lambda/10$ for all subjects. The quality of the Zernike polynomial fit is also indicated by the close agreement in wavefront variances between the input and Zernike reconstructed wavefront. Means for each subject are shown in Table 7.4.

TABLE 7.3 Mean standard error, in wavelengths, for repeated measurements of the wavefront aberration function for each subject. Piston, tilt, defocus terms were removed from the wavefronts used in the “Astigmatism + higher” statistics on row one. Row two shows the repeatability after removal of astigmatism, leaving only the higher order aberrations.

Standard error (λ)	AB (n=5)	DH (n=5)	LT (n=4)
Astigmatism + higher	0.06	0.06	0.20
Higher order only	0.05	0.05	0.08

TABLE 7.4 Comparison of wavefronts reconstructed using 66 Zernike polynomials and input wavefront data. The mean RMS difference between the input wavefront data and wavefront reconstructed by Zernike coefficients, in wavelengths ($\lambda=633$ nm), is listed for each subject. The ratio of the reconstructed wavefront variance to the original wavefront data variance is also shown.

Statistic	AB	DH	LT
RMS difference: reconstructed vs actual wavefront (λ)	0.07	0.10	0.09
Ratio of wavefront variances	1.00	.98	1.00

b. Magnitude of the ocular wavefronts

Table 7.5 summarizes the magnitude of the ocular aberrations measured by the S-H wavefront sensor. Total aberrations and its major subcomponents, astigmatism and higher order aberrations, are quantified by their wavefront variances (top number) and peak-to-valley wavefront errors (parentheses below). Total ocular wavefront variances were less $1 \lambda^2$, and the peak-to-valley magnitudes were less than 5λ . Figure 7.5 gives a qualitative feel for the wavefront aberrations (astigmatism included) by presenting

contour and surface plots for each subject.

Higher order aberrations for the whole eye has less than $0.2 \lambda^2$ wavefront variance, and the peak-to-valley interval was less than 3λ . The shapes of these wavefronts are illustrated in the gray scale and surface plots of Fig. 7.6. Higher order aberrations are analyzed further in Fig. 7.7, which shows the distribution of wavefront variances across Zernike orders 3-10. The relative mix of aberrations within the different orders varies with each subject. For AB, 95% of the higher order aberrations are contained in orders 3 and 4, while for DH and LT the fifth order must be included to account for 85% and 84% of the aberrations respectively. Sixth and seventh order aberrations are larger in the whole eye than for the cornea alone (Fig. 7.1). The radially averaged modulation transfer function (MTF), derived from the S-H higher order wavefront aberrations are shown in Fig. 7.8. MTF's were similar in magnitude to those reported in other studies for similarly sized pupils. Figure 7.9 shows point spread functions (PSF) derived from the higher order wavefront aberration for each subject, along with a diffraction limited PSF (Airy disk) for comparison. Strehl ratios were 0.085 for AB, 0.082 for DH and 0.10 for LT.

TABLE 7.5 Magnitude of the ocular wavefront aberration measured using the S-H wavefront sensor, expressed as wavefront variance (λ^2 ; upper number) and peak-to-valley interval (λ ; parentheses).

Subj	Pupil	Wavefront aberration component		Total
		Astigmatism	Higher order	
AB	5.6	0.26 (2.44)	0.14 (1.86)	0.40 (3.49)
DH	5.2	0.04 (0.96)	0.19 (2.97)	0.23 (2.74)
LT	5.6	0.73 (4.17)	0.06 (1.71)	0.79 (4.84)

7.3.3 Comparison of corneal and ocular astigmatism

Prior to studying the role of the cornea in the higher order aberrations of the eye, I examined the relationship between corneal and ocular astigmatism. This relationship is not difficult to determine using conventional clinical techniques, but I included this analysis for two reason. First, I wanted to see how data obtained by the newer techniques (videokeratography and S-H sensing) compared to that obtained by older methods (keratometry and clinical refraction). Also, it was helpful to quantify astigmatism in order to better appreciate the magnitude of higher order aberrations, which will be discussed later.

Table 7.6 compares the uncorrected refracted error for each subject, determined clinically, with that

obtained from the S-H apparatus. The refractions obtained by the two methods are in close agreement, but not identical. The difference may be partially explained by the fact that clinical refraction is a subjective technique in which the person must judge relative blur in 0.125 or 0.25 diopter increments. In contrast, the objective S-H technique requires no response from the subject and isn't limited to discrete steps. In addition, accommodation was paralyzed during the clinical measurements but not for the S-H measurements. Active accommodation could explain the more negative spherical refractive error seen in the S-H for subject AB, who is hyperopic and probably over-accommodates habitually. Given these differences, the close agreement between the clinical and S-H results, especially for astigmatism, reinforced my confidence in the S-H technique. Similar close agreement was found between keratometer and EyeSys estimates of corneal astigmatism, summarized in Table 5.8 (Chapter 5).

TABLE 7.6 Comparison of uncorrected refractive errors measured by subjective clinical refraction and by the S-H wavefront sensor. The S-H result takes into account a +0.875 diopter correcting lens worn by LT during the measurement. Cycloplegia was used for the clinical refraction, but not for the S-H measurements.

Subject	Clinical refraction	S-H refraction
AB	+0.88 - 0.50 x 030	+0.01 -0.40 x 033
DH	+0.13 -0.38 x 088	-0.05 -0.16 x 075
LT	-0.63 -0.88 x 090	+0.19 -0.67 x 111

Traditionally, the relationship between corneal and ocular astigmatism has been summarized by Javal's rule, which predicts ocular astigmatism from keratometry based on the assumption that the eye's internal astigmatism has a value of -0.50 x 090 (Grosvenor & Ratnakaram, 1990; Horner, Salmon, & Soni, 1998). Having measured the corneal astigmatism with the EyeSys and ocular astigmatism with the S-H techniques, I was able to compute the internal astigmatism for each subject. This is shown in the right column of Table 7.7, which also lists the corneal astigmatism for each subject in the middle column. The values for the internal astigmatism are similar to that expected according to Javal's rule. In the case of astigmatism, perfect corneal/internal aberration balancing occurs when the corneal and internal astigmatism have equal power but opposite (perpendicular) axes. For subject DH, corneal and internal astigmatism nearly cancel each other out; for AB they also balance well, but for LT, corneal and internal astigmatism have similar axes and therefore compound.

TABLE 7.7 Comparison of corneal and internal astigmatism for each subject. Corneal astigmatism was computed from the mode 4 and 6 Zernike coefficients for EyeSys data. Internal astigmatism was computed by the difference of the corneal and ocular Zernike coefficients for modes 4 and 6.

Subj	Corneal astigmatism	Internal astigmatism
AB	-0.94 x 014	-0.68 x 093
DH	-0.54 x 175	-0.72 x 083
LT	-0.47 x 108	-0.21 x 116

7.3.4 Comparison of corneal and ocular higher order aberrations

The left half of Table 7.8 summarizes the relationship between corneal and ocular higher order aberrations by comparing their wavefront variances and by showing the percentage of change between them. When internal aberrations balance and reduce the effect of corneal aberrations, ocular aberrations are smaller than those of the cornea. Such cases are indicated by bold text in Table 7.8. This also indicated by a negative percentage of change in wavefront variance from the cornea (Var_c) to eye (Var_e), where percentage of change is defined as:

$$\% \Delta = (\text{Var}_c - \text{Var}_e) / \text{Var}_c \times 100 \quad (7-18)$$

When the ocular wavefront variance is larger than the corneal variance, the internal aberrations add to and compound the corneal aberrations. This is indicated by a positive change in wavefront variance from the cornea to the eye. For comparison, the relationship between corneal and ocular wavefront variances when astigmatism is included, is shown in the right half of Table 7.8.

Table 7.8 shows that not all of my subjects displayed effective aberration balancing between the cornea and internal optics for the higher order aberrations. Subjects AB and LT both show a decrease in higher order aberrations from the cornea to the whole eye. For them, internal aberrations, primarily from the crystalline lens, helped to offset corneal aberrations and improved overall optical performance for the whole eye. This balancing of higher order aberrations is partial for AB, reducing these aberrations by 33% ($0.21 \lambda^2$ corneal, $0.14 \lambda^2$ ocular). For LT the improvement is more significant, (68%) and this results in very low higher order aberrations for the whole eye (wavefront variance = $0.06 \lambda^2$). Subject DH showed 111% greater aberrations for the eye relative to the cornea, and this indicates that, for the higher order aberrations, an adverse balance exists in which the internal optics add to the aberrations of the cornea.

The relationship between corneal and ocular higher order aberrations, summarized by the wavefront

variances in Table 7.8 can be visualized by the wavefront aberration surface plots in Fig. 7.10. For AB and LT, the general shape of the corneal and ocular wave aberrations are similar, but the magnitudes of the ocular aberrations are slightly smaller. For DH, the ocular aberrations are larger and take on a different shape compared to the corneal wavefront. This shows that internal optics are adding aberrations, which were not present in the cornea.

TABLE 7.8 Comparison of corneal and ocular higher order aberrations. Data is presented in terms of wavefront variances and percentage of change from cornea to eye. A negative percentage indicates that internal aberrations reduce the effect of corneal aberrations on the aberrations of the whole eye. A positive percentage indicates that internal aberrations add to the aberrations of the cornea. Bold numbers indicate cases in which whole eye aberrations were less than aberrations for the cornea alone. A similar analysis for combined (astigmatism + higher order) aberrations is also shown.

Subj	Structure	Higher order aberrations		Astigmatism + higher order	
		W variance (λ^2)	aberration Δ (cornea to eye)	W variance (λ^2)	aberration Δ (cornea to eye)
AB	cornea	0.21		1.62	
	eye	0.14	- 33%	0.40	- 75%
DH	cornea	0.09		0.44	
	eye	0.19	+ 111%	0.23	- 48%
LT	cornea	0.19		0.55	
	eye	0.06	- 68%	0.79	+ 44%

The Zernike coefficients for the internal aberrations were computed by subtracting the corneal coefficients from the corresponding ocular coefficients. A complete list of the internal Zernike coefficients was included in Appendix F. The higher order wavefront variances for the internal optics were in the range of 0.1 to 0.2 λ^2 , which is similar in magnitude to the corresponding corneal and ocular aberrations; 70-80% of the internal aberrations were contained in the third and fourth Zernike modes, and all subjects had a mix of coma (modes 8 and 9) and triangular astigmatism (modes 7 and 10). In addition, LT had a large negative spherical aberration component, and DH had a large aberrations in modes 14 and 17.

Figure 7.11 illustrates the corneal/internal balance for higher order aberrations by plotting the Zernike coefficients, mode by mode for the corneal and internal optics. In these plots, optical aberrations for the whole eye are minimized when the corneal and internal coefficients have similar values but opposite

sign. Figure 7.11 top, shows that for subject AB, the larger corneal aberrations are contained in modes 7, 9, 10, 11, and 13. Among these, internal aberrations effectively balance most of the corneal aberration for mode 7 (triangular astigmatism) only. In mode 9 (coma), internal aberrations compensate for only about half of the large corneal aberration. Ineffective compensation for corneal aberrations is seen in modes 10, 11 and 13; in mode 8, internal aberrations exist where the corneal aberration is nearly zero. Internal aberrations above mode 10 are all comparatively small, though many of them show a good balance between corneal and internal aberrations. Overall, AB's internal higher order aberrations are small and only partially balance corneal aberrations.

For DH (Fig. 7.11 middle), modes 7 and 9 show effective corneal/internal aberration balancing, while mode 13 shows only partial balancing; an adverse balance is noted in mode 8. In general, the magnitude of the internal aberrations are larger than corneal aberrations, which are relatively small. In this case, several internal aberrations modes add aberrations to the eye, where none exist for the cornea (modes 10, 17, 20). Above the twenty-first mode, internal aberrations for DH appear to be larger than those seen in AB, and many of them are not well balanced with corneal aberrations. In comparison to AB, DH appears to have relatively poor corneal/internal balancing for higher order aberrations.

For LT (Fig. 7.11 bottom), most of the corneal aberrations are in the third and fourth orders (modes 7-15) and most are well balanced. The pattern continues among many of the modes above number 16. In a few modes, the cornea/internal balance is not good (18, 21), but in those the aberrations are small, and the net effect on total ocular aberrations is small. Overall LT appears to have very good corneal/internal aberration balancing.

For all three subjects relatively good aberration balancing was observed in modes 7 and 9 (triangular astigmatism and coma respectively). Beyond this the pattern varied with each subject.

7.4

DISCUSSION

This research was unique since it employed, for the first time, the new technologies of videokeratography and S-H wavefront sensing in combination, in an effort to study the optical structure of the human eye. My results provide new information about the optical aberrations of normal corneas, supplements the still limited literature on S-H measurements of normal eyes, and gives insight into the relationship between the corneal and internal optics of the eye.

7.4.1 The corneal wavefront aberration

Considering the pupil sizes which I used (5.6 and 5.2 mm), the overall magnitude of the corneal

higher order aberrations were within the expected range. Peak-to-valley wavefront errors were 2-3 λ and wavefront variances were approximately 0.1 to 0.2 λ^2 . This small sample of data from normal eyes is useful for comparison with corneal aberrations that may appear in abnormally shaped corneas, such as those with keratoconus or following refractive surgery. For example, a recent study (Oshika, *et al.*, 1999) that computed the corneal wavefront aberrations one year after refractive surgery, found that, for photorefractive keratectomy (PRK), the mean wavefront variances were 1.826 μm^2 (4.56 λ^2), and for laser in-situ keratomileusis (LASIK) it was 2.724 μm^2 (6.80 λ^2), for 7.0 mm pupils. My study used slightly smaller pupil sizes than this, so a direct comparison difficult. It is clear, however that, compared to the normal corneas I tested, corneal wavefront aberrations following refractive surgery were much greater.

Earlier research on corneal aberrations primarily focused on spherical aberration, probably because other aberrations were difficult to measure. In view of the sparse data on other cornea aberrations, my results provide valuable insight into the structure of higher order corneal aberrations. In the normal healthy eyes which I tested, essentially all of the higher order aberrations were confined to the third and fourth Zernike orders. The mix of third and fourth order aberration modes was different in each subject. Subject AB's dominant corneal aberrations, in order of importance, were coma (third order modes 8 and 9), primary spherical aberration (fourth order mode 13) and triangular astigmatism (third order modes 7 and 10). DH, on the other hand had very small corneal aberrations, primarily a minuscule amount of coma. For LT, corneal aberrations were dominated by primary spherical, with a small contribution from triangular astigmatism. No fourth order modes other than spherical aberration played a significant role in any of these eyes. With this knowledge, we can suspect an abnormal condition if we find significant corneal aberrations above the fourth order. Eighth and sixteenth order aberrations were observed in eyes that had undergone eight incision radial keratotomy (Schwiegerling, *et al.*, 1996), and fifth and sixth order aberrations were measured in patients following PRK and LASIK (Oshika, *et al.*, 1999).

Although the specific aberration components differed in each eye, the general shape of the wave aberrations of my subjects shared certain basic features. A mound of positive aberration was seen near the central 2 mm of the pupil. This was surrounded by an irregular annular valley of negative aberration, approximately 1 mm wide. The far periphery of the pupil showed a steep increase in positive aberrations (see Figs. 5.14 and 5.19). Generalizing from this limited sample, we can predict that normal corneal wavefront aberrations have a compressed Mexican hat-like shape, and may be decomposed primarily into a combination of non-rotationally symmetric third order aberrations (coma and triangular astigmatism) and symmetric fourth order spherical aberration. The relative mix of these components will vary from person to person, and we don't expect to see significant representation from other aberration modes.

7.4.2 The ocular wavefront aberration

The magnitude and general form of the higher order ocular wavefront aberrations for my subjects were similar to those measured by Liang, who pioneered the S-H technique in eye research (Liang, 1991; Liang, *et al.*, 1994; Liang & Williams, 1997; Liang, *et al.*, 1997). Like the cornea alone, ocular peak-to-valley wavefront errors were 2-3 λ , and wavefront variances were approximately $0.2 \lambda^2$.

Liang showed a steady decline in aberrations from the third to fourth Zernike orders, with markedly smaller aberrations beyond, but two of my subjects actually had greater aberrations in the fourth than the third orders. In the case of AB, this was due to the large primary spherical aberration, a fourth order mode. Two subjects (DH and LT) had a slightly larger relative contribution from fifth order aberrations than Liang reported for his subjects (Liang & Williams, 1997; Liang, *et al.*, 1997). Aberrations beyond the fifth order contributed little to the ocular higher order aberrations. As was noted in the cornea, the mix of individual aberrations for the whole eye differed for each subject. In the case of LT, individual ocular aberration modes were so small that it was difficult to identify a dominant aberration. DH's major aberration was mode 14, and he had a small amount of coma and triangular astigmatism. This limited sample suggests that the higher order aberrations of most normal eyes are composed of a mix of third and fourth order aberrations that vary from person to person.

7.4.3 The corneal/internal aberration balance

Earlier studies showed a variety of relationships between corneal and lenticular aberrations. Sometimes lenticular aberrations seemed to compensate for corneal aberrations (El Hage & Berny, 1973; Tomlinson, *et al.*, 1993), but there were also reports of corneal and lenticular aberrations compounding or adding (Millodot & Sivak, 1979; Tomlinson, *et al.*, 1993). While these studies evaluated aberrations within a single meridian, Artal and Guirao (Artal & Guirao, 1998) compared corneal and ocular aberrations across the entire pupil, based on videokeratoscopic and double-pass measurements. In all five of their subjects, the lens significantly compensated for the major corneal aberrations, with an average of 80% correction for cornea spherical aberrations and 50% correction for corneal coma.

My results did not show such a consistent pattern of aberration balancing; instead, each subject showed a different balance between cornea and internal aberrations. In terms of the overall change in wavefront variance, one subject showed a 68% reduction in aberrations from the cornea to the eye; another showed only a 33% improvement, and the third subject's ocular aberrations were approximately double those of the cornea alone. Interestingly, the subject (LT) who had an excellent cornea/internal aberration balance for higher order aberrations, had an adverse balance for astigmatism. On the other hand, the subject (DH) who had a very poor balance for higher order aberrations, had nearly perfect neutralization of the corneal astigmatism by his internal optics.

While Artal and Guirao’s results suggests that effective corneal/internal aberration balancing may be the norm, my results indicate greater variation between individuals. Differences in our results may be due to inter-subject variability and from differences in our methods. The S-H technique, which I used, directly measures local slopes of the aberrated wavefront exiting the eye, and data processing is straight forward. The double-pass approach is a more indirect way to obtain the wavefront aberration and requires complex, protracted data processing. Because of the difficulty in extracting the wave aberration from double-pass data, that technique is limited to analysis of smaller pupils, smaller aberrations and fewer Zernike modes. Artal paralyzed accommodation and used an artificial 4-mm pupil, but I used no cycloplegia and natural pupil sizes of 5.6 or 5.2 mm. Although both of our studies break new ground in corneal optics research, more work is needed for a more complete understanding of the optical components of the normal human eye.

7.4.4 Compensation for line of sight tilt

As described in the Methods section, I incorporated several steps to improve accuracy of the corneal wavefront aberration data obtained from EyeSys measurements. This included compensation for systematic videokeratoscope error (paragraph 7.2.3d), and correction for the slight angular misalignment between the subject’s line of sight and the videokeratoscope optic axis (paragraph 7.2.3e). A practical question is, Did compensation for the line of sight skew angle make a difference? To evaluate this, I recomputed the corneal wavefront aberration function for subject LT, who had the largest angle lambda (approximately 3 degrees), using a greatly simplified method that ignores the line of sight issue. Section 5.1.3 described the “surface aberration method,” for computing the corneal wavefront aberration (W). It is based on several approximations and can be reduced to the following simple formula, which also appeared as Eq. (5-20).

$$W = SQ(n-1) \tag{7-19}$$

Variable SQ represents the “surface aberration,” which I define as the sag difference between the corneal surface and a theoretical aberration-free cornea (a Cartesian oval); n is the corneal refractive index; for this calculation it was assumed to be 1.363. This computation takes no account of the line of sight tilt.

Table 7.9 lists the Zernike coefficients for selected modes of LT’s corneal wavefront aberration, and it compares the results when line of sight compensation was both included and ignored. As expected, differences (right column) for the tilt coefficients (shaded rows) are large, but for the other modes, the value of the Zernike coefficient changed by 0.01 or less. Note that this was for a 5.6 mm diameter pupil, and the differences would probably be larger for a larger pupil. Coefficients for all higher order modes not listed in Table 7.9 were essentially no different when computed with or without compensation for the line of sight

skew angle.

This analysis shows that, had I ignored line of sight tilt, it would have made little difference in my measurement of the higher order corneal aberrations, or my ultimate conclusion concerning the corneal/internal aberration balance.^a The maximum value for angle lambda among my subjects was 3.3 degrees (subject LT). Some articles report average values for angle lambda as large as 9 degrees (Mandell, *et al.*, 1995), so it would be interesting to see if the line of sight tilt could also be ignored in normal eyes with large angle lambdas. If so, it would greatly simplify computation of the corneal wavefront aberration from videokeratographic data.

TABLE 7.9 Comparison of subject LT's Zernike coefficients for selected modes when the corneal wavefront aberration was computed with and without compensation for line of sight tilt. As expected, coefficients for tilt (shaded rows) are significantly different. For other listed modes the difference was on the order of 0.01. For all higher order modes not listed, compensation for line of sight tilt made no significant (< 0.01) difference.

Zernike Mode no.	Description	Zernike coefficients		Difference (No comp - With comp)
		With LOS comp	No LOS comp	
1	Horizontal tilt	-0.16	0.06	0.22
2	Vertical tilt	-0.62	-0.40	0.23
4	45/135 astigmatism	0.35	0.34	-0.01
6	90/180 astigmatism	0.49	0.48	-0.01
7	Primary coma	-0.06	-0.07	-0.01
8	Primary coma	-0.14	-0.15	-0.01
13	Primary spherical	0.33	0.33	0.01
25	Secondary spherical	-0.01	0.01	0.01

7.4.5 Conclusion

Traditional spectacles do a good job of correcting defocus and astigmatism without severely upsetting the existing aberration structure of the eye. This, of course, depends on careful clinical

^a Subsequent reanalysis of this data lead to a different conclusion—that when angle lambda exceeds 2-3°, line of sight-videokeratoscope misalignment can lead to significant errors in the computation of corneal and internal wavefront aberrations. This is described in detail in the following article: Salmon, T.O. & Thibos, L.N. (2002). Videokeratoscope—line-of-sight misalignment and its effect on measurements of corneal and internal ocular aberrations. *J Opt Soc Am A*, **19**, 657-669. An electronic reprint of this article is available at the following web address: <http://arapaho.nsuok.edu/~salmonto/JOSAA0402.pdf>.

Chapter 7: Corneal Contribution to the Wavefront Aberration of the Eye

measurements of each eye's refractive error. On the other hand, current refractive surgeries haphazardly alter corneal higher order aberrations, while attempting to correct defocus and sometimes astigmatism. The result can be a noticeably reduced optical quality, especially with large pupils, and in reduced lighting. An important step toward improving refractive surgeries is a better understanding of the normal eye's aberration structure and the effect of corneal changes on the aberrations of the whole eye. My study has shown that we cannot presume to know the aberration structure of the internal eye based on corneal surface measurements alone. Klein (Klein, 1998) proved that it is not even necessary to know the corneal topography to compute the ideal aberration-free PRK ablation profile. All that is required is a knowledge of the wavefront aberration for the entire eye and, as is true with spectacle prescriptions, I have shown that this must be measured individually. Recent improvements in corneal topographers have made it feasible to measure the *corneal* wavefront aberration function as a part of normal clinic eye care, especially for refractive surgery patients. Hopefully, it won't be long before new clinical instruments are developed which can, quickly and conveniently, measure the wavefront aberration of the whole eye as well.

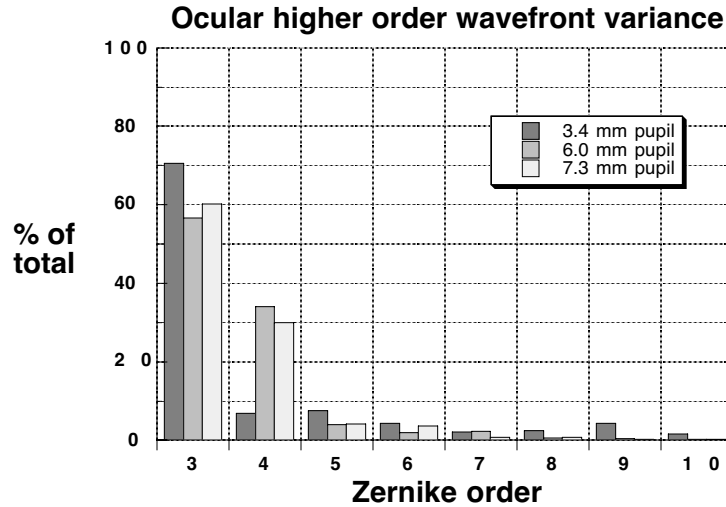


Figure 7.1

Data extracted from two articles [Liang & Williams, 1997; Liang, Williams, & Miller, 1997) shows the distribution of ocular wavefront variances, by Zernike order, measured by a Shack-Hartmann sensor for three pupil sizes. See text for computation of the data shown here.

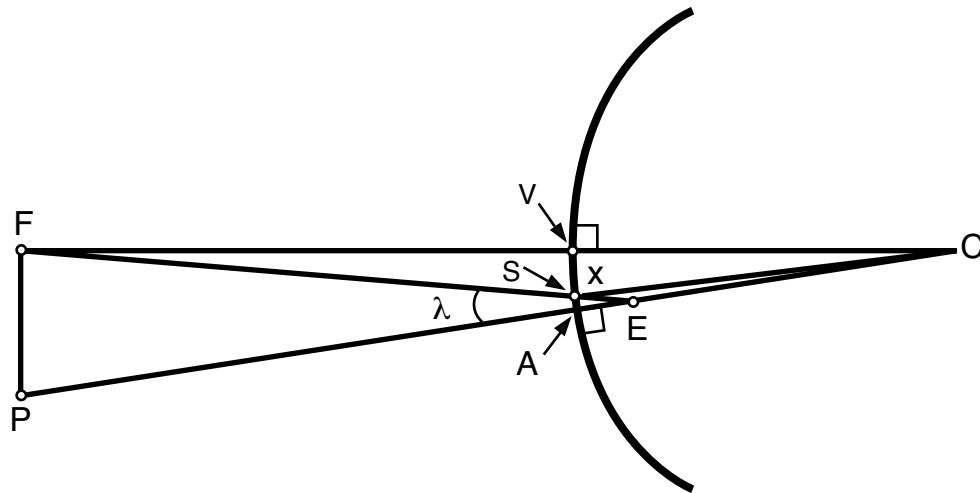


Figure 7.2

During standard videokeratoscope alignment, the patient fixates a light at the center of the keratoscope (F) while the instrument axis (FC) is aligned normal to the cornea. The line of sight (FE) connects the fixation point with the entrance pupil center (E). The pupillary axis is the line which is normal to the cornea, and which passes through the entrance pupil center. Point C represents the corneal center of curvature. The corneal wavefront aberration and corneal topography measurements should be centered on the line of sight, but if angle lambda (λ) is not zero, as shown, the line of sight will be displaced. The point where the line of sight intersects the corneal surface is called the corneal sighting center (S). Distance x is the distance from the keratoscope axis to the corneal sighting center (S).

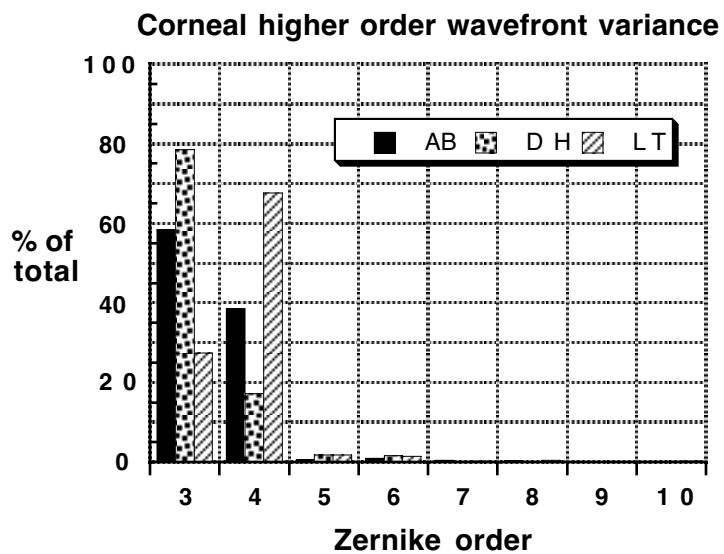


Figure 7.3
Breakdown of corneal wavefront variances contained in Zernike orders 3-10 for three subjects.

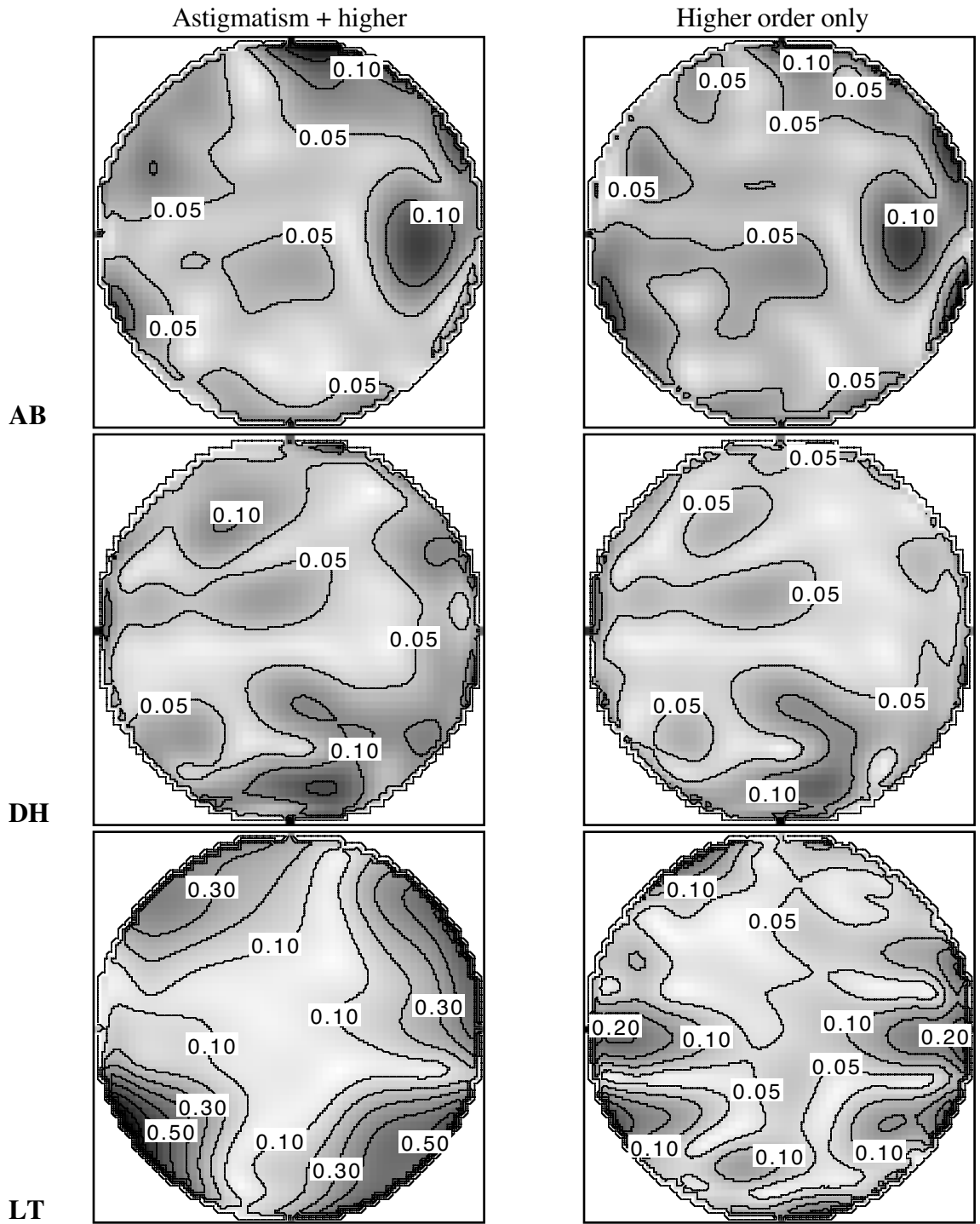


Figure 7.4

Contour plots showing the standard error for multiple Shack-Hartmann measurements for AB ($n = 5$), DH ($n = 5$) and LT ($n = 4$). The left column shows repeatability when astigmatism and higher order aberrations were measured. Astigmatism was removed for the right column plots. Contours lines indicate $0.05\text{-}\lambda$ or $0.1\text{-}\lambda$ intervals.

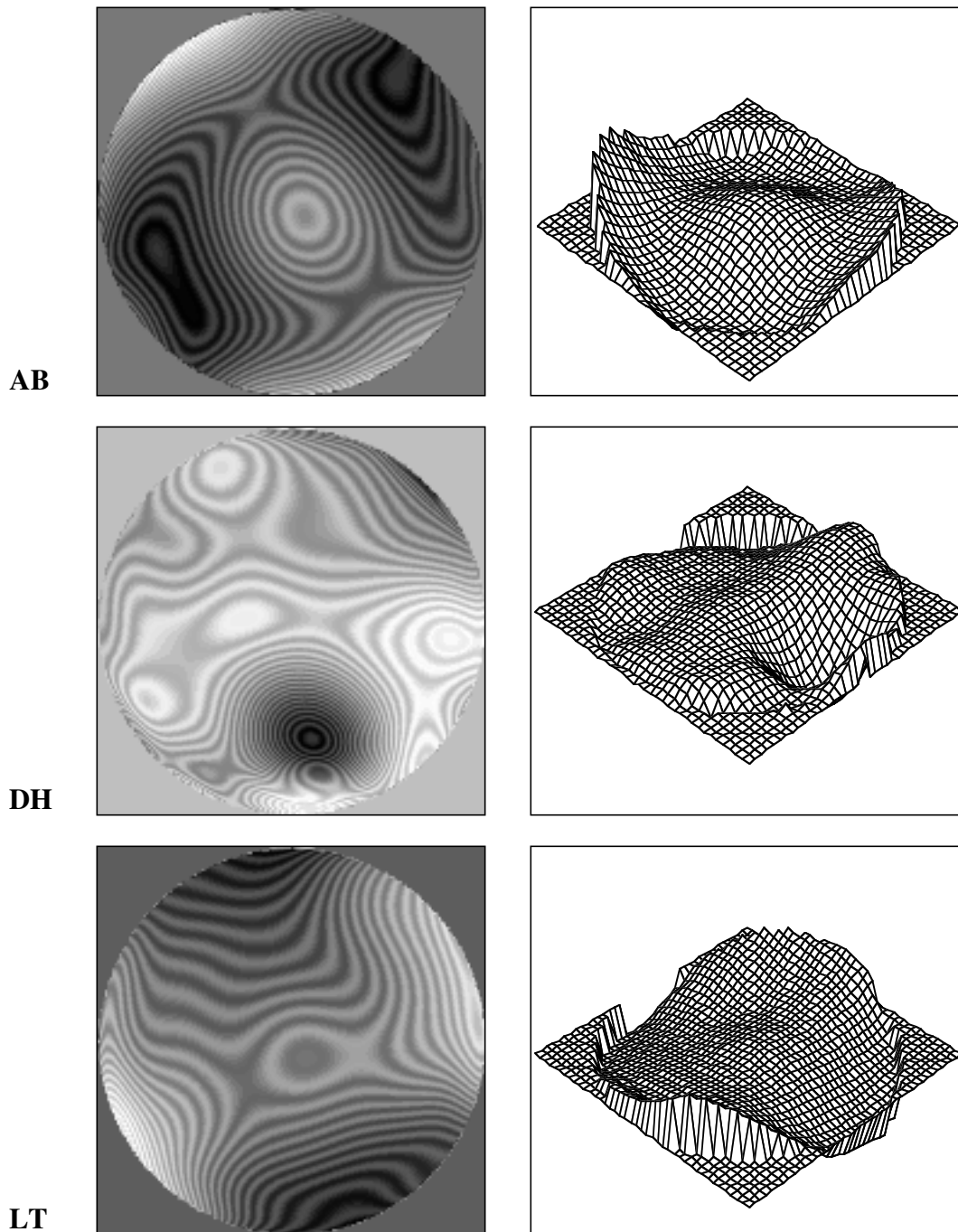


Figure 7.5

Contour and surface plots showing the ocular wavefront aberration function measured by the Shack-Hartmann sensor. Wavefronts were reconstructed from mean Zernike coefficients fitted to raw data. Piston, tilt and defocus were removed. Astigmatism and third through tenth Zernike order aberrations are included. Pupil sizes were 5.6 mm for AB and LT; 5.2 mm for DH.

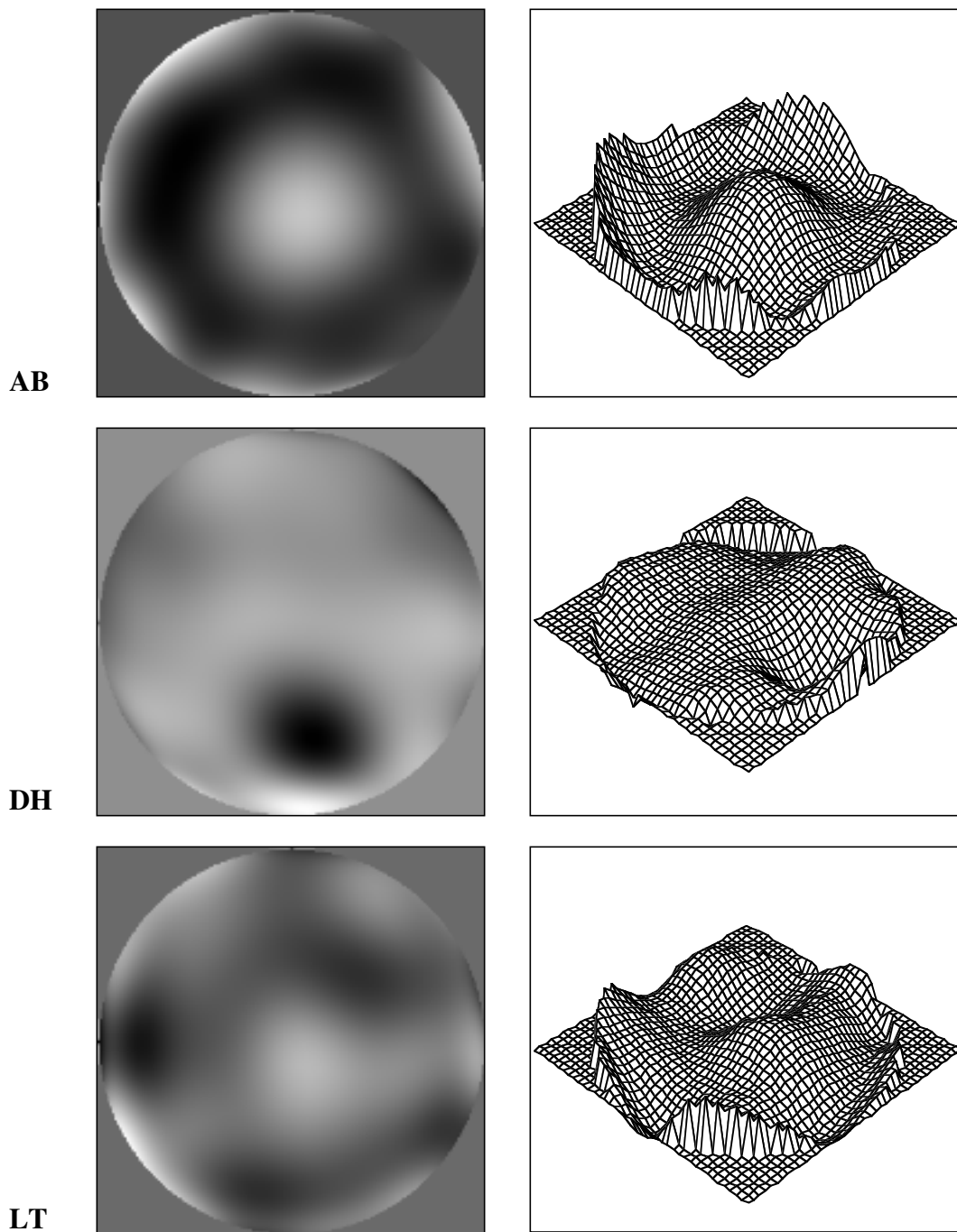


Figure 7.6

Contour and surface plots showing higher order ocular aberrations measured by the Shack-Hartmann sensor. Wavefront were reconstructed from mean Zernike coefficients fitted to raw data. Piston, tilt, defocus and astigmatism were removed, leaving only third through tenth Zernike order aberrations. Pupil sizes were 5.6 mm for AB and LT; 5.2 mm for DH.

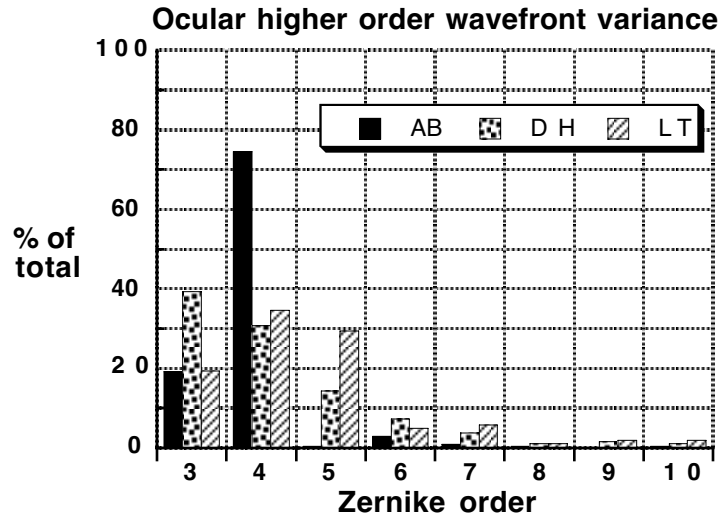


Figure 7.7
Breakdown of ocular higher order wavefront variances contained in Zernike orders 3-10 for three subjects.

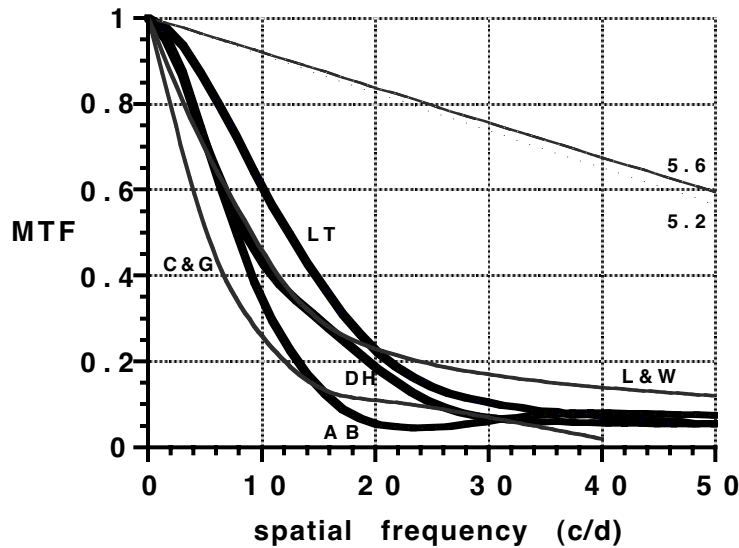


Figure 7.8
Radially averaged modulation transfer functions (MTF's) computed from the ocular higher order wavefront aberration functions of subjects AB, LT (5.6-mm pupil) and DH (5.2-mm pupil). For comparison, MTF's from Liang and Williams' (1997) Shack-Hartmann data (5.5-mm pupil) and from Campbell and Gubish's (1966) double-pass data (5.8-mm pupil) are also shown. The upper straight lines indicate the diffraction limit for 5.6- and 5.2-mm pupils.

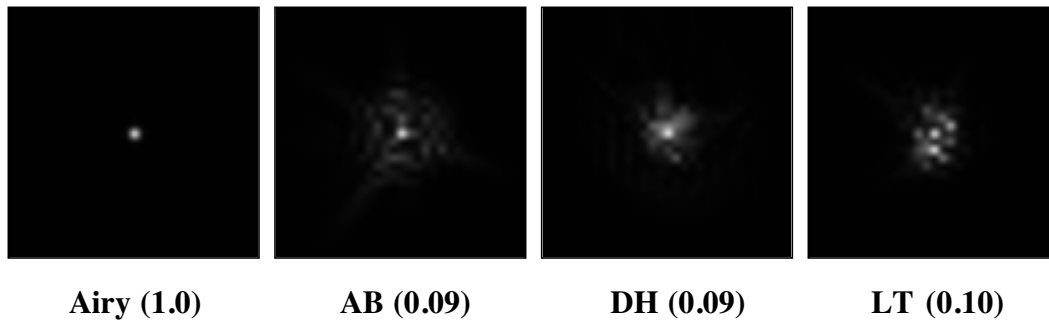


Figure 7.9

Airy disk (left) and point spread functions derived from ocular higher order wavefront aberrations for subjects AB, DH and LT. The Airy disk has diameter of approximately 1 arc minute (5.6-mm pupil) and the windows are approximately 16 arc minutes wide. Numbers indicate Strehl ratios.

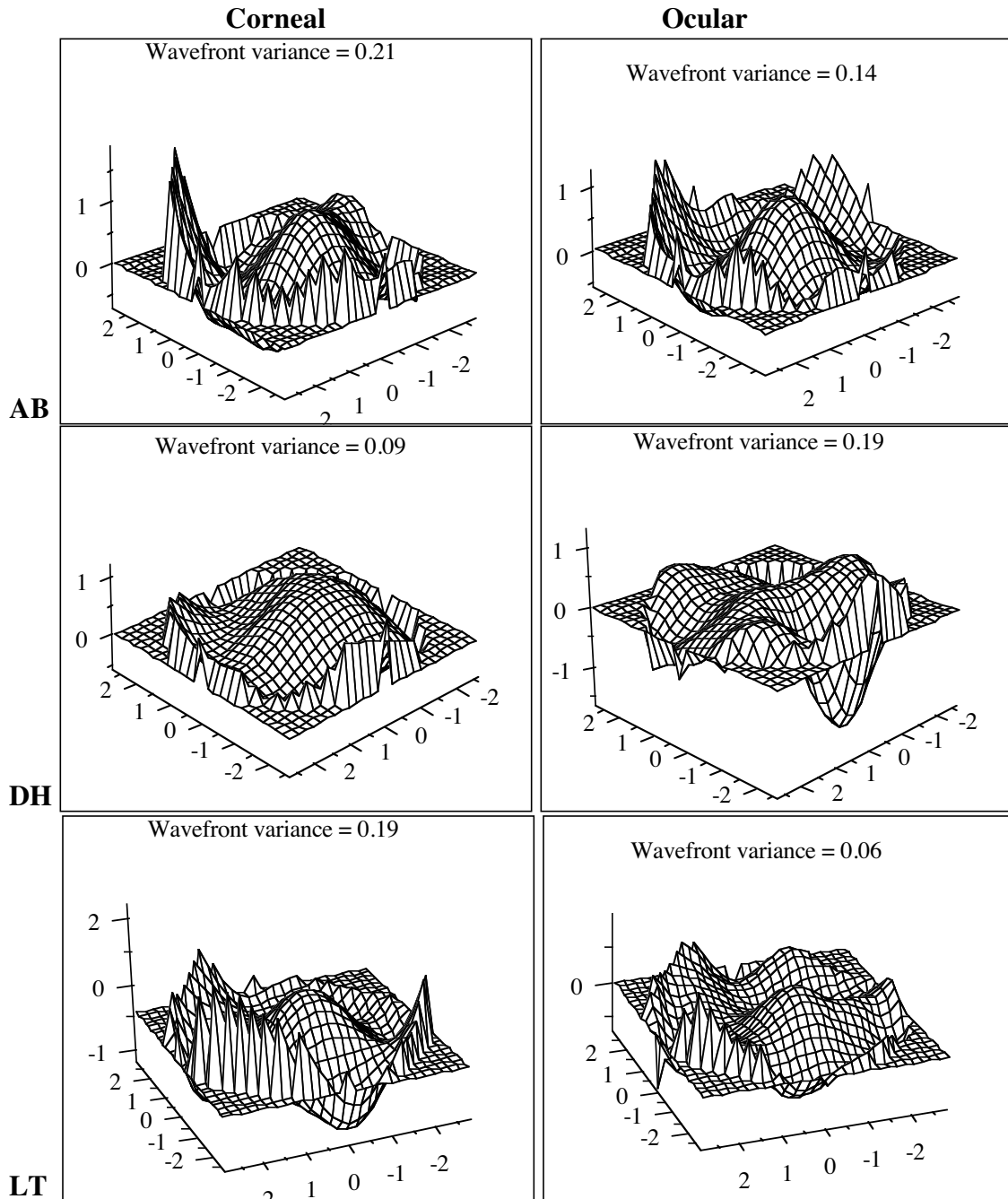


Figure 7.10

Surface plots comparing corneal and ocular higher order aberrations. For AB and LT, corneal and ocular aberrations are partially balanced, so ocular aberrations are smaller. For DH, corneal and internal aberrations compound, so ocular aberrations are greater than corneal aberrations.

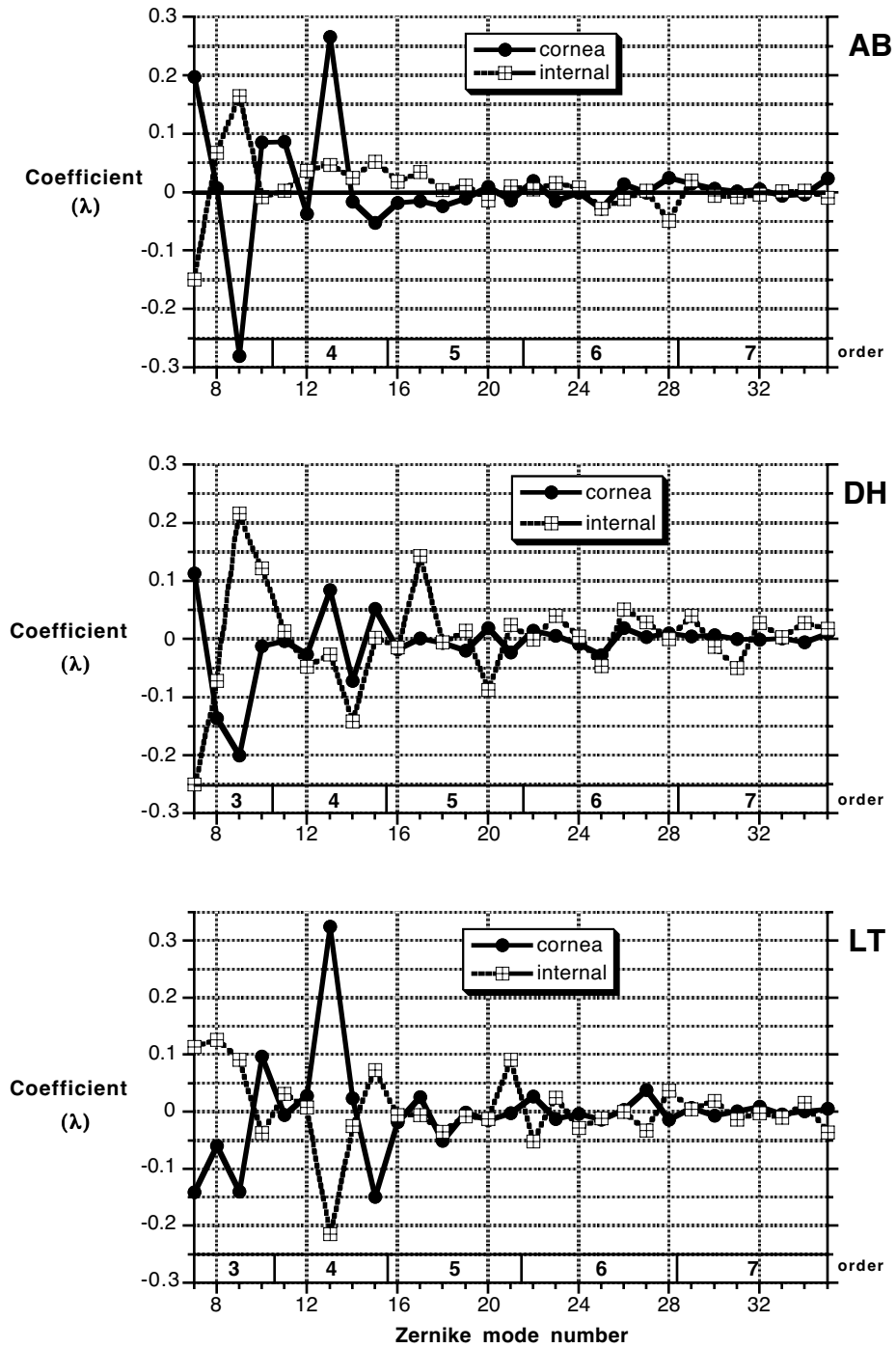


Figure 7.11

Mode by mode comparison of corneal and internal Zernike coefficients for three subjects, for orders 3-7. The magnitude of coefficients for higher orders are small and comparable to those in the seventh order shown here.

References

Aiello, L. (1994). Diagnosis, management, and treatment of nonproliferative diabetic retinopathy and macular edema. In Albert, D., & Jakobiec, F. (Ed.), *Principles and practice of ophthalmology* (pp. 747-60). Philadelphia: W.B. Saunders Company.

ANSI (1993). *American National Standard for the Safe Use of Lasers* New York. Orlando, FL.: American National Standards Institute. Laser Institute of America.

Applegate, R. (1992). Optical and Clinical Issues in the Measurement of Corneal Topography. *Ophthal and Vis Optics Tech Digest (OSA)*, **3**, 19-23.

Applegate, R. (1994). Comment: Inherent Error in Corneal Topography/Roberts. *J Refract Corneal Surg*, **10**, 113-114.

Applegate, R., Hilmantel, G. & Howland, H. (1996). Corneal Aberrations Increase with the Magnitude of Radial Keratotomy Refractive Correction. *Optom Vis Sci*, **73**, 585-9.

Applegate, R. & Howland, H. (1995). Noninvasive measurement of corneal topography. *IEEE Eng Med Biol*, **1995**, 30-42.

Applegate, R., Howland, H., Buettner, J., Cottingham, A., Sharp, R. & Yee, R. (1994a). Changes in the Aberration Structure of the RK Cornea from Videokeratoscopic Measurements. *Invest Ophthalmol Vis Sci*, **35**, 1740.

Applegate, R., Howland, H., Buettner, J., Cottingham, A., Sharp, R. & Yee, R. (1995a). Radial Keratotomy (RK), Corneal Aberrations and Visual Performance. *Invest Ophthal Vis Sci*, **36**, S309.

Applegate, R., Howland, H., Buettner, J., Cottingham, A., Sharp, R. & Yee, R. (1994b). Corneal Aberrations Before and After Radial Keratotomy (RK) Calculated From Videokeratometric Measurements. *Vision Science and its*

Applications, 1994 Technical Digest Series, 2, 58-61.

Applegate, R., Howland, H., Sharp, R., Cottingham, A. & Yee, R. (1998). Corneal Aberrations and Visual Performance After Radial Keratotomy. *J Refr Surg*, **14**, 397-407.

Applegate, R., Nunez, R., Buettner, J. & Howland, H. (1995b). How Accurately Can Videokeratographic Systems Measure Surface Elevation? *Optom Vis Sci*, **72**, 785-92.

Applegate, R., Thibos, L., Bradley, A., Marcos, S., Roorda, A., Salmon, T. & Atchison, D. (2000 (In press)). Reference axis selection: A subcommittee report of the OSA working group to establish standards for the measurement and reporting of the optical aberration of the eye. *Visual Science and Its Applications, Technical Digest Series, 2000*—in press.

Arffa, R., Warnicki, J. & Rehkopf, B. (1989). Corneal topography using rasterstereography. *Refr Corneal Surg*, **5**, 414-29.

Artal, P. & Guirao, A. (1998). Contributions of the cornea and lens to the aberrations of the human eye. *Optics Letters*, **23**, 1713-1715.

Artal, P., Ignacio, I. & Lopez-Gil, N. (1995a). Double-pass measurements of the retinal-image quality with unequal entrance and exit pupil sizes and the reversability of the eye's optical system. *J Opt Soc Am A*, **12**, 2358-66.

Artal, P., Marcos, S., Navarro, R. & Williams, D. R. (1995b). Odd aberrations and double-pass measurements of retinal image quality. *J Opt Soc Am A*, **12**, 195-201.

Atchison, D., Collins, M., Wildsoet, C., Christensen, J. & Waterworth, M. (1995). Measurement of monochromatic ocular aberrations of human eyes as a function of accommodation by the Howland Aberroscope technique. *Vis Res*, **35**, 313-23.

Atchison, D. A. (1984). Visual optics in man. *Aust J Optom*, **67**, 141-50.

Baker, T. (1943). Ray Tracing Through Non-Spherical Surfaces. *Proc Phys Soc*, **55**, 361-364.

Barsky, B., Klein, S. & Garcia, D. (1997). Gaussian Power with Cylinder Vector Field Representation for Corneal

- Topography Maps. *Optom Vis Sci*, **74**, 917-925.
- Belin, M., Cambier, J., Nabors, J. & Ratliff, C. (1995). PAR Corneal Topography System (PAR CTS): The Clinical Application of Close-Range Photogrammetry. *Optom Vis Sci*, **72**, 828-37.
- Benjamin, W. & Rosenblum, W. (1992). Radii of Curvature and Sagittal Depths of Conic Sections. *Int Cont Lens Clin*, **19**, 76-83.
- Bennett, A. (1988). Aspherical and continuous curve contact lenses. *Optom Today*, **28**, 238-242.
- Bennett, A. & Rabbetts, R. (1989a). *Clinical Visual Optics* (2nd ed.) London: Butterworths.
- Bores, L. (1997). Corneal topography central home page. Kerametrix Corporation web page, www.getnet.com/~labores/topotoc.html:
- Born, M. & Wolf, E. (1980). *Principles of Optics* (6th (corrected) ed.) Oxford: Pergamon Press.
- Bour, L. (1980). MTF of the defocused optical system of the human eye for incoherent monochromatic light. *J Opt Soc Am*, **70**, 321-328.
- Bullimore, M., Olson, M. & Maloney, R. (1999). Visual Performance After Photorefractive Keratectomy With a 6-mm Ablation Zone. *Am J Ophthalmol*, **128**, 1-7.
- Burek, H. & Douthwaite, W. A. (1993). Mathematical models of the general corneal surface. *Ophthalm. Physiol. Opt.*, **13**, 68-72.
- Camp, J. J., Maquire, L. J., Cameron, B. M. & Robb, R. A. (1990). A computer model for the evaluation of the effect of corneal topography using rasterstereography. *Refract Corneal Surg*, **5**, 414-417.
- Campbell, F. W. & Gubisch, R. W. (1966). Optical quality of the human eye. *J Physiol*, **186**, 558-78.
- Campbell, M., Bobier, W. & Roorda, A. (1995). Effect of monochromatic aberrations on photorefractive patterns. *J Opt Soc Am A*, **12**, 1637-46.

- Carney, L. & Henderson, B. (1993). Corneal Topography as a Function of Refractive Error. *Invest Ophthalmol Vis Sci*, **35**, 1217.
- Carney, L., Mainstone, J. & Henderson, B. (1997). Corneal Topography and Myopia. *Invest Ophthalmol Vis Sci*, **38**, 311-20.
- Charman, W. (1991). Wavefront Aberration of the Eye: A Review. *Optom Vis Sci*, **68**, 574-83.
- Churms, P. (1981). The sagitta of a toroidal surface in an oblique meridian. *Ophthalm Physiol Opt*, **1**, 29-38.
- Clark, B. (1973). Conventional Kertatoscopy - A Critical Review. *Aust J Optom*, **56**, 140-155.
- Cohen, K. L., Tripoli, N. K., Holmgren, D. E. & Coggins, J. M. (1995). Assessment of the power and height of radial aspheres reported by a computer-assisted keratoscope. *Am J Ophthalmol*, **119**, 723-732.
- Collins, M. J., Wildsoet, C. F. & Atchison, D. A. (1995). Monochromatic aberrations and myopia. *Vision Res*, **35**, 1157-1163.
- Doss, J. D., Hutson, R. L., Rowsey, J. J. & Brown, D. R. (1981). Method for Calculation of Corneal Profile and Power Distribution. *Arch Ophthalmol*, **99**, 1261-1265.
- Douthwaite, W. A. (1995). EyeSys corneal topography measurement applied to calibrated ellipsoidal convex surfaces. *Br J Ophthalmol*, **79**, 797-801.
- Douthwaite, W. A., Pardhan, S. & Burek, H. (1996). Extent and effect of surface tilt on the data display of the EyeSys videokeratoscope. *Br J Ophthalmol*, **80**, 986-993.
- Eghbali, F., Yeung, K. & Maloney, R. (1995). Topographic Determination of Corneal Asphericity and Its Lack of Effect on the Refractive Outcome of Radial Keratotomy. *Am J Ophthalmol*, **119**, 275-80.
- El Hage, S. & Berny, F. (1973). Contribution of the crystalline lens to the spherical aberration of the eye. *J Opt Soc Am*, **63**, 205-211.
- Emsley, H. (1946). Keratometry. In *Visual Optics* (pp. 298-324). London: Hatton Press Ltd.

- Freeman, M. (1990). *Optics* (10th ed.) London: Butterworths.
- Gauthier, C., Holden, B., Epstein, D., Tengroth, B., P, F. & Hamberg-Nyström, H. (1998). Assessment of High and Low Contrast Visual Acuity after Photorefractive Keratectomy for Myopia. *Optom Vis Sci*, **75**, 585-590.
- Ghaith, A. A., Daniel, J., Stulting, R. D., Thompson, K. P. & Lynn, M. (1998). Contrast sensitivity and glare disability after radial keratotomy and photorefractive keratectomy. *Archives of Ophthalmology*, **116**, 12-18.
- Goodman, J. (1996). *Introduction to Fourier Optics* (2nd ed.) New York: McGraw-Hill.
- Gormley, D., Gersten, M., Koplín, R. & Lubkin, V. (1988). Corneal Modeling. *Cornea*, **7**, 30-35.
- Gorrand, J. M. & Delori, F. (1995). A reflectometric technique for assessing photoreceptor alignment. *Vision Research*, **35**, 999-1010.
- Greivenkamp, J., Mellinger, M., Snyder, R., Schwiegerling, J., Lowman, A. & Miller, J. (1996). Comparison of Three Videokeratoscopes in Measurement of Toric Test Surfaces. *J Refr Surg*, **12**, 229-39.
- Grosvenor, T. & Ratnakaram, R. (1990). Is the relationship between keratometric astigmatism and refractive astigmatism linear? *Optom Vis Sci*, **67**, 606-609.
- Guirao, A., Gonzalez, C., Redondo, M., Geraghty, E., Norrby, S. & Artal, P. (1999). Average optical performance of the human eye as a function of age in a normal population. *Investigative Ophthalmology & Visual Science*, **40**, 203-213.
- Gullstrand, A. (1924). The Cornea. In Southall, J. (Ed.), *Helmholtz's Treatise on Physiological Optics* New York: Opt Soc Am.
- Gullstrand, A. (1966). Photographic-ophthalmometric and Clinical Investigations of Corneal Refraction. *Am J Optom Arch Am Acad Optom*, **43**, 143-214.
- Halliday, B. (1995). Refractive and visual results and patient satisfaction after excimer laser photorefractive keratectomy for myopia. *Brit J Ophthalmol*, **79**, 881-7.

- Halstead, M., Barsky, B., Klein, S. & Mandell, R. (1995). A Spline Surface Algorithm for Reconstruction of Corneal Topography from a Videokeratographic Reflection Pattern. *Optom Vis Sci*, **72**, 821-7.
- Hannush, S., Crawford, S., Waring, G., Gemmill, M., Lynn, M. & Nizam, A. (1989). Accuracy and Precision of Keratometry, Photokeratoscopy, and Corneal Modeling on Calibrated Steel Balls. *Arch Ophthalmol*, **107**, 1235-39.
- He, J., Marcos, S., Webb, R. & Burns, S. (1998). Measurement of the wave-front aberration of the eye by a fast psychophysical procedure. *J Opt Soc Am A*, **15**, 2449-2456.
- Heath, G., Gerstman, D., Wheeler, W., Soni, P. & Horner, D. (1991). Reliability and validity of videokeratoscopic measurements. *Optom Vis Sci*, **68**, 946-9.
- Hemenger, R., Garner, L. & Ooi, C. (1995). Change with age of the refractive index gradient of the human ocular lens. *Invest Ophthalmol Vis Sci*, **36**, 703-707.
- Hemenger, R., Tomlinson, A. & Caroline, P. (1997). Role of Spherical Aberration in Contrast Sensitivity Loss with Radial Keratotomy. *Invest Ophthalmol Vis Sci*, **30**, 1997-2001.
- Hemenger, R., Tomlinson, A. & Oliver, K. (1994). Corneal optics from videokeratographs. *Ophthalm Physiol Opt*, **15**, 63-68.
- Hilmantel, G., Blunt, R., Applegate, R. & Howland, H. (1997). Accuracy with which the TMS-1 Can Measure Elevations of Asymmetric Surfaces. *Invest Ophthalmol Vis Sci*, **38**, S850.
- Hilmantel, G., Blunt, R., Garret, B., Howland, H. & Applegate, R. (1999). Accuracy of the Tomey Topographic Modeling System in Measuring Surface Elevations of Asymmetric Objects. *Optom Vis Sci*, **76**, 108-114.
- Holladay, J. (1995). The Holladay Diagnostic Summary. In Gills, J., Sanders, D., Thonton, S., Martin, R., Gayton, J., Holladay, J., & Van Der Karr, M. (Ed.), *Corneal Topography - The State of the Art* (pp. 309-23). Thorofare, NJ: SLACK Incorporated.
- Holladay, J. & Waring, G. (1992). Optics and Topography of Radial Keratotomy. In Waring, G. (Ed.), *Refractive Keratotomy for myopia and astigmatism* (pp. 37-139). St. Louis: Mosby Year Book.

- Hopkins, H. (1950). Wave and Ray Aberrations. In *Wave Theory of Aberrations* (pp. 1-20). London: Oxford University Press.
- Horner, D. & Salmon, T. (1998). Accuracy of the EyeSys 2000 in Measuring Surface Elevation of Calibrated Aspheres. *Int Cont Lens Clin*, **25**, 171-177.
- Horner, D., Salmon, T. & Soni, P. (1998). Chapter 17: Corneal Topography. In Borish, I., & Benjamin, W. (Ed.), *Borish's Clinical Refraction* (pp. 524-558). Philadelphia: WB Saunders.
- Howland, H., Buettner, J. & Applegate, R. (1994). Computation of the Shapes of Normal Corneas and their Monochromatic Aberrations from Videokeratometric Measurements. *Vision Science and its Applications, 1994 Technical Digest Series*, **2**, 54-7.
- Howland, H. C. & Howland, B. (1977). A subjective method for the measurement of monochromatic aberrations of the eye. *J Opt Soc Am*, **67**, 1508-18.
- Iglesias, I., Berrio, E. & Artal, P. (1998). Estimates of the ocular wave aberration from pairs of double-pass retinal images. *J Opt Soc Am A*, **15**, 2466-2476.
- Iglesias, I., Lopez-Gil, N. & Artal, P. (1998). Reconstruction of the point-spread function of the human eye from two double-pass retinal images by phase-retrieval algorithms. *J Opt Soc Am A*, **15**, 326-339.
- Javal, E. (1890). *Mémoires d'ophtalmométrie* Paris: G Masson.
- Kiely, P., Smith, G. & Carney, L. (1982). The mean shape of the human cornea. *Optica Acta*, **29**, 1027-40.
- Kiely, PM., Smith, G. & Carney, L. (1984). Meridional variations of corneal shape. *Am J Optom Physiol Opt*, **61**, 619-626.
- Kinyoun, J., Barton, F., Fisher, M., Hubbard, L., Aiello, L. & Ferris, F. (1989). Detection of diabetic macular edema. *Ophthalmol*, **96**, 746-51.
- Klein, S. (1997a). Axial Curvature and the Skew Ray Error in Corneal Topography. *Optom Vis Sci*, **74**, 931-944.

- Klein, S. (1997b). Corneal Topography Reconstruction Algorithm that Avoids the Skew Ray Ambiguity and the Skew Ray Error. *Optom Vis Sci*, **74**, 945-962.
- Klein, S. (1997c). The Skew Ray Problem in Corneal Topography: Errors and Ambiguities. *Invest Ophthalmol Vis Sci*, **38**, S697.
- Klein, S. (1998). Optimal corneal ablation for eyes with arbitrary Hartmann-Shack aberrations. *J Opt Soc Am A*, **15**, 2580-2588.
- Klein, S. & Mandell, R. (1995). Axial and instantaneous power conversion in corneal topography. *Invest Ophthalmol Vis Sci*, **36**, 2155-59.
- Klein, S. A. (1992). A corneal topography algorithm that produces continuous curvature. *Optom Vis Sci*, **69**, 829-34.
- Klyce, S. D. (1984). Computer-Assisted Corneal Topography. *Invest Ophth & Vis Sci*, **25**, 1426-1435.
- Klyce, S. D. & Wilson, S. E. (1989). Methods of analysis of corneal topography. *Refract Corneal Surg*, **5**, 368-371.
- Koch, D. & Haft, E. (1993). Introduction to Corneal Topography. In Sanders, D. (Ed.), *An Atlas of Corneal Topography* (pp. 1-30). Thorofare, NJ: SLACK Incorporated.
- Lam, A. & Douthwaite, W. (1994). Derivation of corneal flattening factor, p-value. *Ophthal Physiol Opt*, **14**, 423-427.
- Lappin, P. (1968). Retinal Irradiances from the He-Ne CW Laser. *Am J Optom Arch Am Acad Optom*, **45**, 279-291.
- Lappin, P. (1970). Ocular Damage Thresholds for the Helium-Neon Laser. *Arch Environ Health*, **20**, 177-183.
- Last, R. (1968). *Anatomy of the Eye and Orbit* Philadelphia: WB Saunders Co.

- Liang, J. (1991). *A new method to precisely measure the wave aberrations of the human eye with a Hartmann-Shack-Wavefront-Sensor*. Ph.D. Thesis, University of Heidelberg.
- Liang, J., Grimm, B., Goelz, S. & Bille, J. F. (1994). Objective measurement of wave aberrations of the human eye with the use of a Hartmann-Shack wave-front sensor. *J Opt Soc Am A*, **11**, 1949-57.
- Liang, J. & Williams, D. R. (1995). Effect of higher order aberrations on image quality in the human eye. *OSA Technical Digest Series (Vision Science and Its Applications)*, **1**, 70-73.
- Liang, J. & Williams, D. R. (1997). Aberrations and retinal image quality of the normal human eye. *J Opt Soc Am A*, **14**, 2873-83.
- Liang, J., Williams, D. R. & Miller, D. T. (1997). Supernormal vision and high-resolution retinal imaging through adaptive optics. *J Opt Soc Am A*, **14**, 2884-92.
- Liou, H. & Brennan, N. (1996). The prediction of spherical aberration with schematic eyes. *Ophthal Physiol Opt*, **16**, 348-54.
- Lotmar, W. (1971). Theoretical Eye Model with Aspherics. *J Opt Soc Am*, **61**, 1522-9.
- Lundergan, M. (1992). The Corneoscope-Comparator Method of Hard Contact Lens Fitting. In Schanzlin, D., & Robin, J. (Ed.), *Corneal Topography Measuring and Modifying the Cornea* (pp. 117-28). New York: Springer-Verlag.
- Maguire, L., Camp, J. & Robb, R. (1993). A Raytracing Method to Compare Image Quality Before and After Keratorefractive Surgery. *Invest Ophthalmol Vis Sci*, **34**, 805.
- Maguire, L. J. (1994). Keratorefractive Surgery, Success, and the Public Health. *Am J Ophthalmol*, **117**, 394-398.
- Maguire, L. J., Singer, D. E. & Klyce, S. D. (1987). Graphic presentation of computer-analyzed keratoscope photograph. *Arch Ophthalmol*, **105**, 223-230.
- Maguire, L. J., Zabel, R. W., Parker, P. & L, L. R. (1991). Topography and raytracing analysis of patients with excellent visual acuity 3 months after excimer laser photorefractive keratectomy for myopia. *Refr Corneal Surg*, **7**,

122-128.

Mahahan, V. (1994). Zernike Circle Polynomials and Optical Aberrations of Systems with Circular Pupils. *Engineering & Laboratory Notes in Optics and Photonics News*, **5**, s-21 - 24.

Malacara, D. (1992). *Optical Shop Testing* (2nd ed.) New York: John Wiley and Sons, Inc.

Mandell, R. (1960). Jesse Ramsden: inventor of the ophthalmometer. *Am J Optom Arch Am Acad Optom*, **37**, 633-8.

Mandell, R. (1994a). Apparent Pupil Displacement in Videokeratography. *CLAO J*, **20**, 123-7.

Mandell, R. (1994b). Comment: Inherent Error in Corneal Topography/Roberts. *J Refract Corneal Surg*, **10**, 112.

Mandell, R. (1995). Locating the Corneal Sighting Center From Videokeratography. *J Refr Surg*, **11**, 253-9.

Mandell, R., Barsky, B. & Klein, S. (1994). Taking A New Angle On Keratoconus. *CL Spectrum*, **9**, 44-47.

Mandell, R., Chiang, C. & Klein, S. (1995). Location of the Major Corneal Reference Points. *Optom Vis Sci*, **72**, 776-784.

Mandell, R. & Horner, D. (1993). Alignment of Videokeratoscopes. In Sanders, D., & Kock, D. (Ed.), *An Atlas of Corneal Topography* (pp. 197-204). Thorofare, NJ: SLACK Incorporated.

Mandell, R., Klein, S. & Corzine, J. (1998). The Cornea is Not an Ellipse. *Optom Vis Sci*, **75**, 12s:156.

Mandell, R. B. (1992). The enigma of the corneal contour. *CLAO J*, **18**, 267-73.

Mandell, R. B. & St Helen, R. (1971). Mathematical Model of the Corneal Contour. *Br. J. Physiol. Opt.*, **26**, 183-195.

Martinez, C., Applegate, R., Howland, H., Klyce, S., MacDonald, M. & Medina, J. (1996). Changes in Corneal Aberration Structure after Photorefractive Keratectomy. *Invest Ophthalmol Vis Sci*, **37**, S933.

- Matthews, L. & Garcia, G. (1995a). *Laser and Eye Safety in the Laboratory* Bellingham, Washington: IEEE Press.
- Mattioli, R. & Tripoli, N. (1997). Corneal Geometry Reconstruction with the Keratometer Videokeratographer. *Optom Vis Sci*, **74**, 881-894.
- Miller, D. T., Williams, D. R., Morris, G. M. & Liang, J. Z. (1996). Images of cone photoreceptors in the living human eye. *Vision Res*, **36**, 1067-1079.
- Millodot, M. & Sivak, J. (1979). Contribution of the Cornea and Lens to the Spherical Aberration of the Eye. *Vis Res*, **19**, 685-7.
- Mote, H. & Fry, G. (1939). The Significance of Javal's Rule. *Am J Optom*, **16**, 362-365.
- Navarro, R. & Artal, P. (1993). Modulation transfer of the human eye as a function of retinal eccentricity. *J Opt Soc Am A*, **10**, 201-12.
- Navarro, R. & Losada, M. A. (1995). Phase transfer and point-spread function of the human eye determined by a new asymmetric double-pass method. *J Opt Soc Am A*, **12**, 2385-92.
- Oliver, K., Hemenger, R., Corbett, M. & al., e. (1997). Corneal aberrations induced by photorefractive keratectomy. *J Refract Surg*, **13**, 246-254.
- Oliver, K., Hemenger, R., Corbett, M., O'Bart, D., Verma, S., Tomlinson, A. & Marshall, J. (1995). Corneal Aberrations One Year After Photorefractive Keratectomy for Three Types of Ablation Zone. *Optom Vis Sci (supplement)*, **72**, 183.
- Oshika, T., Klyce, S. D., Applegate, R. A., Howland, H. C. & El Danasoury, M. A. (1999). Comparison of corneal wavefront aberrations after photorefractive keratectomy and laser in situ keratomileusis. *American Journal of Ophthalmology*, **127**, 1-7.
- Pole, J. J. & Sather, S. K. (1995). Computer-assisted videography and the aspheric RGP. *CL Spectrum*, **10**, 17-26.
- Rand, R., Howland, H. & Applegate, R. (1997). Mathematical Model of a Placido Disk Keratometer and Its Implications for Recovery of Corneal Topography. *Optom Vis Sci*, **74**, 926-930.

- Reynolds, A. (1992). Introduction: History of Corneal Measurement. In Schanzlin, D., & Robin, J. (Ed.), *Corneal Topography Measuring and Modifying the Cornea* (pp. vii-x). New York: Springer-Verlag.
- Roberts, C. (1994a). The accuracy of 'power' maps to display curvature data in corneal topography systems. *Invest Ophthalmol Visual Sci*, **35**, 3525-3532.
- Roberts, C. (1994b). Characterization of the Inherent Error in a Spherically-Biased Corneal Topography System in Mapping a Radially Aspheric Surface. *J Refrac Corneal Surg*, **10**, 103-111.
- Russ, J. (1995). Processing images in frequency space. In *The image processing handbook* (pp. 332-341). Boca Raton: CRC Press.
- Saleh, B. & Teich, M. (1991). *Fundamentals of Photonics* New York: John Wiley & Sons, Inc.
- Salmon, T. & Horner, D. (1995). Comparison of Elevation, Curvature and Power Descriptors for Corneal Topographic Mapping. *Optom Vis Sci*, **72**, 800-8.
- Salmon, T. & Horner, D. (1996). A new subjective refraction method—the meridional polarized vernier optometer. *J Am Opt Assoc*, **67**, 599-605.
- Salmon, T., Rash, C. & Mora, J. (1998). Videokeratoscopic Accuracy and its Potential Use in Corneal Optics Research (USAARL Report 98-29). US Army Aeromedical Research Laboratory.
- Salmon, T., Thibos, L. & Bradley, A. (1998). Comparison of the eye's wave-front aberration measured psychophysically and with the Shack-Hartmann wave-front sensor. *J Opt Soc Am A*, **15**, 2457-2465.
- Santamaria, J., Artal, P. & Bescos, J. (1987). Determination of the point-spread function of human eyes using a hybrid optical-digital method. *J Opt Soc Am A*, **4**, 1109-14.
- Schwiegerling J & Greivenkamp, J. E. (1997). Using Corneal Height Maps and Polynomial Decomposition to Determine Corneal Aberrations. *Optom Vis Sci*, **74**, 906-916.
- Schwiegerling, J., Greivenkamp, J. & Miller, J. (1995). Representation of videokeratoscopic height data with

- Zernike polynomials. *J Opt Soc Am A*, **12**, 2105-2113.
- Schwiegerling, J., Greivenkamp, J. E., Miller, J. M., Snyder, R. W. & Palmer, M. L. (1996). Optical modeling of radial keratotomy incision patterns. *Am J Ophthalmol*, **122**, 808-817.
- Schwiegerling, J. & Greivenkamp, J. (1996). Keratoconus Detection Based on Videokeratoscopic Height Data. *Optom Vis Sci*, **73**, 721-28.
- Schwiegerling, J. & Snyder, R. (1998). Custom photorefractive keratectomy ablations for the correction of spherical and cylindrical refractive error and higher order aberration. *J Opt Soc Am A*, **15**, 2572-2579.
- Seiler, T., Reckmann, W. & Maloney, R. (1993). Effective spherical aberration of the cornea as a qualitative descriptor in corneal topography. *J Cataract Refr Surgery*, **19**, 155-65.
- Seitz, B., Langenbucher, A., Kus, M. M. & Harrer, M. (1998). Experimental correction of irregular corneal astigmatism using topography-based flying-spot-mode excimer laser photoablation. *American Journal of Ophthalmology*, **125**, 252-256.
- Simonet, P. & Campbell, M. (1990). The transverse chromatic aberration on the fovea of the human eye. *Vision Res*, **30**, 187-206.
- Sliney, D. & Wolbarsht (1981). *Safety with Lasers and Other Optical Sources* New York: Plenum Press.
- Smirnov, M. S. (1961). Measurement of the wave aberration of the human eye. *Biofizika*, **6**, 687-703.
- Smith, W. (1990). *Modern optical engineering* New York: McGraw-Hill, Inc.
- Stein, H., Cheskes, A. & Stein, R. (1995). *The excimer - fundamentals and clinical use* Thorofare, NJ: SLACK Incorporated.
- Thibos, L. (1987). Calculation of the influence of lateral chromatic aberration on image quality across the visual field. *J Opt Soc Am A*, **4**, 1673-80.
- Thibos, L. (1992). The chromatic eye: a new reduced-eye model of ocular chromatic aberration in humans. *Appl*

Optics, **31**, 3594-600.

Thibos, L. (1993). *Fourier Analysis for Beginners - Course notes for V791: Quantitative Methods for Vision Research* Bloomington, Indiana: School of Optometry, Indiana University.

Thibos, L. (1997). The New Visual Optics. *Optom Vis Sci*, **74**, 465-6.

Thibos, L. (1999). Handbook of Visual Optics. Optical Society of America web page, www.aaopt.org/HVO/Handbook_NF.html:

Thibos, L. & Bradley, A. (1997). Use of Liquid-Crystal Adaptive-Optics to Alter the Refractive State of the Eye. *Optom Vis Sci*, **74**, 581-587.

Thibos, L., Wheeler, W. & Horner, D. (1997a). Power Vectors: An Application of Fourier Analysis to the Description and Statistical Analysis of Refractive Error. *Optom Vis Sci*, **74**, 367-375.

Thibos, L., Ye, M., Zhang, X. & Bradley, A. (1997b). Spherical Aberrations of the Reduced Schematic Eye with Elliptical Refracting Surface. *Optom Vis Sci*, **74**, 548-556.

Thibos, L. N., Bradley, A., Still, D. L., Zhang, X. & Howarth, P. A. (1990). Theory and measurement of ocular chromatic aberration. *Vision Res*, **30**, 33-49.

Tomlinson, A., Hemenger, R. & Garriott, R. (1993). Method for Estimating the Spherical Aberration of the Human Crystalline Lens in Vivo. *Invest Ophthalmol Vis Sci*, **34**, 621-629.

Tripoli, N., Cohen, K., Holmgren, D. & Coggins, J. (1995). Assessment of Radial Aspheres by the Arc-Step Algorithm as Implemented by the Keratron Keratoscope. *Am J Ophthalmol*, **120**, 658-64.

Tscherning, M. (1894). Die monochromatischen Aberrationen des menschlichen Auges. *Zeitschrift fuer Psychologie und Physiologie der Sinnesorgane*, **6**, 456-71.

van Blokland, G. & van Norren, D. (1986). Intensity and polarization of light scattered at small angles from the human fovea. *Vis Res*, **26**, 485-494.

- van Meeteren, A. (1974). Calculations on the optical transfer function of the human eye for white light. *Opt Acta*, **21**, 395-412.
- van Meeteren, A. & Dunnewold, C. J. W. (1983). Image quality of the human eye for eccentric entrance pupils. *Vision Res*, **23**, 573-9.
- van Saarloos, P. P. & Constable, I. J. (1991). Improved method for calculation of corneal topography for any photokeratographic geometry. *Optom and Vis Sci*, **68**, 957-965.
- Vargas-Martin, F., Prieto, P. & Artal, P. (1998). Correction of the aberrations in the human eye with a liquid-crystal spatial light modulator: limits to performance. *J Opt Soc Am A*, **15**, 2552-2562.
- Verdon, W., Bullimore, M. & Maloney, R. K. (1996). Visual performance after photorefractive keratectomy: A prospective study. *Arch Ophthalmol*, **114**, 1465-1472.
- Walsh, G., Charman, W. N. & Howland, H. C. (1984). Objective technique for the determination of monochromatic aberrations of the human eye. *J Opt Soc Am A*, **1**, 987-92.
- Walsh, G. & Cox, M. (1995). A new computerized video-aberroscope for the determination of the aberration of the human eye. *Ophthal Physiol Opt*, **15**, 403-408.
- Wang, J., Rice, D. & Klyce, S. (1989). A new reconstruction algorithm for improvement of corneal topographical analysis. *Refract Corneal Surg*, **5**, 379-87.
- Wang, J. & Silva, D. (1980). Wave-front interpretation with Zernike polynomials. *Appl Opt*, **19**, 1510-18.
- Washington, A. (1986). *Technical Calculus with Analytic Geometry* (3rd ed.) Menlo Park, California: The Benjamin/Cummings Publishing Company.
- Webb, R. (1992). Zernike polynomial description of ophthalmic surfaces. *OSA Technical Digest Series (Ophthalmic and Visual Optics)*, **3**, 38-41.
- Webb, R. H., Penney, C. M. & Thompson, K. P. (1992). Measurement of ocular local wavefront distortion with a spatially resolved refractometer. *Appl Opt*, **31**, 3678-86.

- Welford, W. (1986). Wavefront aberrations, transverse ray aberrations and characteristic functions. In *Aberrations of Optical Systems* (pp. 93-98). Bristol: Adam Hilger.
- Westheimer, G. (1963). Optical and motor factors in the formation of the retinal image. *J Opt Soc Am*, **53**, 86-93.
- Westheimer, G. & Liang, J. (1994). Evaluating Diffusion of Light in the Eye by Objective Means. *Invest Ophthalmol Vis Sci*, **35**, 2652-2657.
- Williams, C. & Becklund, O. (1989). *Introduction to the optical transfer function* New York: John Wiley & Sons.
- Williams, D. R., Brainard, D. H., McMahon, M. J. & Navarro, R. (1994). Double pass and interferometric measures of the optical quality of the eye. *J Opt Soc Am A*, **11**, 3123-35.
- Woods, R., Bradley, A. & Atchison, D. (1996). Monocular diplopia caused by ocular aberrations and hyperopic defocus. *Vision Res*, **36**, 3597-3606.
- Wu, C. (1997). Supernormal Vision. *Science News*, **152**, 305-320.
- Yolton, R., Citek, K., Schmeisser, E., Reichow, A. & Griffith, T. (1999). Laser pointers: toys, nuisances, or significant eye hazards? *J Am Optom Assoc*, **70**, 285-289.
- Young, T. (1801). On the mechanism of the eye. *Phil Trans R Soc*, **19**, 23-88.

Appendix A Excel Spreadsheet: Zernike Coefficients to Spectacle Rx Conversion

Zernike coefficients for wavefront aberrations in wavelengths. Myopic wavefronts have a positive sign. See Chapter 2, Section 2.4.5 for details. References: (Thibos, 1997; Salmon, 1996).

DIRECTIONS: ENTER DATA IN SHADED BOX; FIND ANSWER IN BOLD PRINT BELOW.

columns ->	C	D	E	G	H
	2nd order Zernike coefficients				
mode	4	5	6		
description	45/135 ast	defocus	180/90 ast	Pupil dia (mm)	Wavelength (nm)
rows	ENTER DATA			5.6	633
12				0.0028	6.33E-07 meters
13	convert to meters	1.551E-06	2.193E-06	3.101E-06	Axis convert intermediate step
14	Fourier coeff (diopters)	-0.3955	-0.5594	-0.7911	13
15	Thibos terms	J45	M	J0	103
					plus cyl
19	ANSWER	0.33	-1.77	103	Minus cyl
20		-1.44	1.77	13	Plus cyl

Formulas in cells corresponding to column and row labels.

C13 = SQRT(6)*C11*\$H\$12	D13 = 2*SQRT(3)*D11*\$H\$12	E13 = SQRT(6)*E11*\$H\$12
C14 = -2*C13/(C13^2+\$G\$12^2)	D14 = -2*D13/(D13^2+\$G\$12^2)	E14 = -2*E13/(E13^2+\$G\$12^2)
G12 = G11/2000	H12 = H11/1000000000	G14 = DEGREES(ATAN(C14/E14))/2
		G15 = G14+90
C19 = D14-(D19/2)	D19 = -2*SQRT(C14^2+E14^2)	E19 = IF(E14<0,G14+90,IF(C14<0,G14+180,G14))
C20 = D14-D20/2	D20 = 2*SQRT(C14^2+E14^2)	E20 = IF(E14>0,G15,IF(C14>0,G15+90,G15-90))

APPENDIX B

Computing the Axial Radius of Curvature of an Ellipse

Baker's equation (Eq. B-1) is a useful formula for plotting an ellipse based on values for its apical radius of curvature (r_0) and shape factor (p). The shape factor describes the degree of flattening of the ellipse and is related to conic eccentricity by Eq. (B-2). Baker's equation (Eq. 3-2 and 3-5) was discussed in Chapters 3 and 4. Figure B.1 shows the geometric relationships of Baker's equation.

$$y = \sqrt{2rx - px^2} \quad (\text{B-1})$$

$$p = 1 - e^2 \quad (\text{B-2})$$

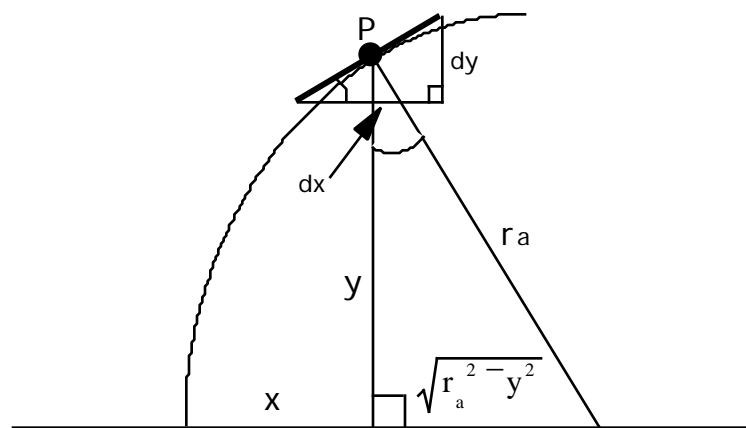


FIGURE B.1 Geometric relationships with an ellipsoidal corneal model.

Appendix B: Computing the Axial Radius of Curvature

The axial radius of curvature (r_a) is the distance from point P on the ellipse to the optic axis along the normal to the curve at P. Because r_a and the slope at point P are perpendicular to each other, two similar triangles may be drawn with congruent acute angles indicated by the arcs. The tangent of the acute angle in the smaller triangle is equal to the slope of the curve at P; this is equal to the derivative of Eq. (B-1), which is shown in Eq. (B-3). The denominator simplified based on Eq. (B-1).

$$\frac{dy}{dx} = \frac{(r_0 - px)}{\sqrt{2r_0x - px^2}} = \frac{(r_0 - px)}{y} \quad (\text{B-3})$$

The tangent of the acute angle in the larger triangle is equal to:

$$\frac{\sqrt{r_a^2 - y^2}}{y} \quad (\text{B-4})$$

Since the angles are congruent, we may set up the following equality:

$$\frac{\sqrt{r_a^2 - y^2}}{y} = \frac{(r_0 - px)}{y} \quad (\text{B-5})$$

After manipulating the equation using the steps shown below, we may derive an equation that solves for the axial radius of curvature. Note that Eq. (B-9) is simplified to Eq. (B-10) using Eq. (B-1).

$$\sqrt{r_a^2 - y^2} = (r_0 - px) \quad (\text{B-6})$$

$$r_a^2 - y^2 = (r_0 - px)^2 \quad (\text{B-7})$$

$$r_a^2 - y^2 = r_0^2 - 2r_0px + p^2x^2 \quad (\text{B-8})$$

Appendix B: Computing the Axial Radius of Curvature

$$r_a^2 - y^2 = r_0^2 - p(2r_0 x - px^2) \quad (\text{B-9})$$

$$r_a^2 - y^2 = r_0^2 - py^2 \quad (\text{B-10})$$

$$r_a^2 = r_0^2 - py^2 + y^2 \quad (\text{B-11})$$

$$r_a^2 = r_0^2 + (1 - p)y^2 \quad (\text{B-12})$$

Equation (B-12) appears in Chapter 4 as Eq. (4-3) and is the basis for Eq. (3-8) in Chapter 3.

APPENDIX C

README File for the EyeSys Utility Program, CORSAG18.EXE

Upon request, EyeSys Vision Group (formerly EyeSys Technologies), provides a utility program named "CORSAG18.EXE," which computes the surface elevation of the cornea based on already-stored data files. The README file that accompanies the program has been copied below with permission from the EyeSys Vision Group.

TEXT OF THE README FILE:

Feb 26 , 1996
Corneal Sag File Generation Utility User's Guide
EyeSys Technologies

The DOS utility CORSAG18.EXE takes as input the curvature and radius files (XX*.* and RA*.* , respectively) for a System 2000 18-ring system exam and creates a corneal sag data file (SG*.*).

File Format

The format of the output file is similar to that of the curvature and radii files. It is an ASCII file and consists of a header section, which is a newline-terminated single string, followed by 360 newline-terminated records.

Each of the records begins with a semi-meridian angle followed by a colon ':' character, and followed by a series of 18 positive sag values (in tenths of microns) corresponding to the abscissa positions in the radius file (RA*.* , where abscissa points are in 1/100 th of mm). These values thus correspond to depth information along a semi- meridian, from the center outwards. Any zero sag values correspond to missing data.

How to use the Utility

- * Copy the file CORSAG18.EXE either to the directory where the input data resides, or to a directory that is present in your DOS command path.
- * Go to the directory where your input data is located.
- * At the DOS prompt, type Corsag18. The program will prompt you for the curvature file name (XX*.*).
- * The utility will produce the output file (SG*.*) in the same directory as the input files.

NOTES:

- * Missing data within any semi-meridian has been linearly interpolated for radius and curvature info for the purpose of providing continuous sag info. for that meridian.
- * This utility does not handle compressed input files. To decompress these files, please use the utility ADD_RL.EXE.
- * The header section of the output file is syntactically similar to the input file headers and can thus be parsed in the same way, but contains only a single blank character per field.
- * If you have any problems running this utility, please contact Edouard (Eddy) Philippe via Internet email (eddy@hti.net) , or via EyeSys.

//.

APPENDIX D

MATLAB Script: Compute the Corneal Wavefront Aberration

This appendix provides a copy of the MATLAB program that I used to compute the corneal wavefront aberration data based on the following input data:

- Polar data array, named “**rho,” with 360 columns for each EyeSys meridian (0 to 359 degrees) and rows containing the radial distances, in micrometers, to each sampled point.
- Polar data array, named “**sag,” with the same dimensions as **rho, but which containing the surface elevation of the cornea, in micrometers, measured from a reference plane.
- Cartesian coordinates (P1x, P1y, P1z) for an distant object point (P1), located on the line of sight. The EyeSys corneal apex is taken as the origin. Distances are in micrometers.
- Cartesian coordinates (CSC1x, CSC1y, CSC1z) for the corneal sighting center (CSC), located on the line of sight. Distances are in micrometers.
- Cartesian coordinates (P2x, P2y, P2z) for paraxial position of image point (P2), refracted by the central cornea. Distances are in micrometers.
- Measured corneal radii (viewed from the front) and interval to which data will be interpolated within each radial meridian, both in micrometers.

This program saves a polar array of data in a text file named “polar_interp.” The data is the corneal wavefront aberration function, in wavelengths, where one wavelength is 633 nm. The program implements the “Fermat” method to compute the wave aberration, which is described in Chapter 5, in Section 5.1.3b.

TEXT OF THE MATLAB SCRIPT:

```
% 7/7/98 Tom Salmon
% Workbook to compute the corneal wave-front aberration function W(x,y)
% from corneal surface data based on Fermat's principle.
```

APPENDIX D: MATLAB Script: Compute the Corneal Wavefront Aberration

```
% SET DATA in steps 1-3 as required then run.

% 1. PUT basic data arrays in the MATLAB path. Load rho & sag data.
clear
load ABrho
load ABSag

% 2. SET data variables
rho = ABrho;
z = ABSag;

% 3. ENTER P1 (object point), CSC (corneal sighting center) and P2 (image point)
% x,y and z coordinates here. All in microns. Corneal vertex is origin. Positive
% z points toward retina.

P1x = 233364663.1;
P1y = 73674279.0;
P1z = -10000000000;

CSCx = 81.801;
CSCy = 2.919;
CSCz = 0.416;

P2x = -488.595;
P2y = -154.253;
P2z = 28812.595

% 4. Enter interpolation parameters.
p_rad=3000; % Pupil radius in microns.Arthur's = 3000; Doug's = 2900; Larry's = 3300.
interval=10; % Data interval in microns

% 5. Build Cartesian x and y arrays for the cornea from current polar data.
% Make meridian array "theta" in radians. Cornea data should be arranged with
% columns 1-360 representing meridians 0-359 and rows represent rings from center
```

APPENDIX D: MATLAB Script: Compute the Corneal Wavefront Aberration

```

% to periphery.

[row,col]=size(rho);
theta = ones(row,1)*[0:1:359]/180*pi;

x = rho.*cos(theta);
y = rho.*sin(theta);

% 6. Compute optical path length of reference ray which is the LOS in object space
% and its continuation in image space after refraction at the CSC. The ray travels
% from point P1 to the CSC in air (OP1), then from the CSC to P2 (OP2) in the cornea.
% Call the reference optical path length, in microns "OP_LOS."

OP1 = sqrt((CSCx-P1x)^2+(CSCy-P1y)^2+(CSCz-P1z)^2);           % a scalar
n = 1.376;                % assumed corneal index
OP2 = sqrt((P2x-CSCx)^2+(P2y-CSCy)^2+(P2z-CSCz)^2) * 1.376; % a scalar
OP_LOS = OP1+OP2;

% 7. Compute optical path from P1 through each corneal point to P2.

OP_to_cornea = sqrt((x-P1x).^2+(y-P1y).^2+(z-P1z).^2);
OP_cornea_to_P2 = sqrt((P2x-x).^2+(P2y-y).^2+(P2z-z).^2)*n;
OP_all = OP_to_cornea + OP_cornea_to_P2;

% 8. Compute wave-front aberration function in microns, then wavelengths

OPD = OP_LOS - OP_all;
W = OPD/.633;

% 9. Add what used to be contained in the MATLAB script, INTERP_POLAR.M so it is all done in one
step:
v=[0:interval:p_rad]';
m=length(v);
polar_interp=ones(m,360);

```

APPENDIX D: MATLAB Script: Compute the Corneal Wavefront Aberration

```
for a=1:360
    polar_interp(:,a)=spline(rho(:,a),W(:,a),v);
end
```

```
% 10. Save data.
```

```
save W.txt W -ascii
```

```
size(polar_interp)
```

```
save polar_interp.txt polar_interp -ascii
```

APPENDIX E

MATLAB Script: Zernike Polynomial Fitting of Wavefront Data

This appendix provides a copy of the MATLAB program I used to compute a least-squares fit of Zernike polynomials (up to the 10th order) to both corneal and ocular wavefront height data. This program used an older version of the Zernike m-file named, "ZernikeRX.m", which numbered the piston term as mode 0. That program has since been updated to renumber the piston term as mode 1.

Chapters 5, 6 and 7 refer to the program copied here. Input data includes the three arrays with the w, x, y Cartesian coordinates for the wavefront aberration:

- Array w contains the discrete wavefront height values in wavelengths.
- Arrays x and y contain coordinates for the sampling grid in mm.
- Pupil radius in mm.

The program returns:

- A 1 5 66 column vector with the Zernike coefficients corresponding to each mode.
- The RMS difference between the wavefront described by the Zernike coefficients and the input wavefront data.
- Two comparisons of the wavefront variance in the original data and the wavefront variance in the wavefront described by the Zernike coefficients.

TEXT OF THE MATLAB SCRIPT:

```
% Given 2-D wavefront data, compute the best fit Zernike coefficients.
% 3/30/98 Tom Salmon Based on 3/18/98 file "Zernike66_fit2D.m."
% This uses Larry's new m-file to compute the ZernikeRX matrix for 65 modes
```

APPENDIX E: MATLAB Script: Zernike Polynomial Fitting of Wavefront Data

```

% Wavefront aberration w,x,y data in Transform files.
% Can't paste in huge arrays, so resample in Transform to:
    % LT and AB 57x57
    % DH 53x53
    % In Transform, x=c(W_xy_rs) and y=r(W_xy_rs)
    % AS LONG AS PUPIL COORDINATE ARRAYS ARE FULL (no zeros in corners)
    % YOU CAN USE THIS.
% Paste into empty m-files and save without .m as "w", "x", and "y".

load w
load x
load y

% Set pupil radius in mm. LT & AB = 2.8; DH = 2.6.
p = 2.8;

% Normalize pupil coordinates.
xn = x/p;      yn = y/p;

% Vectorize matrices.
[m,n]=size(xn);
xv=ones(m*n,1); yv=xv;      wv=xv; xv(:) = xn;
yv(:) = yn;
wv(:) = w;

% Use only points inside the pupil.
n = length(wv);
k = 0; % counter
rv = sqrt(xv.^2+yv.^2);

for i = 1:n,
% if rv(i)<=1 & rv(i) > 0, % Assume no data point at exactly x=0, y=0
% The above line was needed because Excel W(x,y) data set w,x & y values outside the pupil to 0.

```


APPENDIX E: MATLAB Script: Zernike Polynomial Fitting of Wavefront Data

```

% One of them sampled any data at exactly (x,y) = (0,0) so this if statement worked.
% But EyeSys data has been interpolated to a regular cartesian grid and included (x,y)=(0,0).
% Therefor the if statement must be changed to include that data point.
% Note: normalized x and y matrix values must be greater than 1.0 outside the pupil.
    if rv(i)<=1
        k=k+1;
        xx(k,1) = xv(i);
        yy(k,1) = yv(i);
        ww(k,1) = wv(i);
    end;
end;

% Compute [k,66] matrix (A) of Zernike terms evaluated at xx & yy
modes = 65;
for j = 1:modes+1,      A(:,j) = zernikeRX(xx,yy,j-1);      end

% Compute 66 Zernike coefficients (constant + 65 modes)
a = A\ww;

% Find mean value and variance in orignal wavefront data
Wmean = mean(ww);
Wvariance = std(ww).^2;
% Find sum of mode variances based on coefficients vector "a."
aSquared = a.^2;
AllModeVar = sum(aSquared(2:66));

% Reconstruct wavefront & compute variance for each Zernike mode
a_mask = a*ones(1,length(a)).*eye(length(a));
% a_mask is a matrix with the a coefficients along the diagonal
wz_modes = A*a_mask;
% wz_mades is a matrix with reconstruct W for each mode in each column.
% Column 1 corresponds with mode 0, etc.
% Each row corresponds a sampled point.
wz_total = wz_modes*ones(length(a),1);

```

APPENDIX E: MATLAB Script: Zernike Polynomial Fitting of Wavefront Data

```
% Sum the reconstruct W across modes

mode_var = (std(wz_modes).^2);
% The wavefront variance within each reconstructed mode

% See how reconstructed W compares with original W.
RMSError = std(wz_total-ww);

% How do the sum of the mode variances compare with the original variance?
CompareVariances1 = sum(mode_var)/Wvariance;
CompareVariances2 = AllModeVar/Wvariance;

% Display results
RMSError
CompareVariances1
CompareVariances2
```

Appendix F Complete List of Zernike Coefficients

(orders 0 - 5)

(To compute the wavefront aberration in wavelengths)

Order	Mode	Description	Results for subject AB			Results for subject DH			Results for subject LT		
			Cornea	Eye	Internal	Cornea	Eye	Internal	Cornea	Eye	Internal
0	1	piston	2.821	-0.283	-3.104	-6.193	0.011	6.204	3.458	-0.052	-3.509
1	2	y tilt	0.144	0.597	0.453	-0.082	-0.078	0.004	-0.155	0.557	0.713
	3	x tilt	-0.758	0.050	0.808	-0.689	0.574	1.263	-0.625	-1.184	-0.559
2	4	45/135 astig	-0.541	-0.463	0.079	0.099	-0.097	-0.196	0.352	0.560	0.208
	5	defocus	2.027	0.339	-1.688	-3.418	0.217	3.635	2.451	0.266	-2.185
	6	90/180 astig	-1.057	-0.207	0.850	-0.582	0.172	0.755	0.486	0.643	0.157
3	7	tri astig	0.198	0.049	-0.149	0.114	-0.136	-0.250	-0.141	-0.027	0.114
	8	y 1 coma	0.007	0.075	0.068	-0.136	-0.207	-0.071	-0.060	0.067	0.127
	9	x 1 coma	-0.280	-0.115	0.165	-0.200	0.016	0.216	-0.140	-0.049	0.091
	10	tri astig	0.086	0.078	-0.008	-0.012	0.110	0.122	0.098	0.061	-0.037
4	11	1 sph aberr	0.086	0.089	0.003	-0.003	0.010	0.014	-0.005	0.027	0.032
	12		-0.036	0.001	0.037	-0.027	-0.074	-0.048	0.029	0.037	0.008
	13		0.266	0.312	0.047	0.084	0.057	-0.027	0.325	0.111	-0.214
	14		-0.016	0.009	0.025	-0.072	-0.213	-0.142	0.024	-0.001	-0.025
	15		-0.052	0.000	0.052	0.053	0.055	0.002	-0.149	-0.075	0.073
5	16	y 2 coma x 2 coma	-0.018	0.000	0.018	-0.017	-0.031	-0.014	-0.017	-0.023	-0.005
	17		-0.014	0.021	0.035	0.002	0.145	0.144	0.026	0.021	-0.006
	18		-0.024	-0.020	0.004	-0.007	-0.012	-0.005	-0.050	-0.085	-0.035
	19		-0.010	0.001	0.011	-0.019	-0.005	0.015	-0.001	-0.010	-0.008
	20		0.010	-0.004	-0.013	0.019	-0.067	-0.087	-0.014	-0.027	-0.013
	21		-0.014	-0.003	0.011	-0.022	0.003	0.025	-0.002	0.090	0.092

List of Zernike Coefficients, Continued (orders 6 - 8)

(To compute the wavefront aberration in wavelengths)

Order	Mode	Description	Results for subject AB			Results for subject DH			Results for subject LT		
			Cornea	Eye	Internal	Cornea	Eye	Internal	Cornea	Eye	Internal
6	22	2 sph aberr	0.020	0.025	0.005	0.014	0.013	-0.001	0.028	-0.024	-0.052
	23		-0.015	0.001	0.016	0.006	0.046	0.040	-0.012	0.013	0.026
	24		0.000	0.008	0.008	-0.008	-0.003	0.004	-0.003	-0.030	-0.028
	25		-0.028	-0.056	-0.028	-0.027	-0.074	-0.046	-0.013	-0.024	-0.012
	26		0.014	0.002	-0.011	0.020	0.071	0.051	0.004	0.004	0.000
	27		0.000	0.002	0.003	0.004	0.033	0.029	0.039	0.006	-0.033
	28		0.024	-0.024	-0.048	0.011	0.011	0.001	-0.013	0.024	0.038
7	29		0.015	0.036	0.020	0.005	0.045	0.040	0.007	0.012	0.005
	30		0.006	0.000	-0.006	0.006	-0.007	-0.013	-0.006	0.013	0.019
	31		0.002	-0.006	-0.008	0.001	-0.049	-0.050	0.001	-0.012	-0.014
	32		0.005	0.001	-0.004	-0.001	0.028	0.029	0.009	0.007	-0.002
	33		-0.006	-0.003	0.002	0.001	0.004	0.003	-0.005	-0.015	-0.010
	34		-0.003	0.000	0.003	-0.005	0.023	0.028	0.001	0.017	0.016
	35		0.023	0.014	-0.009	0.010	0.029	0.018	0.006	-0.030	-0.036
	36		-0.019	-0.004	0.015	-0.004	0.025	0.029	-0.017	0.039	0.056
8	37		0.009	-0.024	-0.033	-0.003	-0.003	0.001	-0.010	-0.013	-0.003
	38		-0.008	-0.004	0.005	0.000	-0.015	-0.015	-0.028	0.005	0.033
	39		0.001	-0.004	-0.005	-0.002	-0.025	-0.023	0.007	-0.008	-0.015
	40		0.002	-0.006	-0.007	0.005	0.012	0.007	-0.001	0.009	0.010
	41		0.011	0.006	-0.005	0.001	-0.002	-0.003	0.006	0.012	0.006
	42		-0.004	0.000	0.004	-0.001	0.000	0.001	0.002	0.002	0.000
	43		0.007	0.006	0.000	-0.002	-0.029	-0.026	-0.002	-0.007	-0.004
	44		-0.011	0.003	0.014	-0.005	-0.003	0.001	-0.001	-0.007	-0.006
	45		-0.020	0.008	0.027	-0.010	0.018	0.029	-0.012	-0.012	0.001

List of Zernike Coefficients, Continued (orders 9, 10)

(To compute the wavefront aberration in wavelengths)

Order	Mode	Description	Results for subject AB			Results for subject DH			Results for subject LT		
			Cornea	Eye	Internal	Cornea	Eye	Internal	Cornea	Eye	Internal
9	46		0.000	0.006	0.005	0.000	-0.025	-0.025	0.006	-0.016	-0.021
	47		-0.013	-0.011	0.002	-0.007	-0.022	-0.015	-0.001	-0.008	-0.007
	48		-0.003	-0.003	0.000	-0.002	0.027	0.029	0.004	-0.006	-0.010
	49		-0.001	0.002	0.003	-0.001	0.000	0.001	-0.004	-0.002	0.001
	50		0.001	0.000	-0.002	0.002	-0.006	-0.008	0.003	0.009	0.005
	51		-0.003	0.001	0.004	-0.002	-0.006	-0.004	-0.001	0.015	0.016
	52		-0.001	-0.001	0.000	-0.001	0.013	0.014	0.000	0.004	0.004
	53		-0.012	0.001	0.014	-0.008	-0.016	-0.008	-0.005	0.009	0.014
	54		0.010	-0.009	-0.019	0.003	-0.023	-0.026	0.008	-0.002	-0.011
	55		0.005	-0.007	-0.012	-0.004	0.021	0.025	-0.008	0.020	0.028
10	56		0.000	0.006	0.006	0.005	-0.022	-0.027	0.022	-0.014	-0.036
	57		-0.009	0.004	0.013	-0.002	0.018	0.020	-0.002	0.001	0.003
	58		0.007	-0.006	-0.013	-0.001	0.011	0.013	0.014	-0.008	-0.022
	59		0.000	0.003	0.003	0.002	-0.004	-0.006	-0.004	0.001	0.004
	60		0.000	-0.004	-0.004	-0.001	-0.007	-0.007	-0.001	0.000	0.002
	61		-0.009	0.004	0.012	-0.006	-0.005	0.001	-0.006	-0.024	-0.018
	62		0.002	-0.001	-0.003	-0.003	0.008	0.011	-0.001	-0.011	-0.010
	63		0.003	0.001	-0.002	0.001	0.006	0.005	0.002	-0.015	-0.017
	64		0.006	0.000	-0.006	0.003	0.026	0.023	0.002	-0.005	-0.007
	65		0.007	0.002	-0.005	0.004	-0.018	-0.021	0.003	-0.005	-0.008
	66		-0.002	0.024	0.027	-0.006	-0.005	0.001	-0.008	-0.003	0.005

APPENDIX G

Experimental Apparatus Photographs

Chapter 6 describes the Shack-Hartmann wavefront sensor that I used to measure ocular aberrations. Several photographs of the apparatus are included in this appendix. Refer to Fig. 6.2 to identify specific components in the figures below.

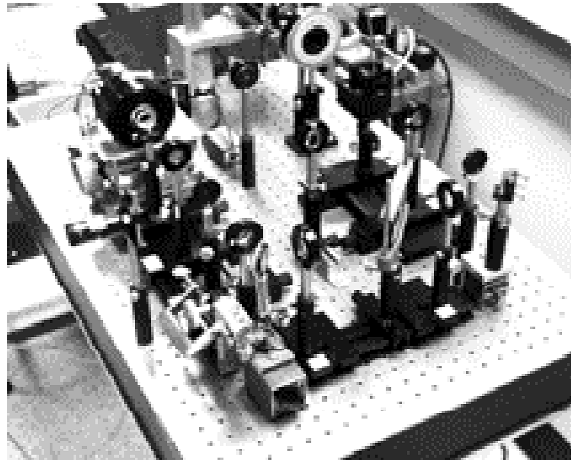


Figure G.1

The Shack-Hartmann sensor, as seen from above the subject's chair. The electronic shutter (white annulus) is located near the right-rear side of the table; the slow-scan camera is located near the left-rear side.

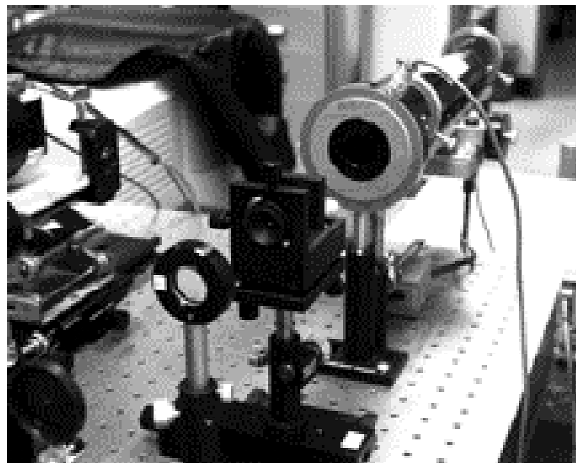


Figure G.2

Close-up view of the laser, electronic shutter, spatial filter assembly, lens L1 and aperture A1.

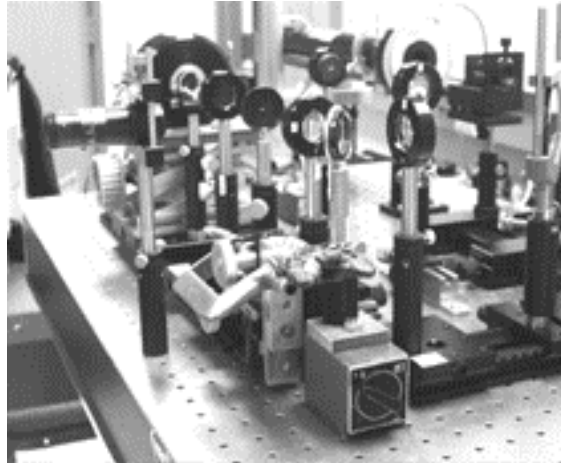


Figure G.3

View of the Shack-Hartmann output channel from behind the subject's chair . From front to rear, the pellicle beam splitter, lens L4, aperture A2, lens L5, the lenslet array and camera are shown.

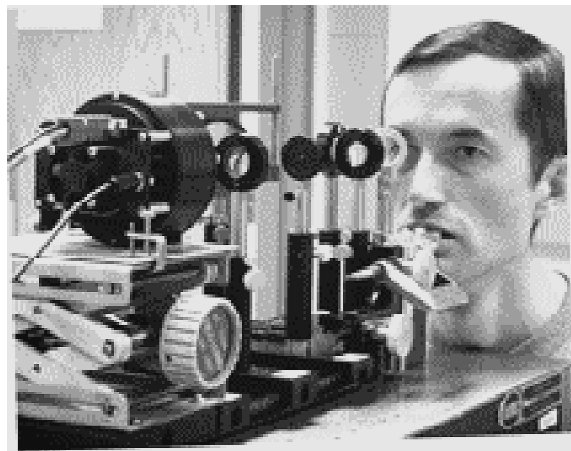


Figure G.4

A subject is shown gazing down the output channel with his right eye, while stabilized on a bite bar. The pellicle beam splitter, lens L4, aperture A2, and lens L5 are arranged, in that order, between the subject and the slow-scan camera (foreground).

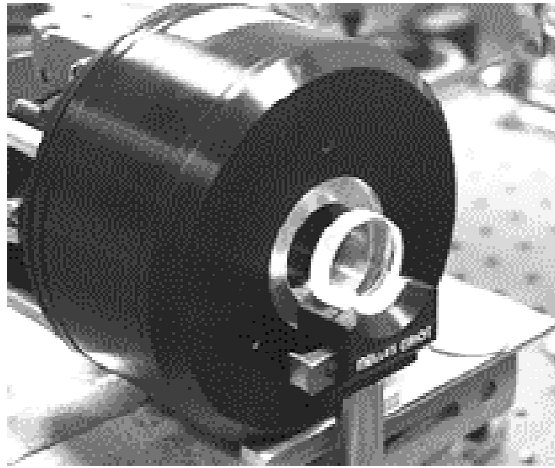


Figure G.5

Close-up view of the lenslet array mounted in its own holder, in front of the round slow-scan camera. A twenty-five-cent coin was placed on the platform to the right of the camera for size comparison.

The Smirnov technique, described in Chapter 6, was used to subjectively measure the wavefront aberration in the horizontal meridian of two subjects. Refer to Fig. 6.3 for details of the layout and operating principles of this method.

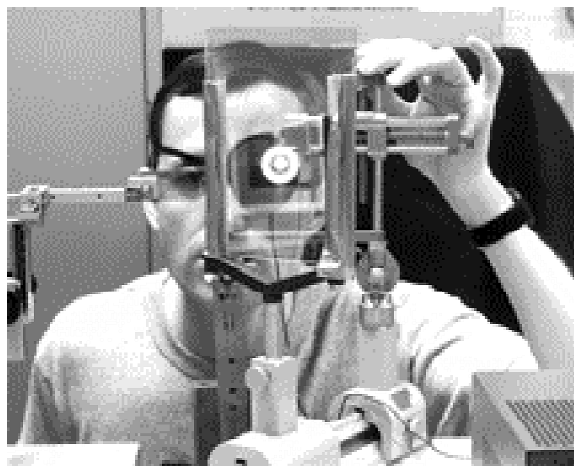


Figure G.6

View of a subject centering the image of a small reflected light in the image of an annulus, which is seen here reflected off a beam splitter. The left eye is occluded while the subject views the targets with the right eye, through a polarizing filter.

APPENDIX H

Laser Safety with the Shack-Hartmann Wavefront Sensor

Lasers concentrate energy so effectively that, depending on the wavelength, power and exposure time, they may injure eyes and even cause skin burns. Laboratory scientists using lasers must therefore be thoroughly familiar with laser safety calculations and procedures. The laser that I used for Shack-Hartmann wavefront measurements presented no skin hazard, but it had the potential to cause retinal burns. This appendix summarizes basic principles of laser safety and reviews the calculations necessary to ensure safe viewing of a laser beam.

H.1

CLASSIFICATION OF LASERS

The American National Standards Institute (ANSI) and the Bureau of Radiological Health (BRH) developed a system to categorize lasers according to their potential for retinal injury. Class I indicated the safest and Class IV the most dangerous groups. The classes are summarized in Table H.1. The helium-neon laser that was part of my Shack-Hartmann wavefront sensor, has a maximum output power of 10 mW and is classified as a Class IIIb device. Diffusely reflected light from a Class III laser cannot injure the eye, but in the case of direct exposure or specular reflections, Class III lasers can produce retinal burns within the quarter-second blink reflex. Since the blink reflex cannot protect the eye from injury, special safety precautions are required when using Class III or Class IV lasers. Note that laser pointers, which are proliferating to the point that some are being used as toys by children, are usually Class IIIa devices (Yolton, Citek, Schmeisser, Reichow, & Griffith, 1999), therefore potentially dangerous.

Table H.1 ANSI laser classes and descriptions

Class	Description	Maximum power	Comment
I	exempt	< 0.38 μ W or enclosed	No ocular hazard
II	Low power	< 1 mW	No retinal burns in less than 0.25
IIIa	Medium power	< 5 mW	1 sec. burn threshold for monkeys
IIIb	Medium power	< 500 mW	No skin burns for < 1.0 sec.
IV	High power		Ocular, skin and fire hazard

H.2

DEVELOPMENT OF EXPOSURE LIMITS

Visible light falling on the retina is strongly absorbed by the retinal pigment epithelium, where it is then transformed into heat. If injury is to be avoided, the heat must be dispersed into the surrounding tissues. This is primarily accomplished by the choroidal vasculature, but if the amount or rate of accumulated heat exceeds this protective mechanism, retinal tissues can be permanently damaged. The exact amount of energy required to cause retinal injury depends on many complex factors such as wavelength, exposure time, spot size, retinal location, pigment density, eye movements, and body temperature and blood flow.

ANSI established its standards after reviewing the best available research data, but in some cases the exposure limits had to be extrapolated or simplified. Most of the laser injury studies titrated laser power and exposure times to determine thresholds for ophthalmoscopically visible retinal damage. In a few studies, histological sections of exposed retinal tissues were examined, and other studies measured the thresholds for vision loss after exposure to a laser beam. These studies generally supported the damage thresholds found by ophthalmoscopy.

Lappin's (1970) findings with rhesus monkeys are particularly relevant to my research since he specifically studied retinal damage caused by the helium-neon laser. Using ophthalmoscopy, he evaluated the effect of 500 exposures to 70 eyes, over a range of powers, exposure times and retinal locations. The animals were essentially emmetropic and pupils were fully dilated. His data showing maximum "no burn" exposure levels for the macula and extramacula are plotted in Fig. H.1. The monkey maculas could sustain 5 mW for 2 seconds with no signs of damage. Since monkey retinas are more heavily pigmented than human retinas, and would therefore have even greater absorption, this level of exposure would presumably

still be safe with humans. For comparison, the ANSI limit for 2.0 seconds, is 0.58 mW.

H.3

CURRENT SAFETY STANDARDS

Prior to publication of the first ANSI laser standard there was no consensus on safe exposure limits, but separate standards had been developed by different agencies. The *American National Standard for the Safe Use of Lasers*, first published in 1973, has become the accepted standard in the United States and is used by many international organizations as well. The current version, ANSI Z-136.1(1993), contains complete information on hazard analysis and control measures to ensure laser safety. This authoritative reference is available from the Laser Institute of America (<http://www.laserinstitute.org/>). The specific data needed to compute safe exposure limits for direct intrapupillary viewing of a laser beam is contained in Table 5 of Z-136.1. A simplified excerpt from that table has been included below as Table H.2.

Table H.2 ANSI Z-136.1 (1993) exposure limits for visible light

Wavelength (nm)	Exposure t (sec)	Maximum permissible exposure (MPE)
400 to 700	10^{-9} to 18×10^{-6}	0.5×10^{-6} J/cm ²
400 to 700	18×10^{-6} to 10	$1.8t^{0.75} \times 10^{-3}$ J/cm ²
550 to 700	10 to 452	$1.8t^{0.75} \times 10^{-3}$ J/cm ²
550 to 700	452 to 10^4	175.79 mJ/cm ²
400 to 700	10^4 to 3×10^4	17.58×10^{-6} W/cm ²

H.4

CALCULATION OF EXPOSURE LIMITS

For most visible wavelengths and exposure times, ANSI's maximum permissible exposures (MPE) are specified in terms of energy flux, but laser light meters generally measure power. It was therefore necessary to convert the energy flux, specified by ANSI, to power in order to establish safe exposures for my subjects. During Shack-Hartmann measurements, my subjects directly viewed the laser beam for one to two seconds. Using an example of a two-second exposure, the steps required to determine

the safe power limit are summarized below.

1. Compute Energy flux. For a wavelength of 633 nm, the maximum permissible exposure (MPE), expressed as mJ/cm², is a simple function of exposure time (t) and is computed using the formula shown in rows two and three of Table H.2, above. For a 2.0-second exposure the maximum permissible energy flux is 3.027 mJ / cm².

$$\text{MPE} = 1.8 \times t^{0.75} = 1.8 \times (2)^{0.75} = 3.027 \text{ mJ/cm}^2 \quad (\text{H-1})$$

2. Compute energy. The ANSI safety standards include certain worst-case assumptions, including an assumed pupil diameter of 7.0 mm. The conversion from energy flux to energy takes into account the area of the pupil based on this diameter. The pupil area is therefore assumed to be 0.3848 cm², and the maximum amount of energy, in mJ, allowed to enter the pupil (E), is found by multiplying the energy flux by the this area.

$$E = 3.027 \times 0.3848 = 1.165 \text{ mJ} \quad (\text{H-2})$$

3. Compute power. Power (P), in mW, is equal to energy (E) divided by exposure time (t). For a 2.0-second exposure the maximum permissible power exposure for our subject is:

$$P = E / t = 1.165 / 2 = 0.5825 \text{ mW} \quad (\text{H-3})$$

Actual damage thresholds for any individual will vary, but ANSI standards include a safety margin to make the standard applicable for general use. Most vision research laboratories provide an additional margin of safety by reducing power well below the ANSI limit. To ensure the safety of my subjects, I arbitrarily decided to limit the power entering their eyes to no more than 1/100th of the ANSI standard. This provides an additional two log unit, or 100 fold safety margin. For a 2.0-second continuous exposure to the helium-neon laser, my limit was therefore 0.0058 mW or approximately 6 μW. I used neutral density filters to reduce the power to below this level, and power was verified using a laser power meter at the position of the cornea prior to exposing any subjects. Table H.3 lists power limits for other exposure times. Table H.4 shows the margin of safety in several other visual optics studies that required subjects to fixate a laser beam.

Table H.3 Calculated helium-neon exposure limits for various exposure times, based on the procedures summarized above.

Time (s)	MPE (mJ/cm ²)	Energy (mJ)	Safe power limit (mW)	
			ANSI standard	100 x safety margin
0.10	0.320	0.123	1.232	0.012
0.25	0.636	0.245	0.980	0.010
0.50	1.070	0.412	0.824	0.008
1.00	1.800	0.693	0.693	0.007
2.00	3.027	1.165	0.582	0.006
5.00	6.019	2.316	0.463	0.005

Table H.4 Comparison of power levels used in several other studies that used either the double-pass or Shack-Hartmann method to measure ocular aberrations.

Study	Exposure Time (s)	ANSI limit (μ W)	Power used (μ W)	Safety margin
Santamaria (1987)	0.067	1,363	300	4.5
Navarro (1993)	0.08	724	40	18
Westheimer (1994)	10	390	0.12	3,250
Williams (1994)	5	463	0.3	1543
Liang (1994)	0.1	1,231	5	250

H.5

RETINAL IRRADIANCE

The information summarized above is sufficient to compute exposure limits for light entering the eye, but computation of actual retinal irradiance requires a few additional steps. Lappin (1968) summarized retinal irradiances calculation for continuous exposure to a 633-nm-helium-neon laser for various cases.

Our use corresponds to his case Ib, in which the entire beam is smaller than the pupil, and the entering beam is nearly collimated. Starting with a knowledge of the incident power, retinal irradiance may be computed in the following steps.

1. Power flux entering the pupil The calculations above summarized the safe power limit for power incident on the cornea in mW, but for the purposes of computing retinal irradiance, power (P) is expressed in watts. Variable d represents the beam diameter in centimeters. Power divided by the cross sectional area of the beam, yields the power flux entering the pupil (H_p), in W/cm^2 .

$$H_p = \frac{P}{\left(\frac{d}{2}\right)^2} = \frac{4P}{d^2} \text{ W/cm}^2 \quad (\text{H-4})$$

2. Power flux on the retina Power flux on the retina (H_r) is concentrated by a factor equal to the incident beam diameter (d) squared divided by the retinal spot diameter (s) squared. Since some laser light is absorbed or scattered by the ocular media during its transit to the retina, a transmission factor () is included.

$$H_r = H_p \left(\frac{d^2}{s^2}\right) = \left(\frac{4P}{d^2}\right)\left(\frac{d^2}{s^2}\right) = P \left(\frac{4}{s^2}\right) \text{ W/cm}^2 \quad (\text{H-5})$$

To compute the maximum feasible irradiance we assume a minimal retinal spot diameter of 15 μm and an attenuation factor of 0.9. Variable P represents power incident at the cornea. The formula then simplifies to:

$$H_r = P(5.093 \times 10^5) \text{ W/cm}^2 \quad (\text{H-6})$$

The ANSI exposure limit for two seconds of direct viewing of a 633-nm-helium-neon laser is 0.5825 mW, and the corresponding retinal irradiance is 296.7 W/cm^2 . This is much greater than the retinal irradiance for direct viewing of the sun, which for a 2-mm pupil is approximately 8 W/cm^2 (Sloney & Wolbarsht, 1981).

Despite the lower power density, the sun is a greater thermal hazard since its 160- μm -diameter retinal image is harder to cool than the 15- μm spot formed by the laser. Taking spot diameter into account, it would require a 500-600- W/cm^2 exposure with a well focused laser beam to cause a thermal burn equivalent to staring at the sun (Lappin, 1968). Figure H.2 compares retinal irradiance levels for other familiar light sources.

Even though nearly 300 W/cm^2 for the 15- μm spot may cause no thermal damage, it will appear to be extremely bright—brighter than the sun! A retinal irradiance of greater than 1.4 W/cm^2 is considered uncomfortably bright (Sloney & Wolbarsht, 1981), and I can attest that, even though I kept laser exposure levels 100 times below ANSI (3 W/cm^2), the laser light was indeed uncomfortably bright and initially prompted an involuntary aversion response. For the purposes of limiting retinal irradiance to a comfortable level ($< 1.4 \text{ W}/\text{cm}^2$), it is necessary to attenuate laser power to 2.33 log units below the ANSI standard.

H.6

POWER LOSS FROM BEAM TRUNCATION

Laser power can be attenuated using neutral density filters, but an aperture can also reduce laser power by truncating portions of the beam. The Shack-Hartmann apparatus (Fig. 6.2) included an aperture that reduced the diameter of the incoming beam, primarily to produce a smaller, diffraction-limited spot on the retina. A side benefit of truncating the beam was that it helped reduce laser power to a safer level. My helium-neon laser produces a Gaussian beam whose intensity profile is described by the formula and curve shown in Fig. H.3.

The diameter of a Gaussian laser beam is normally specified as the central span within which beam irradiance is greater than $1/e^2$ (0.1353) of the peak value. This corresponds to a standard score of $z = 2.0$ for a Gaussian distribution. After passing through the spatial filter and collimating lens, beam diameter was expanded to 10.0 mm, and the measured power (P) contained within this beam was approximately 8 mW. An iris diaphragm truncated this beam to a diameter of 2.0 mm. The power remaining in the central core following truncation by the iris diaphragm (P_t) is proportional to the volume generated by rotating the truncated beam profile about the beam axis, divided by the corresponding volume for the full diameter. The formula for the volume generated by rotating a Gaussian profile (V) is shown in Eq. (H-7). The ratio of the truncated (V_t) to full volume (V_f) is shown in Eq. (H-8).

$$V = -2 \int_0^z \frac{1}{e^{-z^2}} dz = -2 \left. e^{-z^2} \right|_0^z = -2 \left(e^{-z^2} - 1 \right) \quad (\text{H-7})$$

$$\frac{V_t}{V_f} = \frac{-2 \left(e^{\frac{-z^2}{2}} - 1 \right)}{-2 \left(e^{\frac{-2^2}{2}} - 1 \right)} = \frac{\left(e^{\frac{-z^2}{2}} - 1 \right)}{-0.8647} \quad (\text{H-8})$$

If the iris diaphragm truncates the full 10-mm beam ($z = 2$) beam to 2 mm, one fifth of the full diameter ($z = 0.4$) remains, and the truncated power (P_t), in mW, is:

$$P_t = P \frac{\left(e^{\frac{-z^2}{2}} - 1 \right)}{-0.8647} = P \frac{\left(e^{\frac{-0.4^2}{2}} - 1 \right)}{-0.8647} = 8 (0.089) = 0.711 \text{ mW} \quad (\text{H-9})$$

Since the pellicle beam splitter, located immediately in front of the subject's eye, reflects 8% of this light into the eye, the power was further reduced to 0.057 mW, which is about one log unit below the ANSI limit for a two-second exposure. Since my goal was to reduce power to two log units below the ANSI limit, this required an additional 1.0 neutral density filter.

H.7

OTHER SAFETY PRECAUTIONS

Laser warning signs should be posted in rooms containing potentially hazardous lasers, and laser safety glasses designed for the specific wavelength used should be worn by everyone in the room when the laser is on. When not in use, the laser should be turned off.

H.8

SUMMARY

A Class IIIb helium-neon laser was used in this research to create a tiny spot of light on the subject's retina. This is not a skin hazard and is not dangerous for diffuse reflections, but accidental direct viewing of the beam at full power (8 mW) exceeds the ANSI limit for the eye's blink response time and may cause retinal damage. This slightly exceeds the observable no-burn threshold for rhesus monkeys (Fig. H.1). The ANSI Z136.1 (1993) standards provide a simple formula for computing the maximum permissible energy flux, and further computations are necessary to express the exposure limit in terms of mW of power. For a 2.0-second exposure, the ANSI limit is 0.58 mW but I reduced this by two log units to provide an additional margin of safety for my subjects.

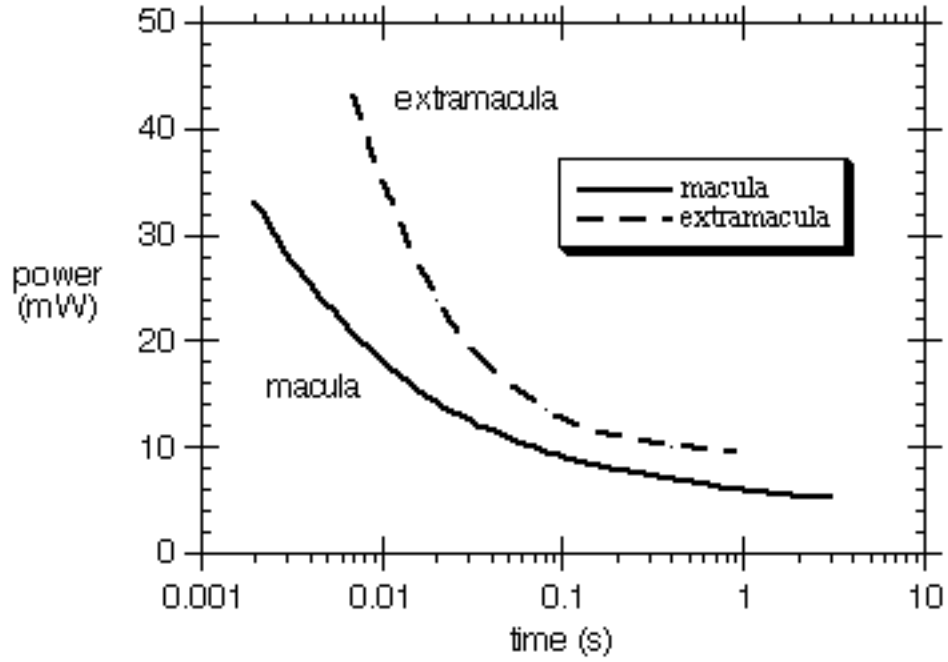


Figure H.1

These curves indicate the highest power levels that caused no observable change in rhesus monkey retinas following helium-neon laser exposure. Replotted from Lappin's (1970) data.

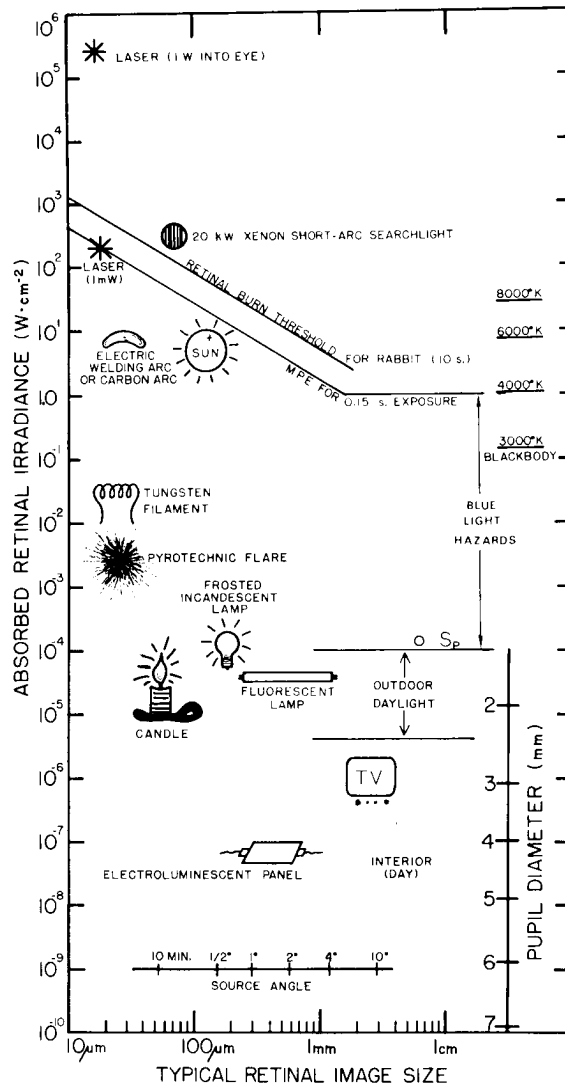
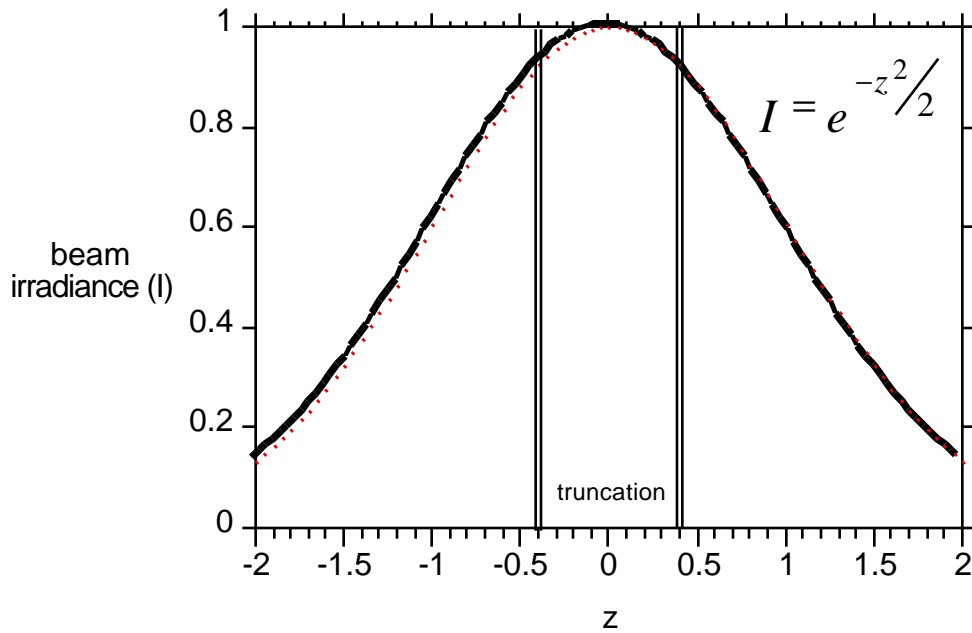


Figure H.2

Retinal irradiance for different light sources with different retinal image sizes. Scanned from Fig. 4.2 in *Safety with Lasers and Other Optical Sources* (Slaney & Wolbarsht, 1981), and used with permission from Plenum Publishing, Inc.

**Figure H.3**

Gaussian beam irradiance profile and zone of truncation (double line). Gaussian laser beam diameters are specified as the central region in which power does not fall below $1/e^2$ (0.1353) of the peak irradiance. This corresponds to a standard score of $z = 2.0$ for a Gaussian distribution. In this example, the beam has been truncated to a width of $z = 0.4$, as indicated by the double lines.



Thomas O. Salmon, O.D., Ph.D.

College of Optometry, Northeastern State University, 1001 N. Grand Ave., Tahlequah, OK 74464
Tel: (918) 456-5511 ext. 4011 Fax: (918) 456-2104
e-mail: salmon@ipa.net web page: arapaho.nsuok.edu/~salmonto

TEACHING INTERESTS

Professional and graduate studies in visual optics, theoretical and applied optics, visual perception, binocular vision, contact lenses, primary care optometry, environmental vision.

RESEARCH INTERESTS

Optical quality of the human eye, corneal topography, spatial vision. Comparison of surgical, contact lens, spectacle and adaptive optics correction of vision. Computer modeling of visual optics. Epidemiology and etiology of refractive error.

EDUCATION

1992 - 1999 Doctor of Philosophy
Indiana University School of Optometry
Committee: Drs. Larry Thibos (chairman), Arthur Bradley, Douglas Horner,
Raymond Applegate, P. Sarita Soni
Major: Vision Science & Physiological Optics; Minor: Computer Science
Dissertation: *Corneal Contribution to the Wavefront Aberration of the Eye*

1991 - 1992 Primary care resident
Northeastern State University College of Optometry, Tahlequah, OK

1975 - 1979 Doctor of Optometry
Indiana University School of Optometry

1973 - 1977 Bachelor of Science
Indiana University School of Optometry

PROFESSIONAL EXPERIENCE

1997 - present Assistant Professor of Optometry
Northeastern State University College of Optometry
Didactic & lab teaching: visual perception, binocular vision, environmental vision
Clinical instructor in primary care, contact lenses, acute care

1983 - present Research optometrist (U.S. Army Reserve)
U.S. Army Aeromedical Research Laboratory, Ft. Rucker, AL

1992 - 1997 Clinical Instructor
Indiana University School of Optometry
Clinical and didactic teaching: Primary care, contact lenses, optics

1991 - 1992 Adjunct Assistant Professor
Northeastern State University College of Optometry, Tahlequah, OK
Clinical and didactic teaching: Primary care, contact lenses

1985 - 1990 Optometry consultant
Umeoka Ophthalmology Clinic & the Sanei Optical Company, Osaka, Japan
Clinical and didactic teaching: Clinical refraction, contact lenses, geometric optics,
physiological optics, ophthalmic optics, ocular anatomy

1984 - 1986 Primary care optometry practice
Tokyo Medical and Surgical Clinic, Tokyo, Japan

1983 - 1985 Contact lens specialty practice
Miura Contact Lens Clinic, Tachikawa, Japan

1979 - 1983 Optometry Officer
U.S. Army Medical Activity, Camp Zama, Japan

1979 Neuroanatomy Assistant Instructor
Indiana University School of Optometry

Associations: Oklahoma Association of Optometric Physicians
 American Optometric Association
 American Academy of Optometry
 American Optometric Foundation
 Optical Society of America
 Fellowship of Christian Optometrists

Licensure: Oklahoma, Indiana, Hawaii

Languages: Japanese (speaking, reading, writing);
Programming: MATLAB, C, BASIC

AWARDS & HONORS

- 1999 Member, Optical Society of America committee to establish standard for measuring and reporting aberrations of the human eye
- 1998 Presider, Workshop on Aberrations, Wavefront Sensing and the Human Eye, Optical Society of America Annual Meeting Symposium.
- 1998 2nd Year Class Instructor of the Year, Optometric Student Association
- 1997 EyeSys Premier Travel Fellowship
- 1997 Certificate of Appreciation, U.S. Army Aeromedical Research Laboratory
- 1996 Promotion to Lieutenant Colonel, U.S. Army Reserve
- 1995 Fellow, American Academy of Optometry
- 1995 William C. Ezell Fellowship, American Optometric Foundation
- 1995- Reviewer: *Optometry and Vision Science*
- 1995 - Reviewer: *Journal of the Optical Society of America A*
- 1994 William C. Ezell Fellowship, American Optometric Foundation
- 1994 Gordon G. Heath Fellowship, Indiana Chapter, Am Acad of Optometry
- 1993 EyeSys Technologies Research Grant
- 1991 American Academy of Optometry Travel Fellowship
- 1990 Japan Optometric Association Certificate of Appreciation,
- 1987 U.S. Army Achievement Medal
- 1983 U.S. Army Commendation Medal
- 1979 John P. Davey Award, Indiana Chapter, American Academy of Optometry
- 1973 Four year Army ROTC Scholarship

SCIENTIFIC & PROFESSIONAL PUBLICATIONS

- 1) Applegate, R., Thibos, L., Bradley, A., Marcos, S., Roorda, A., Salmon, T. & Atchison, D. (2000). *Reference axis selection: A subcommittee report of the OSA working group to establish standards for the measurement and reporting of the optical aberration of the eye*. Visual Science and Its Applications, Technical Digest Series, in press.
- 2) Horner, D.G., Soni, P.S., Salmon, T.O., Swartz, T.S. (1999) *Myopia Progression in Adolescent Wearers of: Soft Contact Lenses vs. Spectacles*, *Optom.Vis. Sci.*, 76, 474-479.
- 3) Horner, D.G., Salmon, T.O. (1998). *Accuracy of the EyeSys 2000 in Measuring Surface Elevation of Calibrated Aspheres*: *Intl. Cont. Lens. Clin.*, 25, 171-177.
- 4) Salmon, T.O., Thibos, L.N. and Bradley, A. (1998). *Comparison of the eye's wave front aberration measured psychophysically and with the Shack-*

- Hartmann wave front sensor*. J Opt Soc Am - A., 15, 2457-2465.
- 5) Salmon, T.O., Rash, C.E. and Mora, J.C. (1998). *Videokeratoscope Accuracy and its Potential Use in Corneal Optics Research*. Ft. Rucker, AL: United States Army Aeromedical Research Laboratory. USAARL Report No. 98-29.
 - 6) Horner, D.G., Salmon, T.O. and Soni, P.S. (1998). *Chapter 17: Corneal Topography*. In: Borish, I.M. and Benjamin, W.J., eds. Borish's Clinical Refraction. Philadelphia: W.B. Saunders Company, 524-558.
 - 7) Salmon, T.O. and Thibos, L.N. (1997). *A New Single Pass Method to Measure the Eye's MTF*. In: Optics & Imaging in the Information Age Proceedings. IS&T - The Society for Imaging Science and Technology, 56-7.
 - 8) Salmon, T.O. and Horner, D.G. (1996). *A new subjective refraction method—the meridional polarized vernier optometer*. J. Am. Optom. Assoc., 67, 599-605.
 - 9) Wang, Y.Z., Thibos, L.N., Lopes, N., Salmon, T.O. and Bradley, A. (1996). *Subjective Refraction of the Peripheral Field Using Contrast Detection Acuity*. J. Am. Optom. Assoc., 67, 584-589.
 - 10) Salmon, T.O. and Horner, D.G. (1995). *Comparison of Elevation, Curvature and Power Descriptors for Corneal Topographic Mapping*. Optom. Vis. Sci., 72, 800-808.
 - 11) Salmon, T.O. (1994). *Minimizing Residual Astigmatism with Rigid Gas Permeable Lens Flexure*. J. Japan Cont. Lens Soc., 35, 285-289.
 - 12) Salmon, T.O. (1993). *Use of Thin Flexible RGP Lenses to Correct Astigmatism*. J. Japan Optom. Assoc., 11, 16-21.
 - 13) Salmon, T.O. (1992). *Beneficial Flexure - Using Thin RGPs to Correct Residual Astigmatism*. Cont. Lens Spectrum, 7, 39-42.
 - 14) Kikkawa, Y. and Salmon, T.O. (1990). *Advantages of the Contact Lens Apical Alignment Fit*. J. Japan Cont. Lens Soc., 32, 290-299.
 - 15) Kikkawa, Y. and Salmon, T.O. (1990). *Rigid Lens Tear Exchange and the Tear Mucous Layer*. Cont. Lens Forum, 1990: Dec., 17-24.
 - 16) Salmon, T.O. (1990). *CLs in the Land of the Rising Sun*. Cont. Lens Forum.1990: Jul., 57-58.
 - 17) Salmon, T.O. (1984). *Overview of Keratoconus and Case Report*. J. Japan Optom.Assoc., 2, 31-41.

SCIENTIFIC PRESENTATIONS

- 1) Salmon, T.O., van de Pol, C., (1999). *Orbscan Accuracy In Measuring Corneal Surface Elevation*. American Academy of Optometry Annual Meeting, Seattle, WA.

- 2) Hatfield, L., Tran, L., Salmon, T.O., Schifanella, L.L., (1999). Post-Lasik Visual Performance In Low Light. American Academy of Optometry Annual Meeting, Seattle, WA.
- 3) Salmon, T.O., Thibos, L.N. (1998). *Relative Contribution of the Cornea and Internal Optics to the Aberrations of the Eye*. American Academy of Optometry Annual Meeting, San Francisco, CA.
- 4) Salmon, T.O., Thibos, L.N. (1998). *The Wavefront Aberration Function of Normal Human Corneas*. American Academy of Optometry Annual Meeting, San Francisco, CA.
- 5) Salmon, T.O., Thibos, L.N. (1998). *Relative balance of corneal and internal aberrations in the human eye*. Optical Society of America Annual Meeting, Baltimore, MD.
- 6) Salmon, T.O., Thibos, L.N., Bradley, A. (1997). *Comparison of wavefront aberration functions measured by the Hartmann-Shack sensor and a psychophysical method for the same eyes*. American Academy of Optometry Annual Meeting, San Antonio, TX.
- 7) Salmon, T.O., Thibos, L.N. (1977). *Eyesys accuracy in surface elevation measurement and estimation of the corneal wavefront aberration function*. American Academy of Optometry Annual Meeting, San Antonio, TX.
- 8) Salmon, T.O., Thibos, L.N., Bradley, A. (1997). *Hartmann-Shack sensor accuracy and precision in measuring aberrations of the eye*. Optical Society of America Annual Meeting Program, Long Beach, CA.
- 9) Salmon, T.O. and Thibos, L.N. (1996). *A New Single Pass Method to Measure the Eye's MTF*. Optical Society of America Annual Meeting Program, 1996, 99.
- 10) Horner, D.G. , Soni, P.S., Salmon, T.O. and Schroeder, T.L. (1996). *Junior High Age Children's Myopia Progression in Soft Lenses vs. Spectacles*. Invest Ophthalmol Vis Sci., 37:3,S1004.
- 11) Horner, D.G. and Salmon, T.O. (1995). *Junior High Age Children's Myopia Progression in Soft Lenses vs. Spectacles*. Optom. Vis. Sci., 72:12s, 96.
- 12) Salmon, T.O. and Horner, D.G. (1995). *Comparison of Surface Elevation, Dioptric Curvature, and Refractive Power Maps of an Ellipsotric Cornea*. Invest. Ophthalmol. Vis. Sci., 36:4, S1032.
- 13) Salmon, T.O. and Horner, D.G. (1994). *Comparison of Four Methods of Corneal Topography Mapping*. Optom. Vis. Sci., 71:12s, 130.
- 14) Horner, D.G., Salmon, T.O., and Soni, P.S. (1994). *Junior High Age Children's*

- Myopia Progression in Soft Lenses vs. Spectacles.* Optom. Vis. Sci., 71:12s, 78.
- 15) Horner, D.G., Salmon, T.O., Moen L.J., and Taylor, L.K. (1994). *Can Residual Astigmatism Account for the Variation in Corrected Acuties in Patients Wearing Soft Toric Lenses?* Optom. Vis. Sci., 71:12s, 56.
 - 16) Salmon, T.O. and Horner, D.G. (1993). *A New Approach To Refraction: The Meridional Polarized Vernier Optometer.* Optom. Vis. Sci., 70:12s, 154-155.
 - 17) Salmon, T.O. (1993). *Minimizing Residual Astigmatism with Rigid Gas Permeable Lens Flexure.* Japan Contact Lens Society Annual Meeting Program, 1994, 78.
 - 18) Salmon, T.O. (1991). *Predicting Residual Astigmatism In RGP Contact Lenses.* Optom. Vis. Sci., 68:12s, 100.